

**Studies of fibrinogen and fibronectin binding to a  
*Staphylococcus aureus* surface protein**

Vaclav Stemberk

PhD

University of York  
Department of Chemistry

September 2011

---

**Abstract**

*Staphylococcus aureus* is a common human pathogen and a major cause of infective endocarditis (IE), an infection of native as well as prosthetic heart valves. The fibronectin-binding protein of *S. aureus* (FnBPA) is a cell-wall attached adhesin that is closely linked with the development of IE owing to its ability to bind the plasma glycoproteins fibrinogen (Fg) and fibronectin (Fn). The FnBPA molecule contains adjacent Fn- and Fg-binding regions. Previous studies identified eleven intrinsically unstructured, homologous repeats from FnBPA (FnBRs) that bind Fn through an unusual tandem  $\beta$ -zipper mechanism. It was proposed that the Fg-binding region of FnBPA comprised two domains, N2 and N3, with predicted IgG folds. The main focus of this work is to characterise the FnBPA-Fg interaction, to define the N2N3/FnBRs boundary and to determine whether simultaneous binding of Fg and Fn to FnBPA is affected by cooperativity or potential steric effects.

Surface plasmon resonance in conjunction with isothermal titration calorimetry showed that the FnBPA N2N3 region retains the Fg-binding activity of intact FnBPA. X-ray crystallography of N2N3 in complex with the Fg-peptide revealed the location of the Fg binding site on N2N3 and that a  $\beta$ -zipper was formed upon Fg binding. A range of new biophysical data led to a redefined N2N3/FnBRs boundary, which, in the form of a ten residue long flexible linker, comprised more residues than originally thought. Simultaneous binding of Fg and the N-terminal domain of Fn to an rFnBPA construct, consisting of the N2N3 region and the first FnBR, was demonstrated for the first time. However, simultaneous binding was not observed when intact Fg and Fn were used, providing the first preliminary evidence for the importance of steric hindrance in regulation of the ternary complex formation.

---

**Table of Contents**

<b>Abstract</b> .....	<b>1</b>
<b>List of Tables</b> .....	<b>9</b>
<b>List of Figures</b> .....	<b>10</b>
<b>Acknowledgements</b> .....	<b>14</b>
<b>Author's declaration</b> .....	<b>15</b>
<b>1 Introduction</b> .....	<b>16</b>
1.1 <i>Staphylococcus aureus</i> .....	16
1.2 Infective Endocarditis (IE) .....	17
1.3 Platelets .....	19
1.3.1 Integrin GPIIbIIIa ( $\alpha_{IIb}\beta_{III}$ ).....	20
1.3.2 GPIIbIIIa activation .....	20
1.3.3 Platelet activation .....	21
1.4 Fibrinogen (Fg).....	23
1.4.1 Overview .....	23
1.4.2 Fg conversion to fibrin .....	24
1.4.3 Fg-platelet interaction .....	26
1.5 Fibronectin (Fn).....	27
1.5.1 Overview .....	27
1.5.2 Fibril formation .....	29
1.6 Staphylococcal adhesins .....	29
1.6.1 FnBPA binds Fn via the Tandem $\beta$ -zipper.....	31
1.6.2 The FnBPA-Fn interaction facilitates invasion of the endothelium.....	33
1.6.3 FnBPA binds to Fg.....	34
1.6.4 Role of FnBPA in platelet activation .....	37
1.7 Biophysical techniques .....	37
1.7.1 Isothermal titration calorimetry.....	37

---

1.7.2	Surface plasmon resonance .....	39
1.7.2.1	Introduction .....	39
1.7.2.2	SPR experiment .....	41
1.7.2.3	Ligand immobilization by amine coupling.....	41
1.7.2.4	Data processing .....	43
1.7.3	Crystallography .....	44
1.7.3.1	Overview .....	44
1.7.3.2	Crystallization .....	44
1.7.3.3	Vapour diffusion.....	45
1.7.3.4	Seeding .....	45
1.7.3.5	Crystal symmetry .....	46
1.7.3.6	X-ray diffraction.....	47
1.7.3.7	Data collection and processing.....	48
1.7.3.8	Phase problem .....	49
1.7.3.9	Experimental phasing.....	49
1.7.3.10	Molecular replacement .....	50
1.7.3.11	Model building, refinement and validation.....	50
1.8	Aims .....	52
<b>2</b>	<b>Materials and Methods .....</b>	<b>53</b>
2.1	Solutions.....	53
2.2	Native proteins .....	54
2.2.1	Fg from human plasma.....	54
2.2.2	Fn from human plasma.....	54
2.3	Synthetic peptides and proteolytic fragments .....	55
2.3.1	Fg peptide (Fg1).....	55
2.3.2	SfBI-5 .....	55
2.3.3	Fg fragment D (FgD) .....	55
2.3.4	N-terminal domain of fibronectin (NTD) .....	56

---

2.4	Molecular biology .....	56
2.4.1	Construct design.....	56
2.4.2	Primer design .....	57
2.4.3	Agarose gel electrophoresis .....	58
2.4.4	Ligation independent cloning using the pET-YSBLIC3C vector .....	58
2.4.4.1	Plasmid linearization .....	58
2.4.4.2	Vector LIC T4 polymerase reaction .....	59
2.4.4.3	Insert polymerase chain reaction (PCR).....	59
2.4.4.4	Insert LIC T4 polymerase reaction and annealing .....	60
2.4.5	Transformation of competent <i>E.coli</i> cells with plasmid DNA.....	60
2.5	Expression of recombinant proteins .....	61
2.6	Purification of recombinant proteins .....	61
2.6.1	Cell lysis and supernatant clarification .....	61
2.6.2	Nickel-affinity purification .....	61
2.6.3	SDS-PAGE.....	62
2.6.4	NATIVE-PAGE .....	63
2.6.5	Cleavage of N-terminal His <sub>6</sub> -tag with HRV 3C.....	64
2.6.6	Anion exchange chromatography .....	64
2.6.7	Size-exclusion chromatography .....	65
2.6.8	Protein concentration measurements and calculations.....	66
2.7	Plasma pull-down assay .....	66
2.8	Biophysical techniques.....	66
2.8.1	NMR spectroscopy.....	66
2.8.2	Surface plasmon resonance .....	67
2.8.2.1	Sample preparation.....	67
2.8.2.2	Ligand immobilization .....	68
2.8.2.3	Affinity .....	69
2.8.2.4	Kinetics.....	69

---

2.8.2.5 Ternary complex.....	70
2.8.3 Isothermal titration calorimetry.....	70
2.8.4 Analytical ultracentrifugation (AUC) .....	71
2.8.5 Differential Scanning Calorimetry (DSC) .....	71
2.8.6 Electrospray ionization mass spectrometry (ESI/MS).....	71
2.8.7 Crystallization of N2N3T.....	71
2.8.8 Data collection and N2N3T structure determination .....	72
2.8.9 Crystallization of the N2N3T-Fg1 complex .....	73
2.8.10 Data collection and N2N3T-Fg1 structure determination.....	73
<b>3 Molecular biology, expression and purification of recombinant FnBPA protein constructs.....</b>	<b>74</b>
3.1 Introduction .....	74
3.2 Aims .....	74
3.3 Overview of rFnBPA proteins used in this study.....	75
3.3.1 N2N3 .....	75
3.3.2 N2N3T .....	76
3.3.3 N2N3E .....	76
3.3.4 The fA .....	76
3.3.5 N1N2 and N3 .....	77
3.3.6 AF1.....	77
3.3.7 <sup>15</sup> N-N2N3, <sup>15</sup> N-N2N3T and <sup>15</sup> N-AF1 .....	77
3.4 Molecular biology of N2N3T and N2N3E.....	78
3.5 Expression of recombinant proteins .....	79
3.5.1 Unlabelled rFnBPA proteins .....	79
3.5.2 <sup>15</sup> N-N2N3, <sup>15</sup> N-N2N3T and <sup>15</sup> N-AF1 .....	80
3.6 Purification of recombinant proteins .....	80
3.6.1 Nickel-affinity chromatography of His <sub>6</sub> -N2N3 .....	81

---

3.6.2	Nickel-affinity chromatography of His <sub>6</sub> -tagged N2N3T, N2N3E, N1N2 and fA .....	86
3.6.3	Nickel-affinity chromatography of His <sub>6</sub> -N3 .....	88
3.6.4	Nickel-affinity chromatography of His <sub>6</sub> -AF1 .....	90
3.6.5	Anion exchange chromatography of AF1 .....	92
3.6.6	Size-exclusion chromatography of N2N3 .....	93
3.6.7	Size-exclusion chromatography of N2N3T, N2N3E, N1N2, fA, N3 and AF1 .....	95
3.7	Oligomerization state of N2N3 and AF1 .....	99
3.8	Initial structural characterization of the rFnBPA proteins by 1D <sup>1</sup> H NMR spectroscopy .....	102
3.9	Solubility and long-term stability of rFnBPA proteins .....	103
3.10	Summary .....	105
<b>4</b>	<b>Structural characterization of N2N3 and its interaction with Fg.....</b>	<b>107</b>
4.1	Introduction .....	107
4.2	Aims .....	108
4.3	Identification of the FnBPA region that binds Fg .....	108
4.4	N2N3 binding to Fg .....	111
4.5	Determining the role of the putative latch strand in Fg binding.....	112
4.6	Intact Fg binds FnBPA with similar affinity to Fg1 .....	114
4.7	Analysis of the FnBPA-Fg interaction by NMR spectroscopy .....	116
4.7.1	Optimization of conditions for HSQC spectra of <sup>15</sup> N-N2N3.....	116
4.7.2	TROSY-HSQC spectra of <sup>15</sup> N-N2N3 and <sup>15</sup> N-N2N3T +/- Fg1 .....	119
4.8	Crystal structure of N2N3T .....	123
4.9	Crystal structure of the N2N3T-Fg1 complex.....	127
4.10	Discussion .....	133
4.10.1	N2N3T retains the Fg-binding ability of the full A-domain.....	133
4.10.2	The putative latch strand is not required for Fg binding.....	133

---

4.10.3	Fg1 is a good model for the Fg-FnBPA interaction.....	133
4.10.4	Structural similarities of N2N3 from FnBPA, SdrG and ClfA .....	134
4.10.5	Fg1 binds N2N3 as a parallel $\beta$ -strand.....	135
4.10.6	The N2N3T-Fg1 interface.....	137
4.10.7	The putative latch strand ‘structural flexibility’ hypothesis .....	138
4.10.8	The minimum Fg-binding region.....	139
<b>5</b>	<b>Does AF1 form a ternary complex with Fn and Fg?.....</b>	<b>140</b>
5.1	Introduction .....	140
5.2	Aims .....	140
5.3	AF1 interacts individually with Fn and Fg.....	141
5.3.1	Determination of the $K_d$ for the AF1-NTD interaction.....	141
5.3.2	Determination of the $K_d$ for the AF1-Fn interaction.....	143
5.3.3	AF1 binding to Fg .....	143
5.4	Analysis of AF1 by NMR spectroscopy.....	145
5.5	Can NTD and FgD/Fg/Fg1 bind AF1 simultaneously to form ternary complexes?.....	147
5.5.1	Determination of the $K_d$ s for the FgD-AF1+/-NTD interactions.....	147
5.5.2	Determination of the $K_d$ s for the NTD-AF1+Fg1 interaction.....	148
5.5.3	Formation of the NTD-AF1-Fg ternary complex.....	149
5.6	Steric hindrance prevents formation of an Fn-AF1-Fg ternary complex. .	151
5.7	Fg and Fn binding to AF1 under physiological conditions demonstrated by a plasma pull-down assay.....	153
5.8	Discussion .....	154
5.8.1	Determination of the $K_d$ for the AF1-NTD interaction.....	154
5.8.2	Determination of the $K_d$ for the AF1-Fn interaction.....	155
5.8.3	Determination of the $K_d$ for the AF1-Fg1/FgD/Fg interactions.....	156
5.8.4	Characterization of AF1 by NMR spectroscopy .....	157
5.8.5	NTD does not affect the FgD-AF1 interaction significantly .....	157



---

5.8.6	Fg1 does not affect the NTD-AF1 interaction .....	159
5.8.7	Formation of the NTD-AF1-Fg ternary complex.....	159
5.8.8	Steric effects prevent simultaneous binding of intact Fg and Fn to the AF1 construct .....	161
5.8.9	AF1 binds Fg and Fn when exposed to human plasma.....	162
<b>6</b>	<b>General discussion.....</b>	<b>164</b>
6.1	The FnBPA-Fg interaction .....	164
6.2	The putative cooperativity of Fg- and Fn-binding to FnBPA .....	168
<b>7</b>	<b>Appendices .....</b>	<b>172</b>
<b>8</b>	<b>Abbreviations .....</b>	<b>176</b>
<b>9</b>	<b>References .....</b>	<b>180</b>

---

**List of Tables**

Table 1.1 The microbiology of IE.....	18
Table 1.2 Crystal systems .....	47
Table 2.1 Composition of all buffers and solutions used in the project.....	54
Table 2.2 Agarose gel electrophoresis parameters.....	58
Table 2.3 PCR set-up .....	59
Table 2.4 Nickel-affinity purification parameters.....	62
Table 2.5 SDS-PAGE parameters. ....	63
Table 2.6 NATIVE-PAGE parameters. ....	63
Table 2.7 Anion exchange chromatography parameters.....	65
Table 2.8 Size-exclusion chromatography parameters. ....	65
Table 2.9 Amine coupling immobilization steps. ....	69
Table 3.1 rFnBPA protein constructs.....	75
Table 3.2 List of primers corresponding to rFnBPA constructs and primers used for sequencing.....	78
Table 3.3 Summary of rFnBPAs properties and expression yields .....	99
Table 4.1 Results of the SPR experiment designed to test the binding of truncated rFnBPA derivatives to FgD.....	110
Table 4.2 Summary of kinetic and thermodynamic parameters for the N2N3-Fg interactions .....	115
Table 4.3 Data collection and refinement statistics for N2N3T.....	124
Table 4.4 Data collection and refinement statistics for the N2N3T-Fg1 complex ..	128
Table 5.1 Summary of kinetic and thermodynamic parameters for the interactions with AF1 .....	145

---

**List of Figures**

Figure 1.1 <i>Staphylococcus aureus</i> .....	16
Figure 1.2 Integrin GPIIb/IIIa activation. ....	21
Figure 1.3 Platelet adhesion and aggregation under flow .....	22
Figure 1.4 Structure of the Fg dimer .....	23
Figure 1.5 Coagulation cascade .....	25
Figure 1.6 Fg polymerization and fibrin crosslinking.....	26
Figure 1.7 Fn domain composition .....	28
Figure 1.8 The domain organization of FnBPA compared with other known MSCRAMMs .....	31
Figure 1.9 Sequence alignment of FnBRs.....	32
Figure 1.10 Possible mechanism of the FnBPA-mediated uptake of staphylococci by endothelial cells.....	33
Figure 1.11 Sequence alignment of N2 and N3 domains of FnBPA and other Fg-binding MSCRAMMs .....	35
Figure 1.12 Superposition of SdrG and ClfA free, and in complex with their cognate Fg peptides .....	36
Figure 1.13 Schematic diagram of a typical isothermal titration calorimeter and an example of experimental data. ....	39
Figure 1.14 Surface plasmon resonance overview.....	40
Figure 1.15 Schematic diagram representing the amine coupling immobilization process.....	42
Figure 1.16 Phase diagram.....	45
Figure 1.17 Bragg's Law .....	48
Figure 2.1 pET-28a vector map .....	57
Figure 3.1 Schematic diagram of native FnBPA .....	74
Figure 3.2 Agarose gel electrophoresis of the PCR products and of the plasmid linearization reaction.....	79

---

Figure 3.3 <i>E. coli</i> growth curves .....	80
Figure 3.4 SDS-PAGE analysis of bench-top nickel-affinity chromatography of N2N3.....	82
Figure 3.5 Nickel-affinity chromatography of N2N3 .....	83
Figure 3.6 SDS-PAGE analysis of the nickel-affinity chromatography of His <sub>6</sub> -N2N3.....	84
Figure 3.7 SDS-PAGE of the HRV 3C cleavage of His <sub>6</sub> -N2N3.....	85
Figure 3.8 Nickel-affinity chromatography of the cleaved N2N3 .....	85
Figure 3.9 Nickel-affinity chromatography of N2N3T and N2N3E.....	86
Figure 3.10 Nickel-affinity chromatography of N1N2 and fA .....	87
Figure 3.11 A trial nickel-affinity chromatography of His <sub>6</sub> -N3. ....	88
Figure 3.12 SDS-PAGE analysis of the trial nickel-affinity chromatography of His <sub>6</sub> -N3.....	89
Figure 3.13 Nickel-affinity chromatography of His <sub>6</sub> -N3.....	89
Figure 3.14 SDS-PAGE analysis of nickel-affinity chromatography of His <sub>6</sub> -N3 .....	90
Figure 3.15 Nickel-affinity chromatography of His <sub>6</sub> -AF1.....	91
Figure 3.16 SDS-PAGE analysis of nickel-affinity chromatography of His <sub>6</sub> -AF1 ...	91
Figure 3.17 Anion exchange chromatography of AF1.....	92
Figure 3.18 SDS-PAGE analysis of AF1 IEX .....	93
Figure 3.19 Size-exclusion chromatography of N2N3 .....	94
Figure 3.20 SDS-PAGE of the size-exclusion chromatography of N2N3.....	94
Figure 3.21 Repeated size-exclusion chromatography of the N2N3 main species....	95
Figure 3.22 Size-exclusion chromatography of N2N3T and N2N3E.....	96
Figure 3.23 Size-exclusion chromatography of N1N2 and fA .....	97
Figure 3.24 Size-exclusion chromatography of AF1 and N3 .....	98
Figure 3.25 Determination of the oligomerization state of N2N3 using sedimentation velocity experiment.....	100
Figure 3.26 Determination of the oligomerization state of AF1 using sedimentation velocity experiment.....	101

Figure 3.27 Comparison of the 1D $^1\text{H}$ NMR spectra of N2N3, AF1 and N1N2 .....	103
Figure 3.28 Raw DSC data for AF1, N2N3 and N2N3T thermal unfolding experiments .....	105
Figure 4.1 SPR Sensorgram .....	109
Figure 4.2 Determination of the $K_d$ for the N2N3-Fg interaction.....	112
Figure 4.3 Binding of N2N3 and N2N3T to FgD .....	113
Figure 4.4 Determination of the $K_d$ for the N2N3-Fg1 interaction.....	114
Figure 4.5 Inhibition of the N2N3-FgD interaction by Fg1 .....	115
Figure 4.6 Comparison of 2D $^1\text{H}^{15}\text{N}$ HSQC and 2D $^1\text{H}^{15}\text{N}$ TROSY-HSQC spectra of $^{15}\text{N}$ -N2N3.....	117
Figure 4.7 Comparison of the 2D $^1\text{H}^{15}\text{N}$ TROSY-HSQC spectra of $^{15}\text{N}$ -N2N3 at pH 6.0 and pH 7.4 .....	118
Figure 4.8 2D $^1\text{H}^{15}\text{N}$ TROSY-HSQC spectra of $^{15}\text{N}$ -N2N3 with and without a 6-molar excess of Fg1 .....	119
Figure 4.9 2D $^1\text{H}^{15}\text{N}$ TROSY-HSQC spectra of $^{15}\text{N}$ -N2N3 and $^{15}\text{N}$ -N2N3T .....	121
Figure 4.10 2D $^1\text{H}^{15}\text{N}$ TROSY-HSQC spectra of $^{15}\text{N}$ -N2N3 and $^{15}\text{N}$ -N2N3T with a 6-molar excess of Fg1 .....	122
Figure 4.11 Image of N2N3T crystals and corresponding diffraction pattern.....	123
Figure 4.12 Ribbon representation of the N2N3T structure .....	125
Figure 4.13 The topology of the domain folds.....	126
Figure 4.14 Hydrophobic surface representation of N2N3T .....	126
Figure 4.15 Image of N2N3T-Fg1 crystals and corresponding diffraction pattern .	127
Figure 4.16 Electron density map for Fg1 .....	129
Figure 4.17 Structure of the F' - G' loop .....	129
Figure 4.18 Ribbon representation of the N2N3T-Fg1 complex .....	130
Figure 4.19 Electrostatic surface representation of the Fg-binding site.....	131
Figure 4.20 Hydrogen bonds between Fg1 and N2N3T .....	132
Figure 4.21 Comparison of N2N3T with ClfA and SdrG .....	135
Figure 4.22 Comparison of N2N3T-Fg1 with ClfA-Fg1 <sub>(D16A)</sub> and SdrG-Fg $\beta$ .....	136

---

Figure 4.23 The crystal structure of Fg.....	136
Figure 4.24 Comparison of the ClfA and ClfA-Fg1 <sub>(D16A)</sub> structures .....	137
Figure 4.25 N2N3 edge-strand protection.....	138
Figure 5.1 Schematic diagram of the potential Fn-FnBPA-Fg complex .....	141
Figure 5.2 Determination of the $K_d$ for the NTD-AF1 interaction .....	141
Figure 5.3 Determination of the $K_d$ for the AF1-NTD interaction .....	142
Figure 5.4 Determination of the $K_d$ for the AF1-Fn interaction .....	143
Figure 5.5 Determination of the $K_d$ for the AF1-Fg1 and AF1-Fg interactions .....	144
Figure 5.6 Determination of the $K_d$ for the AF1-FgD interaction .....	145
Figure 5.7 2D $^1\text{H}^{15}\text{N}$ TROSY-HSQC spectra of $^{15}\text{N}$ -AF1 and $^{15}\text{N}$ -FnBPA1 .....	146
Figure 5.8 2D $^1\text{H}^{15}\text{N}$ TROSY-HSQC spectra of $^{15}\text{N}$ -AF1 and $^{15}\text{N}$ -N2N3T .....	147
Figure 5.9 Determination of the $K_d$ s for the FgD-AF1+/-NTD interactions .....	148
Figure 5.10 Determination of the $K_d$ for the NTD-AF1+Fg1 interaction.....	149
Figure 5.11 Formation of the NTD-AF1-Fg ternary complex .....	150
Figure 5.12 Fg and Fn binding to AF1.....	151
Figure 5.13 Overview of the SPR experiment .....	152
Figure 5.14 SDS-PAGE analysis of fractions from the plasma pull-down assay with N2N3 and AF1 resin columns.....	154
Figure 5.15 The avidity effect associated with the binding of a bivalent analyte....	156
Figure 5.16 Comparison of the SPR sensorgrams given by the FgD-AF1 and FgD-AF1+NTD interactions .....	158
Figure 5.17 Schematic diagram representing the two possible scenarios in the SPR measurements of the $K_d$ for the FgD-AF1+NTD interaction.....	159
Figure 5.18 Predicted conformation of the Fg1-AF1-NTD ternary complex .....	160
Figure 6.1 Sequence alignment of ligands for the Fg-binding MSCRAMMs.....	165
Figure 6.2 Predicted conformation of the Fg1-AF1-NTD ternary complex .....	168

---

## Acknowledgements

First and foremost I wish to thank Dr. Jennifer Potts and Prof. Colin Kleanthous for the opportunity to undertake my PhD under their supervision and for continual support and guidance. I am also grateful for the new ideas and useful suggestions provided by Prof. Anthony Wilkinson throughout the course of my PhD.

I would like to thank the members of the Potts group both past and present: Dr. Nicole Norris, Dr. Nicola Meenan, Dr. Richard Jones, Dominika Gruszka, Adrian Speakman, Dr. Kate Atkin for her help with crystallography, Andy Brentnall for his expertise in NMR, Russell Hobbs for the unlimited supply of stimulating alkaloids, Dr. Richard Bingham for his supervision during the first weeks of my PhD, and especially Dr. Gemma Harris for her help, patience, and invaluable support during the final stages of my PhD.

For data collection and a general introduction into crystallography I thank Dr. Johan Turkenburg, Sam Hart and in particular Dr. Olga Moroz (York Structural Biology Laboratory) for elucidating the wonders of data processing and structure refinement. I also thank Dr. Iain Manfield (University of Leeds) for conducting the DSC experiments and Dr. Andrew Leech and Berni Strongitharm for their continuous help and expertise with various biophysical techniques. I am grateful to Dr. David Williamson for technical NMR support and to Julia Walton (at that time Technology Facility, University of York) for producing some of the rFnBPA constructs.

I am most grateful to Dr. Natasha Brown for her love, endless support and encouragement as well as providing valuable medical insight into all matters cardiovascular, and for teaching me English.

I am deeply indebted to my parents Vera and Vaclav Stemberk, and sister Dagmar and her son Marek for the immeasurable amount of support I have received. This thesis is dedicated to them.

This work was funded by BBSRC.

## **Author's declaration**

I declare that all the work presented herein is my own original work unless explicitly stated in the text.

Vaclav Stemberk

September 2011



# 1 Introduction

## 1.1 *Staphylococcus aureus*

*Staphylococcus aureus* is a facultative anaerobic Gram-positive bacterium and a major human pathogen (Foster, 2004; Foster, 2005). *S. aureus* is a subspecies of the genus *Staphylococcus* which belongs to the bacterial family Staphylococcaceae. Staphylococci have a characteristic spherical shape, approximately one micron in diameter, are non-motile and do not form spores. Cell division occurs successively in three perpendicular planes with sister cells remaining attached following each division, resulting in formation of irregular clusters of cells (Figure 1.1).

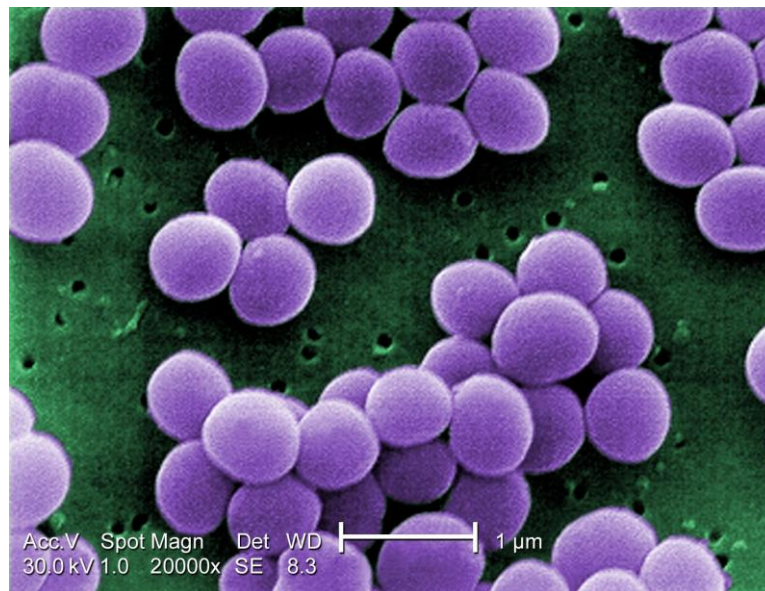


**Figure 1.1** *Staphylococcus aureus*. High magnification (x20 000) of a scanning electron micrograph, depicting clusters of the vancomycin-resistant strain of *S. aureus* (CDC, 2008).

Most commonly a commensal organism, *S. aureus* permanently colonises the skin and nasal mucous membranes of approximately 20% of the population, and up to 60% intermittently (Bergqvist, 1950; Gould and Mc, 1954; Duncan et al., 1957; Rippon and Vogelsang, 1956). As a major nosocomial pathogen, *S. aureus* is associated with infections of surgical wounds and indwelling medical devices (Arrecubieta et al., 2006). Taking advantage of compromised host defence mechanisms, namely mucosal breaches and impaired host immunity, *S. aureus* is implicated in the aetiology of superficial skin lesions as well as primary infections such as osteomyelitis and infective endocarditis (IE) (Claro et al., 2011; Piroth et al., 2008).

*S. aureus* expresses an array of potential virulence factors that facilitate immune evasion as well as colonization and infection of the human host. These factors include adhesins (Fibronectin-binding protein A, Clumping factor A, Protein A) (Edwards et al., 2010; O'Brien et al., 2002a; Uhlen et al., 1984), leukotoxins ( $\gamma$ -haemolysin, Panton-Valentine leukocidin) (Menestrina et al., 2003), enterotoxins (superantigenic toxic shock syndrome toxin-1) (Chesney et al., 1984), the ability to block recognition by neutrophils (through secreted superantigen-like protein) (Wines et al., 2006) and resistance to both lysozyme (membrane-bound O-acetyltransferase) and to oxidative stress (Toll-like receptor 2) (Bera et al., 2005; Watanabe et al., 2007). However, the most concerning aspect of *S. aureus* virulence is its acquired resistance to antibiotics and in particular the rate at which new resistant strains evolve (Diekema et al., 2001). Methicillin-resistant *S. aureus* (MRSA) is now recognised as a worldwide nosocomial pathogen accounting for up to 60% of all nosocomial infections in some parts of the developed world (Fluit et al., 2001; Tiemersma et al., 2004). Moreover, relatively recent cases of community-acquired MRSA have been reported and are becoming more frequent (Baba et al., 2002; Naimi et al., 2001; Adhikari et al., 2002; Dufour et al., 2002). Isolation of the first MRSA strain resistant to vancomycin (the therapeutic antigen effective against MRSA) (VRSA) in 1996 (Hiramatsu et al., 1997), demonstrates the adaptability of *S. aureus* and highlights the need for new therapeutic targets and agents.

## 1.2 Infective Endocarditis (IE)

IE is a life-threatening disease associated with infection of the endocardium (heart endothelium), particularly the heart valves, and with embolism (Que and Moreillon, 2011). IE has a relatively low median incidence of 3.6 per 100 000 per year worldwide (de Sa et al., 2010; Delahaye et al., 1995) albeit with a very high mortality of up to 40% that is dependent on the type of pathogen, underlying condition of the patient and whether a native or prosthetic valve is infected (Hasbun et al., 2003; Chirouze et al., 2004). IE can be classified into one of four groups; left-sided native-valve IE (the most frequent) (Murdoch et al., 2009), left-sided prosthetic-valve IE (the most severe) (Wang et al., 2007), right-sided IE and healthcare-associated IE (Wilson et al., 2002; Benito et al., 2009). The epidemiology of IE has been altered as a result of medical progress. Whilst in the past IE was restricted mainly to children and young adults with chronic heart conditions,

currently the main risk groups include intravenous drug users, patients with prosthetic valves or catheters, patients undergoing haemodialysis and elderly individuals with degenerative valve lesions (Normand et al., 1995; Wilson et al., 2002). Similarly, the change in epidemiology also correlates with a change in the microbiology of IE. Whilst streptococci remain the predominant pathogens in the general population, *S. aureus* is the major cause of IE in intravenous drug users and of healthcare-related IE (Table 1.1) (Que and Moreillon, 2011).

Pathogen	N valve			P valve		
	CA-IE	HA-IE		ID-IE	E-IE	L-IE
		N	N-N			
<i>S. aureus</i>	20	47	42	68	36	18
Coagulase-negative staphylococci	6	12	15	3	17	20
Enterococcus	9	14	17	5	8	13
Viridians streptococci	28	11	6	10	2	10
<i>Streptococcus bovis</i>	10	3	3	1	2	7
HACEK	3	0	0	0	0	2
Fungi	0	2	2	1	9	3
Other	14.6	7.5	10	3	6	14
Negative blood culture	11	5	6	5	17	12

**Table 1.1 The microbiology of IE.** The incidence of each pathogen (%) within infections of different patient groups. The patients were divided into two main groups; native (N) (Benito et al., 2009; Murdoch et al., 2009) and prosthetic (P) (Wang et al., 2007) valve infections, which were then further divided into sub-groups; community-acquired IE (CA-IE) (n=1065), healthcare-associated IE (HA-IE) (n=557), nosocomial (N) (n=303), non-nosocomial (N-N) (n=254), intravenous drug users (ID-IE) (n=237), early IE (E-IE) (n=53) and late IE (L-IE) (n=331). The number *n* corresponds to the number of patients tested within each group. HACEK abbreviation stands for; *Haemophilus* species (*H. parainfluenzae*, *H. aphrophilus* and *H. paraphrophilus*), *Actinobacillus actinomycetemcomitans*, *Cardiobacterium hominis*, *Eikenella corrodens*, and *Kingella* species. The table summarises data from, Benito and colleagues (2009), Murdoch and colleagues (2009) and Wang and colleagues (2007) and was adapted from Que and Moreillon (2011).

The initial stage in the pathogenesis of IE is completed within minutes of infection and involves colonisation of heart valves by bacteria in the bloodstream (Moreillon et al., 2002). The primary attachment of the bacteria to the endocardium is facilitated

by haemostatic events, which occur in response to the appearance of physical lesions that expose the subendothelial extra-cellular matrix (ECM). The most common causes of the lesions include valve damage by turbulent blood flow, catheters, electrodes, inflammation or exposure to chemicals/materials (in intravenous drug users) (Croft et al., 2004; Stehbens et al., 2000). The primary stage of valve colonisation is followed by maturation of the vegetation, further recruitment of platelets and ECM proteins, and eventual bacterial shedding causing continuous bacteraemia and embolization of the vegetation fragments. Consequently, IE is considered as a serious systemic infection which remains universally lethal unless aggressively treated with a combination of antibiotics (Baddour et al., 2005; Habib et al., 2009).

### 1.3 Platelets

Human platelets are small and anucleated megakaryocyte-derived cells essential to numerous pathophysiological processes including haemostasis, thrombosis, vessel repair, inflammation and host defence (Furie and Furie, 2005; Ruggeri et al., 1999). Abnormalities in platelet function lead to numerous disorders, clinically presenting with excessive bleeding or thrombosis (George et al., 1990; George and Shattil, 1991). Platelets have a characteristic discoid shape with the dimensions of 2 - 4 by 0.5  $\mu\text{m}$ , a lifespan of approximately 5 - 10 days and, under normal circumstances, up to  $450 \times 10^9/l$  can be found circulating in the blood stream (Figure 1.3A) (George, 2000). The surface of the platelet membrane is covered with a variety of receptors, most of which are involved in haemostasis (Rivera et al., 2009). Internally, the platelets contain two types of secretory granules, dense and  $\alpha$ , which contribute to the platelet aggregation and coagulation process. The dense granules secrete ADP, serotonin and  $\text{Ca}^{2+}$ , while the  $\alpha$ -granules secrete an array of proteins including von Willebrand factor (vWF), Fibrinogen (Fg), P-selectin, additional integrin GPIIbIIIa (Section 1.3.1) and thrombospondin (Blair and Flaumenhaft, 2009). The content of both the dense granules and the  $\alpha$ -granules is relevant to platelet haemostatic function. The platelet cytoplasm comprises mainly actin and myosin allowing changes in shape and clot retraction (Andrews and Berndt, 2004). Under normal circumstances, and in the absence of activating stimuli, the platelets remain in a resting state constantly surveying the integrity of the vasculature in order to prevent blood loss in the event of tissue trauma (Michelson, 2003).

### 1.3.1 Integrin GPIIbIIIa ( $\alpha_{IIb}\beta_{III}$ )

Integrins are a group of transmembrane heterodimers that play a key part in diverse processes that require interactions between cells, or between a cell and the matrix, such as embryogenesis, haemostasis, thrombosis, cancer metastases or lymphocyte helper and killer cell function (Hynes, 1992). There are 24 different heterodimers in mammals generated by combinations of 18 integrin  $\alpha$  and eight  $\beta$  subunits (Humphries, 2000). Glycoprotein IIbIIIa (GPIIbIIIa) (235 kDa) is the most abundant platelet integrin (40 000 - 80 000 copies on the surface of resting platelets) and is essential for platelet aggregation due to its ability to bind Fg, fibronectin (Fn), vWF and vitronectin (Bennett, 2005). The two subunits IIb and IIIa are expressed, assembled and processed in megakaryocytes. The integrin heterodimer comprises a large extracellular domain, a small cytoplasmic domain and a short transmembrane spanning region (Rocco et al., 2008). Each IIb subunit contains 1008 residues that form two polypeptide chains connected by a disulfide bond. The ectodomain of IIb comprises two Calf domains, a Thigh domain and a  $\beta$ -propeller domain. IIb is associated non-covalently, and in a  $\text{Ca}^{2+}$  dependent manner, with the IIIa subunit ectodomain which contains 762 residues consisting of a  $\beta$ -Tail, four I-EGF repeats, a PSI (plexin, semaphoring and integrin) domain, a hybrid domain and a  $\beta$ 1 domain (Figure 1.2A) (Bennett, 2005; Xiao et al., 2004). Fg is the major ligand for GPIIbIIIa, targeting specific sites within the amino terminal ends of both the IIb and IIIa domains. The binding site consists of the  $\beta$ 1 specificity determining loop (SDL) and a cap subdomain composed of four  $\beta$ -propeller loops. Fg binding to GPIIbIIIa is divalent cation dependent and the Fg-binding site contains three metal-binding sites. The  $\text{Mg}^{2+}$ -binding site (MIDAS; metal ion-dependent adhesion site) is located in the centre of the Fg-binding site. The other two metal-binding sites bind  $\text{Ca}^{2+}$  and are located distal to the  $\beta$ -propeller (ADMIDAS - adjacent to MIDAS) and near the  $\beta$ -propeller LIMBS (ligand-induced metal binding site) (Springer et al., 2008).

### 1.3.2 GPIIbIIIa activation

The integrin GPIIbIIIa ectodomain occupies two conformational states: the compact low affinity conformation and the open and extended high affinity conformation (Figure 1.2B). As a result of the change in conformation, the binding site, which is located in the head piece of the ectodomain, becomes readily accessible to potential

ligands. Structural rearrangement of the extracellular domains, leading to exposure of ligand-induced binding sites (LIBS) and activation of GPIIbIIIa, is induced by a combination of inside-out and outside-in signalling events. It has been shown that the change from the lower to the higher affinity state of GPIIbIIIa can be triggered by exposure to an excessive concentration of peptides containing either the GRGDSP or HHLGGAKQAGDV sequences (Du et al., 1991). It has been proposed that *S. aureus* could be capable of inducing such conformational changes in the integrin ectodomain by adhering to a large number of Fg and Fn molecules which contain both the RGD and the AGDV sequences.

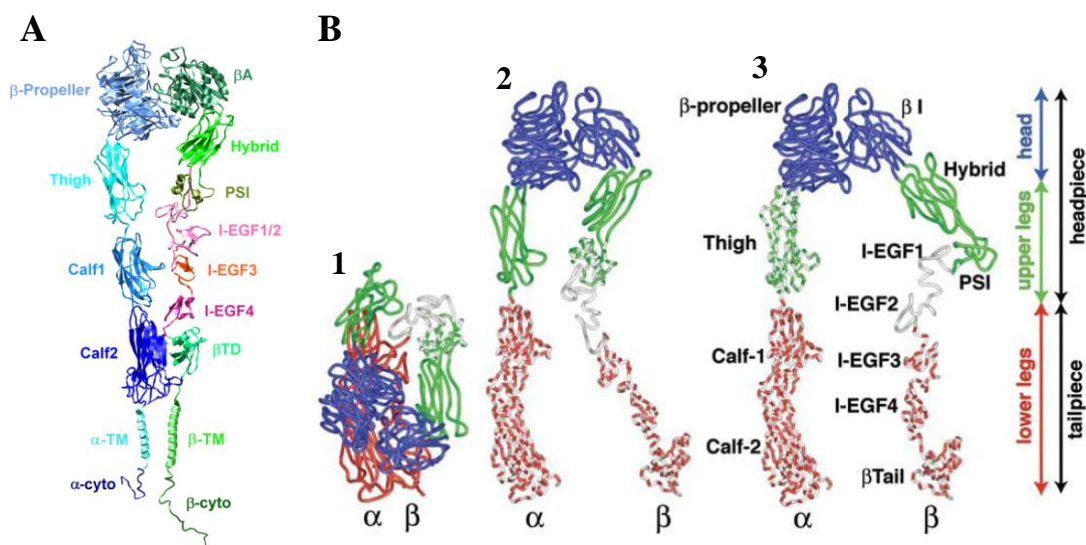


**Figure 1.2 Integrin GPIIbIIIa activation.** (A) The extended model of integrin GPIIbIIIa as generated by homology modelling (Rocco et al., 2008). (B) Different stages of integrin activation are represented by three conformations with varying affinities to ligands. (1) The compact conformation represents the low-affinity state with the ligand-binding sites mostly occluded. (2) The extended form with the closed headpiece conformation exhibits intermediate affinity. (3) By switching the angle between the  $\beta 1$  and hybrid domains from acute to obtuse, the headpiece changes to an open conformation, resulting in an activated high-affinity state of the GPIIbIIIa ectodomain. Figure adapted from Xiao and colleagues (2004).

### 1.3.3 Platelet activation

Platelet activation and aggregation is a complex process requiring the coordination of numerous events that lead to the formation of a stable platelet plug (Ruggeri and Mendolicchio, 2007). Following a vessel injury and exposure of the subendothelial ECM, platelet surface receptors GPIb and GPVI interact with the ECM components vWF and collagen, respectively, in a primary response leading to initial platelet

tethering and activation. Adhesion of the platelets triggers a signalling cascade resulting in cytoskeletal remodelling, spreading and shear-dependent membrane tether formation (Figure 1.3A), secretion of coagulation mediators from both the dense granules and the  $\alpha$ -granules, inside-out signalling activation (Section 1.3.2) and upregulation of GPIIb/IIIa (Blair and Flaumenhaft, 2009; Andrews and Berndt, 2004). Although Fg is the main GPIIb/IIIa ligand, Fn and vWF also bind GPIIb/IIIa, which facilitates inter-platelet interactions that lead to recruitment of additional platelets, rapid aggregation and adhesion to the initial layer of platelets on the vessel wall (Figure 1.3B) (Andrews et al., 2004). The activated platelet aggregate has an upregulatory effect on the coagulation cascade (Section 1.4.2), resulting in further stabilization of the clot by a fibrin network. The multitude and complexity of the interactions involved in aggregation allows the formation of a stable platelet plug in the *in vivo* haemodynamic conditions, which range from low wall shear rates in venules ( $<500 \text{ s}^{-1}$ ) to shear rates as high as  $40\,000 \text{ s}^{-1}$  in stenosed arteries (Jackson, 2007).

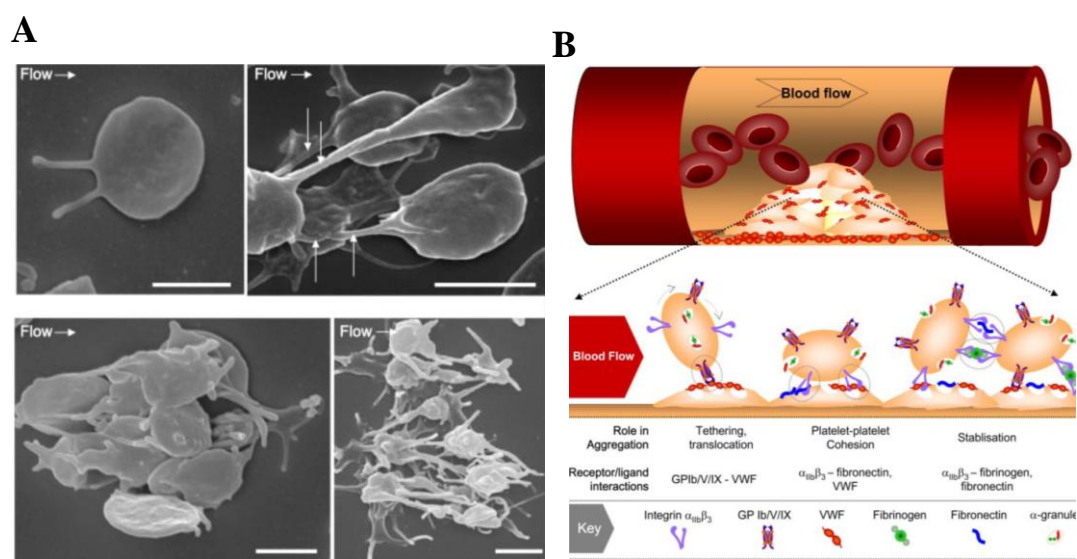


**Figure 1.3 Platelet adhesion and aggregation under flow.** (A) Scanning electron microscopy images of (top left) a single discoid platelet forming initial membrane tethers, (top right) the formation of adhesion contacts between platelets via membrane tethers (arrows), (bottom left) the aggregation of discoid platelets around a central activated platelet and (bottom right) the development of a stable aggregate associated with platelet shape change and extension of filopodial projections. Images from Jackson (2007). (B) A simplified diagram depicting the process of platelet aggregation under shear rate, highlighting the multiple receptor-ligand interactions. Figure adapted from Jackson (2007).



## 1.4 Fibrinogen (Fg)

### 1.4.1 Overview

Fibrinogen is a 340 kDa glycoprotein synthesised primarily in hepatocytes and found either as a soluble protein in plasma (at a concentration of approximately 3 mg/ml) or as a part of the ECM (Herrick et al., 1999). Fg is a major blood clotting agent essential to numerous biological processes including wound healing and haemostasis (Ni et al., 2000). Fg is a dimer of trimers comprising two identical sets of three individual polypeptide chains A $\alpha$ , B $\beta$  and  $\gamma$ . Letters ‘A’ and ‘B’ designate respective fibrinopeptides cleaved by thrombin upon Fg conversion to fibrin (Section 1.4.2). The B $\beta$  chain comprises 461 residues (56 kDa), while several variants of A $\alpha$  and  $\gamma$  chains exist as the direct result of alternative splicing. The major form of the A $\alpha$  chain contains 610 residues (70 kDa). The most frequent  $\gamma$  chain form is called  $\gamma$ A or  $\gamma$  and comprises 411 residues (48 kDa) (Kollman et al., 2009). The minor  $\gamma$  chain variant, called  $\gamma'$ , contains a unique sequence of 20 anionic amino acids ( $\gamma'$ 408-427) in place of the C-terminal AGDV residues found in the  $\gamma$ A variant. The entire native Fg dimer is held together by 29 disulfide bonds and is divided into a single central E region linked to two outer D regions via coiled-coil connectors (Figure 1.4) (Medved and Weisel, 2009).

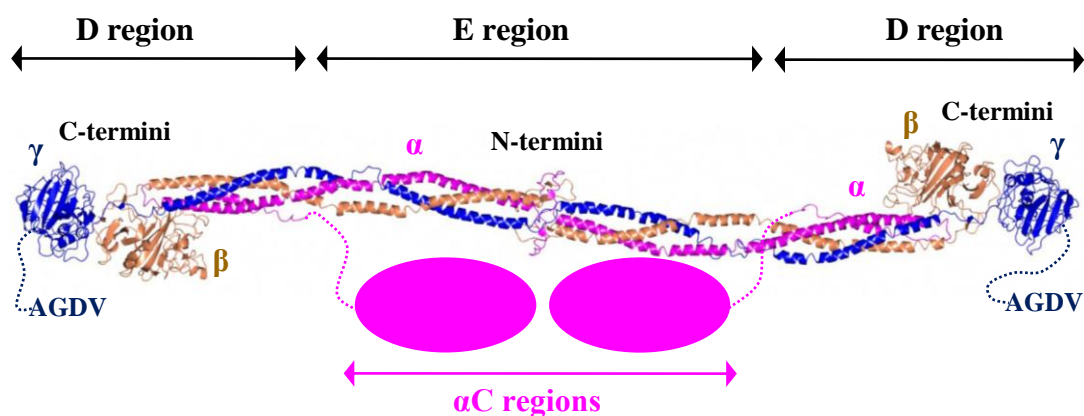


**Figure 1.4 Structure of the Fg dimer.** The crystal structure (PDB entry – 3GHG) depicts Fg comprising two sets of chains, A $\alpha$  (magenta), B $\beta$  (coral) and  $\gamma$  (blue) joined at the N-terminal ends. The  $\alpha$ C regions are indicated (ellipse) and the disordered  $\gamma$  chain C-termini (including the last four C-terminal residues AGDV) are suggested by a dotted line. The C-terminal D regions are connected to the N-terminal E region by coiled-coil connectors (Kollman et al., 2009).



## 1.4.2 Fg conversion to fibrin

In the event of inflammation the synthesis of Fg radically increases and, once at the site of injury, the soluble Fg is converted to insoluble fibrin fibres, the building blocks of a blood clot. This provisional clot is essential to processes including haemostasis, cell migration and wound healing. Conversion of soluble Fg to fibrils, which cross-link to form insoluble fibrin, is one of the final steps of the coagulation cascade (Mosesson, 2005). The concept of haemostasis as a cascade of sequential enzymatic conversions following one of two distinct pathways (intrinsic or extrinsic) provides an easily conceptualized overview of the process (Figure 1.5). The coagulation cascade is governed by a complex regulatory mechanism and involves sequential activation of numerous zymogens ultimately leading to generation of excessive amounts of thrombin (thrombin burst) (Mann et al., 2006; Adams and Bird, 2009). The proteolytic action of thrombin, in combination with the activation of factor XIII (FXIIIa), leads to conversion of Fg to fibrin and ultimately a stable fibrin network. The clot is protected from fibrinolysis by thrombin activatable fibrinolysis inhibitor (TAFI) (Nesheim et al., 1979; Tracy et al., 1992).

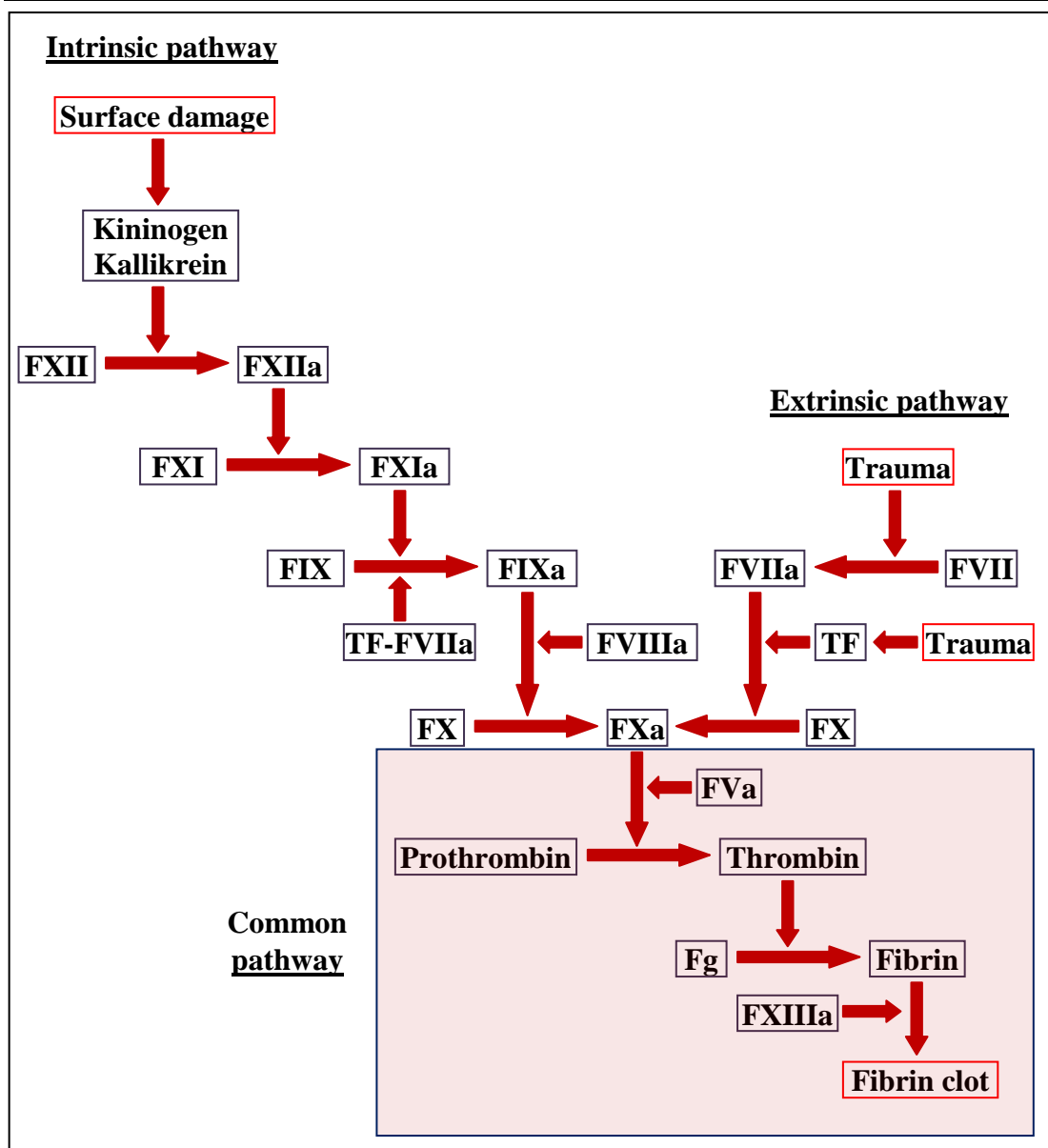


**Figure 1.5 Coagulation cascade.** The cascade model of coagulation depicts the two interlinked pathways leading to thrombin activation and subsequent conversion of Fg to fibrin. Terms denoting individual coagulation factors comprise F followed by the type of the factor, and the ‘a’ at the end of the term indicates the active form. Figure adapted from Adams and Bird (2009).

The process of fibrin assembly is initiated by cleavage of the N-terminal fibrinopeptide A ( $F_pA$ ) by thrombin. As a result a polymerization site  $E_A$ , extending over residues 17-20 (GPRV) of the  $\alpha$  chain, is exposed and is free to interact with the complementary binding pocket ( $D_A$ ) located between residues  $\gamma$ 337-379 of the D region. Intermolecular association between  $E_A$  and  $D_A$  leads to the formation of half-staggered, double-stranded protofibrils (Fowler et al., 1981; Ferry, 1952) (Figure 1.6). Fibrin assembly can also be initiated by the removal of the N-terminal fibrinopeptide B ( $F_pB$ ), albeit at a slower rate (Blomback et al., 1978). Cleavage of

F<sub>p</sub>B also releases the  $\alpha$ C regions which can subsequently participate in the intermolecular interactions between neighbouring fibrils. Monomeric fibrin and fibrin fibrils undergo FXIIIa (plasma protransglutaminase)-catalysed cross-linking ( $\gamma$ 406Lys of one chain and  $\gamma$ 398/399Glu of another) through intermolecular  $\epsilon$ -( $\gamma$ -glutamyl) lysine covalent bonds (Doolittle et al., 1971; Standeven et al., 2005). FXIIIa also mediates the interaction between the  $\alpha$ C regions. Resulting simultaneous lateral fibril association and branching leads to formation of an extensive network (Figure 1.6) (Mosesson, 2005).

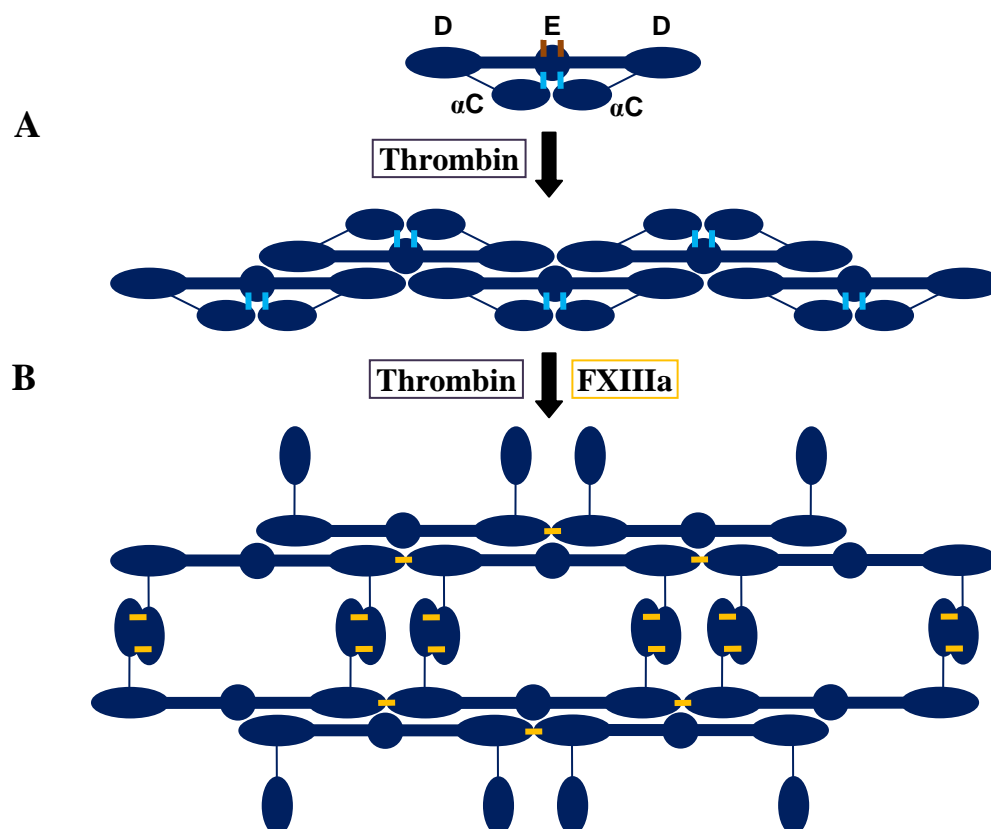


**Figure 1.6 Fg polymerization and fibrin crosslinking.** (A) Cleavage of F<sub>p</sub>A (brown) by thrombin enables polymerization of Fg into fibrils. (B) Thrombin removal of F<sub>p</sub>B (cyan) releases  $\alpha$ C regions. FXIIIa crosslinking (yellow) of the  $\gamma$  chain C-termini as well as the  $\alpha$ C regions leads to formation of fibrin fibres. Figure adapted from Standeven and colleagues (2005).

### 1.4.3 Fg-platelet interaction

Interactions of Fg with platelets occur via multiple integrin receptors located on platelet surfaces. Each Fg monomer contains several potential binding sites that can interact with integrin receptors, two RGD (Arg-Gly-Asp) motifs ( $A\alpha$  95-98 and 572-

574) and a unique C-terminal AGDV (Ala-Gly-Asp-Val) motif ( $\gamma$  408-411). Whilst both motifs have the ability to bind most integrin receptors, the AGDV appears to be the preferred target for the most abundant platelet integrin GPIIbIIIa (Section 1.3.1) (Springer et al., 2008; Fitzgerald et al., 2006a; Hoekstra et al., 1995). The AGDV motif represents the four most C-terminal  $\gamma$  chain residues located within a larger region extending over a minimum of 17 residues, which is also targeted by FnBPA and ClfA (Wann et al., 2000; Hawiger et al., 1982). The C-terminus is highly susceptible to proteolysis suggesting that a large portion of this region is solvent exposed (Yee et al., 1997; Kollman et al., 2009). Using protease inhibitors, the Fg D region terminating with residue  $\gamma$ 403, was produced. Studies of the D region revealed three different conformations for residues 392-403, mainly arising from the differences in the local crystal packing, which also points to the flexible nature of the C-terminus. NMR studies of the  $\gamma$  chain C-terminus, using the synthetic peptides  $\gamma$ 385-411 and  $\gamma$ 392-411, indicated a low population of ordered structure with the exception of loops and  $\beta$  turns (Blumenstein et al., 1992). However, it is important to note that these studies were performed on peptides and that within intact Fg stabilizing interactions might exist.

## 1.5 Fibronectin (Fn)

### 1.5.1 Overview

Fibronectin, a product of hepatocytes, is a glycoprotein found either as a soluble component of human plasma (at a concentration of approximately 0.3 mg/ml), or as a part of the ECM (Matsuda et al., 1978; Hynes, 1985). The carbohydrate content of plasma Fn is approximately 6%, however, very little is known about the role of glycosylation (Ruoslahti et al., 1981). Fn is a complex molecule and an important host adhesin implicated in a wide range of interactions including binding to heparin, transglutaminase, DNA and fibrin (Hynes and Yamada, 1982). Fn contains a gelatin-binding domain (GBD) ( $^6\text{Fn}1$ - $^9\text{Fn}1$ ) and an integrin-binding RGD loop ( $^{10}\text{Fn}3$ ) (Figure 1.7A) (Henderson et al., 2010; Pankov and Yamada, 2002). The major form of Fn is a heterodimer comprising two different isoforms (between 230 and 270 kDa) of the Fn monomer, linked at the C-terminus by disulfide bonds. Each Fn monomer consists of three different types of modules, F1, F2 and F3 (Figure 1.7B). Different module types do not share a high level of sequence homology,

however they all contain  $\beta$ -sheets (Potts et al., 1999; Sticht et al., 1998; Main et al., 1992). The N-terminal domain (NTD) of Fn is composed of five F1 modules ( $^1\text{F1}$ - $^5\text{F1}$ ) and the sequence is highly conserved across species (Potts and Campbell, 1996). NTD is involved in the formation of Fn fibrils, which can then bind to other components of the ECM (Schwarzbauer and Sechler, 1999). Modules  $^2\text{F1}$ - $^5\text{F1}$  also bind to FnBRs of FnBPA via a tandem  $\beta$ -zipper with nanomolar affinity, as described in section 1.6.1 (Schwarz-Linek et al., 2003; Meenan et al., 2007). The level of plasma Fn is regulated by  $\beta 1$  integrin-dependent endocytosis and subsequent degradation (Sottile and Chandler, 2005).

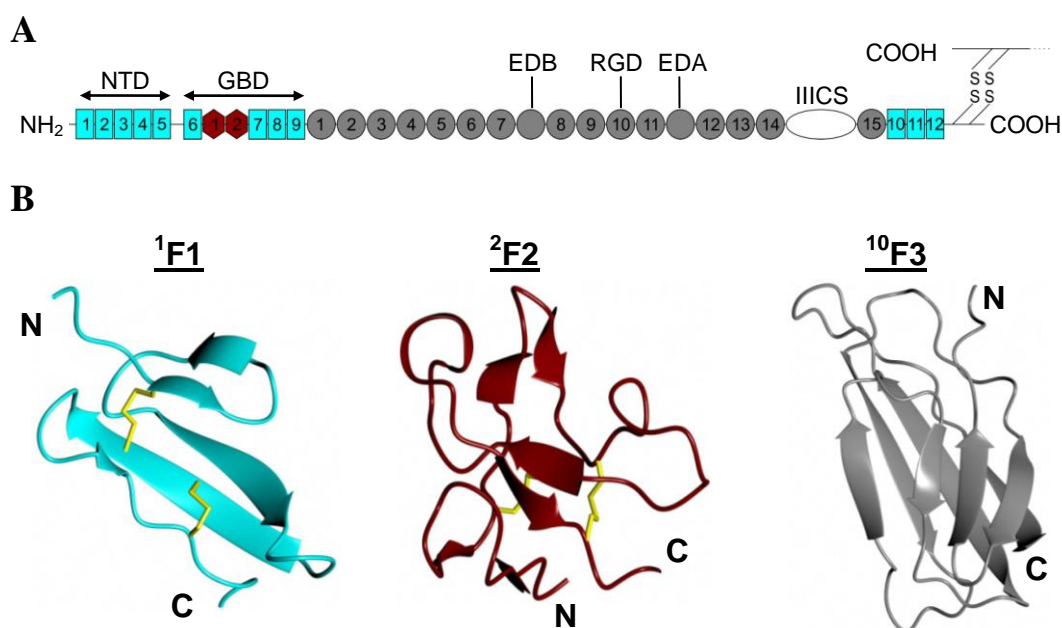


**Figure 1.7 Fn domain composition.** (A) Domain organization of Fn. The Fn monomer is comprised almost entirely of three module types, F1 (cyan), F2 (brown) and F3 (grey). NTD ( $^1$ - $^5\text{F1}$  modules), GBD and the integrin-binding RGD motif are highlighted. The positions of the alternatively spliced regions EDA, EDB and IIICS, and the location of the intra-chain disulfide bonds are also indicated. (B) Ribbon representations of the crystal structures of the three individual Fn modules including disulfide bonds (yellow) and labelled termini. The F1 module (PDB entry 1QGB) (cyan) forms a five strand structure comprising stacked two- and three-strand  $\beta$ -sheets (Potts et al., 1999). The module is stabilized by two disulfide bonds, one formed between the two  $\beta$ -sheets and one between the two C-terminal  $\beta$ -strands. The F2 module (PDB entry 2FN2) has an irregular structure containing a combination of  $\beta$ -strands and loops, stabilized by a pair of disulfide bonds (Sticht et al., 1998). With 90-100 residues, the F3 module (PDB entry 1TTF) is the largest of the three modules (Main et al., 1992). It is composed of a typical  $\beta$  sandwich with a three-stranded  $\beta$ -sheet stacked onto a four-stranded  $\beta$ -sheet. The structure contains no disulfide bridges for stabilisation.

### 1.5.2 Fibril formation

The conversion of Fn to insoluble fibrils, and subsequent incorporation into the ECM, plays a key role in the formation, maintenance and turnover of the ECM, but also facilitates cell attachment to the ECM (Sottile and Hocking, 2002; Sottile and Chandler, 2005; Pereira et al., 2002). The extended fibrils are generated by NTD-dependent self-association of Fn dimers (Schwarzbauer, 1991). However, due to intramolecular interactions the plasma Fn dimer adopts a compact and inactive conformation with occluded NTDs (Erickson and Carrell, 1983). Consequently, a conformational change has to take place to enable fibril formation (Mao and Schwarzbauer, 2005). Such a conformational change is induced upon Fn binding to numerous cell surface integrins via the RGD motif, with  $\alpha_5\beta_1$  representing the main target (Schwarzbauer and Sechler, 1999; Sottile and Wiley, 1994). The interaction with the integrins on the cell surface triggers a plethora of signalling events inside the cell, with the main cascade involving FAK phosphorylation and Src kinase recruitment leading to reorganisation of the actin cytoskeleton (Friedland et al., 2009). Resulting mechanical forces exerted by cells cause Fn to undergo a conformational change from the compact to a more extended state. NTD is exposed as a consequence, initiating Fn self-assembly and fibril formation (Schwarzbauer and Sechler, 1999).

### 1.6 Staphylococcal adhesins

A group of *S. aureus* extracellular proteins collectively referred to as MSCRAMMs (microbial surface components recognizing adhesive matrix molecules) (Patti and Hook, 1994) represent cell-surface adhesins that specifically recognise and interact with components of the ECM including Fn, Fg, collagen, elastin or keratin (Froman et al., 1987; Zong et al., 2005; Roche et al., 2004; McDevitt et al., 1995; O'Brien et al., 2002b). Fn-binding proteins A and B (FnBPA/B) and Clumping factors A and B (ClfA/B) are examples of *S. aureus* MSCRAMMs and they have been implicated in colonisation and invasion of host cells (Piroth et al., 2008; Roche et al., 2004; Schaffer et al., 2006; Arrecubieta et al., 2006). While ClfA and ClfB bind specifically to Fg (Ganesh et al., 2011; Ganesh et al., 2008), both FnBPA and FnBPB are bi-functional proteins that interact with both Fg and Fn (Wann et al., 2000; Burke et al., 2010). Results of several studies, both *in vitro* and *in vivo*,

identified FnBPA of *S. aureus* as a crucial virulence factor implicated in IE (Heying et al., 2007; Piroth et al., 2008; Que et al., 2005) and showed that FnBPA alone confers the ability to promote experimental endocarditis (EE) by the otherwise non-pathogenic *Lactococcus lactis* (Moreillon et al., 2001). Experiments involving truncated derivatives of FnBPA, as well as heterologous gene expression, revealed Fg-binding is responsible for early valve colonization and induction of IE, while Fn-binding is required for invasion of the endothelium and persistence of infection (Piroth et al., 2008; Heying et al., 2009). These results suggest that synergy between Fg and Fn binding might lead to more efficient infection, potentially rendering FnBPA the prime factor in the aetiology of *S. aureus* IE.

FnBPA is a complex extracellular adhesin encoded by the *fnbA* gene. A survey of clinical isolates revealed that the majority also contained the *fnbB* gene for FnBPB (Peacock et al., 2000). Both FnBPA/B share high sequence identity (95% for the Fn-binding region (FnBR) and 45% for the N-terminal Fg-binding region) (Burke et al., 2010), and are implicated in IE development (Figure 1.8) (Fitzgerald et al., 2006b). FnBPA consists of an N-terminal secretory signal sequence required for Sec-dependent secretion, followed by the Fg- and elastin-binding A-domain and adjacent Fn-binding region. The C-terminus contains proline-rich repeats, cell wall and membrane spanning regions, and a sortase recognition motif (LPETG) that is required for anchoring the protein into the cell wall (Wann et al., 2000; Schwarz-Linek et al., 2003; Keane et al., 2007b) (Figure 1.8A). Similarities in structural organisation have also been identified within the N-termini of other MSCRAMMs including FnBPB (*S. aureus*) (Burke et al., 2010), ClfA (*S. aureus*) (Ganesh et al., 2008), SdrC (*S. aureus*) (Barbu et al., 2010), CNA (*S. aureus*) (Zong et al., 2005) and SdrG (*S. epidermidis*) (Ponnuraj et al., 2003) (Figure 1.8B). Like FnBPA, ClfA is also implicated in IE aetiology, however, the *clfA* gene is expressed mainly during the stationary phase of growth, while the *fnbA* gene is expressed during the exponential phase which is more likely to reflect the growth conditions in bacteraemia (Saravia-Otten et al., 1997; O'Brien et al., 2002a). As a result, ClfA and FnBPA are likely to have roles in different stages of infection.

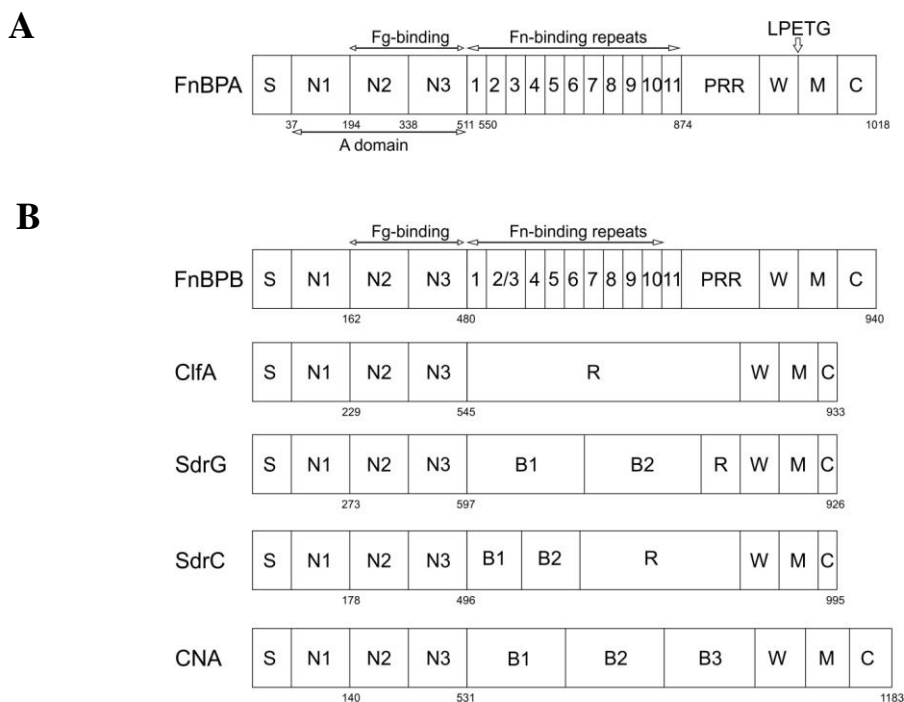


**Figure 1.8 The domain organization of FnBPA compared with other MSCRAMMs. (A)** The domain composition of FnBPA. The N-terminus of FnBPA contains a secretory signal sequence (S) followed by an Fg- and elastin-binding A-domain and an adjacent region of Fn-binding repeats (FnBRs) FnBPA1-11. The C-terminus contains proline-rich repeats (PRR), cell wall (W) and membrane (M) spanning regions, a sortase recognition motif (LPETG) and a short cytoplasmic region (C). **(B)** The domain organisation of other MSCRAMMs; FnBPB, ClfA, SdrG, SdrC and CNA including additional Ser/Asp repeat region (R) and repeats of unknown function (B1-3).

### 1.6.1 FnBPA binds Fn via the Tandem $\beta$ -zipper

The Fn-binding region of FnBPA comprises eleven homologous, intrinsically unstructured FnBRs stretching over 363 residues (FnBPA<sub>512-874</sub>). Each Fn-binding repeat (FnBR) is approximately 40 amino-acids long and has the potential to bind NTD of a single molecule of Fn (Figure 1.9) (Meenan et al., 2007; Edwards et al., 2010; Schwarz-Linek et al., 2003). So far, six repeats (1, 4, 5, 9, 10 and 11) have been shown to exhibit nanomolar affinity binding to NTD (Meenan et al., 2007). The binding interaction occurs via an unusual and efficient tandem  $\beta$ -zipper mechanism, where four short motifs within the FnBR form an additional  $\beta$ -strand anti-parallel to the existing  $\beta$ -sheets of sequential Fn<sup>2-5</sup>F1 modules (Schwarz-Linek et al., 2003; Bingham et al., 2008) (Figure 1.9). The intrinsically disordered character of the FnBRs (Gunasekaran et al., 2003) allows the formation of an extensive intermolecular interface with relatively few residues. The high efficiency is demonstrated by the FnBPA1-NTD tandem  $\beta$ -zipper interaction which results in



approximately 4300 Å<sup>2</sup> of the accessible surface area being buried despite FnBPA1 comprising only 37 residues (Bingham et al., 2008). It is probable that the formation of such an extensive interface compensates to some extent for the entropic penalty associated with the FnBR-NTD interactions. Binding of an intrinsically disordered protein (e.g. FnBR) to its target (e.g. NTD) is often accompanied by disorder-to-order transition, leading to entropy reduction of the system. However, the entropic cost is usually offset by the favourable enthalpic contribution serving as the driving force for the binding. The multivalency of FnBPA (Massey et al., 2001) could potentially allow simultaneous high affinity binding of multiple Fn molecules (Meenan et al., 2007).

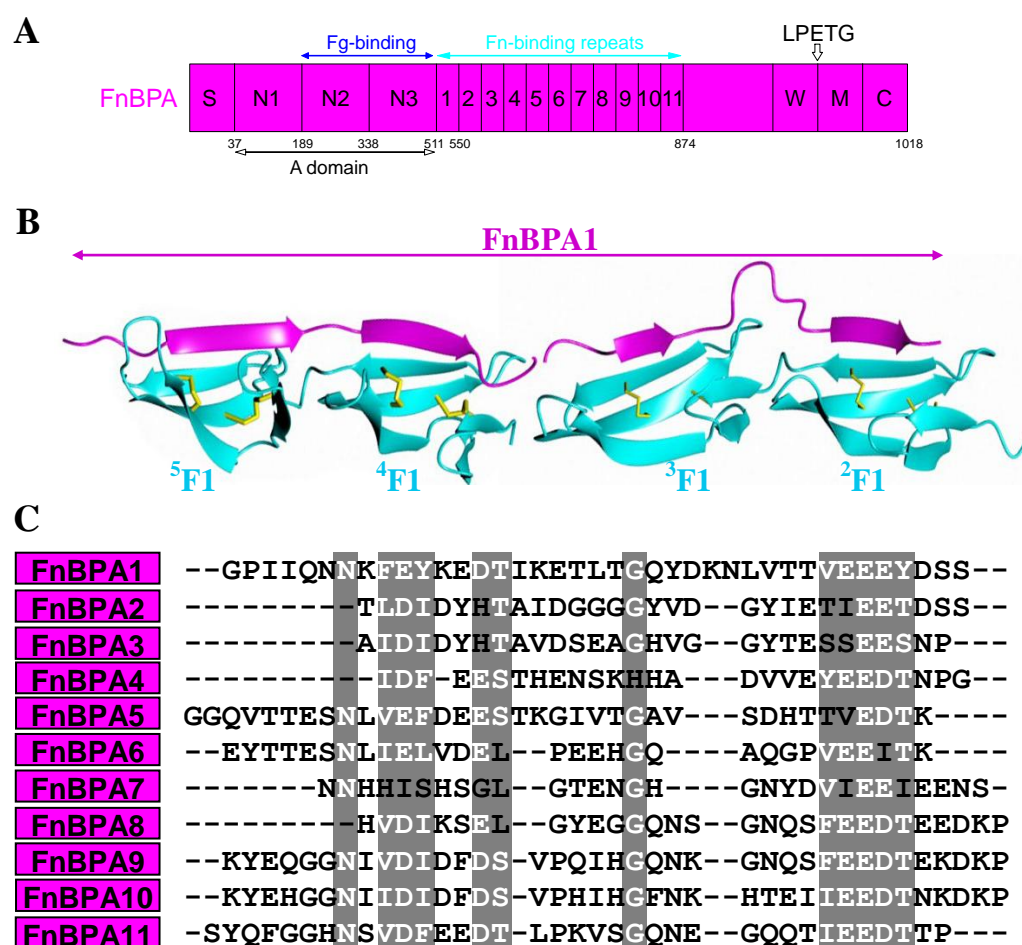


**Figure 1.9 Sequence alignment of FnBRs.** (A) Domain organization of FnBPA (B) Crystal structures of <sup>4</sup>F1<sup>5</sup>F1 and <sup>2</sup>F1<sup>3</sup>F1 module pairs (cyan) in complex with synthetic peptides representing fractions of FnBPA1 (magenta). Disulfide bonds stabilizing the F1 modules are shown (yellow). (C) Sequence alignment of the 11 intrinsically unstructured FnBRs. Functionally important residues conserved between FnBRs are highlighted in white. The multiple sequence alignment was performed using ClustalW2 (Larkin et al., 2007) with some manual editing.

### 1.6.2 The FnBPA-Fn interaction facilitates invasion of the endothelium

The FnBPA-Fn interaction can result in the invasion and activation of host endothelial cells, leading to proinflammatory and procoagulant responses characteristic of IE. The uptake of *S. aureus* is triggered by Fn-mediated contacts between FnBPA and the extracellular domains of the  $\alpha_v\beta_1$  integrins on the surface of endothelial cells (Sinha et al., 1999). It is likely that subsequent clustering of integrins on the cell surface activates the Src kinase signalling cascade, resulting in actin remodelling and ultimately the internalization of *S. aureus* (Figure 1.10) (Schwarz-Linek et al., 2004; Agerer et al., 2005; Schroder et al., 2006). The role of multiple FnBRs within the invasion process has been debated in the past and some of the earlier studies suggested that deletions in the FnBR region did not significantly affect the ability of *S. aureus* to invade endothelial cells (Massey et al., 2001; Piroth et al., 2008). However, a more recent study by Edwards and colleagues (2010) showed that the multivalency of FnBRs directly affects the speed and efficiency of bacterial uptake, and that reducing the number of FnBRs decreases *S. aureus* virulence (Edwards et al., 2010).

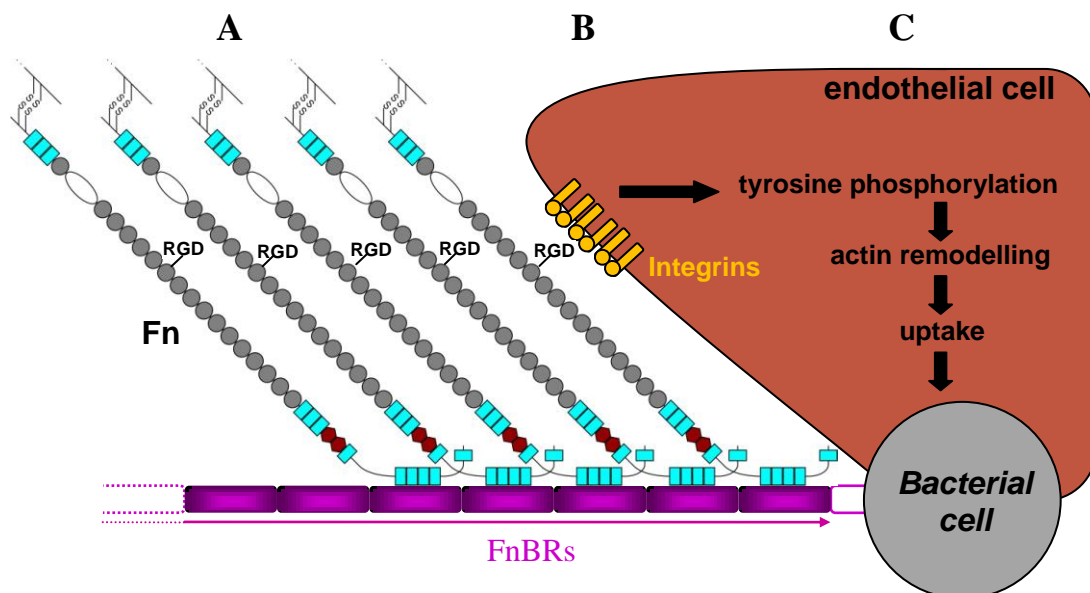


**Figure 1.10 Possible mechanism of the FnBPA-mediated uptake of staphylococci by endothelial cells. (A)** Binding of multiple Fn molecules to FnBPA attached to the bacterial cell wall may result in **(B)** integrin clustering on the surface of the endothelial cell, **(C)** activation of signalling cascade and subsequent internalization of the bacterium. For simplicity, binding of only five Fn molecules to FnBRs is shown in the figure to demonstrate the binding mechanism. Figure adapted from Schwarz-Linek and colleagues (2004).

### 1.6.3 FnBPA binds to Fg

FnBPA has been shown relatively recently to contain a Fg-binding region (Wann et al., 2000), however, the interaction has not yet been described in detail and there is a lack of structural data available. FnBPA binds to the C-terminus of Fg  $\gamma$  chain (Wann et al., 2000; Hawiger et al., 1982) and the Fg-binding activity is within the N-terminal A-domain, which exhibits 26% and 22% sequence identity with the A-domains of ClfA and SdrG, respectively (Altschul et al., 1997). As both ClfA and SdrG bind Fg (McDevitt et al., 1997; Bowden et al., 2003), and because the sequence of the A-domains are similar, the character of the Fg-FnBPA interaction was predicted to resemble that of ClfA/SdrG-Fg.

The minimal ClfA/B and SdrG regions containing the Fg-binding site comprise two distinct domains (N2 and N3) both with immunoglobulin folds (Deivanayagam et al., 2002). Sequence alignment of N2 and N3 from FnBPA with those from FnBPB, ClfA/B and SdrG revealed several conserved regions (Figure 1.11). Despite binding to different regions of Fg (SdrG binds to the  $\beta$  chain N-terminus (Davis et al., 2001) and ClfA to the  $\gamma$  chain C-terminus (Strong et al., 1982; Hawiger et al., 1982)), both SdrG and ClfA use similar mechanisms of Fg binding that have been called the dock-lock-latch (Ponnuraj et al., 2003; Bowden et al., 2008) or its variant the latch-dock (Ganesh et al., 2008), respectively. The ClfA latch-dock model involves changes in the relative orientation of N2 and N3 upon Fg binding, while conformations of the individual domains remain unaltered (Figure 1.12). As a consequence, the protein switches from an open to a more closed conformation allowing the G' (latch) strand to 'latch' to the N2-E strand forming an additional anti-parallel  $\beta$ -strand (Figure 1.12). Thus the Fg peptide is 'locked' into the trench between the N2 and N3 domains (Ponnuraj et al., 2003; Bowden et al., 2008; Ganesh et al., 2008).

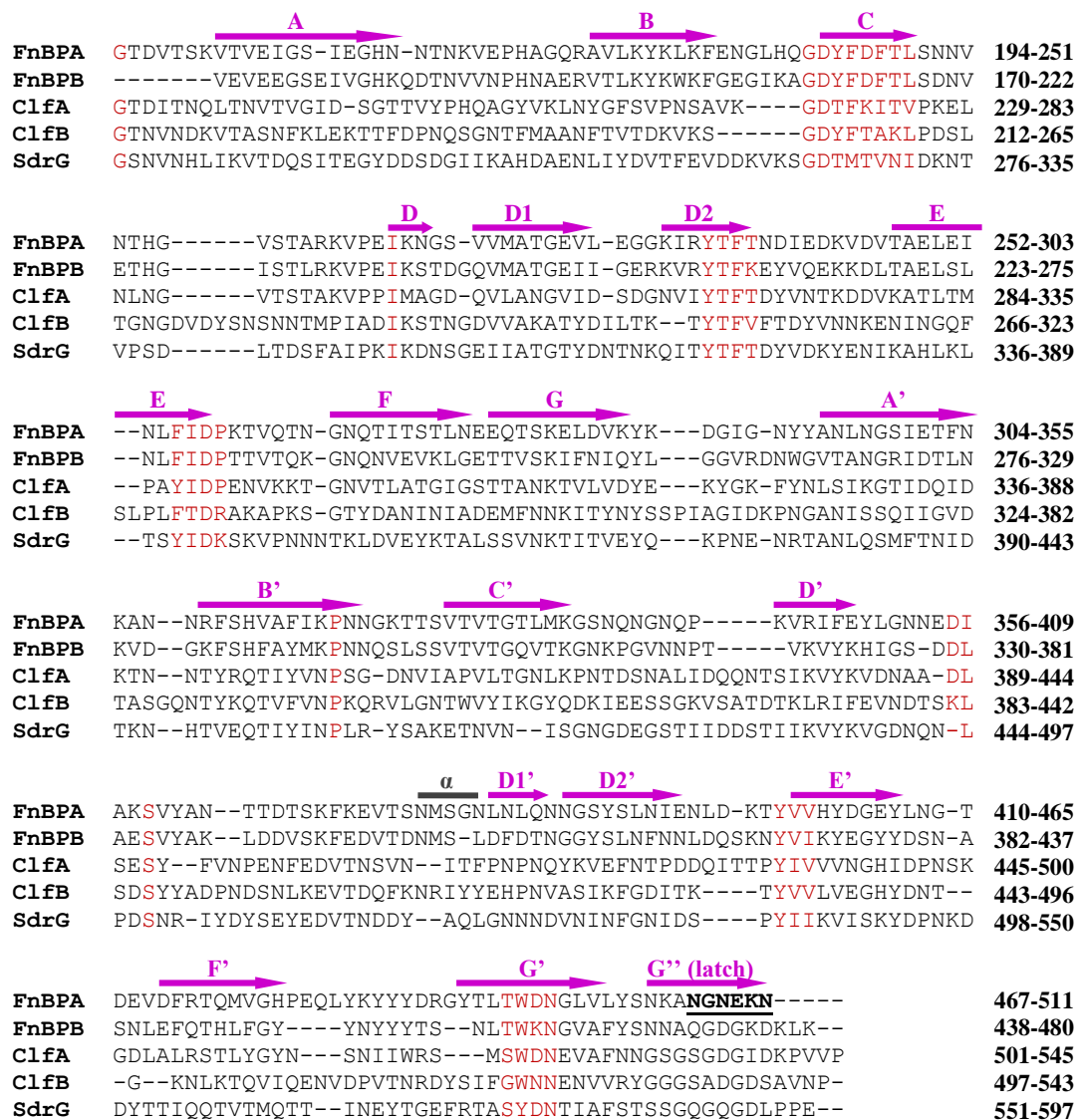


**Figure 1.11** Sequence alignment of N2 and N3 domains of Fg-binding MSCRAMMs. The N2N3 sequence of FnBPA (UniProt entry P14738) was aligned with that of FnBPB (UniProt entry Q53682), ClfA (UniProt entry Q26015), ClfB (UniProt entry Q2FUJ2) and SdrG (UniProt entry Q9KI13) followed by some manual editing. The residue numbering corresponds to that in the UniProt database. Individual  $\beta$ -strands are indicated by arrows (magenta) with labels adopted from Deivanayagam and colleagues, 2002. The short  $\alpha$ -helical feature between D' and D1'  $\beta$ -strands of FnBPA is also indicated (grey). Conserved regions are highlighted in red. The six C-terminal residues missing in the N2N3T construct (Section 3.3.2, Table 3.1) are highlighted in bold and underlined. The multiple sequence alignment was performed using ClustalW2 (Larkin et al., 2007).

Section 1.6.1 describes the tandem  $\beta$ -zipper mechanism of FnBR-Fn binding (Schwarz-Linek et al., 2003), and the predicted formation of consecutive N3-G' and latch  $\beta$ -strands during the N2N3-Fg interaction is outlined in Section 1.6.3. As N2N3 is adjacent to FnBPA1, simultaneous binding of Fg and Fn to N2N3 and FnBPA1

could lead to the formation of an extended  $\beta$ -strand region stretching across both Fg- and Fn-binding sites of FnBPA. Thus the putative Fg-N2N3\_FnBPA1-Fn ternary complex would be based mostly on  $\beta$ -zipper interactions, and its formation might involve cooperativity.

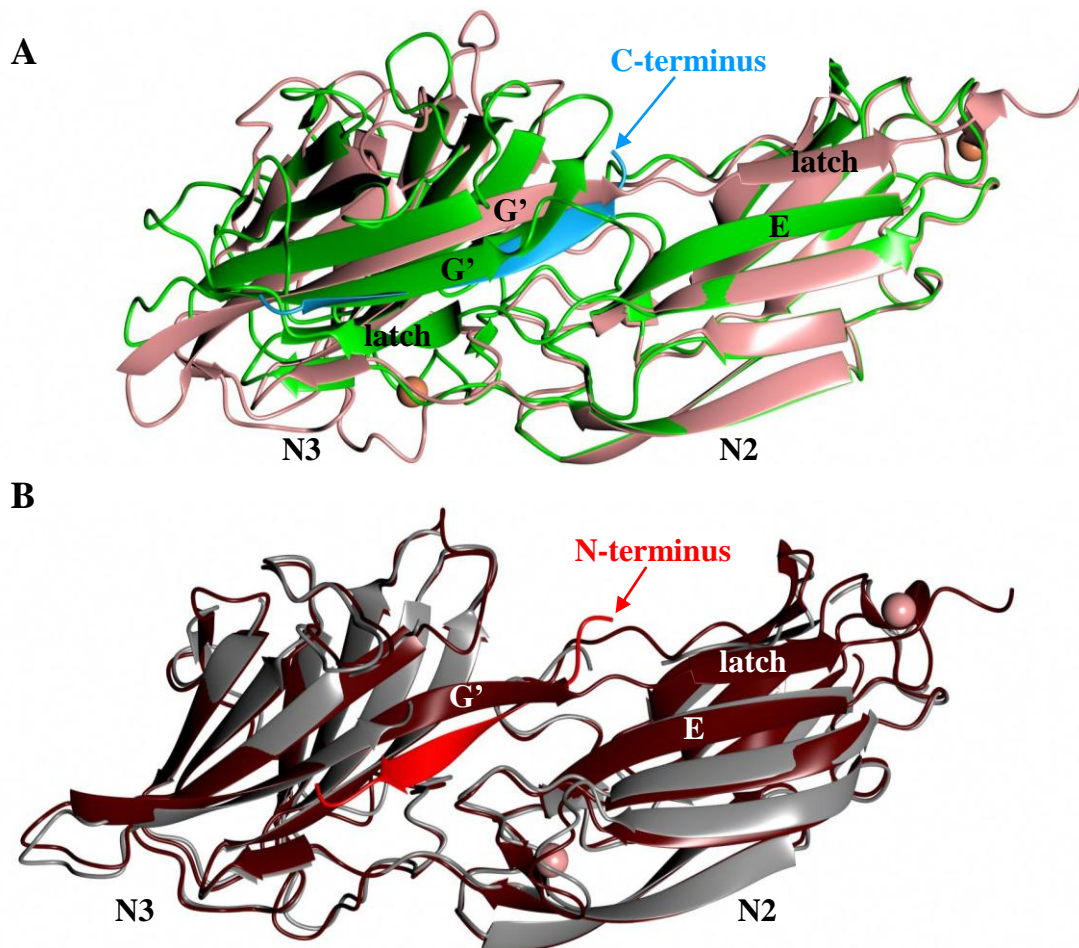


**Figure 1.12 Superposition of SdrG<sub>(273-597)</sub> and ClfA<sub>(229-545)</sub> free, and in complex with their cognate Fg peptides.** Secondary structure superposition of (A) the N2 domains from apoClfA<sub>(229-545)</sub> (green) (PDB entry 1N67) and the ClfA<sub>(229-545)</sub>-Fg1<sub>(D16A)</sub> peptide (PDB entry 2VR3) (Fg1 is a synthetic peptide representing the last 17 C-terminal residues of Fg  $\gamma$  chain; Section 2.3.1) complex (pink) and (B) the N2 domains from apoSdrG<sub>(273-597)</sub> (grey) (PDB entry 1R19) and SdrG<sub>(273-597)</sub>-Fg $\beta$  peptide (PDB entry 1R17) (Fg $\beta$  is a synthetic peptide representing the N-terminal Fg  $\beta$  chain sequence 6-20) complex (brown). Ca<sup>2+</sup> atoms are shown as spheres. Fg-binding sites on ClfA and SdrG are located in the cleft between N2 and N3 and, in both cases, the peptides bind via a  $\beta$ -zipper mechanism. However, the Fg1<sub>(D16A)</sub> peptide (blue) binds in a parallel orientation to the ClfA N3-G' strand while the Fg $\beta$  peptide (red) aligns antiparallel to the N3-G' strand of SdrG. Binding of both SdrG and ClfA to Fg involves the alignment of the latch strand along the N2-E edge strand, thereby forming a  $\beta$ -sheet extension, a key element of the dock-lock-latch and latch-dock binding mechanisms (Ganesh et al., 2008; Bowden et al., 2003). The ClfA G' and latch strands are labelled in both the apoClfA<sub>(229-545)</sub> and the ClfA<sub>(229-545)</sub>-Fg1<sub>(D16A)</sub> complex.

### 1.6.4 Role of FnBPA in platelet activation

A plethora of experimental evidence demonstrates that *S. aureus* induces platelet aggregation and colonization of host endothelial cells, processes closely associated with the development of IE (Piroth et al., 2008; Moreillon and Que, 2004; Fitzgerald et al., 2006a; Fitzgerald et al., 2006b). Under normal circumstances, the role of platelet aggregation is to control blood loss at the site of vascular injury, facilitate wound healing and to prevent infection (Jackson, 2007). However, multiple pathogens, including *S. aureus*, have developed the ability to trigger aggregation in order to facilitate its survival within the host (Kerrigan and Cox, 2009). Interactions with platelets contribute not only to the pathogen's ability to adhere to the endothelium but also the ability to evade the immune system while surrounded by platelet thrombi (Foster, 2005). FnBPA has been described as a key virulence factor of *S. aureus* in relation to IE, mainly due to its ability to interact with receptors on the surface of both platelets and endothelial cells (Heilmann et al., 2004; Edwards et al., 2010).

Platelet aggregation is a complex multistep process involving variety of receptors and adhesive ligands (Section 1.3.3). Activation of quiescent platelets by *S. aureus* FnBPA, in the absence or presence of a tissue trauma, requires the formation of Fn and Fg bridges between FnBPA and GPIIb/IIIa, and a recognition of the FnBPA-specific Fc antibody by the platelet Fc $\gamma$ RIIa IgG receptor (Fitzgerald et al., 2006a; Fitzgerald et al., 2006b; Loughman et al., 2005). The initial interactions between *S. aureus* and the platelet trigger an outside-in signalling cascade resulting in further activation of nearby platelets and formation of a thrombus as described in section 1.3.3, even in the absence of a vessel wall injury (Rivera et al., 2009).

## 1.7 Biophysical techniques

### 1.7.1 Isothermal titration calorimetry

Isothermal titration calorimetry (ITC) is a solution based technique designed to determine the thermodynamic parameters of molecular interactions (Sheehan, 2000). The binding parameters; enthalpy change ( $\Delta H$ ), entropy change ( $\Delta S$ ), change in Gibbs free energy ( $\Delta G$ ), association constant ( $K_a$ ) and stoichiometry ( $n$ ) can be

determined from a single ITC experiment by measuring the heat evolved or absorbed during an interaction (Pierce et al., 1999). The heat change is a direct result of the protein-protein interactions. The calorimeter is a closed adiabatic system with constant pressure ( $p$ ) and volume ( $V$ ), thus all energy changes occur in the form of heat. As a result, the heat evolved or absorbed can be described as the enthalpy change (Equations 1.1 and 1.2) (Cooper et al., 2001; Velazquez-Campoy et al., 2004b).

$$\Delta H = \Delta U + p\Delta V \quad (1.1)$$

$$\Delta H = Q \quad (1.2)$$

The calorimeter comprises reference and sample cells mounted in an adiabatic environment and a syringe, designed to fit inside the sample cell (Figure 1.13). In a typical ITC experiment, the sample cell is filled with a solution of the macromolecule while the syringe is filled with a solution of the ligand. Small volumes of the ligand solution are injected into the sample cell until the binding sites on the macromolecule are saturated. Mixing is provided by the rotating syringe. If an interaction occurs, heat is either evolved (exothermic reaction) or absorbed (endothermic reaction), resulting in a temperature change in the sample cell. The differential power necessary to equilibrate the temperatures of the sample and reference cells is subsequently converted and represented as a change in calories per unit time. The entire experiment, including data analysis, takes place under computer control. Parameters  $\Delta H$ ,  $K$  and  $n$  can be determined directly from a binding isotherm obtained by non-linear least squares fitting of the equations in Appendix II to the calorimetric data, using appropriate binding model.  $\Delta G$  and  $\Delta S$  can be calculated subsequently using Equation 1.3 and 1.4 (Indyk and Fisher, 1998; Velazquez-Campoy et al., 2004a).

$$\Delta G = -RT\ln K_a \quad (1.3)$$

$$\Delta G = \Delta H - T\Delta S \quad (1.4)$$



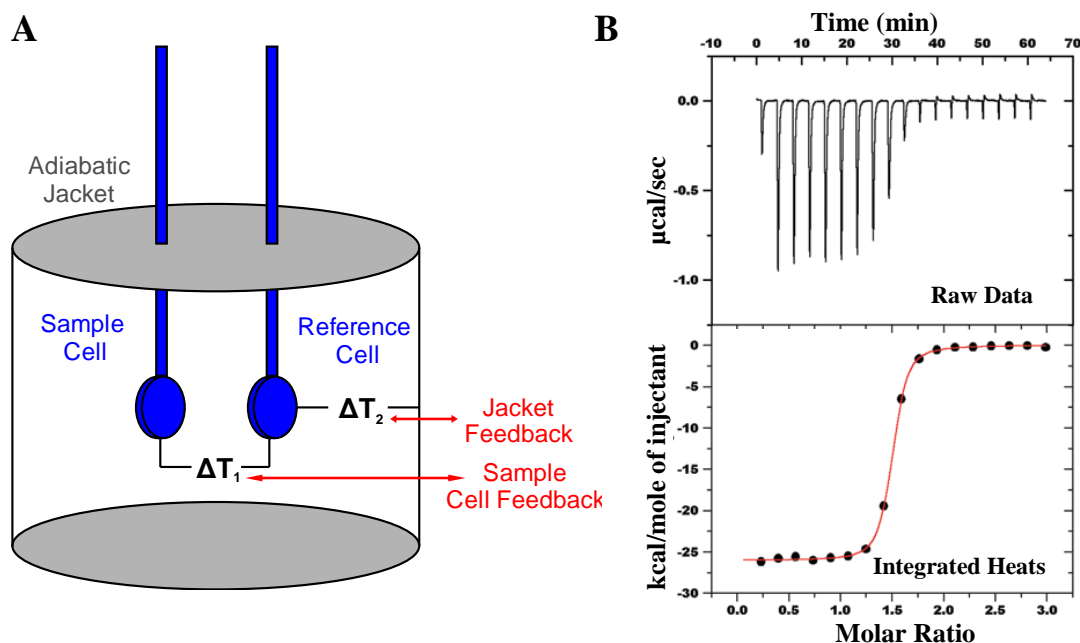


**Figure 1.13 Schematic diagram of a typical isothermal titration calorimeter and an example of experimental data.** (A) Coin-shaped sample and reference cells are kept within the closed environment of the adiabatic jacket. A constant temperature difference between sample and reference cells ( $\Delta T_1$ ) but also between the reference cell and the adiabatic jacket ( $\Delta T_2$ ) is maintained by a system of feedbacks. (B) Typical ITC data. (Top panel) Raw data consists of ‘injection peaks’ that represent total heats generated upon every ligand injection. (Lower panel) Areas under the peaks are integrated and plotted against the molar ratio of ligand to macromolecule within the cell, allowing for a binding isotherm to be fitted to the data (red) using a suitable binding model (MicroCal, 2008).

## 1.7.2 Surface plasmon resonance

### 1.7.2.1 Introduction

Surface plasmon resonance (SPR) is a matrix-based technique designed for analysis of molecular interactions in real time (Schasfoort and Tudos, 2008). The ligand is immobilised on the surface of a specific chip while a solution containing its binding target, called the analyte, is flowed over. SPR utilizes the phenomenon of total internal reflection (TIR). When a beam of polarised light travels from a medium with a higher refractive index (RI) to a medium with lower RI, under an angle of incidence exceeding a specific critical angle, none of the beam crosses the boundary. Instead, all of the light is reflected internally reaching TIR (Pattnaik, 2005). In the case of SPR, the medium with higher RI is a thin metal layer (usually gold), and the medium with a lower RI is the analyte solvent. Under the conditions of TIR and the combination of correct wavelength and angle of incidence (the SPR Angle), a small



amount of energy is absorbed by the gold layer resulting in a decrease in the energy of the reflected light. The SPR angle is affected by changes in the dielectric constants of the two media, which in turn can be influenced by molecular processes in the vicinity of the interface. The detector tracks small shifts in the SPR angle producing a sensorgram representing the changes of the SPR angle with time (Figure 1.14) (Schuck, 1997).

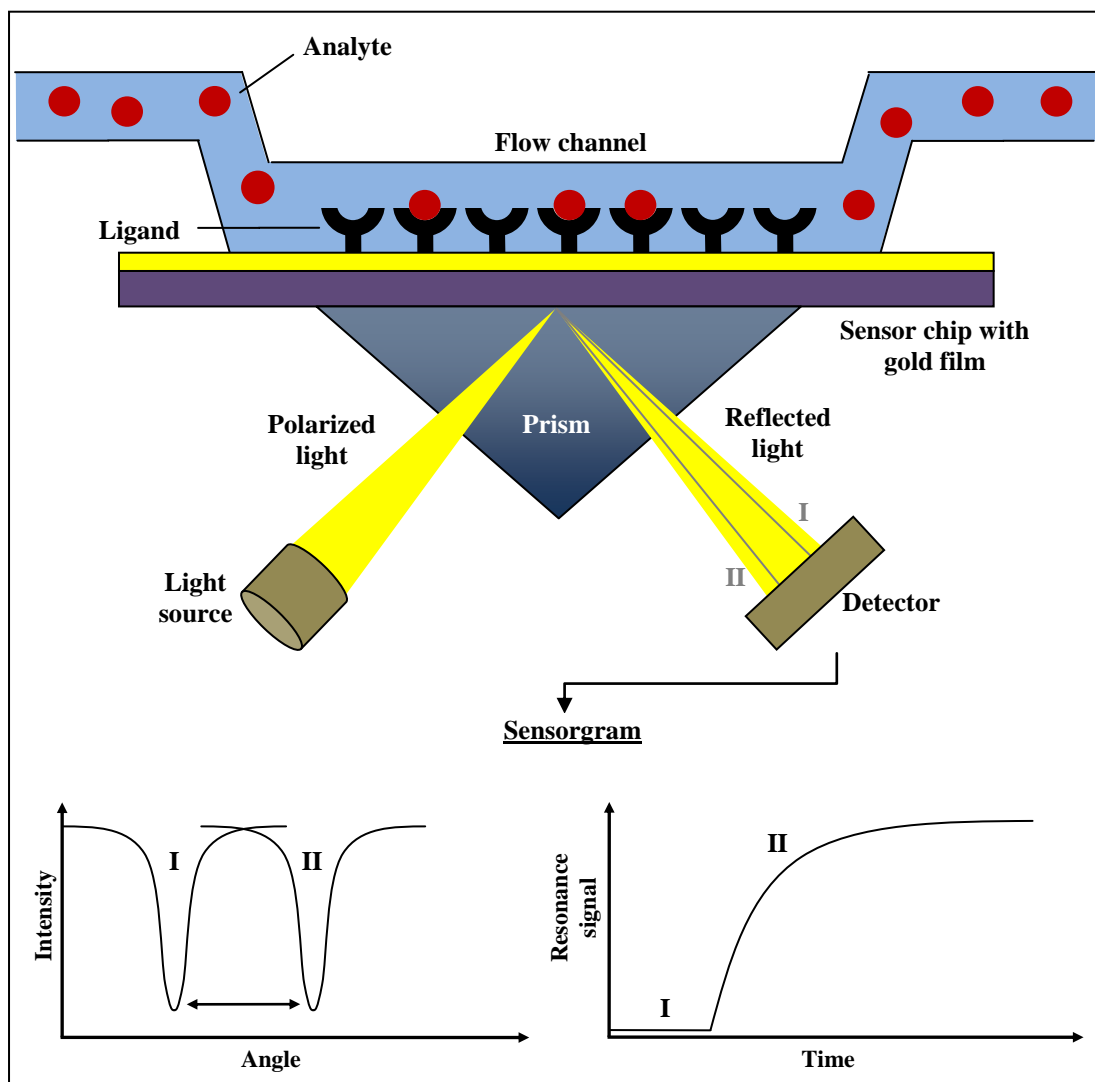


**Figure 1.14 Surface plasmon resonance overview.** The ligand, immobilized on the gold surface of a sensor chip, is exposed to an analyte in solution (represented by red spheres) while a single beam of polarised light is aimed at the opposite side of the chip through a glass prism under TIR conditions. The shift in the SPR angle (represented by a dip in the intensity of reflected light) is measured by an optical detector and presented on a sensorgram as response units as a function of time (Cooper, 2002).

### 1.7.2.2 SPR experiment

A typical SPR experiment aimed at assessing the kinetics or affinity of a particular protein-protein interaction comprises injections of increasing concentrations of an analyte over a ligand immobilized on the surface of a sensor chip. An interaction between the ligand and analyte generates a response measured in arbitrary response units (RU) in real time, with one response unit corresponding to a shift in the SPR angle by approximately  $10^{-4}$  degrees (Pattnaik, 2005). The magnitude of the response is proportional to the change in the molecular mass at the gold/buffer interface, and therefore to the molecular mass and the amount of analyte bound to the ligand. The difference in response between the sample cell and a reference cell is measured, thus compensating for any non-specific change in response that may occur due to the discrepancies between running and sample buffers, or non-specific binding of the analyte to the un-modified chip surface.

### 1.7.2.3 Ligand immobilization by amine coupling

An interaction can only be monitored by SPR if one of the reactants (ligand) is immobilized on the surface of a sensor chip. An array of immobilization techniques are available including covalent immobilization (amine coupling, thiol coupling and aldehyde coupling) (Johnsson et al., 1991; Lofas et al., 1995), high affinity capture (streptavidin-biotin, antibody-based and tagged proteins) (Hutsell et al., 2011) and hydrophobic attachment (mono/bilayer attachment). All SPR experiments performed in this project involved ligand immobilization by amine coupling.

Amine coupling is a relatively non-specific immobilization technique utilizing the amino group at the N-termini of polypeptide chains and/or the  $\epsilon$ -amino groups of lysine residues. First, the carboxylated sensor chip surface is activated with a solution of 1-ethyl-3-(3-dimethylaminopropyl) carbodiimide (EDC) and N-hydroxysuccinimide (NHS). This generates reactive succinimide esters, which subsequently react with the amine groups on the ligand (Johnsson et al., 1991) (Figure 1.15). Electrostatic pre-concentration is essential to achieve accumulation of a sufficient amount of ligand at the surface of the sensor chip. To promote the interaction, the pH of the immobilization buffer should lie between the isoelectric point (IP) of the ligand and the pKa of the surface (<3.5). This insures a positively

charged ligand will interact with the negatively charged sensor chip surface. It is preferable to use a pH close to the physiological conditions of the ligand to avoid degradation or aggregation during the immobilization process. Once the activated surface has been exposed to the ligand, ethanolamine is flowed over the chip surface to deactivate remaining active groups and to remove any non-covalently bound ligand (O'Shannessy et al., 1992).

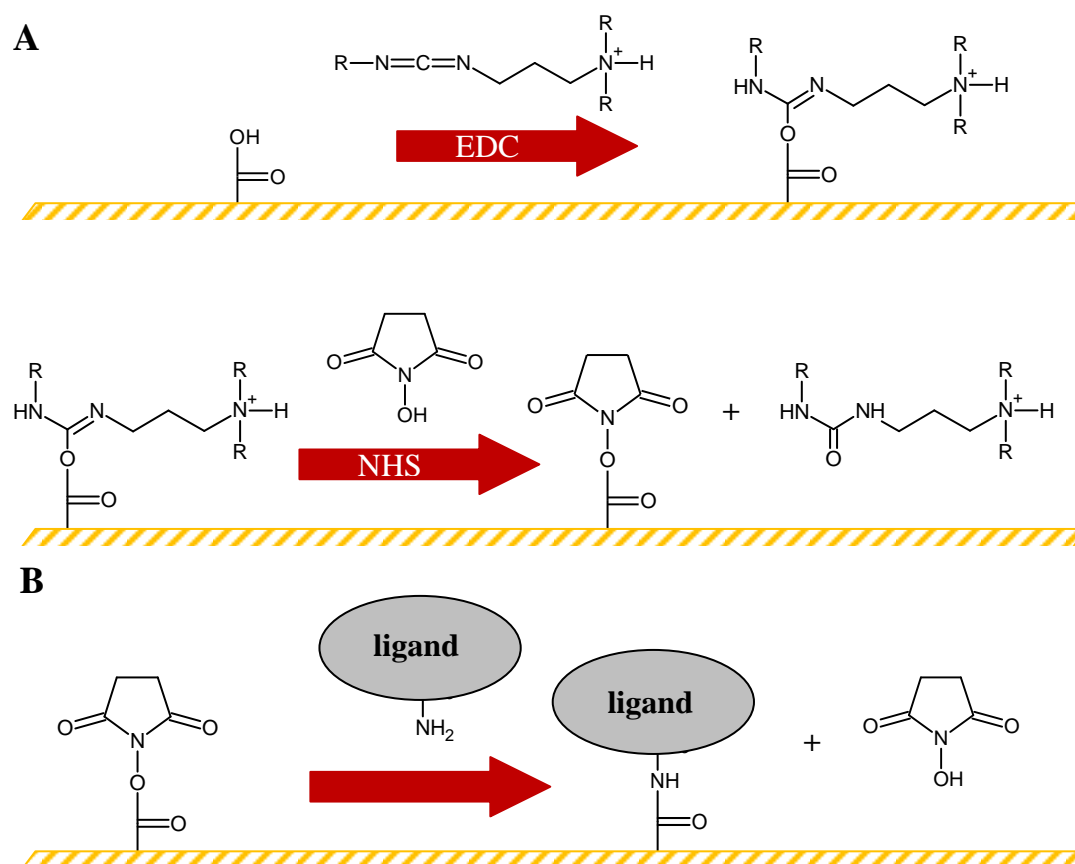


**Figure 1.15 Schematic diagram representing the amine coupling immobilization process. (A)** The first step involves sensor chip surface activation with EDC/NHS. Initially EDC reacts with carboxyl groups on the chip surface to form a reactive *O*-acylisourea intermediate which is reactive towards nucleophiles including primary and secondary amines but also water. Due to the rapid hydrolysis, the *O*-acylisourea intermediate is converted to the more stable active *N*-hydroxysuccinimide ester by NHS to allow sufficient contact time with the ligand molecules (Gedig, 2008). **(B)** During the second step, the activated surface is exposed to a specific ligand resulting in aminolysis of the active esters by lysines or *N*-terminal amino groups of the ligand. Figure adapted from Gedig (2008).

### 1.7.2.4 Data processing

Rate constants  $k_a$  and  $k_d$ , and the equilibrium constant  $K_d$ , can be derived from a basic SPR experiment (O'Shannessy et al., 1993; Karlsson et al., 1991; Vandermerwe et al., 1993). For a reversible reaction between ligand L and analyte A



the rate of formation of the product [AL] can be described as follows;

$$\frac{d[AL]}{dt} = k_a[A][L] - k_d[AL] \quad (1.6)$$

After some reaction time  $t$ , a certain amount of [AL] is formed, thus Equation 1.6 can be re-written as;

$$\frac{d[AL]}{dt} = k_a[A]([L]_0 - [AL]) - k_d[AL] \quad (1.7)$$

Since the ligand is immobilized, the intensity of the response (R) is proportional to the formation of the AL complex at the surface of the sensor chip and the maximum response ( $R_{MAX}$ ) is proportional to the concentration of active ligand on the surface. Consequently, for an SPR experiment the above equation can be rewritten as follows

$$\frac{dR}{dt} = k_a[A](R_{MAX} - R) - k_dR \quad (1.8)$$

Interactions with rate constants outside the measurable limits of the T100 (GE Healthcare) instrument ( $k_a$   $10^3 - 10^7$   $M^{-1}s^{-1}$  and  $k_d$   $10^{-5} - 0.5$   $s^{-1}$ ) can be assessed using equilibrium analysis. Providing that a steady state is reached during all analyte injections, and that ligand saturation is achieved, the equilibrium dissociation constant ( $K_d$ ) can be determined by plotting the steady state binding level ( $R_{eq}$ ) for each injection against the appropriate analyte concentration (Vandermerwe et al., 1993). The resulting saturation curve has a hyperbolic shape described by Equation 1.9.

$$y = \frac{ax}{b + x} \quad (1.9)$$

Applied to the reversible binding interaction described by Equation 1.1,  $y$  is the fraction of the ligand bound to analyte,  $a$  is the maximum value for  $y$  (i.e. 1),  $x$  is the

analyte concentration and  $b$  represents the analyte concentration at half-maximal ligand saturation (i.e.  $y$ ). The equation can therefore be rewritten as follows;

$$\frac{[AL]}{[L]} = \frac{[A]}{K_d + [A]} \quad (1.10)$$

When  $[A]$  is equal to  $K_d$ , the ligand reaches half-maximal saturation as demonstrated by Equation 1.11.

$$\begin{aligned} \text{if} \quad [A] &= K_d \\ [AL] &= \frac{1}{2}[L] \end{aligned} \quad (1.11)$$

In an equilibrium experiment the formation of the AL complex can be represented by the response  $R$  and the total concentration of immobilized ligand  $[L]$  as the maximum response ( $R_{MAX}$ ) (Equation 1.12).

$$R = \frac{1}{2}R_{MAX} \quad (1.12)$$

### 1.7.3 Crystallography

#### 1.7.3.1 Overview

Protein crystallography is a technique used to determine structures of proteins and their complexes. During this process a crystalline form of a single protein or protein complex has to be produced which is then exposed to an X-ray beam resulting in a diffraction pattern on the X-ray detector. Applying a combination of mathematical functions, the diffraction pattern is translated into an electron density map. A three-dimensional model of the protein structure can then be refined against the data using a suite of software packages (McPherson, 2004).

#### 1.7.3.2 Crystallization

Crystallization can take place when the concentration of a protein exceeds its solubility limit. Most of the time this would result in the protein precipitating out of the solution, however, in certain cases, the protein reaches a supersaturated metastable phase where protein crystals can grow but cannot spontaneously nucleate. Similar to a conventional chemical reaction, the protein has to overcome an energy barrier in order for the nucleation centre to form (Asherie, 2004). Once the protein reaches the labile supersaturated phase, and the centre of nucleation is formed, the

concentration of the protein in solution drops slightly and the system enters a metastable phase, ideal for crystal growth (Figure 1.16) (McPherson, 1999).

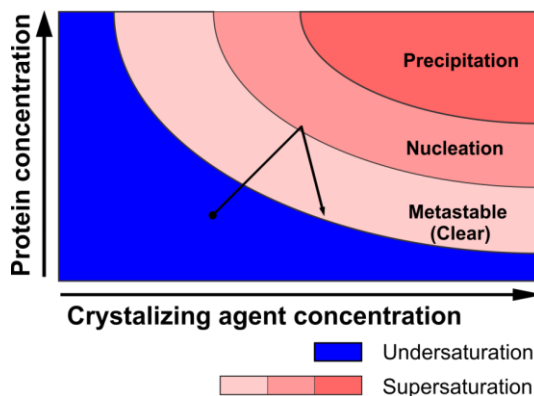


**Figure 1.16 Phase diagram.** The optimum trajectory through the different saturation phases is indicated by the arrow. Initially, due to vapour diffusion, the concentration of both protein and precipitant increases until the nucleation phase is reached. Nuclei formation leads to a decrease in protein concentration and the system within the drop reaches a metastable phase, ideal for crystal growth. Figure adapted from Asherie, 2004.

### 1.7.3.3 Vapour diffusion

A common method for obtaining diffracting crystals is the vapour diffusion experiment (Rhodes, 2000). A typical set-up involves mixing solutions containing protein and precipitant which are subsequently either placed in a well next to (sitting drop approach) or suspended over (hanging drop method) a larger reservoir of the precipitant solution (mother liquor). The difference in the concentrations of precipitant in the drop and the reservoir solution is compensated by vapour diffusion. During this process water evaporates from the drop (which has a lower concentration of precipitant) and condenses in the reservoir solution (which has higher precipitant concentration) in order to reach equilibrium. Water evaporation results in a gradual increase in protein concentration inside the drop, moving the system towards a supersaturated state (McPherson, 2004; Davey and Garside, 2000).

### 1.7.3.4 Seeding

Seeding is a means of altering the phase trajectory and allows nucleation and subsequent crystal growth in the metastable phase. Introducing seeds or a solution of seeds to a supersaturated solution in the metastable phase provides the nucleation centres necessary to initiate crystal growth. The microseeding technique utilizes a

stock of sub-microscopic seeds in stabilizing mother liquor, generated by pulverization of non-diffracting crystals into crystalline particles (Bergfors, 2003; Luft and DeTitta, 1999). Serial dilution of the seeding stock can be performed to obtain the required number of nuclei. Sub-microlitre volumes of the seeding stock are introduced into new drops and equilibrated at a lower level of supersaturation usually in combination with automation. Seeding makes it possible to control the number of nucleation centres and consequently the number of crystals grown in each drop (Stura and Wilson, 1990). Microseeding offers the advantage of high throughput screening, which improves the likelihood of successful crystallization and reproducibility

### 1.7.3.5 Crystal symmetry

The crystalline form of a protein contains multiple copies of the same protein molecule. Each crystal is defined by a three-dimensional lattice of repeating structural features known as the unit cell, characterised by length of its edges ( $a$ ,  $b$ ,  $c$ ) and the angles between them ( $\alpha$ ,  $\beta$ ,  $\gamma$ ) (Clegg, 1998). The shape of unit cell is restricted to one of seven potential crystal systems by the 2, 3, 4 and 6-fold rotational symmetries allowed within the crystal lattice. The other two symmetries, reflection and inversion, are not allowed within lattices formed by biological systems as it would require alteration in the amino acid stereochemistry. The combination of the seven crystal systems with the different lattice centring systems generates 14 Bravais lattices (Table 1.2) (Drenth, 2007). The symmetry of the entire crystalline lattice is defined by one of 65 possible space groups for chiral molecules, with each space group representing a specific combination of symmetry elements and the lattice type. The smallest unit of a crystal and the unique part of the unit cell is called the asymmetric unit, from which the rest of the unit cell and crystal can be derived if specific symmetry operations are applied. These symmetry operators can be rotational, translational or a combination of both known as 'screw axis'. An example of a common 'screw axis' is a  $2_1$ , which involves rotation about a two-fold symmetry axis and translation by a half of the unit cell length. As the name suggests, the asymmetric unit has no symmetry on its own and often more than one candidate can be identified for a single crystal, albeit of identical volume. If the content of asymmetric unit is known together with the unit cell and space group, the position of all atoms within the crystal can be identified (Drenth, 2007).

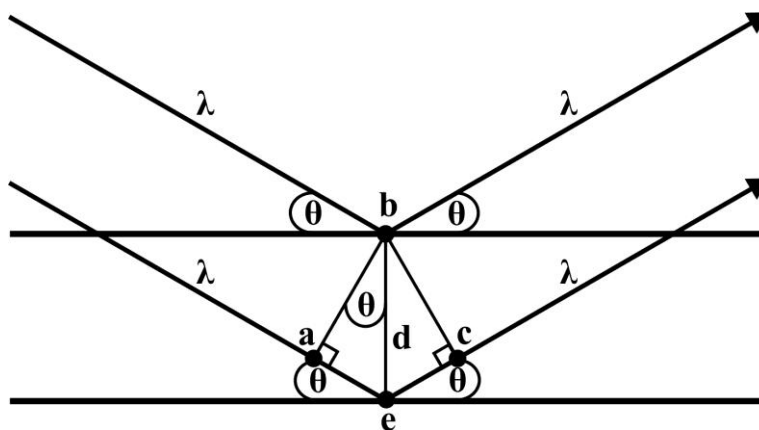
Crystal system	Bravais	Essential symmetry	Unit cell restriction
Triclinic	P	none	none
Monoclinic	P, C	one two-fold	$\alpha = \gamma = 90^\circ$
Orthorhombic	P, I, F	three two-fold	$\alpha = \beta = \gamma = 90^\circ$
Tetragonal	P, I	one four-fold	$a = b; \alpha = \beta = \gamma = 90^\circ$
Rhombohedral	P, R	one three-fold	$a = b = c; \alpha = \beta = \gamma (\neq 90^\circ)$
Hexagonal	P	one six-fold	$a = b; \alpha = \beta = 90^\circ; \gamma = 120^\circ$
Cubic	P, I, F	four three-fold	$a = b = c; \alpha = \beta = \gamma = 90^\circ$

**Table 1.2 Crystal systems.** Besides the seven crystal systems, symmetry and unit cell diameters, individual spacegroups are determined by five different lattice types: Primitive (P), C-centered (C), Body-centred (I), Face-centred (F), Rhombohedral (R). Table adapted from Clegg, 1998.

### 1.7.3.6 X-ray diffraction

The protein crystal, when exposed to a single wavelength X-ray beam, generates a specific diffraction pattern on the detector, resulting from the scattering of the X-rays by electrons within the crystal. The crystal can only produce reflections under conditions described by Bragg's Law (Equation 1.13) which relates the distances between reflecting planes, the wavelength of the X-rays and the angle of incidence (Figure 1.17) (Drenth, 2007). The spacing between the layers of atoms within the crystalline lattice ( $d$ ) that satisfies Bragg's Law is defined by Miller indices ( $h, k$  and  $l$ ). The  $h, k$  and  $l$  integers represent the number of times the unit cell edges  $a, b$  and  $c$  are divided by Bragg's planes. Only a few planes would satisfy Bragg's law in a crystal at a fixed position, thus the crystal is rotated through  $360^\circ$  while exposed to the X-ray beam, thereby generating a three-dimensional diffraction pattern (Drenth, 2007). Geometry, symmetry and intensity are three important properties associated with the diffraction pattern, which relate to the geometry, symmetry and the positions of individual atoms within the unit cell. The symmetry of the diffraction pattern intensities however, is not identical to the crystal symmetry and is known as the Laue symmetry. Since there are only eleven Laue groups for all 65 space groups, Laue symmetry cannot uniquely determine the correct space group. The relationship between the crystal and reflections is determined by the dimensions of the unit cell. If the unit cell can be described by its edge lengths  $a, b$  and  $c$ , then the diffraction spots will be spaced in the ratio  $1/a, 1/b$  and  $1/c$ , thus the diffraction pattern is said to be in reciprocal space while the crystal itself is in real space (Rhodes, 2000).





$$2d \sin(\theta) = n\lambda \quad (1.13)$$

**Figure 1.17 Bragg's Law.** Waves of the reflected beams are in phase at points *b* and *c* only if the distance  $ae + ec$  equals multiples of the beam wavelengths ( $\lambda$ ). Since the lengths of  $ae$  or  $ec$  are equal to  $d \sin(\theta)$ , the relationship between reflective plane spacing, wavelength and the angle of incidence can be summarised by the Equation 1.13.

### 1.7.3.7 Data collection and processing

Collection of diffraction data is often performed at 100 K to reduce the effects of radiation damage to the crystal. The crystal is usually vitrified in liquid nitrogen, in the presence of cryoprotectant (e.g. glycerol), prior to exposure to the X-ray beam. Given its three-dimensional lattice, the crystal is rotated in the beam to ensure a complete data set representing the entire unit cell is obtained. In practice, it is not necessary to collect data through  $360^\circ$  in order to obtain a complete data set. The degree of rotation required depends on the crystal symmetry, i.e.  $180^\circ$  is sufficient for 2-fold symmetry,  $120^\circ$  for 3-fold symmetry, etc. However, it is common to collect more than the minimum amount data to achieve improved completeness.

Following successful collection of all reflections from the crystal, the diffraction images have to be processed in order to obtain a set of data suitable for Fourier transformation. The initial processing can be carried out using a variety of software including HKL2000 (Otwinowski and Minor, 1997) and Xia2 (Winter, 2009). Initially, software has to locate the diffraction spots and identifies repeating patterns corresponding to a unit cell, a process known as indexing. The diffraction pattern can subsequently be compared to those expected for the seven crystal systems (Table 1.2). The system with highest symmetry and the best fit is used to determine the

space group (Blow, 2002). Integration is the second step and involves measurements of the raw intensity for each spot. Further corrections are applied later in order to obtain the final intensity for the structure solution. Scaling is a data processing step designed to correct the raw summed intensity affected by factors including the beam strength variability over time, radiation damage or the rotation of a crystal with unequal dimensions. Finally, a single intensity value for each unique reflection is obtained in the merging process by averaging the intensity of multiply measured reflections (Rhodes, 2000). At this point the quality of the data can be evaluated statistically using  $R_{merge}$ , representing the agreement between symmetry related reflections (Equation 1.14) (Drenth, 2007).

$$R_{merge} = \frac{\sum_{hkl} \sum_i |I_{i(hkl)} - \langle I_{(hkl)} \rangle|}{\sum_{hkl} \sum_i I_{i(hkl)}} \quad (1.14)$$

Where  $\langle I_{(hkl)} \rangle$  represents the average intensity of all reflections and  $I_i$  the intensity of reflection  $i$  with indices  $hkl$ .

### 1.7.3.8 Phase problem

Only the amplitude of the reflected wave is recorded by the detector while the phase is lost (Drenth, 2007). This ‘phase problem’ can be solved by several approaches. While direct mathematical methods can be applied to high resolution data ( $<1.2\text{\AA}$ ) from small molecules or peptides, much more complex methods known as experimental phasing or molecular replacement are required for protein crystals.

### 1.7.3.9 Experimental phasing

Experimental phasing is the only way to solve the phase problem for structures with new protein folds (Drenth, 2007). Since the detectors can only detect the intensity of the reflection, the phase information has to be measured through variations in the intensities. This is achieved through interference between a diffracted wave of unknown phase and a reference wave of known phase. There are two possible sources of such a reference wave that can be introduced into the structure, a heavy atom (isomorphous replacement method) or anomalous atoms such as selenium, which resonate with incoming X-ray radiation (anomalous scattering method) (Blow, 2002; Drenth, 2007).

### 1.7.3.10 Molecular replacement

Molecular replacement utilizes the solved structure of a homologous protein as a model and source of the initial phases for the new structure (Blow, 2002). Only structures exhibiting high structural similarity can be considered as a suitable model. It is vital that both the orientation and position of the model are aligned with the target structure. The alignment is carried out using maximum-likelihood methods (McCoy, 2004), a recently developed statistical concept designed to identify a set of parameters for a model that fits the experimental data with the highest probability. This is done by trial and error approach, where the orientation and position of the model within the unit cell are set using rotational and translational functions, respectively. Subsequently, the phases obtained from the model structure can be combined with the intensities from the unknown structure to produce an initial electron density map. Unlike the experimental phasing methods, molecular replacement is a very fast and relatively straightforward approach, providing a suitable homology model is available (Dodson, 2008).

### 1.7.3.11 Model building, refinement and validation

Once an initial electron density map has been obtained, an iterative process involving a combination of manual model building with automated refinement is performed, resulting in improved phases, better electron density and a final model closely resembling the real structure. The manual building and adjustment of the fitted model is usually performed using standard map-fitting software packages such as COOT (Emsley and Cowtan, 2004), while the refinement is carried out automatically by the REFMAC program (Murshudov et al., 1997) included in the CCP4 program suite (Winn et al., 2011). REFMAC is based on the maximum-likelihood approach (McCoy, 2004). As a consensus, the quality of the model is assessed by the crystallographic reliability-value ( $R_{factor}$ ) defined as the average fractional error between the calculated amplitudes of the model and the observed amplitudes Equation 1.15.

$$R = \frac{\sum ||F_o| - |F_c||}{\sum |F_o|} \quad (1.15)$$

---

The aim is to achieve as low an  $R_{factor}$  as possible, however, it is generally accepted that a value of 25% or lower is sufficient. It is essential that the refinement progress is assessed regularly by the  $R_{free}$ , which is a means of ensuring the model is not ‘over-fitted’, potentially leading to structure over-interpretation. The  $R_{free}$  is calculated using a small subset of reflections, set aside prior to any model building or refinement.

The final stage of structure solution involves the validation process. Numerous errors are usually introduced into the structure model during the fitting procedure and it is paramount that as many of those errors are corrected as possible. Common problems include disallowed  $\phi$  and  $\psi$  backbone angles, unusual sidechain rotamers, hydrogen clashes, and unusually high B-factors or bond lengths. All of these can be identified and corrected using software such as COOT (Emsley and Cowtan, 2004), however, it is vital that the final structure is validated using independent software or a server such as MolProbity (Chen et al., 2010).

## 1.8 Aims

Despite the growing evidence attributing a vital role to FnBPA in *S. aureus* IE aetiology, very little attention has been paid to the structural aspects of the Fg-binding region, the interaction with Fg and ultimately its potential effects on the Fn-binding ability of FnBPA. Fn and Fg are fundamental to the process of platelet aggregation and endothelial cell colonization and invasion by *S. aureus*. Containing binding sites for both Fg and Fn, FnBPA emerges as a key virulence factor in IE and possibly other major *S. aureus* infections. FnBPA has the potential to bind both Fg and Fn simultaneously to form an extensive multi-protein complex via multiple  $\beta$ -zipper interactions, however, the existence of such a complex has not been demonstrated. The question of whether the co-localisation of the two binding sites within FnBPA simply results in avidity, by harbouring an additional point of attachment, or whether Fg- and Fn-binding events exhibit a synergistic character leading to a much more complex mechanism of action within the infection, remains to be answered. The primary objectives of this research were to define the A-domain/FnBPA1 boundary and to determine whether simultaneous binding of Fg and Fn to FnBPA is affected by negative/positive putative cooperativity or potential steric effects. The specific aims were:

- To design, express and purify a set of novel rFnBPA constructs suitable for the analysis of Fg- and Fn-binding, most notably N2N3 and AF1 (Chapter 3)
- To establish the minimal region of FnBPA containing the native Fg-binding activity of intact FnBPA (Chapter 4)
- To identify the Fg-binding site on FnBPA and the mechanism of the FnBPA-Fg interaction (Chapter 4)
- To define the boundary between the A-domain and FnBPA1 (Chapters 4 and 5)
- To test negative/positive putative cooperativity between the Fg/Fn-AF1 (AF1 contains N2N3 and FnBPA1) interactions and whether the formation of the Fg-AF1-Fn ternary complex is inhibited by steric effects (Chapter 5)

## 2 Materials and Methods

### 2.1 Solutions

BUFFER / SOLUTION	COMPOSITION
Tris-borate-EDTA buffer (TBE)	890 mM Tris-HCl (10.8 g), 890 mM Boric acid (5.5 g), 20 mM EDTA (0.8 g), pH 8.3
Phosphate buffered saline (10xPBS)	1.4 M NaCl (81.8 g), 27 mM KCl (2.0 g), 100 mM Na <sub>2</sub> PO <sub>4</sub> ·2H <sub>2</sub> O (17.8 g), 18 mM KH <sub>2</sub> PO <sub>4</sub> (2.5 g), pH 7.4 after dilution (x10)
Tris-HCl buffer	50 mM Tris-HCl (6.1 g), 50 mM NaCl (2.9 g), pH 7.4

#### SDS-PAGE

MES (x20) running buffer	1 M MES (97.6 g), 1 M Tris (60.6 g), 69.3 mM SDS (10.0 g), 20.5 mM EDTA (3.0 g)
MOPS (x20) running buffer	1 M MOPS (104.6 g), 1 M Tris (60.6 g), 69.3 mM SDS (10.0 g), 20.5 mM EDTA (3.0 g)

#### Nickel-affinity purification

Loading/Wash buffer	20 mM Na/K phosphate (0.8 ml 4 M NaH <sub>2</sub> PO <sub>4</sub> ·H <sub>2</sub> O and 4.2 ml 4 M K <sub>2</sub> HPO <sub>4</sub> ), 150 mM NaCl (8.8 g), 30 mM Imidazole (2.0 g), pH 7.4
Elution buffer	20 mM Na/K phosphate (0.8 ml 4 M NaH <sub>2</sub> PO <sub>4</sub> ·H <sub>2</sub> O and 4.2 ml 4 M K <sub>2</sub> HPO <sub>4</sub> ), 150 mM NaCl (8.8 g), 0.5 M Imidazole (34.0 g), pH 7.4

#### Anion Exchange buffers

Loading/Wash buffer	20 mM Bis-Tris (4.2 g), pH 6.2
Elution buffer	20 mM Bis-Tris (4.2 g), 1M NaCl (58.4 g), pH 6.2

#### Size exclusion

Running buffer	20 mM Na/K phosphate (0.8 ml 4 M NaH <sub>2</sub> PO <sub>4</sub> ·H <sub>2</sub> O and 4.2 ml 4 M K <sub>2</sub> HPO <sub>4</sub> ), 150 mM NaCl (8.8 g), pH 7.4
----------------	---

BUFFER / SOLUTION	COMPOSITION
<b>SPR Buffers (Stock solutions from Biacore)</b>	
Running buffer HBS-P+	10 mM HEPES, 150 mM NaCl, 0.05% (v/v) P20, pH 7.4
Initial wash buffer	10 mM Glycine-NaOH, pH 12.0
Immobilization buffer	10 mM Sodium Acetate, pH 5.0
Regeneration buffer	HBS-P+ (pH 1.5)

**Table 2.1** Composition of all buffers and solutions used in the project. Appropriate volumes and weights of all chemicals were calculated for a total volume of 1 litre (made with qH<sub>2</sub>O).

## 2.2 Native proteins

### 2.2.1 Fg from human plasma

Human plasma glycoprotein Fg (341 kDa) was obtained as a white powder resulting from lyophilisation of purified Fg in 20 mM Na citrate-HCl pH 7.4 (Calbiochem/Merck). Lyophilised powder (1 g) was reconstituted in 24 ml of pre-warmed sterilised water (37°C) and left at 37°C without disturbing until the Fg was completely dissolved (approximately two hours). Subsequently the Fg solution was aliquoted and stored at -80°C. Fg was readily soluble at temperatures equal to or above room temperature but precipitated quickly at lower temperatures. The batch of Fg was analysed by SDS-PAGE, which confirmed its purity.

### 2.2.2 Fn from human plasma

Native human plasma glycoprotein Fn (440 kDa) was obtained as a clear solution of 1 mM Fn in 0.05 M TBS, pH 7.5 (Sigma Aldrich). Each batch of Fn was analysed by non/reducing SDS-PAGE to confirm purity and the dimeric nature of Fn. Results revealed only a small percentage (<10%) of the Fn sample occupied monomeric state. Following NaN<sub>3</sub> addition (final concentration 0.02% v/v), sample was stable at 4°C for several weeks.

## 2.3 Synthetic peptides and proteolytic fragments

### 2.3.1 Fg peptide (Fg1)

Fg1 is a synthetic peptide representing the last 17 C-terminal residues of Fg  $\gamma$  chain  $\text{CH}_3\text{CO-GEGQQHHLGGAKQAGDV-NH}_2$  ( $M_w = 1738$  Da) (Severn Biotech Ltd). This C-terminal sequence had been shown, by solid state binding assays, to be the minimum fragment conferring FnBPA binding comparable with the full length Fg (Wann et al., 2000). The Fg1 peptide was supplied as a lyophilised powder containing variable amounts of water and traces of peptide counter-ion usually trifluoroacetic acid. The N- and C-termini of the peptide contain acetyl and amino caps, respectively. The synthetic peptide was readily soluble at high concentrations ( $\leq 3$  mM) in water and most low pH buffers, however its solubility decreased significantly at a pH above 6.0.

### 2.3.2 SfbI-5

SfbI-5 represents the fifth Fn-binding repeat (residues 541-591) from the *Streptococcus pyogenes* extracellular protein SfbI (UniProt entry Q01924). SfbI-5 binds specifically to NTD ( $^{1-5}\text{F1}$ ) with high affinity (nanomolar) (Schwarz-Linek et al., 2003). The construct was originally designed and created by Sophie Raibaud (Schwarz-Linek et al., 2003) but the SfbI-5 sample used in this work was kindly provided by Dr Nicole C Norris (at that time; Department of Biology, University of York).

### 2.3.3 Fg fragment D (FgD)

FgD is a proteolytic fragment containing a single D region. It is produced by plasmin digestion of purified Fg (Calbiochem/Merck) and has the ability to bind FnBPA. FgD comprises C-terminal regions of all three chains  $\alpha$ ,  $\beta$  and  $\gamma$  and has an approximate molecular weight of 85 kDa. The fragment was supplied as a white powder obtained by lyophilisation of FgD in 400 mM Glycine and 150 mM NaCl. Lyophilised powder (200  $\mu\text{g}$ ) was dissolved in 1 ml of sterile water, aliquoted and stored at  $-80^\circ\text{C}$ . The stock could then be diluted into appropriate buffer to desired concentration when required. FgD was readily soluble in most buffers at neutral pH at room temperature but formed precipitate at  $4^\circ\text{C}$ .



### 2.3.4 N-terminal domain of fibronectin (NTD)

NTD ( $M_w = 28880$  Da; as determined by MS/ESI) is a proteolytic fragment generated by tryptic digestion of the N-Terminal 70 kDa Fn fragment, which is in turn produced by Cathepsin D digestion of purified native Fn (Sigma-Aldrich). NTD is supplied as a white powder resulting from lyophilisation of NTD in phosphate buffered saline with sucrose as a cryoprotectant. The lyophilised powder (0.5  $\mu$ g) was dissolved in 1 ml of sterilised water, aliquoted and stored at  $-20^\circ\text{C}$ . Prior to any further experiments the stock solution of NTD was dialysed against water or the desired buffer solution to remove traces of sucrose. NTD was soluble in most buffer solutions at room temperature but its solubility decreased significantly at lower temperatures.

## 2.4 Molecular biology

### 2.4.1 Construct design

*Escherichia coli* (*E. coli*) strains DH5 $\alpha$  (Genotype:  $F^- \Phi 80lacZ\Delta M15 \Delta(lacZYA-argF)$  U169 *recA1 endA1 hsdR17* ( $r_K^-$ ,  $m_K^+$ ) *phoA supE44*  $\lambda$ - *thi-1 gyrA96 relA1*) (Invitrogen) and BL21(DE3) Gold (Genotype: B  $F^- ompT hsdS(r_B^- m_B^-) dcm^+$  Tet<sup>r</sup> *gal*  $\lambda$  (DE3) *endA Hte*) (Stratagene) were used as hosts for cloning and expression of recombinant FnBPA (rFnBPA) proteins, respectively. Genes encoding all of the FnBPA recombinants were subcloned from pQE-30 vector containing the full FnBPA DNA (GenBank J04151.1, *S. aureus* 8325-4 strain) (Prof Tim Foster, Dublin) into a locally engineered pET-28a variant pET-YSBLIC-3C vector (York Structural Biology Laboratory, University of York), suitable for ligation independent cloning (LIC) (Section 2.4.4) (Bonsor et al., 2006). The FnBPA constructs were designed based on the full length FnBPA (UniProt entry P14738). The correct sequence of all rFnBPA clones was confirmed by DNA sequencing (Genomics Laboratory, Technology Facility, Department of Biology, University of York).

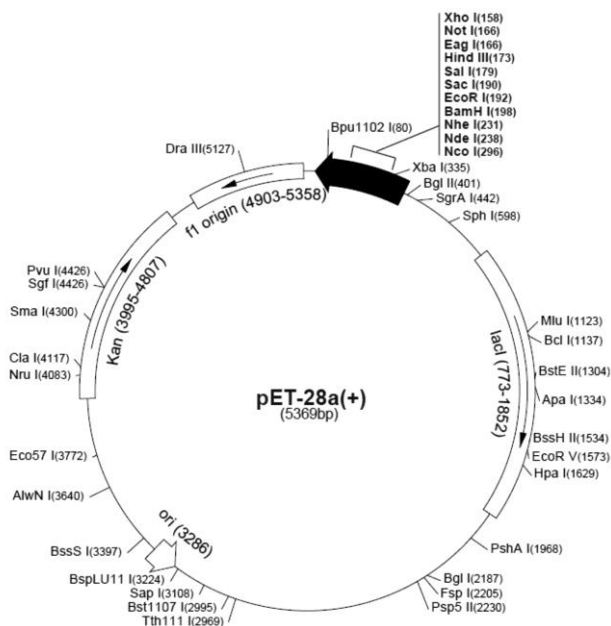


**Figure 2.1 pET-28a vector map.** The pET-YSBLIC3C is an N-terminal His<sub>6</sub>-tagged vector based on a modified pET-28a vector, with the thrombin cleavage site replaced by a Human rhino virus (HRV) 3C protease site. Cleavage of the His<sub>6</sub>-tag results in four additional residues Gly, Pro, Ala and Met at the N-terminus of the recombinant protein. The vector comprises 5369 bp, contains kanamycin resistance gene and all pET-28a restriction sites remain intact.

## 2.4.2 Primer design

All primers comprised three main parts: the LIC specific end, a gene specific sequence and either a start (ATG) or stop (TTG/A) codon for the forward or reverse primer, respectively. Ideally, all of the designed primers should be between 25 to 45 bases long, have minimum of 40% GC content, a melting temperature above 78°C and terminate with either a G or C base. Unfortunately, due to the character of the template DNA sequence it was not always possible to match every criteria, nevertheless all the primers eventually produced constructs with correct sequence. All primers were synthesised by Eurofins MWG/Operon. The theoretical melting temperature was calculated for each primer using Equation 2.1.

$$T_m = 81.5 + 0.41(\%GC) - \frac{675}{N} - \% \text{ mismatch} \quad (2.1)$$

N - total number of bases

### 2.4.3 Agarose gel electrophoresis

Agarose gel electrophoresis is a quick and straightforward method of separating mixed population of DNA or RNA based on their length. Each DNA sample was mixed with (6x) DNA loading buffer (Fermentas) and loaded on a 1% (w/v) agarose gel (Table 2.1) together with 1 Kbp and 100 bp DNA markers (Fermentas). When an electric current was applied to the gel, the negatively charged nucleic acids travelled through the agarose matrix towards the positively charged electrode. Smaller species move easily through the porous agarose hence travelled further than larger species. Details of the experimental setup are listed in the Table 2.2. Addition of SYBRsafe to the 1% (w/v) agarose gel mixture enabled the visualisation of the DNA bands with UV light. Presence of the correct insert in the plasmid DNA was tested by sequencing (Genomics Laboratory, Technology Facility, University of York).

Components	Parameters
Agarose Gel	0.8% or 1% (w/v) Agarose, 0.01% (v/v) SYBRsafe, TBE (Table 2.1)
Sample buffer	6x Orange DNA loading dye (Fermentas)
Running buffer	TBE
Voltage (V)	100
Current (mA)	~ 35
Duration (minutes)	50 - 60

**Table 2.2** Agarose gel electrophoresis parameters.

### 2.4.4 Ligation independent cloning using the pET-YSBLIC3C vector

#### 2.4.4.1 Plasmid linearization

1  $\mu$ l of circular plasmid (50 ng/ $\mu$ l) (kindly provided by YSBL) was transformed into a host strain (*E. coli* DH5 $\alpha$ ) and retrieved via the Qiagen miniprep kit. The vector was then linearized by incubating it with the restriction enzyme BseRI (NEB) at 37°C for one hour and fifteen minutes. The BseRI digest reaction composition was as follows: 50  $\mu$ g vector DNA, 50  $\mu$ l BseRI, 100  $\mu$ l buffer NEB2 (10x), autoclaved qH<sub>2</sub>O up to a final volume of 1 ml. The reaction mixture was analysed on a 0.8 % (w/v) agarose gel and the vector was subsequently retrieved using the Qiagen gel extraction kit.

#### 2.4.4.2 Vector LIC T4 polymerase reaction

The linearized vector was treated with LIC qualified T4 DNA polymerase (Novagen) to produce sticky ends which are recognised by the sticky ends on the insert DNA. The T4 polymerase reaction composition was as follows: 4 pmol linearized vector (calculated as the number of bp x 650 pg/pmol), 40 µl T4 polymerase buffer (10x), 40 µl dTTP (25 mM stock), 20 µl DTT (100 mM stock), 8 µl LIC qualified T4 DNA (2.5 U/µl) and sterile qH<sub>2</sub>O to a final volume of 400 µl. The reaction mixture was incubated at 22°C for 30 minutes and then the reaction was stopped by incubating at 75°C for 20 minutes (the T4 polymerase reaction was carried out on a programmed PCR machine). The final product was diluted to a working concentration of 15 ng/µl.

#### 2.4.4.3 Insert polymerase chain reaction (PCR)

Primers (MWG) were resuspended in sterile qH<sub>2</sub>O to give stock concentration of 100 pmol/µl (100 µM), which was then diluted to give working concentration of 20 µM. The composition of the PCR reaction mix was as follows: 1 µl forward primer, 1µl reverse primer, 5 µl dNTP's (2 mM), 2 µl MgSO<sub>4</sub> (25 mM), 5 µl KOD Hot start polymerase buffer (10x), 0.5 µl template DNA (50 ng/µl), 1 µl KOD Hot start polymerase (1 U/µl) (Merck) and sterile qH<sub>2</sub>O up to a final volume of 50 µl. The PCR programme used is shown in Table 2.3. The PCR product was analysed using a 1% agarose gel (Section 2.4.3) and retrieved via the Qiagen gel extraction kit.

	Temperature (°C)	Time (seconds)	Number of Cycles
Initial denature	94	120	1
Denature	94	30	35
Anneal	70	30	
Extension	72	180	
Final extension	72	300	1

**Table 2.3 PCR set-up.** Annealing and extension temperatures were determined based on the properties of individual primers and optimized in order to achieve the purest product.

#### **2.4.4.4 Insert LIC T4 polymerase reaction and annealing**

The insert was treated with LIC qualified T4 DNA polymerase to produce sticky ends recognised by sticky ends on the linearized vector DNA. The T4 polymerase reaction composition was as follows: 0.2 pmol insert (calculated as the number of bp x 650 pg/pmol), 2 µl T4 polymerase buffer (10x), 2 µl dATP (25 mM stock), 1 µl DTT (100 mM stock), 0.4 µl LIC qualified T4 DNA (2.5 U/µl) (Novagen) and sterile qH<sub>2</sub>O to a final volume of 20 µl. The reaction mixture was incubated at 22°C for 30 minutes and then the reaction was stopped by incubating at 75°C for 20 minutes (the T4 polymerase reaction was carried out on a programmed PCR machine). The T4 polymerase treated vector and insert anneal without the use of ligase. 4 µl of insert was mixed with 2 µl of linearized vector (15 ng/µl) and incubated at room temperature (20-22°C) for ten minutes. The reaction was quenched with 2 µl of EDTA (25 mM) for ten minutes to give a final volume of 8 µl.

#### **2.4.5 Transformation of competent *E. coli* cells with plasmid DNA**

The transformation protocol was based on (Novagen/Merck). Briefly, the whole LIC annealing reaction (8 µl) or 1 µl plasmid DNA (50 ng/µl) was added to approximately 100 µl of competent cells and incubated on ice for a minimum of thirty minutes followed by a heat shock (45 seconds at 42°C and then five minutes on ice) to enable the plasmid DNA to enter the cells. Prior to spreading on agar plates containing kanamycin (50 µg/ml), 500 µl of pre-warmed Luria-Bertani media (LB) (42°C) was added to the cell sample and incubated at 37°C for an hour with shaking to enable initial expression of the kanamycin resistance gene. The agar plates were incubated at 37°C overnight, and then stored at 4°C. Competent cells lacking the vector were used as a negative control.

All construct DNA was submitted for sequencing to the Genomics Laboratory (Technology Facility, University of York) to confirm correct sequence. Plasmid DNA of each construct was sequenced from both the forward and reverse directions using T7 and T7term pET-YSBLIC3C specific primers, respectively, which were supplied by the Genomics Laboratory.

## 2.5 Expression of recombinant proteins

Plasmid DNA containing the specific rFnBPA gene was transformed into the expression strain of *E. coli* (BL21 (DE3) Gold) using the same procedure as in 2.4.5. A single colony was picked from the kanamycin containing agar plates and used to inoculate 100 ml of fresh (LB) containing kanamycin (30 µg/ml), which was then incubated overnight at 37°C with shaking. Pre-warmed baffled flasks (37°C) containing 500 µl of fresh sterilised LB with kanamycin were inoculated with 5 ml of the overnight culture each and incubated at 37°C with shaking (200 rpm) until the culture reached an optical density (OD<sub>600</sub>) of 0.7 (approximately two to three hours). Once the optimum density had been reached the expression of the desired gene was initiated by adding 200 µl of a filter-sterilised 1 M stock solution of isopropyl-β-thiogalactopyranoside (IPTG) (working concentration - 0.4 mM). The cell culture was then incubated at 37°C with shaking (200 rpm) for four additional hours from the time of induction. Cells were harvested and pelleted using a Sorvall centrifuge, SLC-6000 rotor (20 minutes, 5000 rpm, 4°C). The cell pellet was resuspended in a small volume of nickel-affinity chromatography loading buffer (Table 2.1) (final volume of 35 ml) and stored at -20°C.

## 2.6 Purification of recombinant proteins

### 2.6.1 Cell lysis and supernatant clarification

Frozen cell pellets were thawed at room temperature and homogenized thoroughly using a pasteur pipette. The resuspended cells were lysed using a pre-programmed sonicator 3000 (Misonix) with 60 x 3-second pulses (7 second intervals) at 70 W while on ice. The cell lysate was centrifuged using a Sorvall centrifuge rotor ss-34 (30 minutes, 18000 rpm, 4°C) and the clarified supernatant carefully retrieved to be used in further purification steps.

### 2.6.2 Nickel-affinity purification

All constructs were purified from the supernatant using a pre-packed 5 ml HisTrap HP column (GE Healthcare) connected to the ÄKTA Purifier 10 system (GE Healthcare) at room temperature. The whole system, including columns, was equilibrated with several column volumes of binding buffer (Table 2.1) prior to

loading cell lysate onto the column. The lysate was loaded onto the column at rate of 3 ml/min followed by a wash with approximately 25 column volumes of binding buffer (or until the UV absorbance at 280 nm of the column eluent was reduced to values below 50 mAU). The His<sub>6</sub>-tagged protein was retrieved from the column using gradient elution (apart from N3, which was retrieved using step-wise elution comprising 10% increments) with a buffer containing 0.5 M imidazole. Details of the method are listed below (Table 2.4).

<b>Components</b>	<b>Parameters</b>
Column	HisTrap HP 5 ml
Binding buffer	20 mM Na/K phosphate (Table 2.1)
Flow rate	1 ml/min
Gradient	0 – 40% Elution buffer (Table 2.1)
Gradient length	25 column volumes
Fractions	2 ml
Detection	Absorbance at 280 nm

**Table 2.4 Nickel-affinity purification parameters.**

### **2.6.3 SDS-PAGE**

Sodium dodecyl polyacrylamide gel electrophoresis (SDS-PAGE) is a quick and straightforward method of analysing sample purity and estimating of the molecular mass of proteins. Gel electrophoresis is based on the separation of protein species on a polyacrylamide gel according their molecular mass and net charge. The technique was performed to analyse the results of every purification step, however, the definitive method for determining the precise mass of purified proteins was MS/ESI (see chapter 2.8.6). Each sample, containing approximately 1 µg of protein was mixed with SDS (an anionic denaturing agent that also applies a negative charge to each protein) and, in some cases, dithiothreitol (DTT) (reducing agent) containing loading buffer, boiled if required to ensure complete denaturation and loaded on the polyacrylamide gel. As electric current was applied to the gel resulting in migration of the negatively charged proteins across the gel towards the positively charged electrode. Details of the experimental setup are listed in the Table 2.5. Most of the SDS-PAGE system (pre-cast 4-12% Bis-Tris 1.0 mm gradient gels, protein markers (molecular weight reference), lithium dodecyl sulphate (LDS) loading buffer, MES/MOPS running buffers and a gel tank) was supplied by Invitrogen. The power-pack was purchased from Biorad. The polyacrylamide gels were stained with

a solution of Coomassie Brilliant Blue R-250 for minimum of 1 hour and subsequently de-stained with a solution of 10% (v/v) Acetic acid.

<b>Components</b>	<b>Parameters</b>
Gel	4-12 % Bis-Tris 1.0 mm Gradient (Invitrogen)
Running buffer	MOPS/MES (Table 2.1)
Loading buffer	NuPAGE LDS sample buffer (Invitrogen)
Voltage (V)	200
Current (A)	~ 400
Duration (min)	35 to 50
Sample volume ( $\mu$ l)	10 (~ 1 $\mu$ g)

**Table 2.5 SDS-PAGE parameters.**

#### **2.6.4 NATIVE-PAGE**

NATIVE-PAGE analysis is based on the same principle as SDS-PAGE, though as the name suggests the aim of NATIVE-PAGE is to analyse intact proteins in their native state. Consequently, the NATIVE-PAGE set up is similar to that for SDS-PAGE albeit with non-denaturing buffers (to ensure the proteins remain intact) and gels with the appropriate resolution. All components, including buffers and pre-cast gels, were supplied by Invitrogen. Details of the experimental setup are listed in the Table 2.6.

<b>Components</b>	<b>Parameters</b>
Gel	4-16 % Bis-Tris 1.0 mm Gradient (Invitrogen)
Running buffer	NativePAGE-Running buffer (Invitrogen)
Loading buffer	NativePAGE-Sample buffer (Invitrogen)
Voltage (V)	150
Current (A)	~ 400
Duration (min)	60-100
Sample volume ( $\mu$ l)	10 (~1 $\mu$ g)

**Table 2.6 NATIVE-PAGE parameters.**



### 2.6.5 Cleavage of N-terminal His<sub>6</sub>-tag with HRV 3C

Pooled fractions from the nickel-affinity purification were dialysed overnight at 4°C in size exclusion buffer (Table 2.1) to remove imidazole which could interfere with the activity of the HRV 3C protease. HRV 3C protease (4.6 mg/ml; expressed and purified by HiTel) was subsequently added to the protein sample at ~ 1:500 protease:protein molar ratio, mixed gently and incubated at 4°C for 4 hours. The HRV 3C cleavage reaction was analysed by SDS-PAGE. A HisTrap HP 5 ml column and ÄKTA Purifier 10 system (identical setup to the nickel-affinity purification) was used to remove the HRV 3C protease (contains a His<sub>6</sub>-tag), the cleaved histidine tag and any remaining protein fragments with an uncleaved His<sub>6</sub>-tag. The column was equilibrated in binding buffer without imidazole and the flow-through of the HRV 3C cleavage reaction was collected and analysed by SDS-PAGE. All N2N3 constructs were almost pure (less than 5% contaminants detectable), however the AF1 sample still contained a significant amount of impurities and degradation products. Therefore, before the final purification step, size-exclusion chromatography, could be performed, an anion exchange chromatography (IEX) was carried out on the AF1 sample as an additional purification step.

### 2.6.6 Anion exchange chromatography (IEX)

The flow-through from the nickel-affinity purification, containing AF1, was dialysed against 5 litres of IEX binding buffer (Table 2.1) overnight at 4°C to significantly reduce the salt content of the sample. AF1 was purified using a pre-packed HiTrap Q sepharose 5 ml column (GE Healthcare) connected to the ÄKTA Purifier 10 system (GE Healthcare). The whole system, including column was equilibrated in several column volumes of binding buffer before the AF1 containing solution was loaded onto the column. AF1 was loaded at flow rate of 5 ml/min and was followed by a wash with three column volumes of the binding buffer. AF1 was retrieved by gradient elution with buffer containing a high salt concentration (Table 2.6). Identity and purity of the resulting peaks was tested by SDS-PAGE. The main elution peak contained pure AF1.

<b>Components</b>	<b>Parameters</b>
Column	HiTrap Q Sepharose Fast Flow (GE Healthcare)
Loading buffer	20 mM Bis-Tris (Table 2.1)
Elution buffer	20 mM Bis-Tris, 1 M NaCl (Table 2.1)
Flow rate	0.7 ml/min
Gradient	0-35% elution buffer (Table 2.1)
Gradient length	30 column volumes
Fractions	2 ml
Detection	Absorbance at 280 nm

**Table 2.7 Anion exchange chromatography parameters.**

### 2.6.7 Size-exclusion (gel filtration) chromatography

Size-exclusion chromatography was performed as the last purification step in order to remove any remaining contaminants with significantly different molecular weights and to separate the monomeric form of the protein from multimeric species. All rFnBPA proteins (with the exception of N1N2) were purified using a pre-packed Superdex S75 16/60 HiLoad column (GE Healthcare) connected to the ÄKTA Purifier 10 system (GE Healthcare). The whole system, including the column, was equilibrated with minimum of two column volumes (240 ml) of running buffer (Table 2.1) prior to the injection of the sample onto the column. Samples were concentrated down to the volume of 1 ml in concentrators (Vivaspin, MWCO 10 kDa) using a Sigma centrifuge (7500 g at 4°C) to allow the injection onto the column using a 2 ml injection loop. Details of the method setup are listed in Table 2.8. Fractions of the main peak were pooled and stored at -20°C. The molecular mass of all recombinant proteins was confirmed using MS/ESI. The oligomeric state for N2N3 and AF1 was determined by AUC (Section 2.8.4).

<b>Components</b>	<b>Parameters</b>
Column	Superdex S75 16/65 Prep HiLoad (GE Healthcare)
Running buffer	20 mM Na/K phosphate (Table 2.1)
Flow rate	1 ml/min
Duration	240 ml (2 column volumes)
Fractions	2 ml
Detection	Absorbance 280 nm
Sample volume	1 ml

**Table 2.8 Size-exclusion chromatography parameters.**

### 2.6.8 Protein concentration measurements and calculations

The absorbance of the protein in solution at 280 nm wavelength was measured in plastic cuvettes (1 cm pathlength) using a Biophotometer (Eppendorf). The molar concentration was determined using the Beer-Lambert law;

$$c = \frac{A}{\epsilon \times l} \quad (2.2)$$

$A$  represents the absorbance at 280 nm,  $\epsilon$  the molar extinction coefficient and  $l$  the cuvette pathlength. The theoretical molar extinction coefficient is calculated according to following equation (Gasteiger et al., 2003);

$$\epsilon_{\text{protein}} = (N_{\text{cys}} \times \epsilon_{\text{cys}}) + (N_{\text{tyr}} \times \epsilon_{\text{tyr}}) + (N_{\text{trp}} \times \epsilon_{\text{trp}}) \quad (2.3)$$

$N$  represents the number of the particular amino acid and  $\epsilon$  represents the molar extinction coefficient associated with each amino acid (cys – cysteine, 125 M<sup>-1</sup> cm<sup>-1</sup>; tyr – tyrosine, 1490 M<sup>-1</sup> cm<sup>-1</sup> and trp - tryptophan, 5500 M<sup>-1</sup> cm<sup>-1</sup>).

## 2.7 Plasma pull-down assay

The pull-down assay was conducted mainly by Andrew Brentnall (Department of Biology, University of York) using the ‘AminoLink Plus Immobilization Kit’ (Thermo Scientific) and the appropriate protocols as designed by the manufacturer. N2N3 and AF1 (20 mg each) were immobilised on two separate beaded agarose gravity-flow columns by amine coupling, utilizing the protein primary amines. One column was left uncharged and used as a negative control. Each column was equilibrated in PBS prior to applying 3 ml of human plasma, followed by wash in PBS (5 column volumes) and subsequent elution with citrate buffer pH 3.0. Solutions of purified Fg (Section 2.2.1), Fn (Section 2.2.2) or mixture of both were used as a control. The results were analysed by SDS-PAGE. The assay was carried out at room temperature.

## 2.8 Biophysical techniques

### 2.8.1 NMR spectroscopy

Buffer solutions of all protein samples were exchanged to 20 mM Na/K phosphate, 100 mM NaCl, pH ranging between 6.0 and 8.0. Each protein sample comprised 540

$\mu\text{l}$  of protein solution, 60  $\mu\text{l}$  D<sub>2</sub>O (10% (v/v)) and 1.2  $\mu\text{l}$  of NaN<sub>3</sub> (0.02% (v/v)). The final protein concentration in the sample solution was 0.2 mM. Binding studies involving rFnBPA proteins and Fg1 required step wise addition of the peptide to the protein solution to enable spectra acquisition of the protein-peptide complex at different molar ratios. The required protein peptide ratios were achieved using lyophilised aliquots of Fg1, which were dissolved in the protein solution, followed by pH adjustment to the original value.

All 2D <sup>15</sup>N<sup>1</sup>H transverse relaxation optimized spectroscopy heteronuclear single quantum coherence (TROSY-HSQC) spectra were recorded using the trosytf3gpsi pulse sequence with echo/antiecho gradient selection, excitation sculpting for solvent suppression and sensitivity improvement incorporated into TopSpin 2.1 (Bruker BioSpin). All 1D and 2D spectra were recorded at 37°C on a Bruker Avance 700 MHz Ultrashield system with a 5 mm TXI-ATM-z-gradient probe (Centre for Magnetic Resonance, University of York). The acquired spectra were processed with NMRPipe (Delaglio et al., 1995) and analysed using Analysis 1.0 software packages (Vranken et al., 2005).

## **2.8.2 Surface plasmon resonance**

All SPR experiments were carried out on T100 system (Biacore) with SPR buffers and consumables obtained solely from Biacore (Table 2.1). Analyte samples were dialysed extensively against the running buffer HBS-P+. Two types of sensor chips were used in the experiments, namely, the CM5 chip with a carboxymethyl dextran coated gold surface or the C1 chip with a non-dextran carboxylated surface. All binding experiments were carried out at flow rate of 30  $\mu\text{l}/\text{min}$ . Reagents were kept at 25°C in the sample compartment and all data were collected at 25°C. Prior to all experiments a minimum of 5 start-up cycles were performed in order to stabilise the baseline.

### **2.8.2.1 Sample preparation**

Due to high sensitivity of the SPR it was essential that all samples (analytes and ligands) are pure and the analyte solvent is identical to the running buffer (Table 2.1). For all rFnBPA proteins, the analyte solvent was exchanged for the running

buffer and the samples were concentrated to a desired concentration to form a stock from which the required dilutions were made. A commercial sample of Fg stock was dialysed against the running buffer and concentrated to the required concentration prior to each SPR experiment. Different concentrations of analyte in the kinetics/affinity SPR experiment were prepared by serial dilutions of the highest concentration. The commercial sample of NTD (Sigma-Aldrich), used as a ligand, was supplied as a lyophilised powder and dissolved in qH<sub>2</sub>O, then dialysed against a further 5 litres of qH<sub>2</sub>O at room temperature to remove any traces of lyophilisation cryo-protectant which could potentially affect the SPR results. The sample of NTD in qH<sub>2</sub>O was then lyophilised and subsequently dissolved in a small volume of qH<sub>2</sub>O to form a high concentration stock which could be diluted into the immobilization buffer to the required concentration. The commercial sample of lyophilised FgD powder (Fisher), used as a ligand, was simply resuspended in qH<sub>2</sub>O and subsequently diluted into the immobilization buffer.

### 2.8.2.2 Ligand immobilization

Ligands in 10 mM Na acetate buffer (pH 5.0) were covalently coupled to the sample cell via the N-terminus of the polypeptide chain and the  $\epsilon$ -amino groups of the lysine residues to reach baseline level ( $R_L$ ) between 50-120 response units (RU). First, the carboxylated sensor chip surface was activated with a solution of EDC and NHS (Section 1.7.2.3) (Johnsson et al., 1991) generating reactive succinimide esters, which react readily with the amine groups on the ligand. Next, the activated surface was exposed to the ligand containing solution under conditions allowing electrostatic pre-concentration. Since the pKa of the surface is <3.5 and the isoelectric point of all ligands used in the project was >6, sodium acetate buffer (10 mM) pH 5.0 was used in all immobilizations, as it is close to the ligand physiological solution conditions. Once a sufficient amount of the ligand had been accumulated at the surface of the sensor chip, ethanolamine was used to deactivate any remaining active groups and to remove any non-covalently bound ligand. A breakdown of the amine coupling procedure carried out is in Table 2.9.

Step	Injection	Contact time (s)	Flow rate ( $\mu\text{l}/\text{min}$ )	Flow cell
1	Surface activation (EDC/NHS)	420	5	2,1
2	Immobilization (ligand)	30-200 (based on the ligand type)	5	2
3	Deactivation of excess reactive groups (ethanolamine)	420	5	2,1

**Table 2.9 Amine coupling immobilization steps.**

### 2.8.2.3 Affinity

The majority of the binding interactions exhibited very fast on/off rates, which were outside the measurable limitations of the instrument (Section 1.7.2.4) and therefore unsuitable for determination of the  $K_d$ . However, in most cases they reached steady state allowing for affinity of the interaction to be determined based on the equilibrium binding ( $R_{eq}$ ). Each experiment consisted of a minimum of 10 cycles during which the ligand-coated sensor chip was exposed to analyte concentrations between approximately two orders of magnitude below and above the predicted  $K_d$ . Each cycle comprised an analyte injection (association period) (180 s), a dissociation period (300 s) and equilibration (120 s) at flow rate 30  $\mu\text{l}/\text{min}$ . Interactions analysed by this method are as follows; FgD-N2N3, FgD-N2N3T, FgD-AF1, FgD-AF1+NTD and NTD-AF1+Fg1. Data processing and evaluation was carried out using Biacore T100 evaluation software.

### 2.8.2.4 Kinetics

AF1 binding to the native Fn was the only interaction assessed using kinetic parameters. In a typical kinetic experiment the equilibrium constant ( $K_d$ ) is determined based on the rate constants of the association and dissociation phase. The experiment comprised 10 cycles where the immobilized AF1 was exposed to concentrations of intact Fn between 0.0122 and 6.25 nM. Each cycle comprised an association period (100 s), a dissociation period (600 s), a regeneration phase (60 s) and an equilibration phase (120 s). 10 mM glycine buffer pH 2.5 was used for regeneration. Data were processed and analysed using Biacore T100 evaluation software

### 2.8.2.5 Ternary complex

In the ternary complex experiments either NTD or AF1 was immobilized as described above, followed by a series of injections containing combinations of varying concentrations and concentration ratios of the complex forming analytes. Sfb1-5 peptide, representing the fifth NTD-binding repeat of SfbI (Section 2.3.2), and Fg1 or N2N3 were used in control experiments as specific inhibitors of the interactions between AF1 and NTD or Fg/FgD, respectively. Data analysis was performed using Biacore T100 evaluation software allowing for subsequent visual assessment of the  $R_{eq}$  and the character of both the association and dissociation phases.

### 2.8.3 Isothermal titration calorimetry

All ITC experiments were carried out on the same VP-ITC calorimeter (MicroCal Inc.) with the cell and syringe volumes of 1.4 ml and 275  $\mu$ l, respectively. All measurements were performed in PBS at a constant temperature (25°C). The concentration of the cell sample was identified based on the unitless constant  $c$  describing the shape of the binding isotherm and a suitable molar ratio of cell/syringe sample was chosen to achieve full saturation approximately half-way through the titration. Each experiment consisted of the initial single 2  $\mu$ l injection of the syringe solution into the cell followed by 27 x 10  $\mu$ l injections at 0.5  $\mu$ l/s in 6 minute intervals with the stirring speed set to 307 rpm for all titrations with the exception of the experiments involving native Fg, where the stirring speed had to be increased to 321 rpm due to the high viscosity of the solution. Where applicable, the titration was repeated under identical conditions but with no protein in the cell (blank titration). Heats generated during the blank titration were subtracted from the heats of the actual titrations to rule out potential distortion of the fitted data caused by heats of dilution. The raw ITC data were integrated and binding isotherms fitted by an iteration process based on the 'one-set of sites' model (MicroCal Origin software). Equations used to generate the single binding isotherm based on the obtained data are listed in Appendix II.

### **2.8.4 Analytical ultracentrifugation (AUC)**

Sedimentation velocity experiments were conducted by Dr Andrew Leech (Technology Facility, University of York) on a Beckman Optima XL/I analytical ultracentrifuge, using Beckman cells with a 12 mm path length double sector charcoal-filled Epon centrepieces and sapphire windows, in an AN-50Ti rotor (five cells plus counterbalance). Approximately 420  $\mu\text{l}$  reference buffer (20mM Na/K phosphate, 100mM NaCl, pH 7.4) and 416  $\mu\text{l}$  of sample (in reference buffer) were loaded into the cells. Absorbance scans were taken at 3000 rpm in order to check concentrations and uniform distribution of the cell content. The speed was increased to 35000 rpm and absorbance scans taken at approximately 3 minute intervals until sedimentation was complete. The run lasted 10 hours and was conducted at 20°C. Samples of N2N3, AF1 and N2N3T with Fg1 were at concentration of 25  $\mu\text{M}$  and Fg1 at a twenty-fold molar excess. Data were analysed using the SEDFIT (Schuck, 2000) software package with partial specific volumes, buffer densities and viscosities estimated using the program SEDNETRP (Laue et al., 1992).

### **2.8.5 Differential Scanning Calorimetry (DSC)**

Protein samples were dialysed into 20 mM Na/K phosphate buffer, 100 mM NaCl, pH 7.4 and the concentration adjusted to 1 mg/ml. DSC experiments were carried out by Dr Iain Manfield (Astbury Centre, University of Leeds) on a VP-DSC system (MicroCal). Data analysis was performed using MicroCal Origin software.

### **2.8.6 Electrospray ionization mass spectrometry (ESI/MS)**

Protein samples (typically 100  $\mu\text{M}$ ) usually dialysed into  $\text{dH}_2\text{O}$  or a Tris-HCl buffer with low salt were submitted for analysis by mass spectrometry. ESI/MS measurements were performed by Berni Strongitharm (Technology Facility, University of York) on ABI Qstar tandem mass spectrometer.

### **2.8.7 Crystallization of N2N3T**

Diffraction crystals of N2N3 grew in a Clear Strategy Screen (CSS) II condition containing polyethylene glycol (PEG) 20000 (8% (w/v)), PEG monomethyl ether (mme) 550 (8% (v/v)), 0.2 M calcium acetate, with added 50 mM Tris-HCl, 50 mM



NaCl, pH 7.4 at a protein concentration of 30 mg/ml using the sitting drop vapour diffusion method. Each drop comprised 100 nl of reservoir solution, 50 nl of seed stock and 150 nl of protein solutions. Seed stock was prepared by adding several non-diffracting crystal clusters into 100  $\mu$ l of the same reservoir solution described above, containing a single Seed Bead (Hampton Research) and subsequent sonication in a sonication bath generating a homogeneous solution suitable for dispensing by the Mosquito® nano-drop dispensing system (TTP Labtech). Automated set up of crystallization screens and sitting drops was carried out using the HYDRA and Mosquito® liquid handling systems. Clusters of protein crystals grew after three days at 18°C. Whole clusters were transferred into cryo-protectant (reservoir solution with additional 10% (w/v) of PEG 20000 and 10% (v/v) of PEG mme 550) where a single diffracting crystal was broken off and vitrified in liquid nitrogen.

### 2.8.8 Data collection and N2N3T structure determination

Diffraction data for the N2N3T crystals were collected on the European Synchrotron Radiation Facility (ESRF) (Grenoble, France) beamline ID29 at 100 K. Collected diffraction data were indexed and integrated with HKL2000 (Otwinowski and Minor, 1997) and scaled using SCALA (Evans, 2006). The N2N3T crystal structure was solved using the molecular replacement pipeline BALBES (Long et al., 2008) with the combination of ClfA (PDB entry 1n67) (Deivanayagam et al., 2002) and SdrG-Fg peptide complex (PDB entry 1r17) (Ponnuraj et al., 2003) identified as the suitable two-domain model. After a few initial cycles of Refmac 5 (Murshudov et al., 1997), ARP (Lamzin and Wilson, 1993)/WARP (Perrakis et al., 1997) incorporated into CCP4 software suite (Winn et al., 2011) was used to improve the electron density map and to build in water molecules. Final refinement was carried out by a combination of manual building in COOT (Emsley and Cowtan, 2004) and automatic refinement by Refmac 5 until a sufficiently low  $R_{factor}$  and  $R_{free}$  were achieved. The structure was verified using MolProbity server (Chen et al., 2010). All root mean square deviation (r.m.s.d.) values were determined using secondary structure matching (s.s.m.) (Krissinel and Henrick, 2004), an algorithm incorporated into the CCP4mg molecular graphics software (McNicholas et al., 2011). The calculations of solvent accessible surface were performed using PISA (Krissinel and Henrick, 2007) incorporated into the CCP4 software package.

### 2.8.9 Crystallization of N2N3T-Fg1 complex

Synthetic Fg1 peptide was dissolved slowly in the N2N3T sample buffer (50 mM Tris-HCl, 100 mM NaCl, pH 7.4) and its pH adjusted to 7.4. Diffracting crystals were grown in a CSS II screen condition containing PEG 2000 mme (25% (w/v)), 0.2 M calcium acetate, with added 50 mM Tris-HCl, 100 mM NaCl, isopropanol (10% (v/v)), pH 7.4 at a protein concentration of 25 mg/ml with a 20 fold molar excess of Fg1. Sitting drop vapour diffusion with the micro-seeding technique was set up as described in 1.6.8. Crystals were obtained after 48 hours incubation at 18°C. Again, protein crystal clusters were transferred into cryo-protectant (reservoir solution with additional PEG 2000 (5% (w/v))) where a single diffracting crystal was broken off and vitrified in liquid nitrogen.

### 2.8.10 Data collection and N2N3T-Fg1 structure determination

Diffraction data for the N2N3-Fg1 complex crystal were collected on the Diamond beamline i04-1 at 100 K. Collected diffraction data were indexed, integrated and scaled automatically using xia2 (Winter, 2009). The N2N3T-Fg1 crystal diffracted to 1.83 Å and the structure was solved by molecular replacement using the structure of N2N3T as a model. Residues corresponding to the Fg1 peptide were modelled manually into a well defined electron density area with the subsequent refinement again carried out by a combination of manual building in COOT (Emsley and Cowtan, 2004) and automatic refinement by Refmac 5 (Murshudov et al., 1997) until a sufficiently low  $R_{factor}$  and  $R_{free}$  were achieved. All r.m.s.d. values were determined using the s.s.m. algorithm (Krissinel and Henrick, 2004) incorporated into the CCP4mg molecular graphics software (McNicholas et al., 2011). The calculations of solvent accessible surface were performed using PISA (Krissinel and Henrick, 2007) incorporated into the CCP4 software package.

### 3 Molecular biology, expression and purification of recombinant FnBPA protein constructs

#### 3.1 Introduction

Numerous *in vitro* and *in vivo* studies have been carried out on native FnBPA (Figure 3.1), utilizing an array of solid phase assays as well as single gene-knock out mutants and recombinant bacterial strains. Consequently, FnBPA has been identified as a major virulence factor of *S. aureus* (Que et al., 2001b; Shinji et al., 2011) associated with a variety of life threatening conditions such as osteomyelitis and endocarditis (Musher et al., 1994; Moreillon and Que, 2004), mainly due to its ability to interact with multiple ECM proteins such as Fg, Fn and elastin (Wann et al., 2000; Froman et al., 1987; Keane et al., 2007a). The adjacent Fg and Fn binding sites and their putative cooperativity, have been linked with the development of infective endocarditis (Piroth et al., 2008; Que et al., 2001a; Fitzgerald et al., 2006b). While the Fn-binding region of FnBPA has been investigated in great detail using a range of recombinant FnBPA proteins (Massey et al., 2001; Bingham et al., 2008; Schwarz-Linek et al., 2003; Meenan et al., 2007), only a limited amount of data is available regarding the adjacent Fg-binding site and its interaction with Fg.

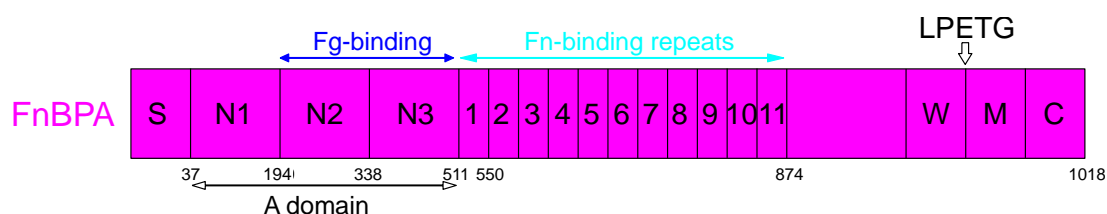


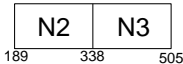
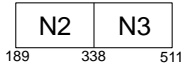
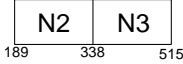
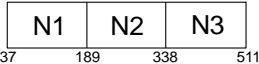
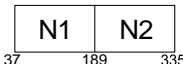
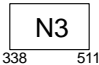
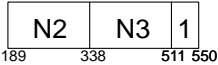
**Figure 3.1 Schematic diagram of native FnBPA.** Fn- and the predicted Fg-binding regions (Keane et al., 2007a; Loughman et al., 2008) are shown in cyan and blue respectively. Domain boundaries are also indicated by residue numbers.

#### 3.2 Aims

The main aim was to produce a set of recombinant FnBPA (rFnBPA) protein constructs, with the intention of characterising in detail the Fg-binding region and the putative cooperativity between Fg and Fn binding to FnBPA. The establishment of reliable and reproducible molecular biology, expression and purification strategies was the first step in the process. Procedures were optimised to achieve maximum yields and to identify the most favourable solution conditions for maintaining each

rFnBPA protein in a stable and soluble form. Some of the rFnBPA proteins were uniformly labelled with  $^{15}\text{N}$  to facilitate analysis by 2D NMR spectroscopy. The rFnBPA proteins utilized in this project are listed in Table 3.1.

### 3.3 Overview of rFnBPA proteins used in this study

Residues	Name / Domain	Schematics
rFnBPA <sub>(189-505)</sub> / ( $^{15}\text{N}$ )	N2N3T (truncated)	
rFnBPA <sub>(189-511)</sub> / ( $^{15}\text{N}$ )	N2N3	
rFnBPA <sub>(189-515)</sub>	N2N3E (extended)	
rFnBPA <sub>(37-511)</sub>	A-domain (fA)	
rFnBPA <sub>(37-335)</sub>	N1N2	
rFnBPA <sub>(335-511)</sub>	N3	
rFnBPA <sub>(189-550)</sub> / ( $^{15}\text{N}$ )	N2N3, FnBR-1 (AF1)	

**Table 3.1 rFnBPA protein constructs.** The list includes the FnBPA residue numbering, according to accession code P14738 (*S. aureus* strain NCTC 8325-4), domain composition and the abbreviations used throughout the thesis. A schematic representation of each rFnBPA protein (based on Figure 3.1) is also shown. Recombinant proteins that were also expressed uniformly labelled with  $^{15}\text{N}$  are indicated.

#### 3.3.1 N2N3

N2N3 comprises the complete N2 and N3 domains and is predicted to represent the minimum region of FnBPA that retains the ability to bind Fg (Loughman et al., 2008; McDevitt et al., 1995; Keane et al., 2007b). However, there is no structural data (and little functional data) regarding this region and its interaction with Fg (Keane et al., 2007b). N2N3 unbound and in complex with Fg1 was subjected to extensive crystallization trials to produce diffracting crystals, which eventually lead to high resolution crystal structures of N2N3 and the N2N3-Fg1 complex. The FnBPA-Fg interaction was also investigated using N2N3 and a variety of biophysical techniques including SPR and ITC.

### 3.3.2 N2N3T

N2N3T is a truncated version of the full length Fg-binding region formed by the domains N2 and N3. The recombinant protein lacks six C-terminal residues (Asn-Gly-Asn-Glu-Lys-Asn) of the N3 domain (Figure 1.9). Based on previous studies of the homologous proteins ClfA and SdrG (Ponnuraj et al., 2003; Ganesh et al., 2008), these residues form a large portion of a putative latch strand which interacts with the N2 domain, a process thought to be involved in Fg binding (Section 1.6.3). The putative latch strand is also predicted to be intrinsically unstructured in the absence of bound Fg (Ponnuraj et al., 2003; Bowden et al., 2008). The two reasons for generating this particular protein were, firstly, to test whether the latch strand is essential to Fg binding and secondly, to obtain a more suitable candidate for crystallization trials (as the potentially disordered nature of the putative latch strand could interfere with the crystallization process).

### 3.3.3 N2N3E

The N2N3E is an extended version of the Fg-binding region containing four additional C-terminal residues (Gly-Pro-Ile-Ile) following the latch strand. The sole purpose of this construct was to produce protein suitable for crystallization and structure determination of the N2N3 region. Sequence alignment of FnBPA with the recombinant SdrG and ClfA proteins (Ganesh et al., 2008; Ponnuraj et al., 2003) used for crystal structure determination, revealed a number of additional residues at the C-terminus. N2N3E was used in crystallization trials to test its ability to form diffracting crystals.

### 3.3.4 The fA

Residues 37 to 511 represent the complete A-domain which, besides N2 and N3, also contains the N1 domain (residues 37 to 189). N1 is the most N-terminal region of the A-domain and, unlike N2 and N3, is completely unstructured (unpublished results). N1 has a much higher level of sequence conservation across different strains of *S. aureus* compared with the N2 and N3 domains (Loughman et al., 2008). However, solid phase binding assays ruled out a role for N1 in Fg binding and no other putative function has yet been identified (Keane et al., 2007b). The interaction

between fA and Fg was analysed by SPR and the results compared with those for the N2N3-Fg interaction to test whether N2N3 contained the Fg-binding activity of the full length A-domain.

### 3.3.5 N1N2 and N3

N1N2 comprises domains N1 and N2, while N3 contains the N3 domain only. The extent of the contribution to the strength of the overall N2N3-Fg interaction by the individual domains N2 and N3 is not clear. While some publications state that the minimum Fg-binding region consists of N2 and N3, others show only a fragment of N3 retains the Fg-binding ability (Loughman et al., 2008; Piroth et al., 2008; Keane et al., 2007b). Both N1N2 and N3, in combination with fA, were used in the preliminary SPR binding experiments aimed at establishing the individual contributions of N2 and N3 towards the overall intermolecular interaction of FnBPA with Fg.

### 3.3.6 AF1

Residues 189 to 550 that form AF1 not only encompass the full length N2N3 region but also the first FnBR (FnBPA1). As a result, AF1 has the capacity to bind both Fg and Fn. AF1 is arguably the most important rFnBPA construct, designed specifically to address the question of simultaneous binding of Fg and Fn to FnBPA and the putative cooperativity of the interactions.

### 3.3.7 $^{15}\text{N}$ -N2N3, $^{15}\text{N}$ -N2N3T and $^{15}\text{N}$ -AF1

Three rFnBPA proteins; N2N3, N2N3T and AF1 were uniformly labelled with  $^{15}\text{N}$  (Marley et al., 2001) to facilitate the study of these recombinant proteins and their interactions with Fg and Fn peptides by NMR spectroscopy. The  $^{15}\text{N}$ -N2N3 and  $^{15}\text{N}$ -N2N3T were produced for the purpose of analysing Fg1 binding and the potential effect of the missing latch strand on the interaction. The  $^{15}\text{N}$ -AF1 protein should enable the evaluation of the putative cooperativity between Fg1 and NTD binding to AF1.

### 3.4 Molecular biology of N2N3T and N2N3E

All rFnBPA-containing pET-YSBLIC3C vectors were produced by HiTEL (University of York, Technology facility) with the exception of N2N3T and N2N3E, which were designed and generated as described in Section 2.4. Primers used in the PCR to generate correct products are listed in Table 3.2. PCR results were analysed by agarose gel electrophoresis (Figure 3.2B). Subsequent incorporation of the PCR product into the pET-YSBLIC3C vector, using ligation-independent cloning (LIC) (Section 2.4.4) (Bonsor et al., 2006), can only be carried out providing the vector is in linear form. This was achieved by incubation of circular vector with the restriction enzyme BseRI (NEB). Linearized vector travels slower through agarose gel compared with vector in circular form, thus the result of plasmid linearization can be verified using agarose gel electrophoresis (Figure 3.2A). The final step in LIC involves annealing of the insert and linearized vector. The presence of the insert within the plasmid was tested by utilizing the restriction sites flanking the insert region. Incubation of the annealing reaction with restriction enzymes NdeI and NcoI yielded two products, the linearized vector and the insert as demonstrated by agarose gel electrophoresis (Figure 3.2B). The correct sequence of all rFnBPA genes was confirmed by sequencing conducted by members of the Technology Facility at the University of York (Appendix III).

Primer	Sequence (5' - 3')	T <sub>M</sub> (°C)	GC %	bp
N2N3 <sub>(189-505/515)</sub> Fw	CCAGGGACCAGCAATGGC GAAAGTGGAAACGGGTA	85.6	57.1	35
N2N3 <sub>(189-505)</sub> Rev	GAGGAGAAGGCGCGTTACGCTT TATTACTGTATAAAACTAAACC	82.9	40.9	44
N2N3 <sub>(189-515)</sub> Rev	GAGGAGAAGGCGCGTTAAATAA TCGGACCATTTTTCTCATTT	70.4	40.5	42
T7 (HiTel)	TAATACGACTCACTATAGGG	64.2	40.0	20
T7 term (HiTel)	TATGCTAGTTATTGCTCAGCGGT	70.0	43.5	23

**Table 3.2 List of primers corresponding to rFnBPA constructs and primers used for sequencing.** The primer sequence is shown in 5' to 3' direction with the LIC-specific ends highlighted in red and the start codons in blue in the new primers. The table also includes information regarding melting temperature (T<sub>M</sub>), GC content and the number of base pairs.

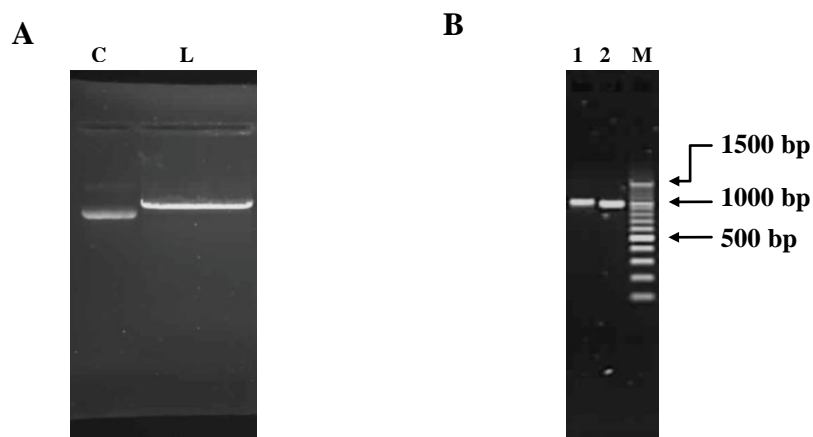


**Figure 3.2** Agarose gel electrophoresis of the PCR products and of the plasmid linearization reaction. **(A)** Results of plasmid linearization show the circular (C) and linearized (L) form of the pET-YSBLIC3C vector following digestion with BseRI. A 0.8% (w/v) agarose gel was used to ensure sufficient resolution. **(B)** The PCRs show two bands corresponding to a larger species N2N3E (lane 1) and a smaller construct N2N3T (lane 2). 1.5 kbp DNA ladder (M) (Fermentas) was also included to enable estimation of the construct sizes.

## 3.5 Expression of recombinant proteins

### 3.5.1 Unlabelled rFnBPA proteins

Plasmid DNA containing the rFnBPA sequence was transformed into an expression strain of *E. coli* (BL21 (DE3) Gold) as described in Section 2.4.5. Baffled flasks, each containing 500 ml of fresh sterilised LB with kanamycin and inoculated with the starter cultures, were used to produce rFnBPA proteins (Section 2.5). Conditions including the temperature, length of expression, volume of LB in each flask, time of induction and final concentration of IPTG were optimized to achieve maximum yields. The final growth curves associated with each recombinant protein are shown in Figure 3.3. The presence of the overexpressed recombinant protein within the cell culture was verified by SDS-PAGE prior to the first purification step. Details of the SDS-PAGE methods are in Section 2.6.3.



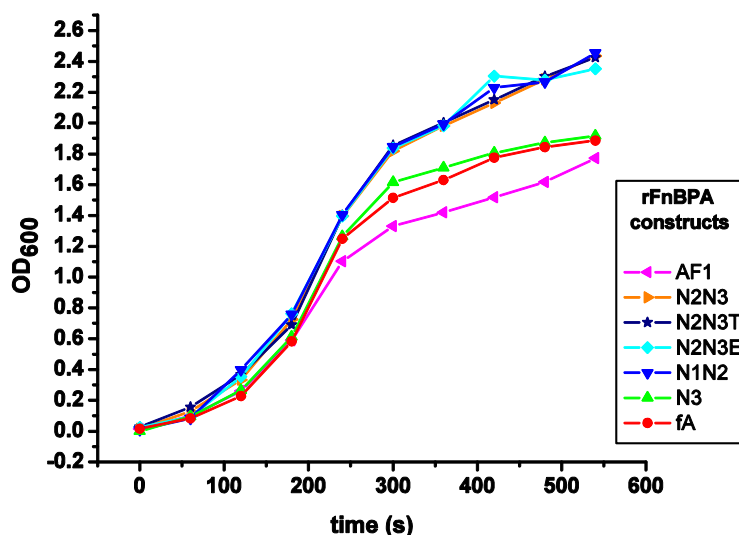


**Figure 3.3** *E. coli* growth curves. Growth of BL21 (DE3) Gold *E. coli* transformed with rFnBPA constructs was monitored by measuring the OD<sub>600</sub> of the culture for ten hours at 60 minute intervals. All LB cultures reached an OD<sub>600</sub> of ~ 0.7 after approximately 180 minutes.

### 3.5.2 <sup>15</sup>N-N2N3, <sup>15</sup>N-N2N3T and <sup>15</sup>N-AF1

Expression protocols for <sup>15</sup>N-N2N3, <sup>15</sup>N-N2N3T and <sup>15</sup>N-AF1 involved incubation at 25°C overnight in M9 minimal media (Appendix I) following induction of expression with IPTG (Section 2.5). To achieve a sufficient level of labelling, all three constructs were expressed in M9 minimal media with <sup>15</sup>N (NH<sub>4</sub>)<sub>2</sub>SO<sub>4</sub> as the sole source of nitrogen. Although cell cultures grew much slower in minimal media, the final protein yields were marginally higher than yields from expressions in LB. The final <sup>15</sup>N content of the purified protein was determined by comparison of the theoretical mass (ProtParam) (Gasteiger et al., 2003) with the molecular mass obtained by MS/ESI (Table 3.3).

## 3.6 Purification of recombinant proteins

Cell extracts from cultures expressing each of the rFnBPA constructs were prepared by sonication and subsequent separation of the clarified supernatant from the cell debris by centrifugation (Section 2.6.1). The first purification step for all rFnBPA proteins was to retrieve the His<sub>6</sub>-tagged protein from the clarified supernatant by nickel-affinity chromatography. The nickel-affinity purification protocol applied to all rFnBPA proteins was designed using N2N3 (Section 3.6.1).

### 3.6.1 Nickel-affinity chromatography of His<sub>6</sub>-N2N3

Initial expression and purification trials revealed problems relating to the stability and solubility of His<sub>6</sub>-N2N3. Nickel-affinity chromatography was carried out first on a system comprising a pre-packed nickel-affinity column connected to an ÄKTA purifier (GE Healthcare) using 50 mM Tris loading buffer, 150 mM NaCl, pH 7.4 and an imidazole concentration gradient for protein elution. After elution the recombinant protein underwent rapid aggregation forming a visible precipitate. Concentration measurements confirmed the precipitate contained the majority of the His<sub>6</sub>-tagged protein. The precipitation of the His<sub>6</sub>-tagged protein was not reversed by subsequent dialysis. Digestion with HRV 3C protease could potentially improve the solubility of the His<sub>6</sub>-tagged protein, however, the high imidazole concentration within the sample interfered with the activity of the protease. Interestingly, a small fraction of the protein was cleaved despite the presence of imidazole, rendering the protein stable in solution over a long period of time. This indicated that the low stability stemmed from the additional His<sub>6</sub>-tag rather than the rFnBPA protein itself.

The first approach to solving the solubility issue associated with the His<sub>6</sub>-tag entailed utilization of bench top gravity flow columns and nickel-coated beads in an attempt to cleave off the His<sub>6</sub>-tag while the protein was bound to the nickel-coated beads. 100 µl of nickel NTA slurry (GE Healthcare) was equilibrated in binding buffer (50 mM Tris buffer, 150 mM NaCl, 10 mM imidazole pH 7.4) then mixed with 300 µl of cell lysate supernatant and an additional 500 µl of the binding buffer. Following a 30 minute incubation at 4°C on a slow speed rotor, the nickel slurry was left to settle and the supernatant collected. Subsequently, 500 µl of binding buffer with 0.5 mg HRV 3C protease was added and the mixture incubated overnight at 4°C with gentle shaking. The nickel slurry was then poured into a gravity flow column. Three wash steps with binding buffer ensured the collection of the cleaved protein. Samples from all steps were analysed by SDS-PAGE (Figure 3.4).

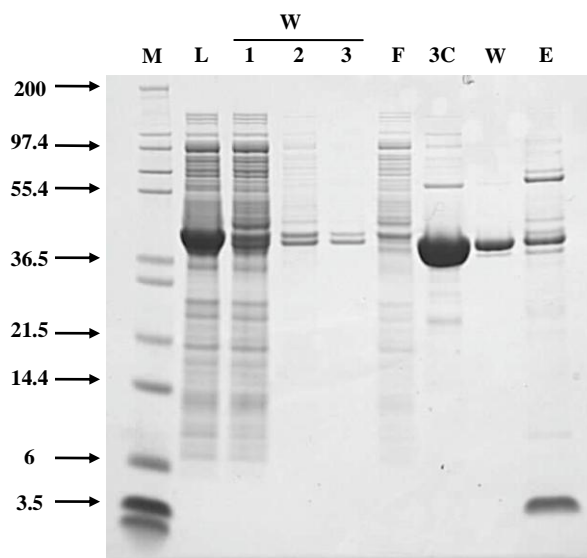


**Figure 3.4 SDS-PAGE analysis of bench-top nickel-affinity chromatography of N2N3.** Samples of both the cell lysate (L) and flow-through (F) were diluted ten-fold prior to loading onto the 4-12% gradient gel. Samples containing the three washes following protein binding (W1-W3), cleaved protein and HRV 3C protease (3C), subsequent wash (W), final imidazole elution (E) and protein marker (M / kDa) were also loaded onto the gel. The major bands located between the protein markers 55.4 and 36.5 kDa correspond to the expected molecular weight of His<sub>6</sub>-N2N3 (38 kDa).

Comparison of the rFnBPA protein content within the cell lysate, flow-through and the three washes clearly demonstrates that the majority of the protein bound the nickel-coated beads. The theoretical mass of His<sub>6</sub>-N2N3 (38.5 kDa - ProtParam) (Gasteiger et al., 2003) was in good agreement with the apparent mass (~ 38kDa). The SDS-PAGE result also verified that the HRV 3C digestion was successful, as most of the recombinant protein was present within the HRV 3C reaction solution. However, it also revealed the presence of numerous low level contaminants of both higher and lower molecular weight. Surprisingly, neither size-exclusion nor anion exchange chromatography achieved complete separation of N2N3 from the contaminants. The concentration of the lower molecular weight contaminant in particular did not seem to decrease with additional purification steps while some of the protein was lost, possibly due to degradation. The molar mass of the contaminant was eventually determined by MS/ESI as 26.6 kDa.

Although the level of contaminant was not overwhelming, it could potentially interfere with the crystallization trials and some of the sensitive biophysical techniques such as SPR or ITC. Moreover, the purification procedure was cumbersome, time-consuming and impractical for larger culture volumes. To

improve the purity of the final protein sample and to increase the efficiency and reproducibility of the protocol, a system comprising a pre-packed NTA column (GE Healthcare) connected to an ÄKTA purifier was again employed. Method parameters are listed in Table 2.4. This time Na/K phosphate buffers were used for loading and elution (Table 2.1) in an attempt to improve the stability of the protein. The imidazole content of the loading buffer was increased to 30 mM resulting in fewer contaminants binding to the column. The imidazole elution gradient was adjusted to 30-230 mM which achieved better resolution between elution species (Figure 3.5). The main elution peak reaches a maximum at an approximate imidazole concentration of 130 mM (taking into account the 30 mM imidazole in the loading buffer).

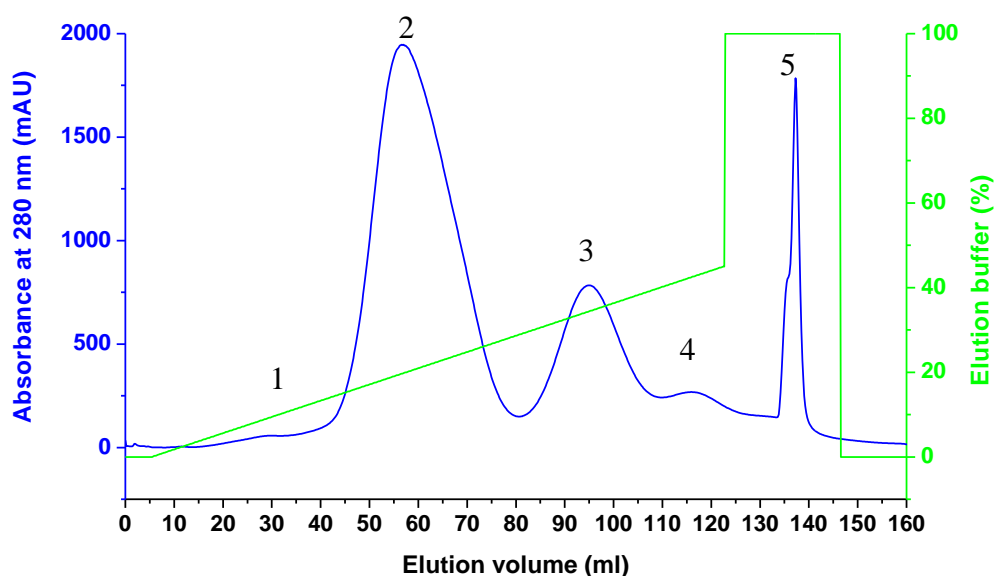


**Figure 3.5 Nickel-affinity chromatography of N2N3.** The chromatogram shows the absorbance at 280 nm (blue) and percentage (v/v) of the elution buffer (green). Five elution peaks of varying size were detected demonstrating the presence of multiple species within the cell lysate supernatant. The numbering of the elution peaks corresponds to the labels in the SDS-PAGE analysis (Figure 3.6).

SDS-PAGE analysis of the nickel-affinity chromatography shows successful expression of His<sub>6</sub>-N2N3 in soluble form and efficient binding to the affinity column, as demonstrated by the analysis of lysate, supernatant and flow-through (Figure 3.6). Examination of the lanes corresponding to the eluted peaks revealed that all contained His<sub>6</sub>-N2N3. The difference in elution times possibly stems from different accessibility of the His<sub>6</sub>-tag caused by ambiguities in protein folding. It is clear from the SDS-PAGE analysis of the major elution peak that most contaminants were removed successfully by nickel-affinity chromatography.

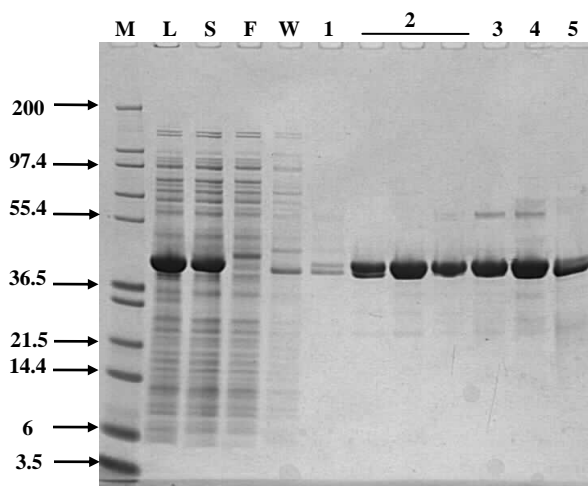


**Figure 3.6 SDS-PAGE analysis of the nickel-affinity chromatography of His<sub>6</sub>-N2N3.** Results of the analysis include protein marker (M / kDa), cell lysate (L), flow-through (F), wash (W) and the five elution peaks (1 to 5). Lanes representing peak 2 correspond to the beginning, maximum, and end of the peak elution (left to right). Samples of the cell lysate and flow-through were diluted ten-fold. The major bands located between the protein markers 55.4 and 36.5 kDa correspond to the expected molecular weight of His<sub>6</sub>-N2N3 (38 kDa).

Crucially, precipitation was avoided by immediate dilution of the pooled fractions to a concentration below 0.5 mg/ml. It was essential that the temperature and composition of the dilution buffer, especially the imidazole content, matched that of the protein solvent otherwise His<sub>6</sub>-N2N3 precipitate appeared. Once sufficiently dilute, the His<sub>6</sub>-N2N3 could be carefully transferred into dialysis tubing and dialysed overnight at 4°C in 5 litres of the same Na/K phosphate buffer but without imidazole. The dialysed protein solution was treated with an appropriate concentration of HRV 3C protease (Section 2.6.5). The His<sub>6</sub>-tag was cleaved off after a 4 h incubation with protease (1:500 enzyme:protein molar ratio) at 4°C. The results of the HRV 3C digestion were analysed by SDS-PAGE (Figure 3.7). It is clear from the SDS-PAGE results that the vast majority of the His<sub>6</sub>-rFnBPA was fully cleaved after 4 hours. A second nickel-affinity purification step separated cleaved N2N3 from remaining His<sub>6</sub>-N2N3, the His<sub>6</sub>-tagged HRV 3C protease, the cleaved His<sub>6</sub>-tag and any other protein fragments or contaminants interacting with the affinity column (Figure 3.8).

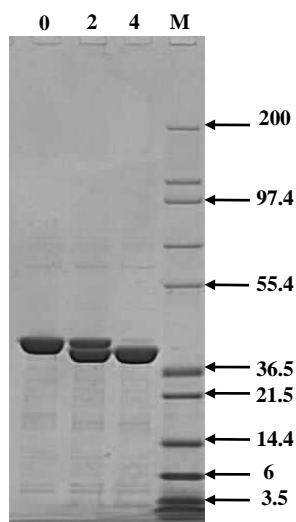


**Figure 3.7 SDS-PAGE of the HRV 3C cleavage of His<sub>6</sub>-N2N3.** Samples of His<sub>6</sub>-N2N3 (lane 0), His<sub>6</sub>-N2N3 after incubation with HRV 3C protease for 2 hours (lane 2) and 4 hours (lane 4) are shown including protein molecular weight markers (M / kDa). The major bands located between the protein markers 55.4 and 36.5 kDa correspond to the expected molecular weight of His<sub>6</sub>-N2N3 (38 kDa) and N2N3 (36 kDa), respectively. MOPS buffer (Table 2.1) was used as a running buffer in order to achieve the higher resolution required for assessing of cleavage of the His<sub>6</sub>-tag.

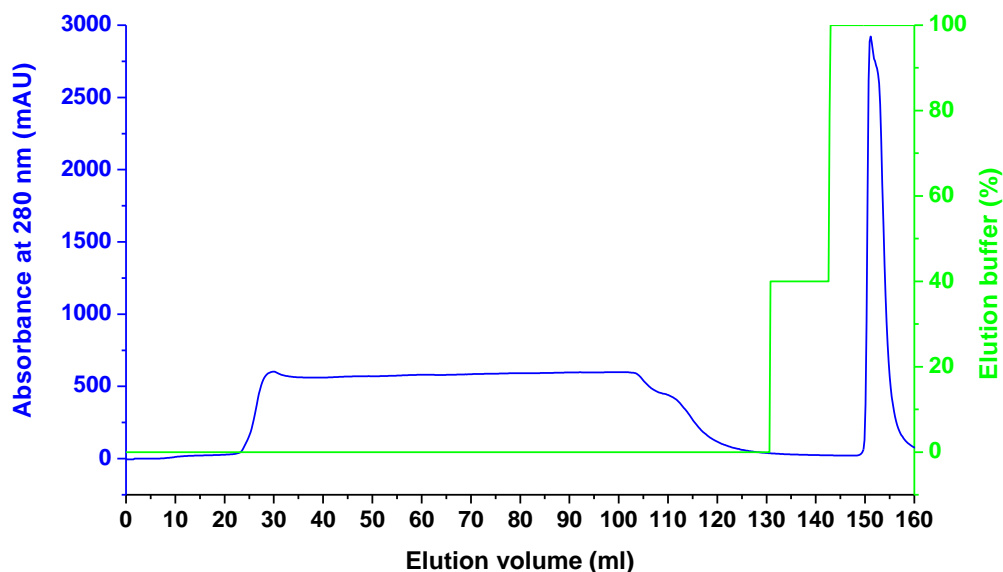


**Figure 3.8 Nickel-affinity chromatography of the cleaved N2N3.** The chromatograph shows the absorbance at 280 nm (blue) and the percentage (v/v) of elution buffer (green). The broad peak corresponded to the flow-through containing cleaved N2N3 (Figure 3.7), while the narrow peak corresponds to the elution of the HRV 3C protease, remaining His<sub>6</sub>-N2N3, His<sub>6</sub>-tag and any other protein fragments or contaminants interacting with the affinity column.

### 3.6.2 Nickel-affinity chromatography of His<sub>6</sub>-tagged N2N3T, N2N3E, N1N2 and fA

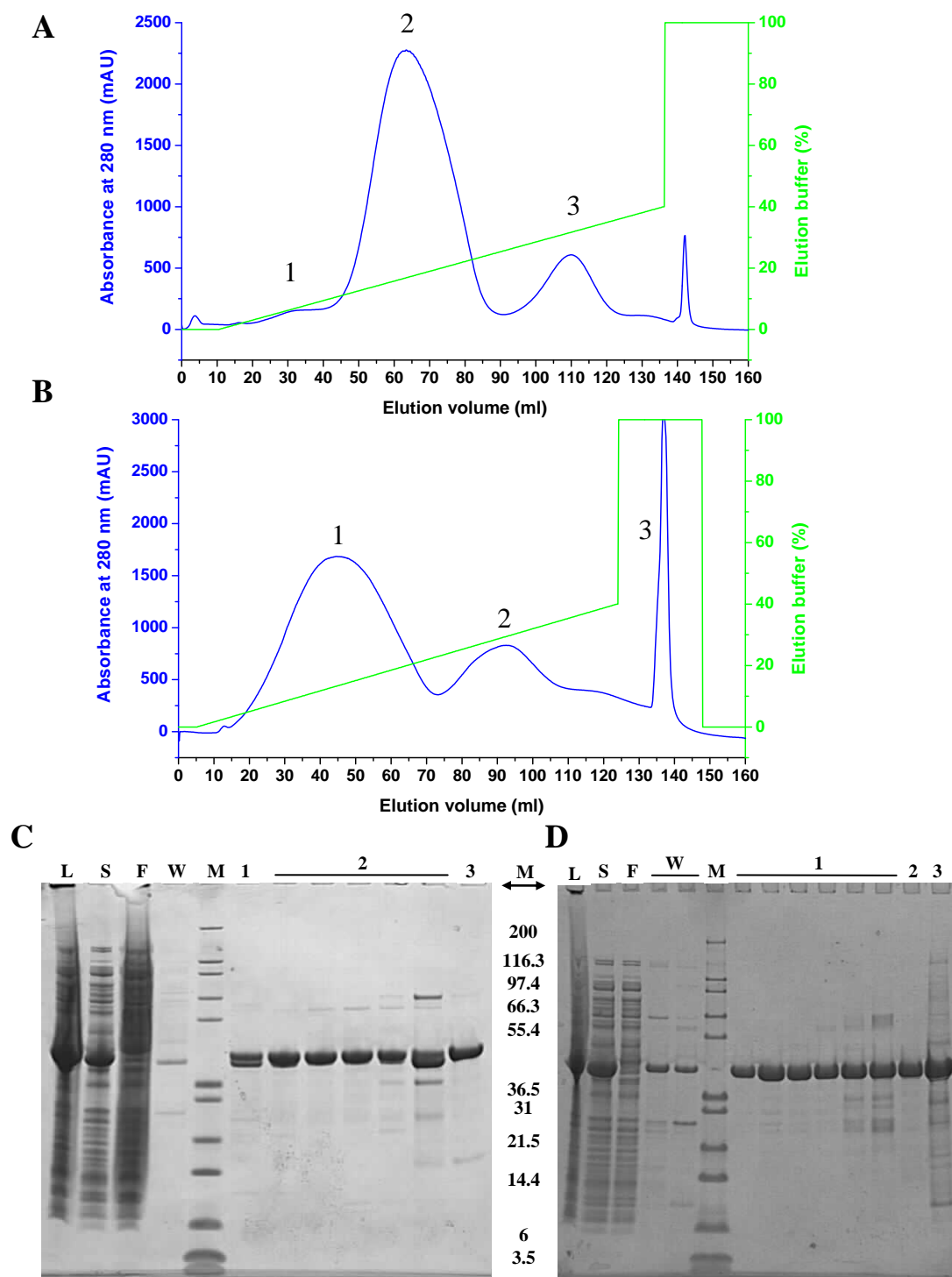


**Figure 3.9** Nickel-affinity chromatography of N2N3T and N2N3E. Chromatograms for (A) N2N3T and (B) N2N3E show the absorbance at 280 nm (blue) and the percentage (v/v) of the elution buffer (green). SDS-PAGE analysis of respective purification steps of (C) N2N3T and (D) N2N3E contains protein marker (M / kDa), cell lysate (L), flow-through (F), clarified supernatant (S), wash (W) and elution peaks (1 to 3). The major bands located between the protein markers 55.4 and 36.5 kDa correspond to the expected molecular weights of His<sub>6</sub>-N2N3T (38 kDa) and His<sub>6</sub>-N2N3E (39 kDa), respectively.

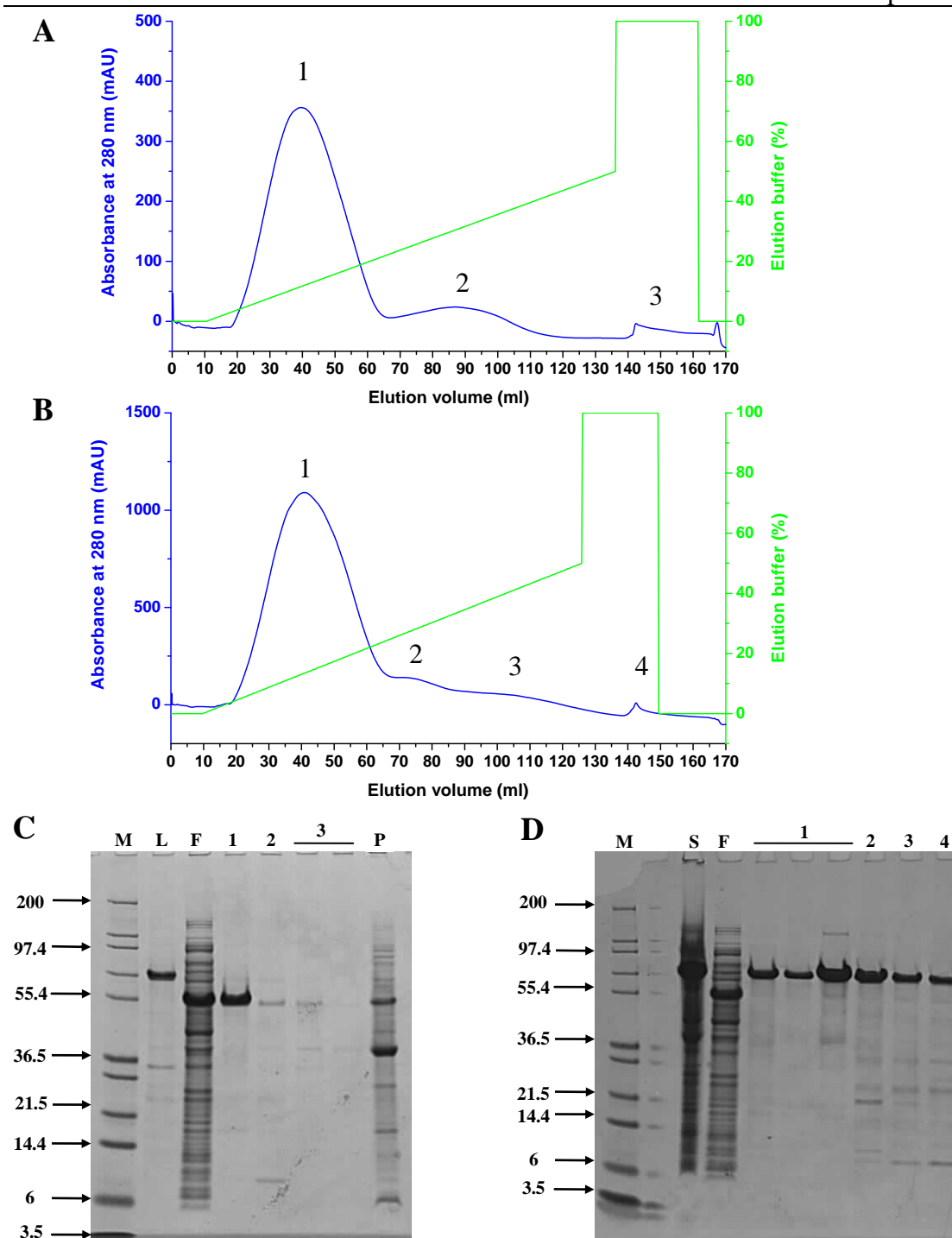


**Figure 3.10 Nickel-affinity chromatography of N1N2 and fA.** Chromatograms for (A) N1N2 and (B) fA show the absorbance at 280 nm (blue) and the percentage (v/v) of the elution buffer (green). SDS-PAGE analysis of respective nickel-affinity chromatography steps of (C) N1N2 and (D) fA contain protein marker (M / kDa), cell lysate (L), cell pellet (P) (resuspended and diluted ten-fold; only in the N1N2 SDS-PAGE), clarified supernatant (S) (in the fA SDS-PAGE only), flow-through (F), wash (W) and elution peaks (1 to 3). The major bands located at the protein markers 55.4 (N1N2) and 66.3 kDa correspond to the expected molecular weight of His<sub>6</sub>-N1N2 (35 kDa) and His<sub>6</sub>-fA (55 kDa), respectively. Molecular mass of both recombinant proteins appear higher on the gradient gel, most likely due to the high content of negatively charged amino acids within the disordered N1 domain.



The same procedure for nickel-affinity purification and His<sub>6</sub>-tag removal was utilized for the recombinant proteins N2N3T, N2N3E, N1N2 and fA (Figure 3.9 and Figure 3.10). The different rFnBPA proteins exhibited only small variations in elution volumes and in some cases, required alteration of the duration of the HRV 3C protease digestion. Any potential complications associated with the solubility of the four His<sub>6</sub>-tagged rFnBPA proteins were also solved by the same approach as that used for N2N3.

### 3.6.3 Nickel-affinity chromatography of His<sub>6</sub>-N3

The method used for the purification of N2N3 did not result in sufficient resolution of the His<sub>6</sub>-N3 elution peaks (Figure 3.11). Figure 3.12 shows that all peaks in the chromatogram correspond to His<sub>6</sub>-N3. It is possible that the different elution times arise from His<sub>6</sub>-N3 species with different fold, thus different accessibility of the His<sub>6</sub>-tag. It is important to obtain a single species, hence the protocol was optimized further.

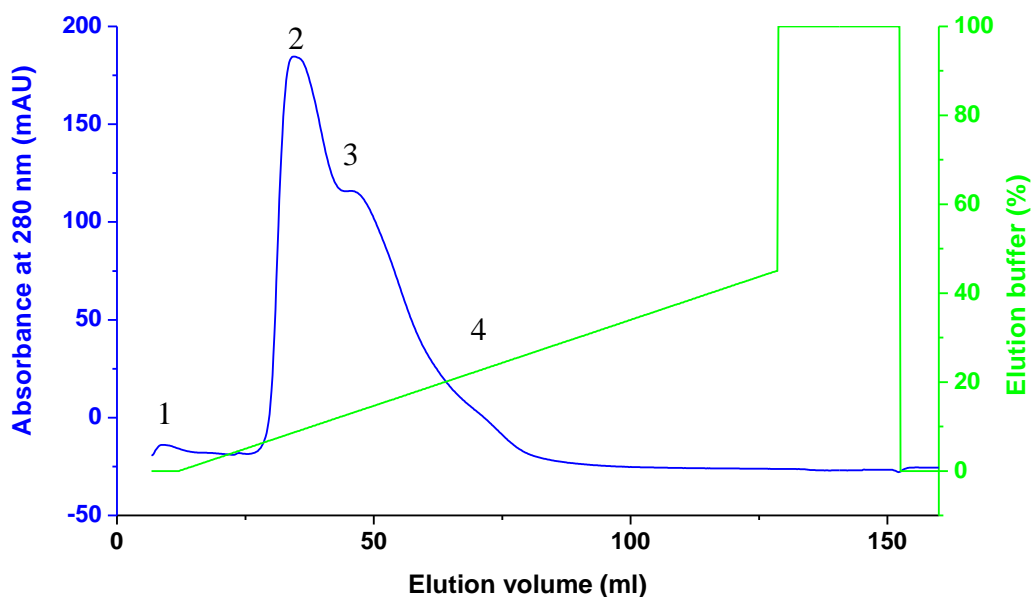


**Figure 3.11** A trial nickel-affinity chromatography of His<sub>6</sub>-N3. The chromatogram shows the absorbance at 280 nm (blue) and the gradient increase in the percentage (v/v) of the elution buffer (green). Four elution peaks were detected demonstrating the presence of multiple species within the cell lysate supernatant. Numbering of the elution peaks corresponds to the labels in the SDS-PAGE analysis (Figure 3.12).

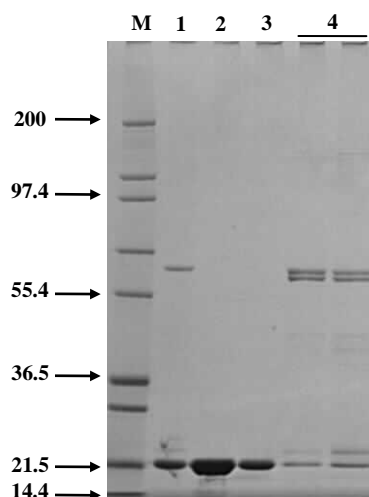


**Figure 3.12 SDS-PAGE analysis of the trial nickel-affinity chromatography of His<sub>6</sub>-N3.** Results of the analysis include protein marker (M / kDa) and the four elution peaks (1 to 4). The major band located between protein markers 36.5 and 21.5 kDa corresponds to the expected molecular weight of His<sub>6</sub>-N3 (23 kDa).

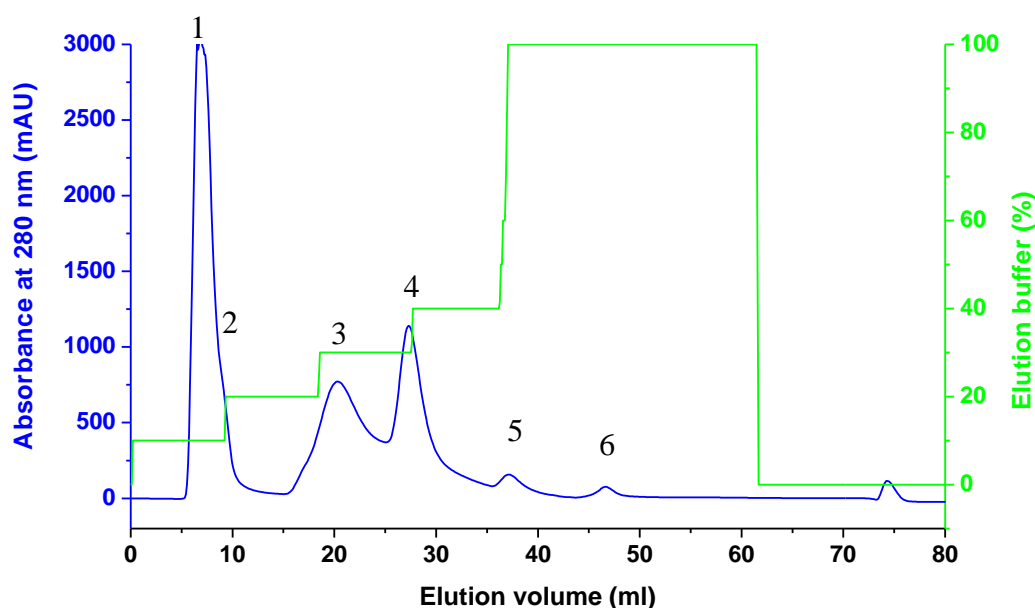


**Figure 3.13 Nickel-affinity chromatography of His<sub>6</sub>-N3.** The chromatogram shows the absorbance at 280 nm (blue) and step-wise increases (10%) in the percentage (v/v) of the elution buffer (green). Six separate elution peaks were detected demonstrating the presence of multiple species within the cell lysate supernatant. Numbering of the elution peaks corresponds to the labels in the SDS-PAGE analysis (Figure 3.14).

Figure 3.13 shows that significant improvement in the resolution was achieved using step-wise elution (Section 2.6.2). Figure 3.14 shows that His<sub>6</sub>-N3 was expressed, is soluble and binds to the nickel-affinity column. Elution peaks 1, 2, 3 and 4 correspond to sufficiently pure His<sub>6</sub>-N3 (>95%). The main peak elutes early, at an

imidazole concentration of  $\sim 80$  mM and contains peaks 1 and 2. However, the early elution suggests the His<sub>6</sub>-tag of the corresponding N3 is the least accessible. Subsequently, His<sub>6</sub>-N3-containing fractions corresponding to peak 4 (which binds to the column more tightly) were pooled, diluted, dialysed and treated with HRV 3C protease as described previously (Section 3.6.1).

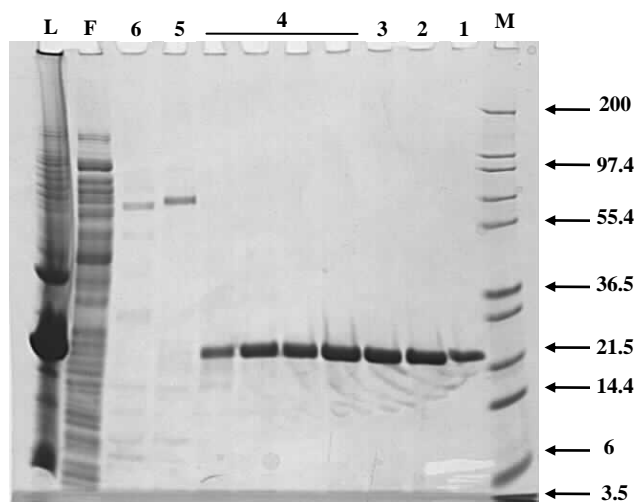
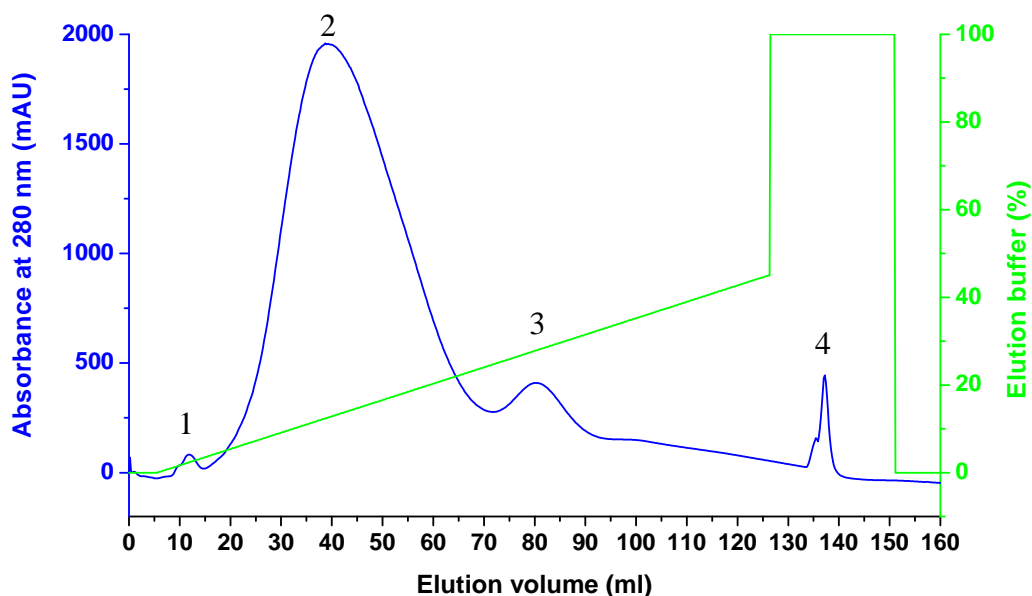


**Figure 3.14 SDS-PAGE analysis of nickel-affinity chromatography of His<sub>6</sub>-N3.** Results of the analysis include protein marker (M / kDa), cell lysate (L), flow-through (F) and the six elution peaks (1 to 6). The major band located between protein markers 36.5 and 21.5 kDa corresponds to the expected molecular weight of His<sub>6</sub>-N3 (23 kDa).

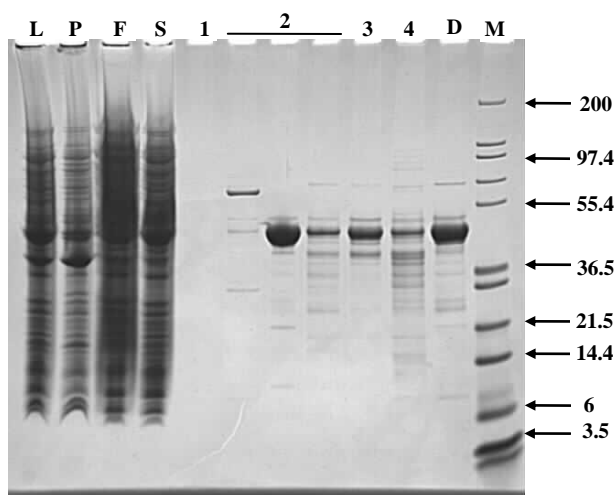
### 3.6.4 Nickel-affinity chromatography of His<sub>6</sub>-AF1

Figure 3.15 demonstrates the successful expression of the His<sub>6</sub>-AF1 construct in soluble form and efficient binding to the affinity column, under conditions similar to those used for N2N3. One major and three minor elution peaks were detected. The main elution peak reaches a maximum at an imidazole concentration of  $\sim 130$  mM (taking into account the 30 mM imidazole in the loading buffer). Eluted peaks 2, 3 and 4 all appear to contain AF1, albeit with relatively high level of contaminants (Figure 3.16). Considering the lower molecular weight and ladder-like character of the additional bands on the gradient gel, it is likely that the majority of these are a product of partial degradation of His<sub>6</sub>-AF1 at the C-terminus. FnBPA1 might be susceptible to degradation, due to its intrinsically unstructured character (Schwarz-Linek et al., 2003), but has been expressed previously (Meenan et al., 2007). As the His<sub>6</sub>-tag is located on the N-terminus of AF1, the truncated His<sub>6</sub>-AF1 species retain their ability to bind to the nickel-affinity column, thus cannot be separated from full

length His<sub>6</sub>-AF1 by nickel-affinity chromatography. Consequently, an anion exchange chromatography (IEX) step was added to the protocol (Sections 2.6.6 and 3.6.5). Prior to IEX, His<sub>6</sub>-AF1 was dialysed and subjected to HRV 3C protease digest in order to remove the His<sub>6</sub>-tag, using a similar protocol to that for N2N3 (Section 2.6.5). The His<sub>6</sub>-tagged HRV 3C protease, remaining His<sub>6</sub>-AF1 and its fragments were removed by the same second nickel-affinity purification step as used for N2N3 (Section 3.6.1).



**Figure 3.15 Nickel-affinity chromatography of His<sub>6</sub>-AF1.** The chromatogram shows the absorbance at 280 nm (blue) and the percentage (v/v) of the elution buffer (green). The numbering of the elution peaks corresponds to the labels in the SDS-PAGE analysis (Figure 3.16).



**Figure 3.16 SDS-PAGE analysis of nickel-affinity chromatography of His<sub>6</sub>-AF1.** The SDS-PAGE shows protein marker (M / kDa), cell lysate (L), cell pellet (P), flow-through (F), clarified supernatant (S), the four elution peaks (1 to 4) and the pooled fractions of peak 2 (D). The major band located between protein markers 55.4 and 36.5 kDa corresponds to the expected molecular weight of His<sub>6</sub>-AF1 (43 kDa).

### 3.6.5 Anion exchange chromatography of AF1

A solution containing cleaved AF1 was first dialysed into IEX loading buffer (Table 2.1) to lower the concentration of NaCl prior to loading onto the HiTrap Q FF Sepharose (GE Healthcare) IEX column. Elution was achieved with an increasing concentration gradient of NaCl. The theoretical pI of AF1 is 5.16, thus Bis-Tris buffer at pH 6.0 was used to ensure minimum amount of contaminants interacts with the column. Following initial rounds of IEX purifications, it became clear that AF1 eluted at approximately 180 mM NaCl. The gradient used in subsequent IEX was therefore 0 to 350 mM NaCl over 30 CV (150 ml). The main elution peak was clearly asymmetrical indicating presence of multiple species (data not shown). As a final optimization step, the flow rate was gradually lowered from 5 to 0.7 ml/min in order to resolve the multiple peaks. This approach to optimization of IEX parameters produced a method able to remove the majority of the contaminants from AF1 resulting in a protein of sufficient purity (>95%), as established by SDS-PAGE analysis (Figure 3.17 and Figure 3.18). The main peak eluted at a NaCl concentration of approximately 180 mM.

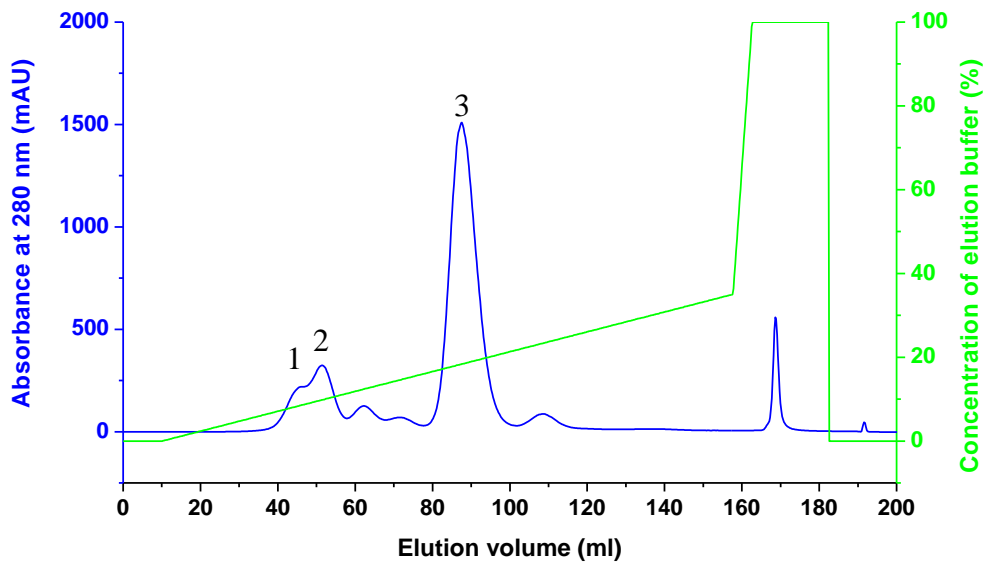


**Figure 3.17 Anion exchange chromatography of AF1.** The chromatogram shows absorbance at 280 nm (blue) and the percentage (v/v) of the elution buffer (green) over 30 CV. The numbering of the elution peaks corresponds to the SDS-PAGE analysis (Figure 3.18).

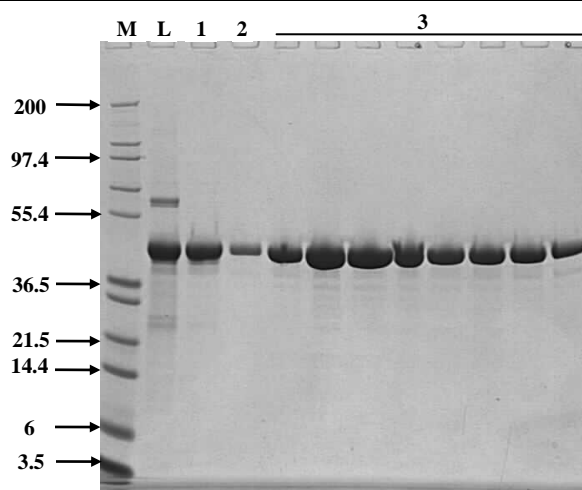


**Figure 3.18 SDS-PAGE analysis of AF1 IEX.** The SDS-PAGE contains protein marker (M / kDa), cell lysate (L), samples of elution peaks 1 and 2 and samples from 8 fractions corresponding to the third (and main) elution peak. The major band located between protein markers 55.4 and 36.5 kDa corresponds to the expected molecular weight of AF1 (41 kDa).

### 3.6.6 Size-exclusion chromatography of N2N3

The final purification step applied to N2N3 and all other rFnBPA proteins was size-exclusion chromatography (Section 2.6.7). The purpose of this final round of purification was to remove the last traces of contaminants and to separate oligomeric and monomeric species of rFnBPA proteins. Following nickel-affinity chromatography, a sample containing N2N3 in Na/K phosphate buffer (Table 2.1) was concentrated to a final volume of 1 ml (approximately 0.5 mM), which could be easily loaded onto the size-exclusion column via a 2 ml loading loop. The main species elutes between 65 and 75 ml while the other species exhibit shorter elution times. Multiple peaks clearly demonstrate the presence of multiple species of different mass (and/or conformation) in the protein sample following the nickel-affinity purification step (Figure 3.19). The only species present within the elution fractions had a mass consistent with N2N3 (Figure 3.20), suggesting the different elution times stem from different oligomerization states of N2N3. The purity of the final N2N3 sample was >95%, as determined by the SDS-PAGE analysis. The sample of N2N3 was stored at -20°C for four days prior to the another size-exclusion chromatography step where all of N2N3 eluted simultaneously between 65 and 75 ml of elution volume (Figure 3.21), indicating the equilibrium between the different forms of N2N3 is not dynamic. The major N2N3 species was later confirmed as a monomer by analytical ultracentrifugation (Section 3.7)

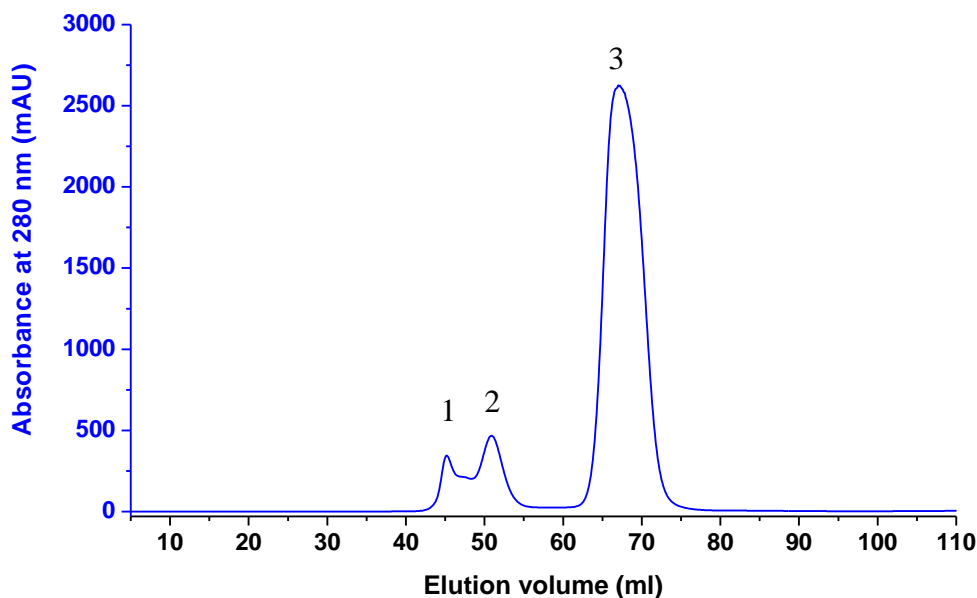


**Figure 3.19 Size-exclusion chromatography of N2N3.** The chromatogram shows the absorbance at 280 nm (blue) over 1 CV (approximately 120 ml). Numbering of the elution peaks corresponds to the labels in the SDS-PAGE analysis (Figure 3.20).

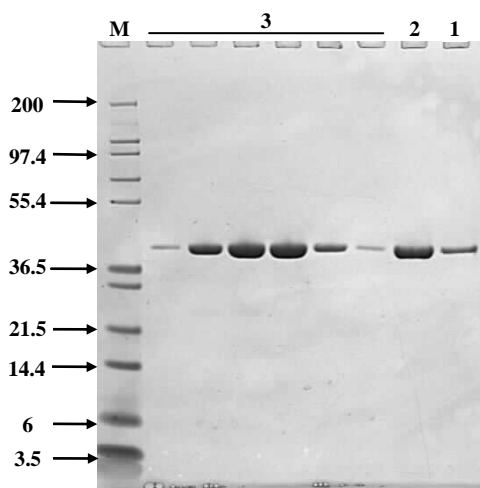


**Figure 3.20 SDS-PAGE of the size-exclusion chromatography of N2N3.** The SDS-PAGE shows protein marker (M / kDa) and fractions corresponding to the three elution peaks. The single band located between protein markers 36.5 and 55.4 kDa corresponds to the expected molecular weight of N2N3 (36 kDa). The molecular mass of N2N3 appears higher on the gel, possibly due to a higher content of negatively charged amino acids. The correct mass was confirmed by MS/ESI (Table 3.3).

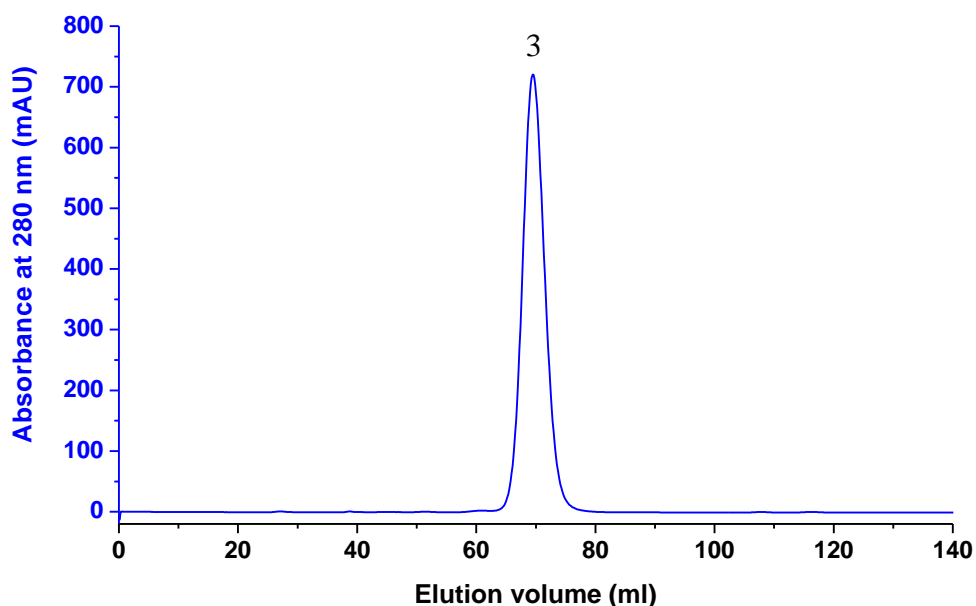


**Figure 3.21** Repeated size-exclusion chromatography of the N2N3 main species. The chromatogram depicts the absorbance at 280 nm (blue) over 1 CV (approximately 120 ml). The number of the elution peak corresponds to that in the first size-exclusion chromatography step (Figure 3.19).

### 3.6.7 Size-exclusion chromatography of N2N3T, N2N3E, N1N2, fA, N3 and AF1

Identical size-exclusion chromatography procedures to that for N2N3 (Section 3.6.6) and subsequent SDS-PAGE analyses were utilized when purifying other rFnBPA proteins, with a similar outcome. No visible contaminant could be detected by SDS-PAGE indicating that the minor eluted species arise from oligomerizing rFnBPA proteins. Elution chromatograms for N2N3T and N2N3E (Figure 3.22) were comparable with that of N2N3, while subtle differences could be observed in elution of fA, N1N2, N3 and AF1 (Figure 3.23 and Figure 3.24). The final rFnBPA protein samples were analysed by SDS-PAGE, which revealed a purity of >95% (Figure 3.22 and Figure 3.23 and Figure 3.24). N1N2, unlike the rest of rFnBPAs, was purified using a smaller Superdex 75 10/300GL size-exclusion column (CV = 20 ml) (GE Healthcare). The chromatogram indicates the presence of multiple minor forms of N1N2 with elution times both longer and shorter than that of the major species.



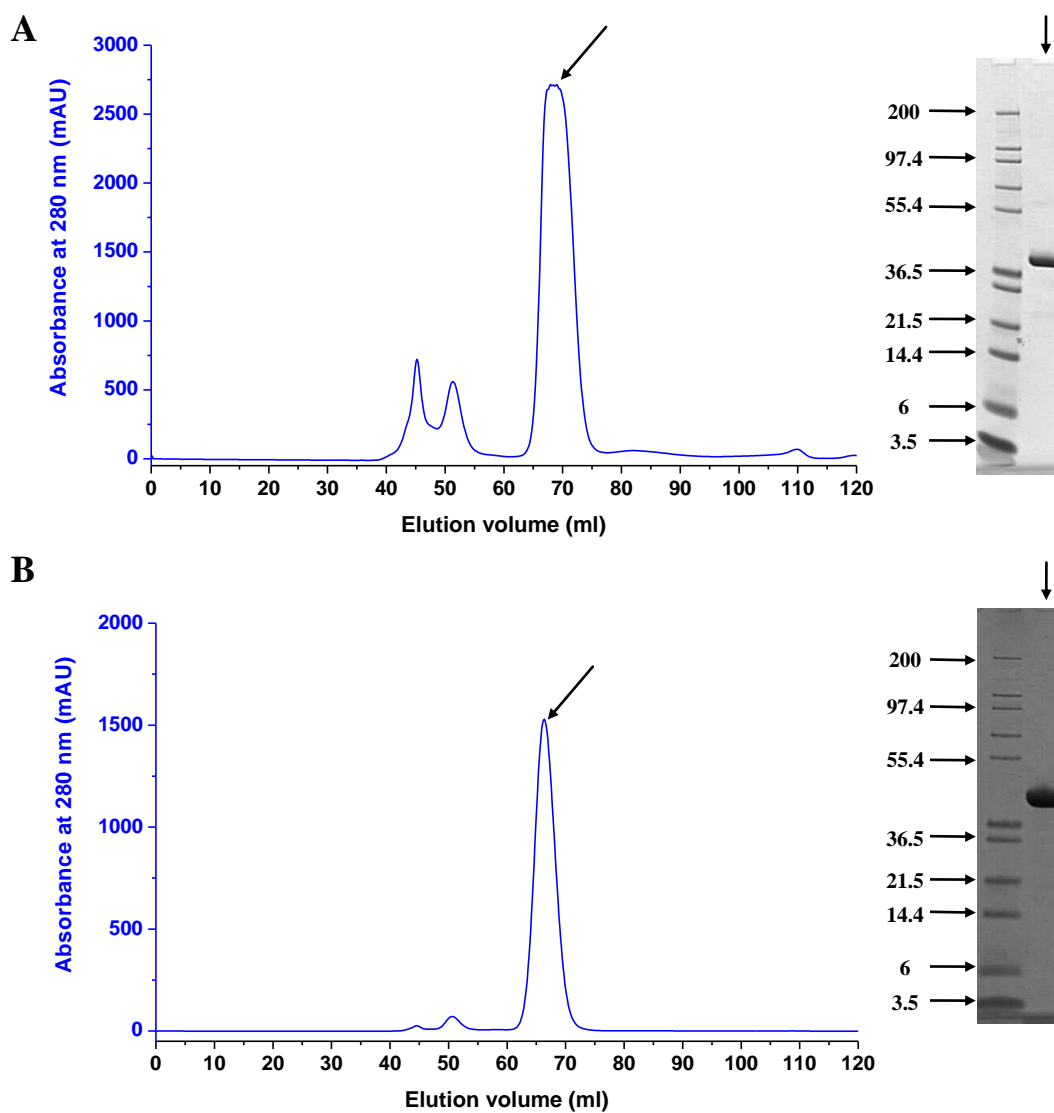


**Figure 3.22** Size-exclusion chromatography of N2N3T and N2N3E. The chromatograms for the elution of (A) N2N3T and (B) N2N3E show the absorbance at 280 nm (blue) over 1 CV (approximately 120 ml). (RIGHT) SDS-PAGE analyses of the final samples (arrows) of N2N3T and N2N3E are also shown.

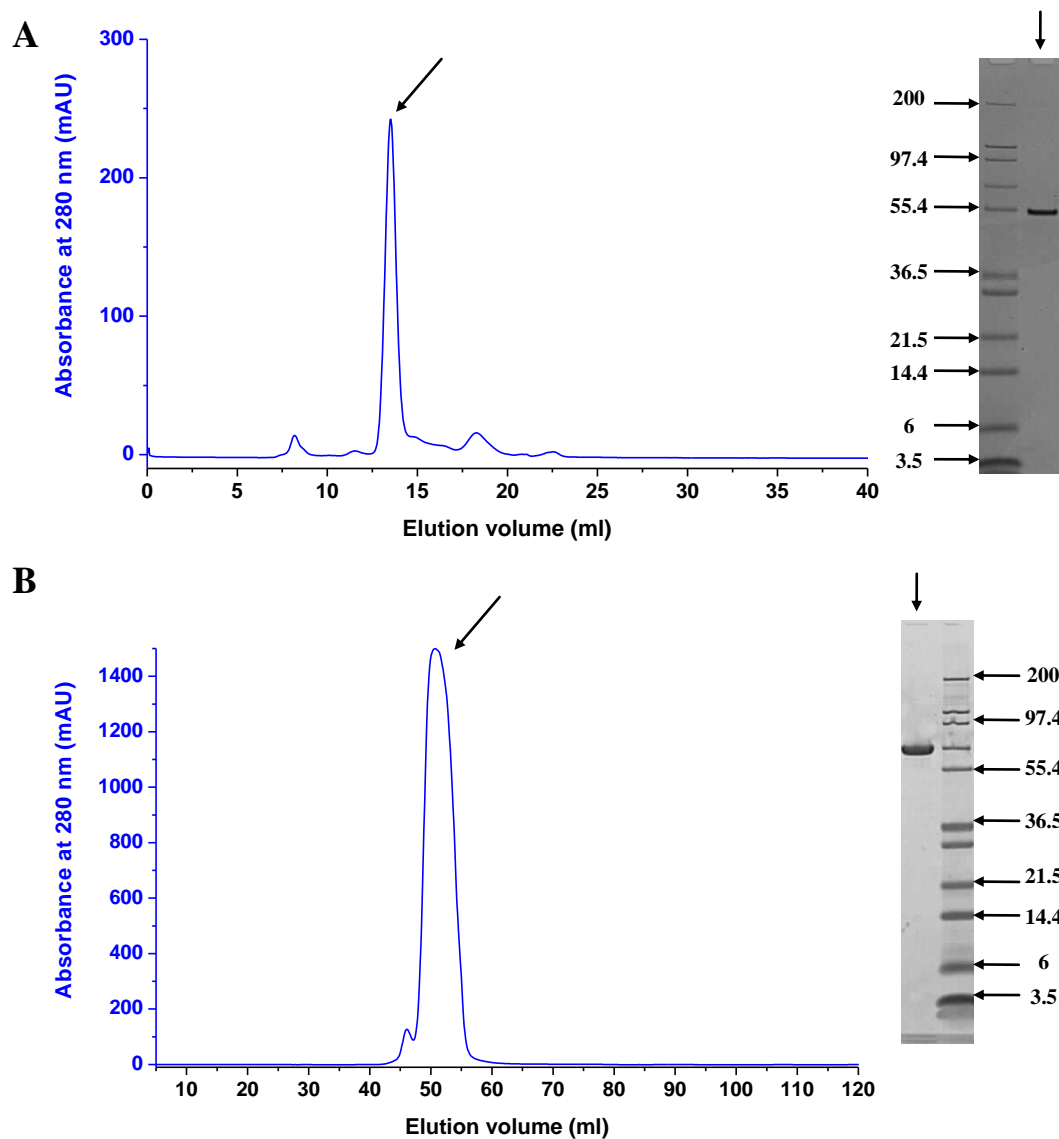


**Figure 3.23 Size-exclusion chromatography of N1N2 and fA.** The chromatograms for the elution of (A) N1N2 and (B) fA show the absorbance at 280 nm (blue). Size-exclusion chromatography of N1N2 was carried out on a Superdex 75 10/300GL (CV = 20 ml) column (GE Healthcare). The relatively low absorbance maximum results from the low extinction coefficient of N1N2 ( $\epsilon = 7450$ ). (RIGHT) SDS-PAGE analyses of the final samples (arrows) of N1N2 and fA are also shown. The molecular masses of both recombinant proteins appear higher on the gradient gel, most likely due to the high content of negatively charged amino acids within the disordered N1 domain.

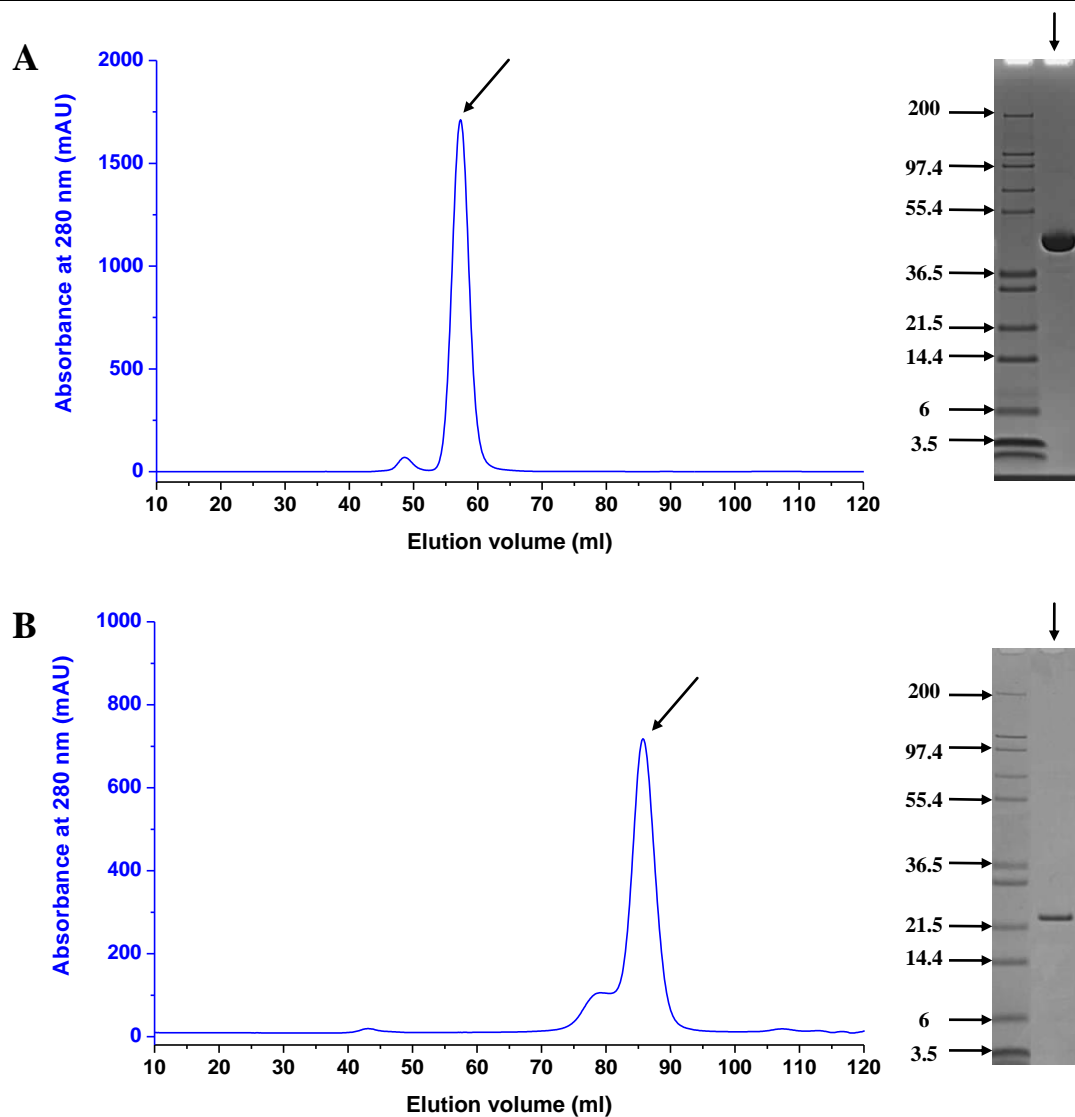


**Figure 3.24 Size-exclusion chromatography of AF1 and N3.** The chromatograms for the elution of (A) AF1 and (B) N3 show the absorbance at 280 nm (blue) over 1 CV (approximately 120 ml). (RIGHT) SDS-PAGE analyse of the final samples (arrows) of AF1 and N3 are also shown.

The purity of eluted recombinant proteins was in each case established as >95% by SDS-PAGE analysis and the correct mass confirmed by MS/ESI (Section 2.8.6). Final yields of all rFnBPA proteins were calculated based on the protein concentration estimated using the absorbance at 280 nm (Section 2.6.8). The final yields and basic properties of all purified rFnBPA proteins are listed in Table 3.3.

rFnBPA	tM <sub>w</sub> (Da)	M <sub>w</sub> (Da)	Yield (mg/l)	ε	pI
N3	20366	20368	11	27850	7.03
N1N2	32759	32763	28	7450	4.81
N2N3T	35716	35711	21	32320	5.58
N2N3	36373	36373	25	32320	5.59
N2N3E	36753	36755	27	32320	5.59
fA	52751	52749	14	33810	5.09
AF1	40896	40903	6	36790	5.18
<sup>15</sup> N-N2N3T	36145	36130 (97%)	24	32320	5.58
<sup>15</sup> N-N2N3	36812	36807 (99%)	25	32320	5.59
<sup>15</sup> N-AF1	41383	41381 (99%)	8	36790	5.18

**Table 3.3 Summary of rFnBPAs properties and expression yields.** The table includes domain composition and shows the estimated molecular mass (tM<sub>w</sub>) (ProtParam) (Gasteiger et al., 2003), as well as the molecular mass determined by MS/ESI (M<sub>w</sub>) (including the level of isotope labelling for <sup>15</sup>N-N2N3, N2N3T and AF1). Estimated values for the extinction coefficient (ε) and the theoretical pI (ProtParam) of individual proteins are also included.

### 3.7 Oligomerization state of N2N3 and AF1

Oligomerization states of the final N2N3 and AF1 samples were determined by AUC (Section 2.8.4). Sedimentation velocity experiments and the subsequent data analysis were conducted by Dr Andrew Leech (Technology Facility, University of York). Overlaid plots of N2N3 and AF1 scans taken at regular intervals are shown in Figure 3.25A and Figure 3.26A. Data were analysed using the SEDFIT software package (Schuck, 2000), with the partial specific volumes, buffer densities and viscosities estimated using the program SEDNETRP (Laue et al., 1992). A single symmetrical peak centred on the sedimentation coefficient values of 2.82S and 2.86S for N2N3 and AF1, respectively, points to the presence of single protein forms. The main peaks account for approximately 91% (N2N3) and 99% (AF1) of the detected signal with the rest relating to a peak at the upper limit of sedimentation coefficient detection, which probably corresponds to a small amount of aggregate in the samples (Figure 3.25 and Figure 3.26B). The molecular mass estimated based on the sedimentation coefficients were 36 kDa for N2N3 and 39 kDa for AF1 (Figure 3.25C and Figure 3.26C). The result confirmed the monomeric character of the N2N3 and AF1 size-exclusion chromatography samples (Figure 3.19 and Figure 3.24A).

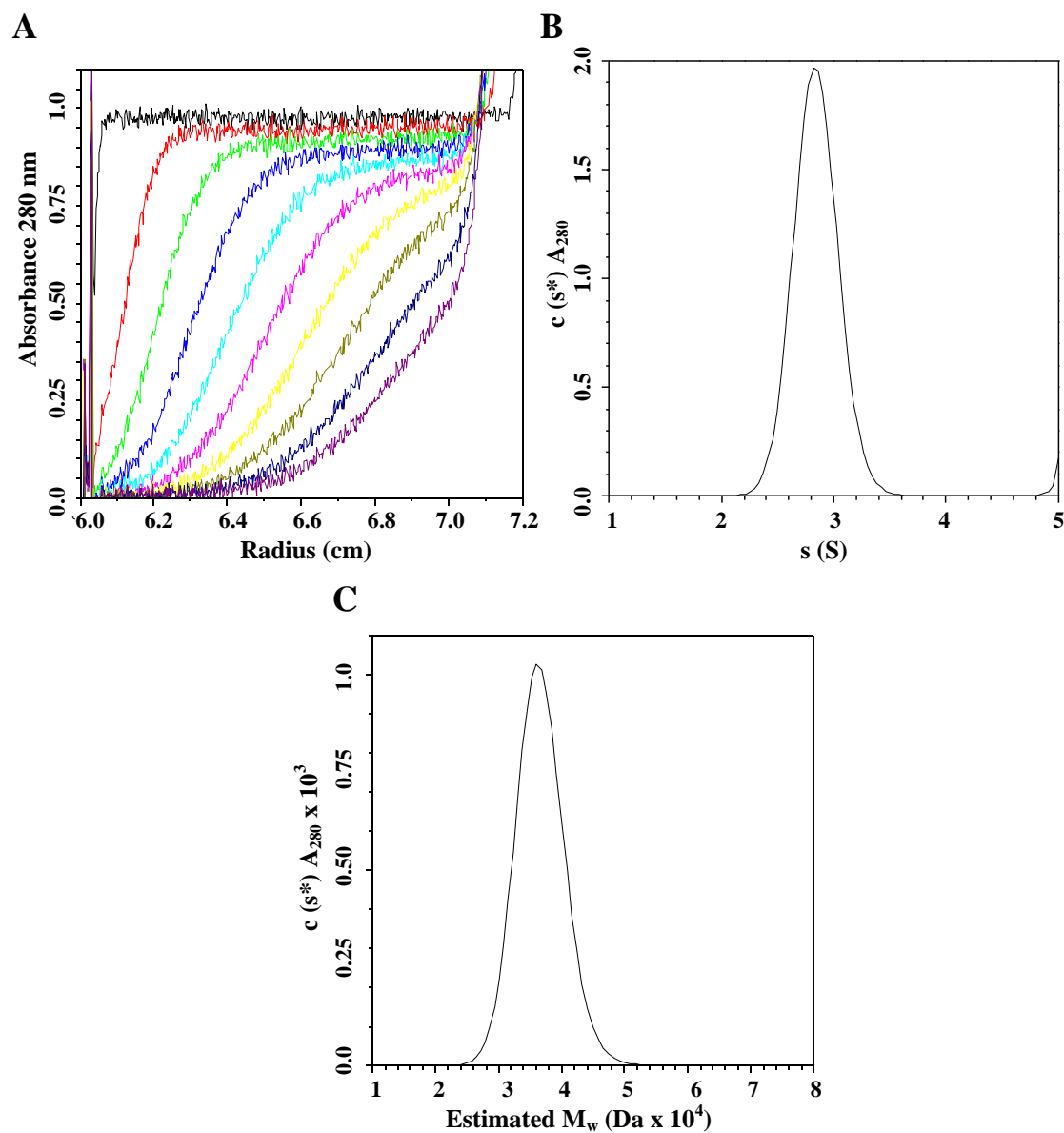


**Figure 3.25 Determination of the oligomerization state of N2N3 using sedimentation velocity experiment.** (A) The raw data comprise overlaid plots of individual scans showing the absorbance at 280 nm throughout the radius of the sample cell (boundaries). (B) The apparent differential sedimentation coefficient  $s$  distribution ( $c (s)$ ). (C) The molar mass distribution. The data analysis was performed by Andrew Leech (Technology Facility, University of York).

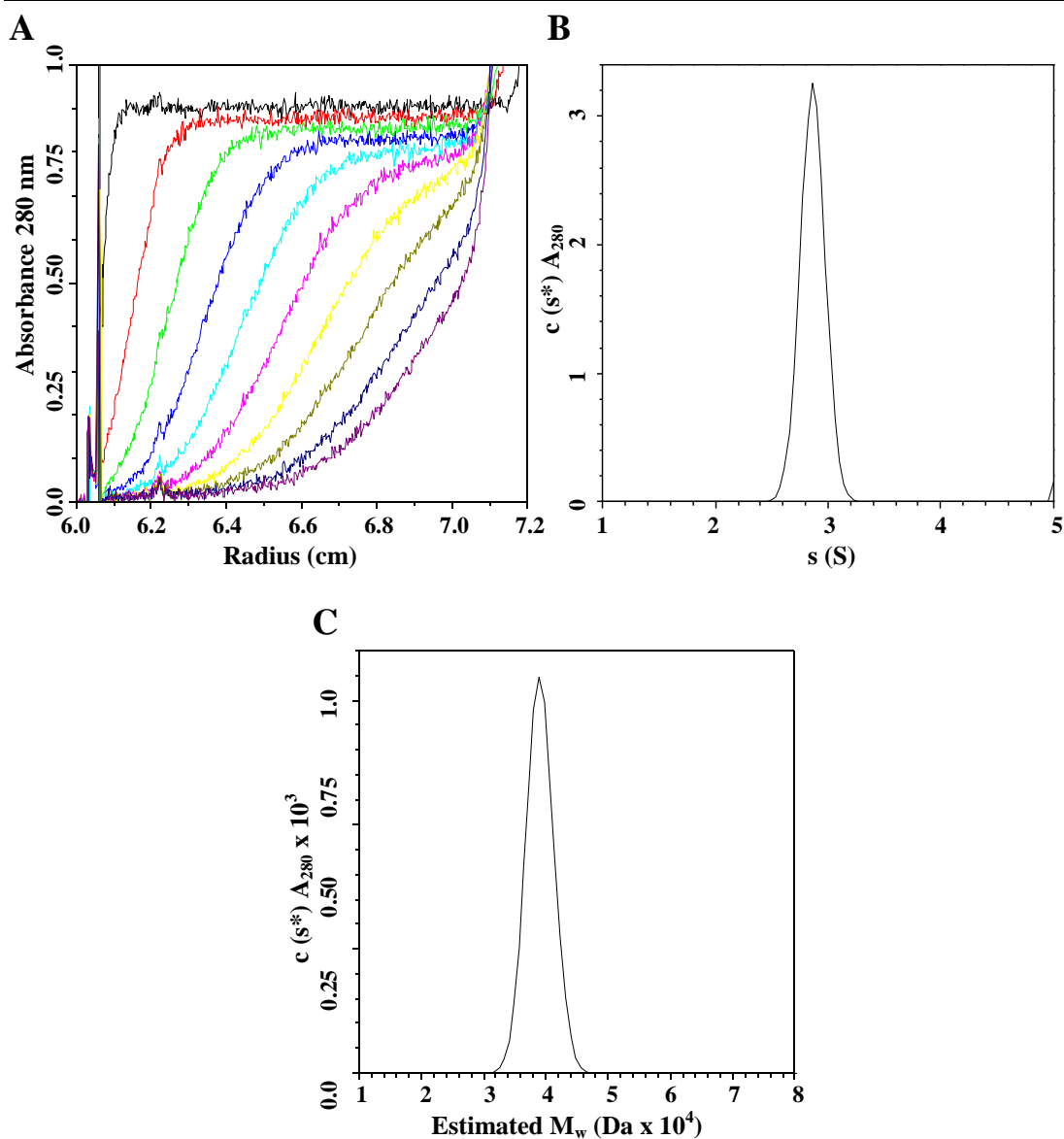


**Figure 3.26 Determination of the oligomerization state of AF1 using sedimentation velocity experiment.** (A) The raw data comprise overlaid plots of individual scans showing the absorbance at 280 nm throughout the radius of the sample cell (boundaries). (B) The apparent differential sedimentation coefficient distribution ( $c (s)$ ). (C) The molar mass distribution are also shown. The data analysis was performed by Andrew Leech (Technology Facility, University of York).

### 3.8 Initial structural characterization of the rFnBPA proteins by 1D $^1\text{H}$ NMR spectroscopy

The 1D  $^1\text{H}$  NMR spectrum can provide information regarding the folded state of a protein (Wishart et al., 1991). The spectrum of an unfolded protein is basically the sum of the random coil chemical shifts of the amino acids within the protein (Bundi and Wuthrich, 1979a; Schwarzingger et al., 2000). On the other hand, the signals in a folded protein are often shifted away from the random coil value as a result of the different chemical microenvironments associated with the protein structure (Bundi and Wuthrich, 1977; Wuthrich, 1986; Bundi and Wuthrich, 1979b). Consequently, the dispersion of signals in the spectrum of an unfolded protein is much narrower in comparison with spectrum of a folded protein (Schwarzingger et al., 2000).

Samples of N1N2, N2N3 and AF1 were prepared as described in Section 2.8.1 and the 1D  $^1\text{H}$  NMR spectra acquired with identical acquisition parameters for all three samples (Section 2.8.1). A comparison of the three spectra revealed differences, most likely arising from the different levels of folding present in each protein (Figure 3.27). The presence of strong peaks with relatively low dispersion across the spectrum of N1N2 suggests a significant portion of N1N2 is unstructured. Further NMR studies revealed the entire N1 domain is unstructured (unpublished results). On the other hand, the spectra of N2N3 and AF1 reveal much wider signal dispersion, which is particularly apparent in the amide (10 - 6 ppm) and aliphatic (4 - 0 ppm) regions. Visible single methyl resonances at low ppm values (-0.5) is a further confirmation that a well defined fold is present within both N2N3 and AF1. Nevertheless, a subtle difference can be observed between the spectra of N2N3 and AF1. It is predominantly in the region corresponding to the signals from the amide nuclei and those within aromatic side chains, where the spectrum of AF1 shows some characteristics of disordered protein. This suggests that FnBPA1 remains unstructured in the AF1 context.

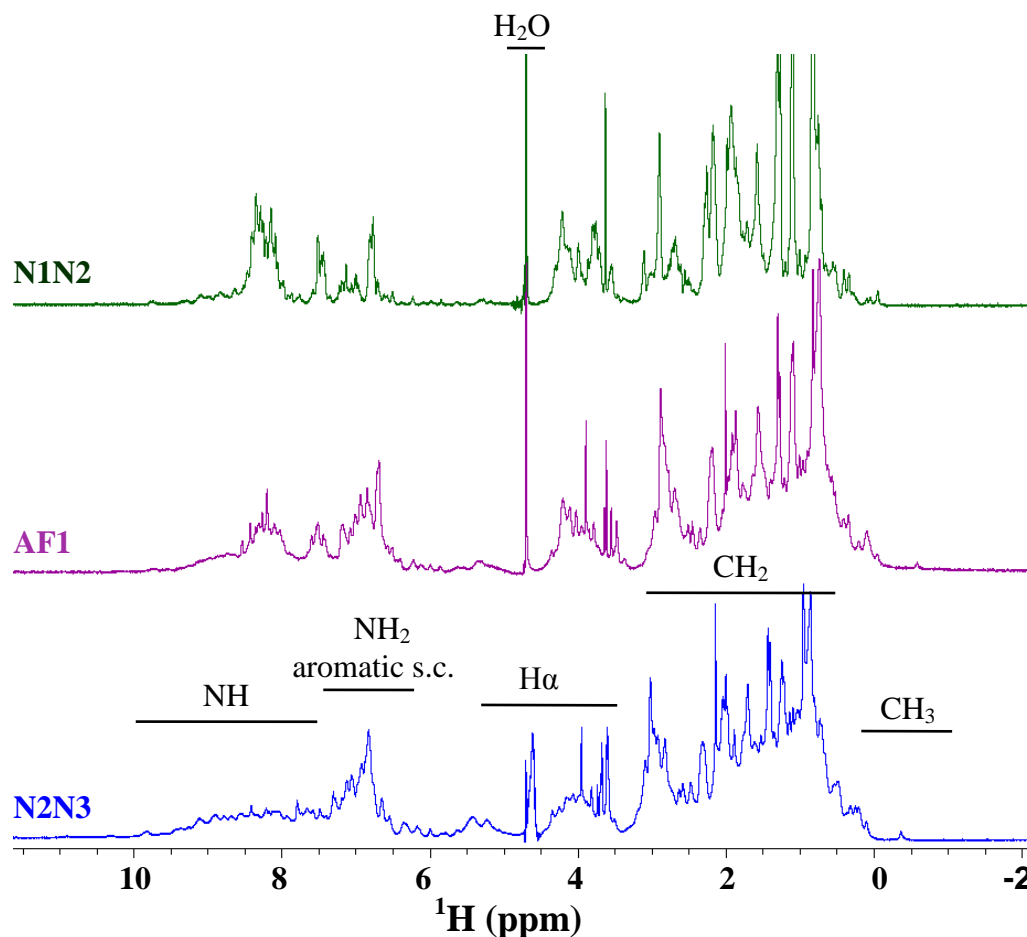


**Figure 3.27** Comparison of the 1D  $^1\text{H}$  NMR spectra of N2N3 (blue), AF1 (purple) and N1N2 (green). Typical chemical shift ranges associated with  $^1\text{H}$  nuclei in different protein environments are shown (Wishart et al., 1991). The strong peak at  $\sim 4.8$  ppm, corresponding to the not-fully suppressed  $\text{H}_2\text{O}$  signal is also indicated. 2,2-Dimethyl-2-silapentane-5-sulfonate (DSS) was used as an external reference.

### 3.9 Solubility and long-term stability of rFnBPA proteins

Removal of the His<sub>6</sub>-tag solved the initial solubility issues observed for rFnBPA proteins and facilitated purification of sufficient yields of pure protein. However, solubility and long-term stability of rFnBPA proteins is required for techniques such as NMR spectroscopy and X-ray crystallography. Moreover, preliminary NMR spectroscopy of  $^{15}\text{N}$ -N2N3 revealed that an acquisition temperature of  $37^\circ\text{C}$  might be required to achieve high resolution spectra (data not shown).  $^{15}\text{N}$ -labelled N2N3T, N2N3 and AF1 were readily soluble at high concentration ( $<1$  mM) and stable for up to several days at  $4^\circ\text{C}$ , as determined by monitoring the sample concentration using absorbance at 280 nm (Section 2.6.8) and by analysing the protein solution using SDS-PAGE and NATIVE-PAGE (Sections 2.6.3 and 2.6.4). However, problems



arose when the concentrated protein samples were exposed to 37°C over a period of several hours in an NMR spectrometer, resulting both from protein degradation and aggregation followed by precipitation. This was associated with a significant decline in the quality of the spectra. A systematic search for the optimum solution for NMR spectroscopy was carried out using a methodical optimization process testing a wide range of different buffers and additives (Golovanov et al., 2004; Howe, 2004; Kelly et al., 2002). Protein sample analysis was carried out using a combination of SDS- and NATIVE-PAGE (Sections 2.6.3 and 2.6.4) to detect any potential degradation or aggregation, respectively. Unfortunately, optimization did not lead to the identification of suitable conditions for the NMR sample, with all samples undergoing degradation and/or aggregation after 24 hours at 37°C. Eventually, the temperature stability of specific rFnBPA proteins was analysed using differential scanning calorimetry (DSC) (Section 2.8.5, Figure 3.28), a technique designed to measure the partial heat capacity of a solution as a function of temperature (Jelesarov and Bosshard, 1999; Cooper et al., 2001; Edgcomb and Murphy, 2000). All the DSC experiments were conducted by Dr Iain Manfield (Astbury Centre, University of Leeds).

Model-fitting and subsequent determination of reliable thermodynamic parameters from DSC data can only be performed successfully if the unfolding is a single, cooperative and reversible process. For the rFnBPA data, this is not the case (Figure 3.28). Results of the DSC experiments suggest that for the N2N3 region there are two separate transition periods, most likely corresponding to the unfolding of the two individual domains N2 and N3. The first signs of unfolding, marked as the beginning of the first transition period (T1-T2), were detected at approximately 36°C. The  $C_p$  maximum (also known as transition midpoint  $T_{m1}$ ) was reached at approximately 43°C, followed by a sharp decline in  $C_p$ , indicative of rapid aggregation. A second transition period occurs between 60 and 70°C leading to further aggregation. It is difficult to predict which domain is the less stable but there is little doubt that the overall unfolding process is complex and irreversible, thus unsuitable for model fitting and determination of  $\Delta H_{cal}$ . Nevertheless, the T1 and  $T_{m1}$  values of 36°C and 43°C provide an explanation for the low stability by N2N3 at 37°C. It is also probable that rFnBPA proteins would exhibit limited long-term stability at any temperature above 30°C, leading to a conclusion that either the NMR acquisition

parameters would have to be altered significantly to generate high resolution spectra at temperatures below 30°C or a new approach, excluding NMR spectroscopy, will have to be considered.

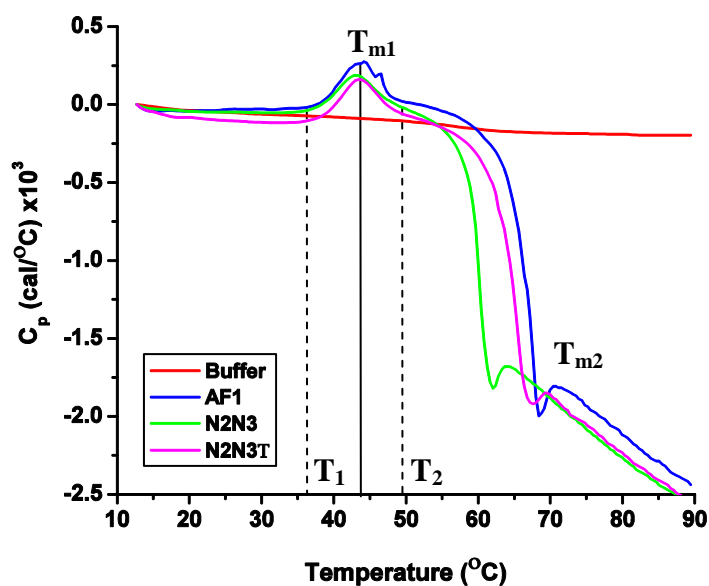


**Figure 3.28 Raw DSC data for AF1, N2N3 and N2N3T thermal unfolding experiments.** Thermograms for  $C_p$  for AF1 (blue), N2N3 (green) and N2N3T (magenta). The temperature dependence of  $C_p$  for buffer (red) was also measured and used as a baseline. Two transition midpoints ( $T_{m1}$  and  $T_{m2}$ ) corresponding to two separate unfolding processes are also indicated. Temperatures  $T_1$  ( $\sim 36^\circ\text{C}$ ) and  $T_2$  ( $\sim 49^\circ\text{C}$ ) mark the temperature limits of the first transition period.

### 3.10 Summary

Seven rFnBPA protein constructs, namely; N1N2, N3, N2N3T, N2N3, N2N3E, fA and AF1 (Section 3.3), were designed, cloned, expressed and purified, achieving relatively high yields and purity (Sections 3.6.6 and 3.6.7). Three of these constructs; N2N3, N2N3T and AF1 were also expressed uniformly labelled with  $^{15}\text{N}$  (Section 3.5.2). The purification required systematic optimization and extensive troubleshooting. Some of the initial complications were associated with the low solubility of His<sub>6</sub>-tagged rFnBPA proteins (Section 3.6.1) and the additional His<sub>6</sub>-tag was identified as the probable cause. Other issues included the relatively high level of degradation products and contaminants within the purified His<sub>6</sub>-AF1 (Section 3.6.4). Utilization of an optimized IEX purification step led to a significant reduction in the level of contaminants, resulting in a sufficiently pure AF1 sample (>95%), as determined by SDS-PAGE analysis (Section 3.6.5). The monomeric states of N2N3 and AF1 were later confirmed by AUC (Section 3.7).  $^1\text{H}$  NMR spectra of N1N2,

N2N3 and AF1 provided an initial level of protein structural characterization (Section 3.8). The spectra revealed that N2N3 comprised mostly well defined folds, while, as expected, AF1 contained an additional unfolded region. A significantly larger proportion of intrinsic disorder was apparent in the spectrum of N1N2, most likely associated with the N1 domain. The spectra provide preliminary evidence that the novel rFnBPA proteins are folded and are therefore suitable for functional studies. All of the rFnBPA proteins appeared relatively stable for up to a few days at temperatures equal to or below 25°C, which is suitable for most techniques. However, preliminary NMR spectroscopy revealed that high resolution spectra of <sup>15</sup>N rFnBPA proteins would require acquisition at 37°C for a period of up to several days. Unfortunately most of the rFnBPA proteins exhibit limited stability at temperatures above 30°C, as demonstrated by the DSC experiment (Section 3.9). For this reason and due to the size of the rFnBPA proteins, X-ray crystallography was used to solve the structures of unbound N2N3 and of N2N3 in complex with Fg1 (Section 2.3.1). The temperature stability would also need to be considered with respect to functional experiments.

## 4 Structural characterization of N2N3 and its interaction with Fg

### 4.1 Introduction

Previous studies have addressed the question of where Fg binds to FnBPA by using recombinant truncated derivatives of rFnBPA, albeit with contrasting results (Wann et al., 2000; Keane et al., 2007b; Piroth et al., 2008). The  $K_d$  for the interaction of rFnBPA<sub>37-605</sub> (contains the full A-domain and the first two FnBRs) with Fg was determined by SPR and fluorescence polarization (FP) as 11 and 2.4  $\mu$ M, respectively (Wann et al., 2000). However, in two different studies the  $K_d$ s for the interaction of Fg with the FnBPA A-domain, as well as rFnBPA<sub>(194-511)</sub>, were determined by ELISA as 4.5 nM (Keane et al., 2007b; Loughman et al., 2008). There is also a lack of structural data for the N2N3 region or the whole A-domain of FnBPA. However, since N2N3 from FnBPA shares 26% and 22% sequence identity with N2N3 from ClfA and SdrG, respectively (Altschul et al., 1997), the N2 and N3 domains of FnBPA are predicted to accommodate  $\beta$ -sandwich folds similar to those found in ClfA and SdrG.

FnBPA, like ClfA, interacts with the C-terminal end of the Fg  $\gamma$  chain (Section 1.6.3) (Wann et al., 2000; McDevitt et al., 1997), however, FnBPA is expressed predominantly in the exponential phase of bacterial growth while ClfA is expressed in the stationary phase (Saravia-Otten et al., 1997; O'Brien et al., 2002a). Inhibition studies identified the last 17 C-terminal residues of the  $\gamma$  chain as the minimal Fg fragment retaining similar activity to intact Fg (Wann et al., 2000). A combination of crystallization and NMR experiments revealed this region is intrinsically disordered within intact Fg (Blumenstein et al., 1992; Kollman et al., 2009; Yee et al., 1997). Interestingly, the same Fg region also targets the platelet integrin GPIIb/IIIa and is involved in the cross-linking process leading to fibrin formation (Fitzgerald et al., 2006a; Fitzgerald et al., 2006b; Wolberg, 2007; Mosesson, 2005). As FnBPA has the potential to interfere with haemostasis, a better understanding of the interaction between native Fg and FnBPA could provide valuable insight into events associated with *S. aureus* infections.

## 4.2 Aims

The primary objectives of the research were to identify the structural features of N2N3 and to characterise its interaction with Fg. Both SPR and ITC were used extensively to achieve this. Sections 1.7.1 and 1.7.2 describe these techniques and their use to study the molecular interactions.

## 4.3 Identification of the FnBPA region that binds Fg

Numerous studies have demonstrated the Fg-binding ability of the FnBPA A-domain, however, only a handful of these focused on which domains (N1, N2 and N3) are involved in the Fg-binding process and the studies had different outcomes (Que et al., 2005; Keane et al., 2007b; Piroth et al., 2008). The following SPR experiment assessed the binding of recombinant truncated derivatives of FnBPA to FgD (Section 2.3.3) to obtain preliminary data regarding the contribution of the individual domains to the interaction.

Response intensity  $R$  (in RU) in a typical SPR experiment is directly proportional to the association constant ( $K_a$ ) for the analyte-ligand interaction, and to the molecular mass and concentration of the analyte (Schuck, 1997). Providing these factors are taken into account, the steady-state binding level ( $R_{eq}$ ) can be used to compare the relative affinities of the interactions of rFnBPA analytes with FgD. The experimental setup involved immobilization of FgD on the surface of a sensor chip followed by exposure of the FgD-coated surface to equi-molar concentrations (10  $\mu$ M) of the rFnBPA variants. The steady-state levels of binding generated upon interaction of the ligand with different analytes were measured and the resulting values compared (Figure 4.1).

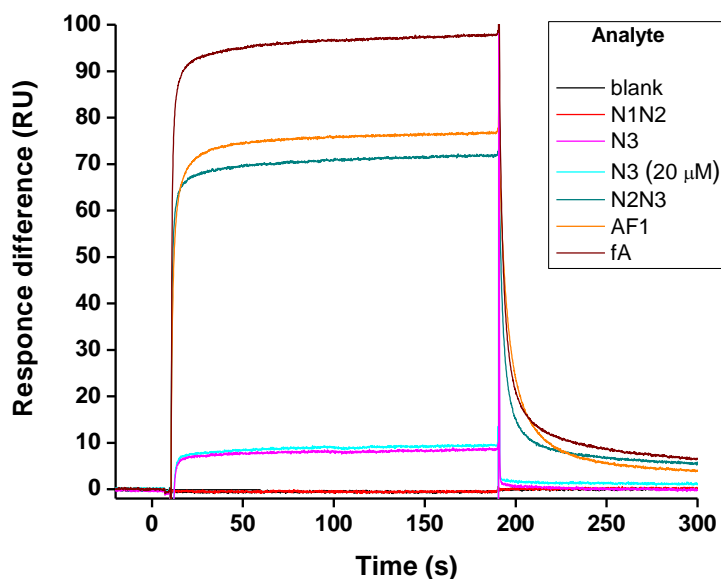


**Figure 4.1 SPR Sensorgram.** Representative sensorgrams corresponding to the  $R_{eq}$  generated upon exposure of a FgD-coated sensor chip to the rFnBPA truncated derivatives at a concentration of 10  $\mu\text{M}$ . N3 was also tested at a concentration of 20  $\mu\text{M}$  (cyan).

The recombinant FnBPA proteins used were as follows; fA, N1N2, N2N3, N3 and AF1 (Table 3.1). The highest  $R_{eq}$  value corresponded to the injection of fA, followed by AF1 and then N2N3, with the value for N3 considerably lower, and no response was detected upon injection of N1N2. The association phases for all four reactions exhibit similar characteristics, reaching a steady-state. The dissociation phase appears faster for N3 than for N2N3, AF1 and fA. The order of  $R_{eq}$  values correlated with the respective molecular masses of the recombinant proteins that bound FgD. The relatively small variability in  $R_{eq}$  for fA, AF1 and N2N3 most likely originates from the difference in molecular mass rather than affinity. However, the  $R_{eq}$  generated upon N3 injection is considerably smaller than that of N2N3, indicating that the Fg-binding site might have been compromised. Injection of N3 was repeated at a higher concentration (20  $\mu\text{M}$ ) with no significant change in the  $R_{eq}$ .

The maximum response generated upon analyte injection is reached when the immobilized ligand is fully saturated, thus the  $R_{MAX}$  value corresponds to the analyte binding capacity of the surface (in RU). The theoretical  $R_{MAX}$  ( $tR_{MAX}$ ) can be calculated based on the level of immobilised ligand  $R_L$  (519 RU) and the molecular masses of the ligand  $M_L$  (85 kDa) and analyte ( $M_A$  36 kDa) using Equation 4.1.

$$tR_{MAX} = \frac{R_L \times M_A}{M_L} \quad (4.1)$$

The  $K_d$  for the interaction between the A-domain and Fg has been determined previously by SPR as 11  $\mu$ M (Wann et al., 2000). Consequently, it can be assumed that at an analyte concentration of 10  $\mu$ M, the response  $R_{eq}$  should be approximately equal to half of the  $R_{MAX}$ . The observed  $R_{eq}$  (half- $R_{MAX}$ ) can thus be used to estimate the final  $R_{MAX}$  which can be presented as a percentage of the  $tR_{MAX}$ . The normalized values can then be compared directly, as they are independent of the analyte molecular mass. As the same conditions, including ligand immobilization, were used for all analytes, the percentages should be similar, providing the  $K_d$ s for the analyte-ligand interactions are identical (Table 4.1). It is, however, important to consider that the  $tR_{MAX}$  is the ideal value and often does not reflect the real  $R_{MAX}$ , as it cannot be guaranteed that all of the immobilized ligand is either functional or accessible to the analyte.

Protein	Mass (Da)	$tR_{MAX}$ (RU)	$R_{eq}$ (RU)	$eR_{MAX}$ (RU)	%
fA	52679	322	97.8	196	61
AF1	40900	250	76.7	154	62
N2N3	36323	222	71.7	143	64
N1N2	33149	202	0	0	0
N3	19903	122	8.7 (9.3)	17	14

**Table 4.1 Results of the SPR experiment designed to test the binding of truncated rFnBPA derivatives to FgD.** The table includes the  $tR_{MAX}$  calculated from Equation 4.1, different responses determined from the sensorgram and the estimated  $R_{MAX}$  ( $eR_{MAX}$ ) based on the observed steady state binding level ( $R_{eq}$ ). The  $eR_{MAX}$  value is also shown as a percentage of  $tR_{MAX}$  to allow comparison of the relative values, independent of the differences in molecular mass of the individual analytes.

Table 4.1 clearly shows there is no detectable interaction between N1N2 and FgD, and only a weak interaction between N3 and FgD. This leads to the conclusion that both N2 and N3 are required for Fg-binding and that FgD binds N2N3 with affinity similar to that for the A-domain. While these results are only preliminary, they are consistent with previous studies, analysing the effects of mutations in the N2N3 region of ClfA on Fg binding (Josefsson et al., 2008; Deivanayagam et al., 2002; Keane et al., 2007b).

#### 4.4 N2N3 binding to Fg

The dissociation constant for the interaction between the FnBPA A-domain and native Fg was determined previously utilizing SPR and FP as 11.0 and 2.5  $\mu\text{M}$ , respectively (Wann et al., 2000). Broadly consistent  $K_d$ s of 5.8 and 0.1  $\mu\text{M}$  were determined for the respective ClfA- and SdrG-N2N3 regions (McDevitt et al., 1997; Davis et al., 2001). The sequence similarity between FnBPA and ClfA/SdrG, combined with the SPR results described in Section 4.3, suggests that N1 is not required for the FnBPA-Fg interaction.

In the following experiment, the  $K_d$  for the N2N3-Fg interaction was measured by ITC, where intact Fg was titrated into a cell containing N2N3 (Section 2.8.3). The binding isotherm was fitted based on the ‘single set of sites’ model, and the  $K_d$  determined as  $2.3 \pm 0.2 \mu\text{M}$ . It is similar to that for the FnBPA<sub>(37-605)</sub> interaction with Fg ( $11.0 \pm 1.2 \mu\text{M}$ ) measured previously, using SPR (Wann et al., 2000). Thus the Fg-binding site appears to be located entirely within the N2N3 region. The derived stoichiometry of 2.14 (N2N3:Fg) corresponds to the presence of two identical binding sites on the intact Fg (dimer) (Section 1.4). Thermodynamic parameters for the interaction and their associated errors are listed in Table 4.2.



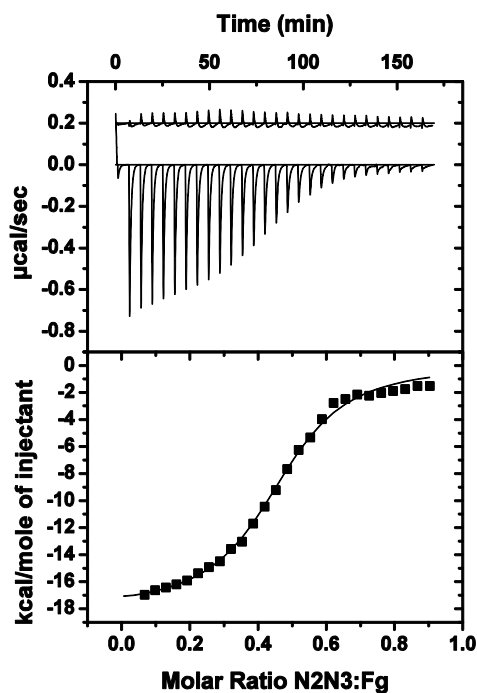


**Figure 4.2** Determination of the  $K_d$  for the N2N3-Fg interaction. Peaks in the upper panel represent heats generated upon injections of Fg into N2N3. The experiment also includes a titration of Fg into the cell buffer to evaluate the heats of dilution. Measured heats were integrated, heats of dilution subtracted, and the best fit was calculated based on a ‘single set of sites’ model using Origin 7 (Microcal). The ITC binding isotherm is shown in the lower panel. Thermodynamic parameters are listed in Table 4.2.

## 4.5 Determining the role of the putative latch strand in Fg binding

The proposed dock-lock-latch model for the SdrG (*S. epidermidis*)-Fg ( $\beta$  chain) interaction (Section 1.6.3) attributed a particularly important role to the latch strand (Figure 1.11), comprising the C-terminal extension of N3 which binds along the N2-E strand (Ponnuraj et al., 2003). Crystal structures of apoSdrG<sub>(273-597)</sub> and SdrG<sub>(273-597)</sub> in complex with the Fg $\beta$ -peptide show that the latch strand interacts with the E strand of the N2 domain upon Fg binding. An SPR experiment revealed that the removal of the latch strand significantly reduced the affinity of the interaction (Ponnuraj et al., 2003). Thus it has been proposed that the latch strand has a stabilizing effect on the structure of the complex. The latch strand in ClfA (*S. aureus*) also interacts with the N2 domain E strand (Figure 1.12), however, its importance in Fg ( $\gamma$ -chain) binding has not yet been established (Ganesh et al., 2008). The aim of the following SPR experiment was to test the importance of the putative latch strand in the FnBPA-Fg interaction.

The  $K_{ds}$  for interactions between FgD and N2N3 (Section 3.3.1) or N2N3T (Section 3.3.2) were determined using SPR. FgD was immobilized on the surface of a sensor chip and subsequently exposed to increasing concentrations of N2N3 or N2N3T (Figure 4.3). The resulting sensorgrams show that both the association and dissociation rates are fast, and outside the measurable range of the Biacore T100 (GE Healthcare) instrument (Section 1.7.2.4). Consequently,  $K_{ds}$  for the interactions were derived by analysis of equilibrium binding (Section 2.8.2.3).  $K_{ds}$  for the interactions of N2N3 and N2N3T with immobilized FgD were  $1.5 \pm 0.1 \mu\text{M}$  and  $3.7 \pm 0.2 \mu\text{M}$ , respectively. The similarity between the  $K_d$  values indicates that the putative latch strand is not essential for the FnBPA-Fg interaction.

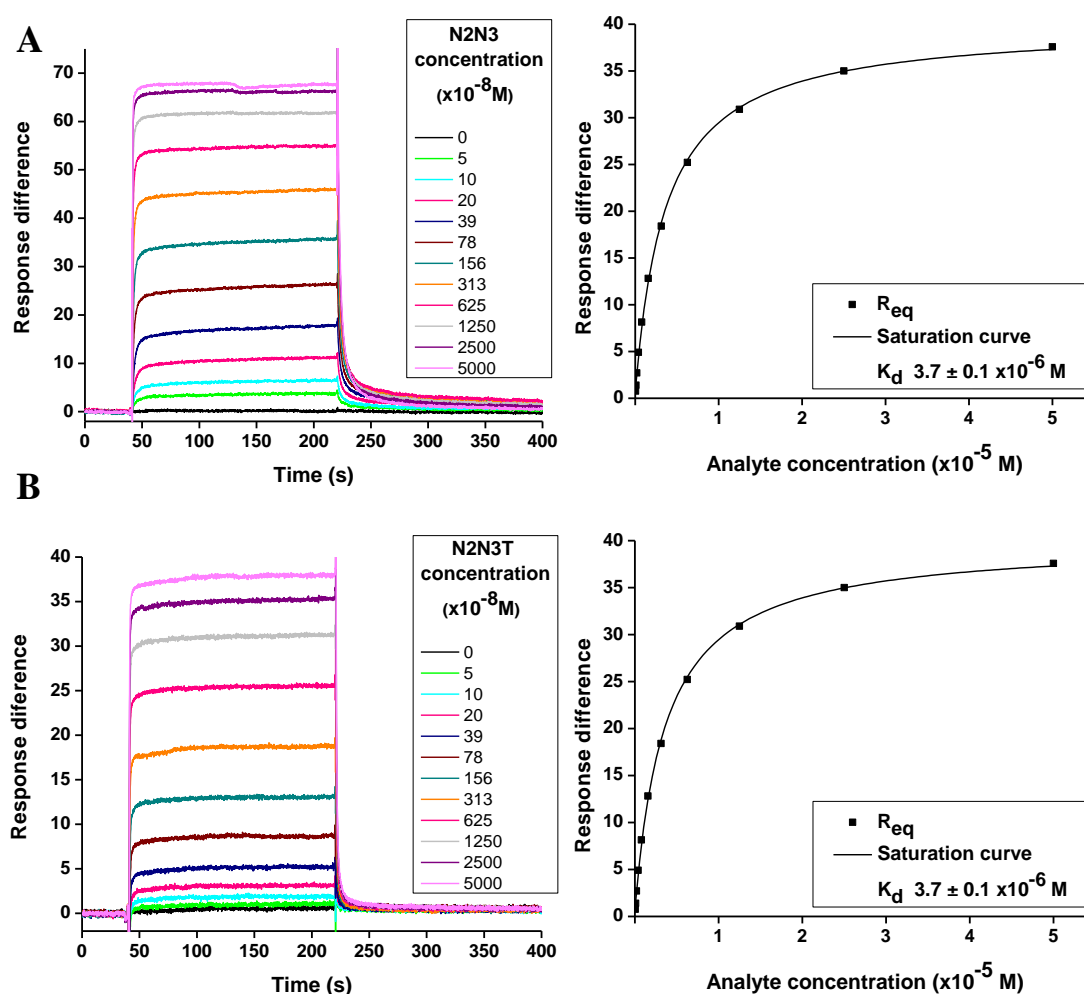


**Figure 4.3 Binding of N2N3 and N2N3T to FgD.** Representative SPR sensorgrams show responses generated upon interactions of immobilized FgD with increasing concentrations of N2N3 (A) and N2N3T (B). Affinity evaluation using equilibrium analysis is also shown.

## 4.6 Native Fg binds FnBPA with similar affinity to Fg1

All previous binding experiments have been carried out using either intact Fg (~ 340 kDa) (ITC) or FgD (~ 85 kDa) (SPR). However, both Fg and FgD are large macromolecular species whose utilization in an NMR spectroscopy structural characterisation of N2N3 (and its binding to Fg) would present numerous complications. The physiological relevance of the Fg1 peptide (~ 1.7 kDa) (Section 2.3.1) as a model of the FnBPA binding site on Fg had to be established.

Initially, the  $K_d$  for the N2N3-Fg1 interaction was determined by ITC, where the ligand (Fg1) within the syringe was titrated into N2N3 in the cell (Section 2.8.3). A ‘single set of sites’ model was utilized to fit the binding isotherm and the  $K_d$  was  $21.4 \pm 1.0 \mu\text{M}$  (Figure 4.4). Specific thermodynamic parameters for the interaction are summarised in Table 4.2. A comparison of the  $K_d$ s for the N2N3-Fg1 and the N2N3-Fg ( $2.3 \pm 0.2 \mu\text{M}$ ) interactions reveals a relatively small difference in affinity.

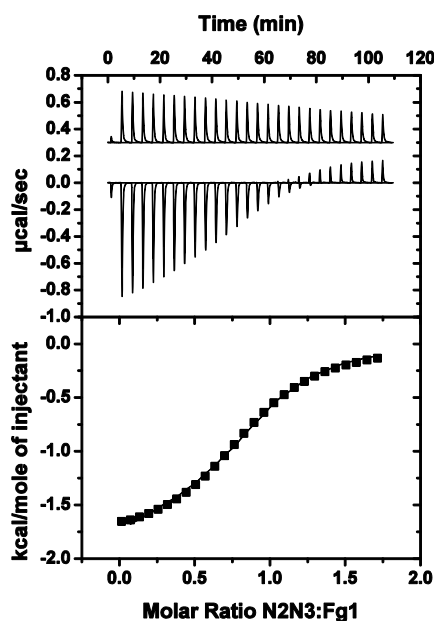


**Figure 4.4** Determination of the  $K_d$  for the N2N3-Fg1 interaction. Peaks in the upper panel represent heats generated upon every Fg1 injection into N2N3. The Experiment also includes a titration of Fg1 into the cell buffer, which was used to evaluate the heats of dilution. Measured heats were integrated, heats of dilution subtracted and the best fit was calculated based on a ‘single set of sites’ model using MicroCal Origin 7 software. The ITC binding isotherm for the titration of Fg1 into N2N3 is shown in the lower panel. Thermodynamic parameters are listed in Table 4.2.

In order to further investigate Fg1's suitability as a model for Fg in FnBPA binding studies, an SPR experiment with immobilized FgD and N2N3 as the analyte was performed. The experimental set-up was identical to that in Section 4.5, with the addition of excess Fg1 as an inhibitor. Addition of a fifty- and hundred-fold molar excess of Fg1 to the solution of N2N3 resulted in reduction of the original response intensity of 35.8 RU to 11.1 and 3.8 RU, respectively. A solution containing N2N3 with a fifty-fold molar excess of N1N2 was used as a negative control, with no effect on the response (Figure 4.5). The outcomes of the ITC and SPR experiments show that Fg and Fg1 bind N2N3 with similar affinities and use the same or overlapping binding sites, but also that Fg1 binds somewhat less effectively.

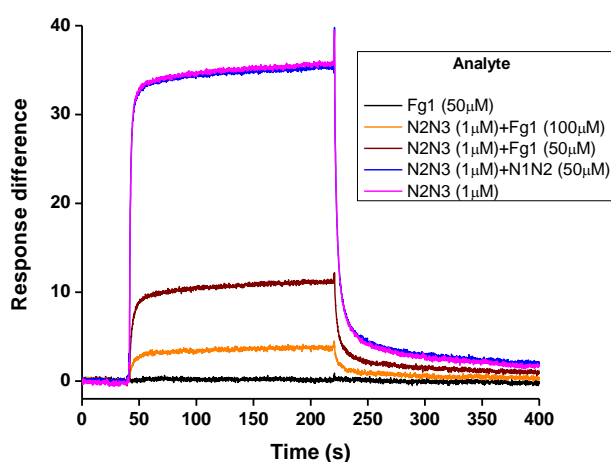


**Figure 4.5** Inhibition of the N2N3-FgD interaction by Fg1. Representative sensorgrams generated upon exposure of an FgD-coated sensor chip to N2N3 in the presence and absence of excess Fg1 or N1N2.

Interaction	$K_d$	$\Delta H$ / kcal mol <sup>-1</sup>	$\Delta S$ / cal mol <sup>-1</sup> K <sup>-1</sup>	n	Technique
N2N3-Fg1	21.4 ± 1.1 μM	-1.28 ± 0.02	15.0	0.86	ITC
N2N3-FgD	1.4 ± 0.2 μM	-	-	-	SPR
N2N3-Fg	2.3 ± 0.2 μM	-8.30 ± 0.09	-2.05	2.14	ITC
N2N3T-FgD	3.7 ± 0.1 μM	-	-	-	SPR

**Table 4.2** Summary of kinetic and thermodynamic parameters for the N2N3-Fg interactions. The table includes  $K_d$ s determined by either ITC or SPR. Values for the enthalpy ( $\Delta H$ ) and entropy change ( $\Delta S$ ) and stoichiometry (N2N3:Fg1/Fg) (n) were also determined for the interactions studied by ITC.

## 4.7 Analysis of the FnBPA-Fg interaction by NMR spectroscopy

The aim of the following set of NMR experiments was to gain further insight into the structural characteristics of FnBPA and the binding interaction with Fg. This involved acquisition of a 2D  $^1\text{H}^{15}\text{N}$  HSQC spectrum of uniformly  $^{15}\text{N}$ -labelled N2N3 and subsequent comparison with spectra of  $^{15}\text{N}$ -N2N3 titrated with Fg1 (Section 2.8.1). Peaks in the HSQC spectrum correspond to the N2N3 amide protons, and the extent of the chemical shift perturbations (upon Fg1 binding) relates to the degree of environmental changes on the protein:peptide interface (Stevens et al., 2001; Pellecchia et al., 2000). The kinetics of the binding during the titration results in characteristic perturbations indicative of fast, slow or intermediate exchange on the NMR timescale. Fast exchange is usually associated with weaker binding and rapid dissociation rates. Consequently, only a single set of resonances representing the population weighted average of the unbound and bound chemical shifts is visible with peaks appearing to ‘move’ in continuous fashion during the titration (Hall et al., 2001). Slow exchange is often observed for tighter interactions and corresponds to a very slow dissociation rate. Resonances representing the unbound protein gradually disappear through the course of the titration and are replaced by a set of resonances for the bound protein (Williamson et al., 1997). Finally, in intermediate exchange peaks shift and broaden on increasing ligand concentration (Zuiderweg et al., 1981; McAlister et al., 1996). The exchange rate is also dependent on the chemical shift difference between free and bound states. Thus, peaks involved in the same interaction can be in different exchange regimes.

### 4.7.1 Optimization of conditions for HSQC spectra of $^{15}\text{N}$ -N2N3.

Initially, an HSQC spectrum was acquired for  $^{15}\text{N}$ -N2N3 (Figure 4.6A). The sample preparation and acquisition of the spectra were performed as described in Section 2.8.1. The resulting spectrum exhibited poor resolution and a low signal to noise ratio. While the relatively wide peak dispersion in the  $^1\text{H}$  dimension was indicative of folded state, clearly, the sample conditions and/or the experimental set-up needed adjustment to generate a better spectrum.

The problem with low resolution of the spectrum was most likely the consequence of the relatively high molecular mass of N2N3 (36 kDa). The tumbling rate of large

proteins in solution is slower, causing a fast decay of the NMR signal (relaxation). Transverse nuclear spin relaxation leads to line broadening and a loss of NMR signal. Factors contributing to the increase in the rate of the transverse relaxation also include chemical shift anisotropy (CSA) and dipole-dipole coupling (DD) (Wuthrich, 1998; Riek et al., 1999). Incorporating transverse relaxation optimized spectroscopy (TROSY) into an NMR experiment can significantly reduce the relaxation rate and improve spectral resolution and sensitivity (Pervushin et al., 1997). TROSY exploits constructive interference between DD (magnetic field independent) and CSA (proportionate to magnetic field), thus in a certain  $^1\text{H}$  frequency range (950-1050 MHz) the transverse relaxation is reduced to a near zero level. TROSY has proved particularly useful in NMR studies of proteins with high molecular mass, allowing acquisition of high resolution spectra which would not be possible with previous NMR approaches (Wider and Wuthrich, 1999; Venters et al., 2002). The result of the TROSY-HSQC experiment with  $^{15}\text{N}$ -N2N3 is shown in Figure 4.6B. Although 700 MHz is not the optimum frequency, a significant reduction of transverse relaxation was achieved leading to improvement in both the signal intensity and the resolution of individual peaks (Figure 4.6).

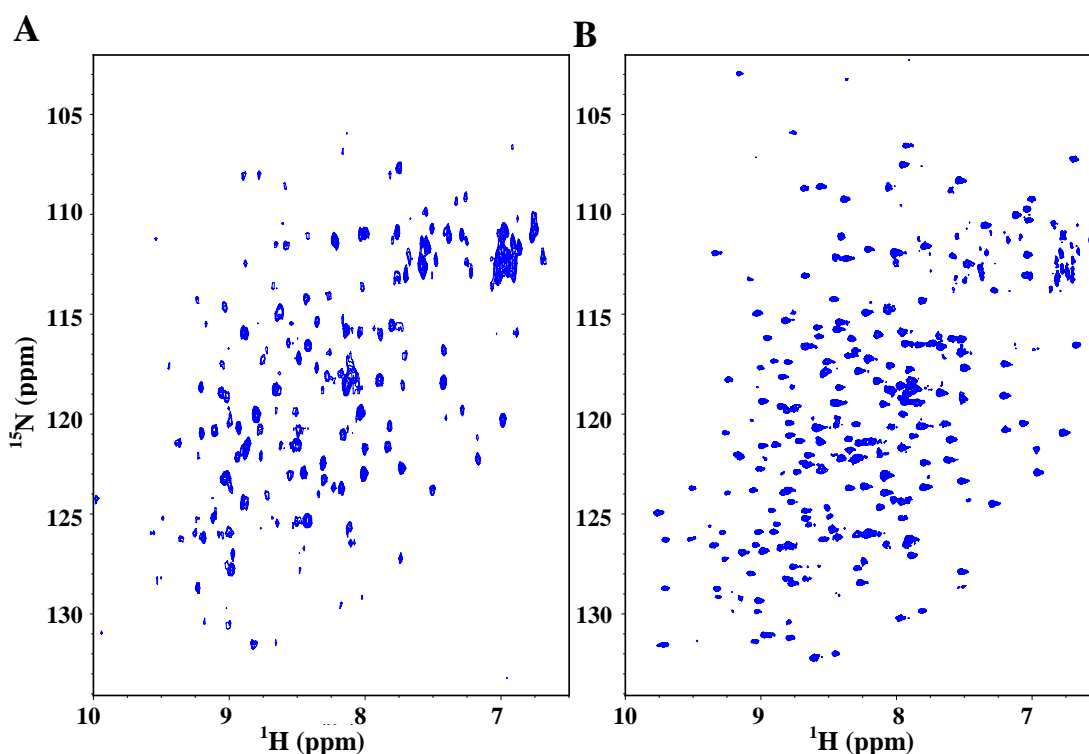


**Figure 4.6** Comparison of (A) 2D  $^1\text{H}$ - $^{15}\text{N}$  HSQC and (B) 2D  $^1\text{H}$ - $^{15}\text{N}$  TROSY-HSQC spectra of  $^{15}\text{N}$ -N2N3. Both spectra were acquired on a 700 MHz spectrometer (Section 2.8.1) at 310 K, at pH 7.4, using an identical sample of  $^{15}\text{N}$ -N2N3. Data processing was performed using NMRPipe (Delaglio et al., 1995) and analysis using NMRView (Johnson and Blevins, 1994).

In an attempt to further improve the quality of the spectra, the sample pH was lowered to reduce the exchange rate between amide protons and solvent, thereby, potentially improving the intensity of the recorded signal (Woodward and Hilton, 1979; Richarz et al., 1979). Three TROSY-HSQC spectra of  $^{15}\text{N}$ -N2N3 were acquired at pH 7.1, 6.5 and 6.0. The effect of pH on protein stability is clearly demonstrated by a marked deterioration in the quality of the spectra below pH 7.0, with the worst spectrum acquired at pH 6.0. Both the number of visible peaks and the overall dispersion in the  $^1\text{H}$  dimension decreased significantly, indicating the stability of the protein has been compromised through partial denaturation and/or aggregation (Figure 4.7A). No significant difference was observed when comparing TROSY-HSQC spectra recorded between pH 7.0 and pH 8.0, thus the original sample pH 7.4 appears to be optimal.

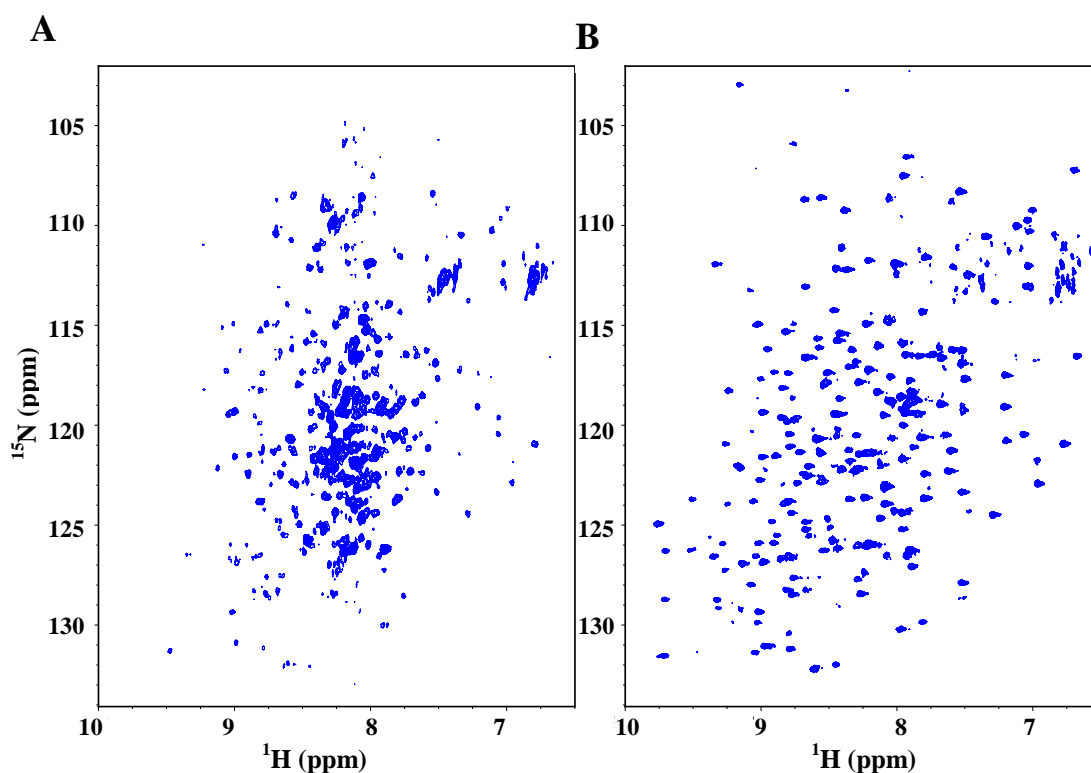


**Figure 4.7** Comparison of the 2D  $^1\text{H}$ - $^{15}\text{N}$  TROSY-HSQC spectra of  $^{15}\text{N}$ -N2N3 at (A) pH 6.0 and (B) pH 7.4. Both spectra were acquired on a 700 MHz spectrometer (Section 2.8.1) at 310 K, using identical sample of  $^{15}\text{N}$ -N2N3. Processing was performed using NMRPipe (Delaglio et al., 1995) and analysis using NMRView (Johnson and Blevins, 1994).

### 4.7.2 TROSY-HSQC spectra of $^{15}\text{N}$ N2N3 and $^{15}\text{N}$ N2N3T +/- Fg1

A set of  $^{15}\text{N}$ -N2N3 spectra with Fg1 at protein/peptide molar ratios ranging from 1/0.05 to 1/6 were recorded under otherwise identical conditions and compared (Figure 4.8). Despite the reduced quality of the final  $^{15}\text{N}$ -N2N3-Fg1 spectrum, it is clear that a significant number of peaks undergo a change in chemical shift after the addition of the Fg1 peptide. The spectra exhibit a combination of slow and intermediate exchange rate indicative of relatively strong binding (Section 4.7.1).

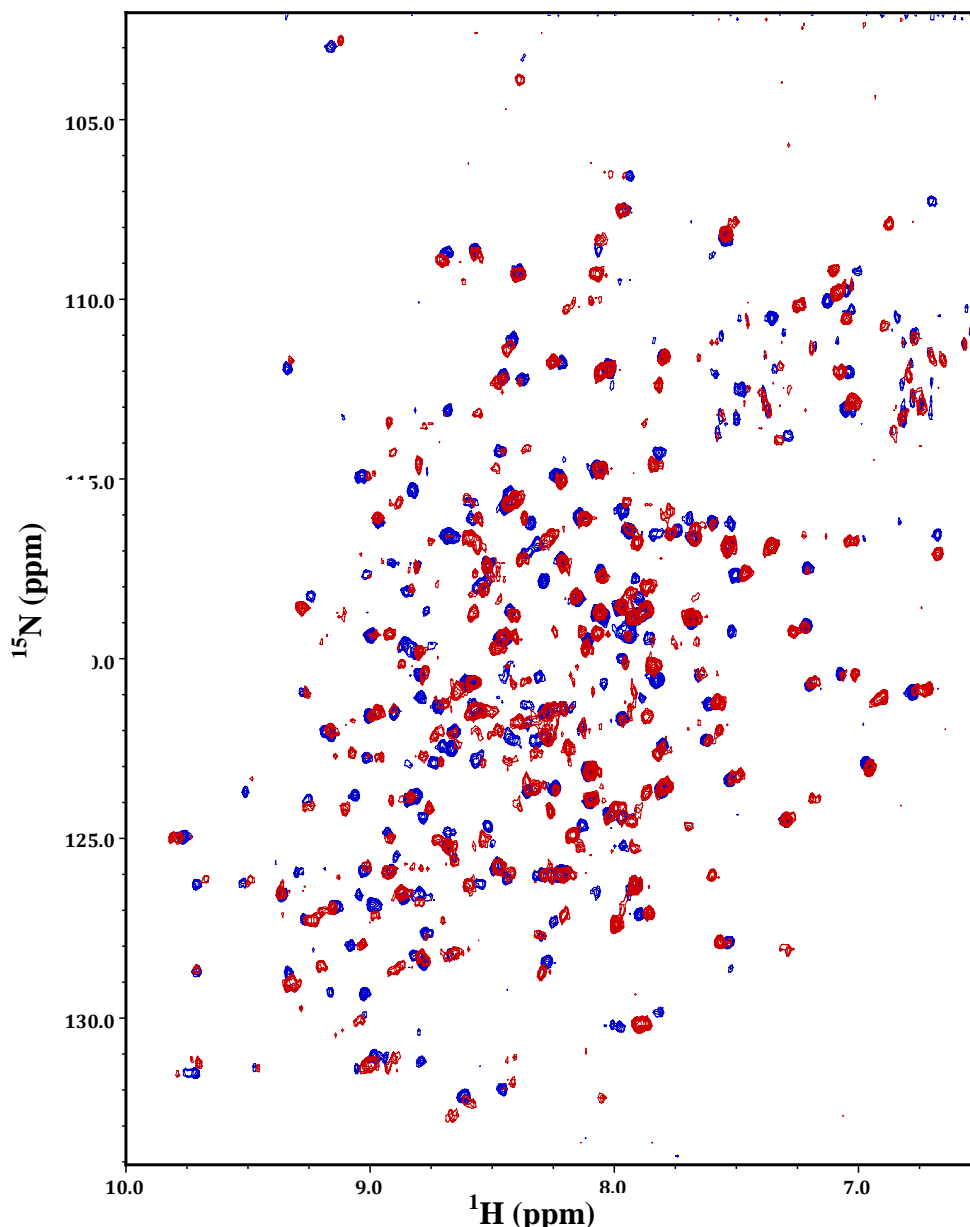


**Figure 4.8** 2D  $^1\text{H}$  $^{15}\text{N}$  TROSY-HSQC spectra of  $^{15}\text{N}$ -N2N3 with and without a 6-molar excess of **Fg1**. The spectra were acquired on a 700 MHz spectrometer (Section 2.8.1) at 310 K at pH 7.4. Data processing was performed using NMRPipe (Delaglio et al., 1995) and analysis by NMRView (Johnson and Blevins, 1994). The spectrum of unbound N2N3 is shown in blue, while the spectrum of Fg1-bound N2N3 is shown in red.



In the N2N3 spectrum, 260 peaks of an expected 318 were visible. The spectrum of N2N3 fully saturated with Fg1 peptide shows that approximately 80 peaks undergo chemical shift change and a further 19 new resonances appear in comparison with the spectrum of N2N3. The chemical shift changes demonstrate the presence of an interaction between N2N3 and Fg1. The proportion of residues affected on Fg1 binding points to the formation of an extensive interface and potentially a significant conformational change in N2N3. The newly appeared peaks in the spectrum of the N2N3-Fg1 complex most likely correspond to N2N3 residues that are in exchange between multiple conformational states in the absence of Fg1.

Finally, to investigate the effect of partial truncation of the putative latch strand on the N2N3 conformation and its interaction with Fg1, TROSY-HSQC spectra of <sup>15</sup>N-N2N3T in the absence and presence of excess Fg1 were recorded. The spectra were acquired under conditions identical to those described previously. Spectra of apoN2N3 and apoN2N3T are almost identical with the exception of several additional peaks appearing in the spectrum of N2N3T (Figure 4.9A). These extra peaks are likely to arise due to the lack of transient interactions with the dynamic putative latch strand present in N2N3. Comparison of the N2N3-Fg1 and N2N3T-Fg1 spectra revealed that the majority of peaks overlaid, a few had different chemical shifts and the N2N3-Fg1 spectrum contained at least four additional peaks (Figure 4.9B). These extra peaks might correspond to residues from the putative latch strand.

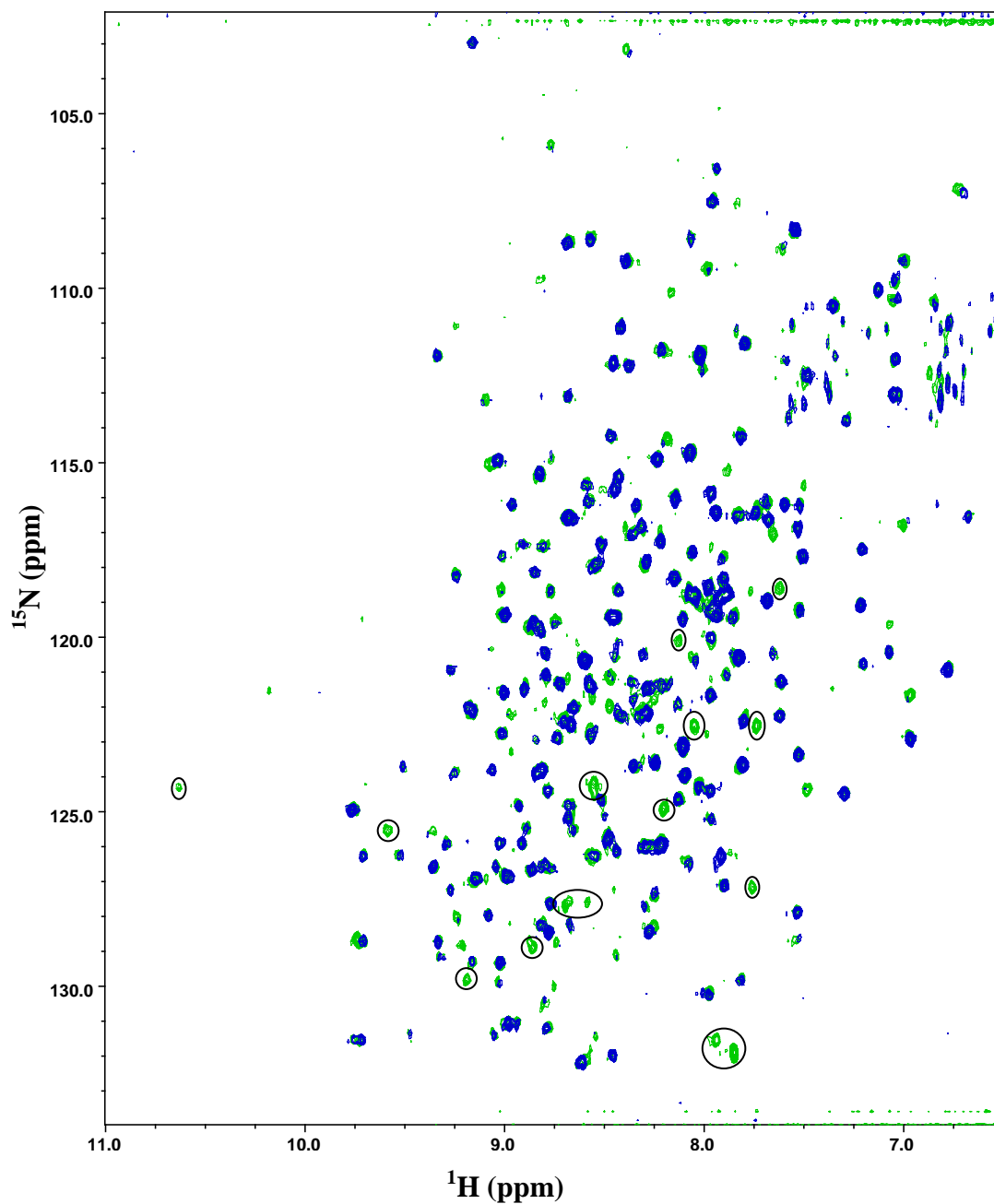


**Figure 4.9** 2D  $^1\text{H}$  $^{15}\text{N}$  TROSY-HSQC spectra of  $^{15}\text{N}$ -N2N3 (blue) and  $^{15}\text{N}$ -N2N3T (green). The spectra were acquired on a 700 MHz spectrometer (Section 2.8.1) at 310 K at pH 7.4. Data processing was performed using NMRPipe (Delaglio et al., 1995) and analysis using NMRView (Johnson and Blevins, 1994). Additional peaks are indicated by circles.

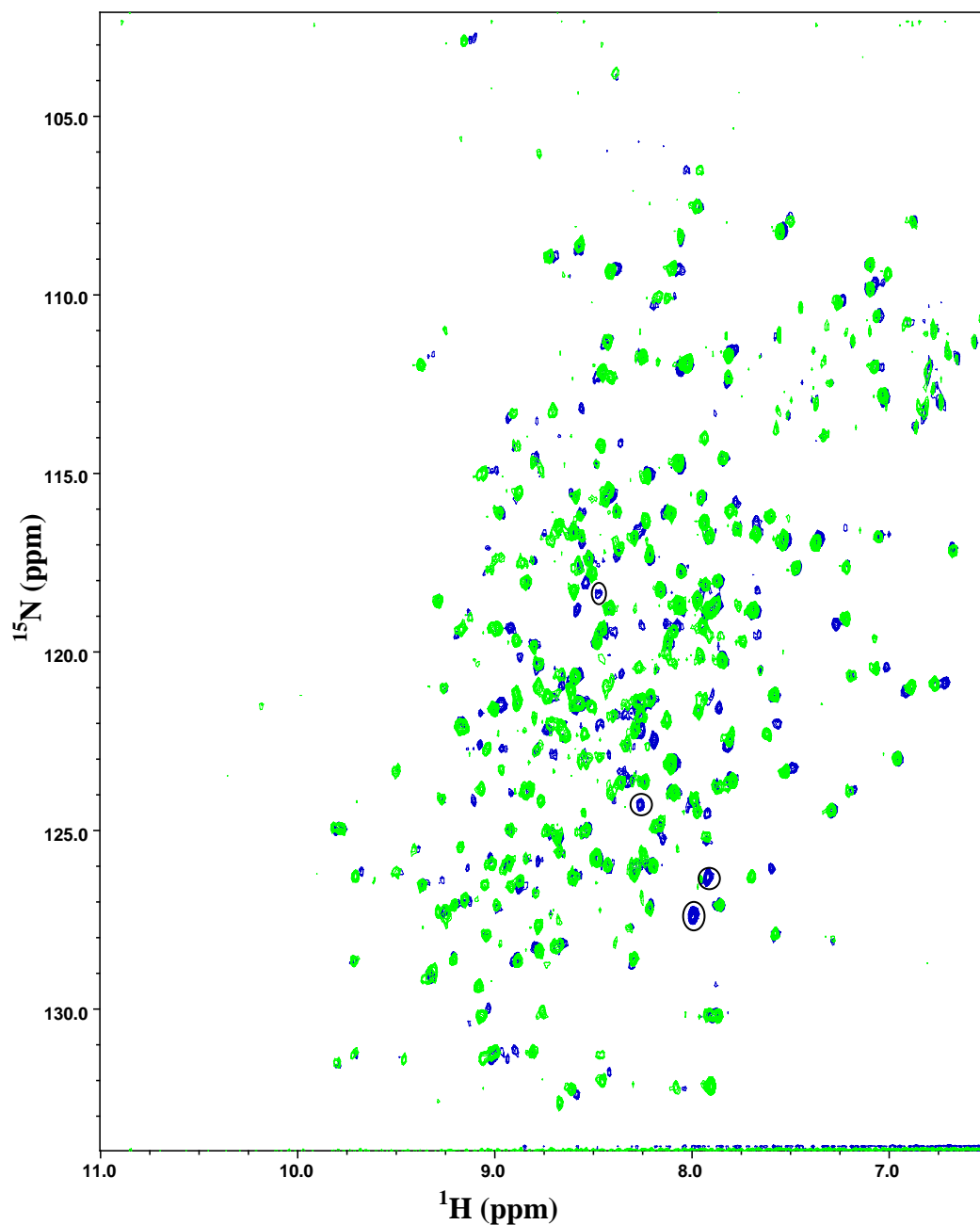


**Figure 4.10** 2D  $^1\text{H}$  $^{15}\text{N}$  TROSY-HSQC spectra of  $^{15}\text{N}$ -N2N3 (blue) and  $^{15}\text{N}$ -N2N3T (green) with a **6-molar excess of Fg1**. The spectra were acquired on a 700 MHz spectrometer (Section 2.8.1) at 310K at pH 7.4. Data processing was performed using NMRPipe (Delaglio et al., 1995) and analysis using NMRView (Johnson and Blevins, 1994). Additional peaks are indicated by circles.

## 4.8 Crystal structure of N2N3T

Initial crystallization trials were carried out with N2N3 using the sitting drop vapour diffusion method as described in Section 2.8.7. Clusters of fragile, needle-like crystals grew in several different conditions in the 96-well plates overnight, however these were unsuitable for data collection due to the lack of diffraction properties. Unfortunately, optimization of numerous conditions including protein concentration, buffer solution, pH, temperature or protein:solvent ratio within the drop, did not lead to improvement of the crystal characteristics. The predicted flexible nature of the N2N3 putative latch strand might have been interfering with the crystallization process, thus preventing the formation of stable and diffracting crystals of N2N3. Consequently, N2N3T was considered more suitable for crystallization trials. Large clusters of stable N2N3T crystals grew in optimized conditions (Section 2.8.7) and diffracted to 2.19Å (Figure 4.11). Crystallization, data collection and structure refinement were carried out as described in Section 2.8.8. The refinement statistics are shown in Table 4.3.

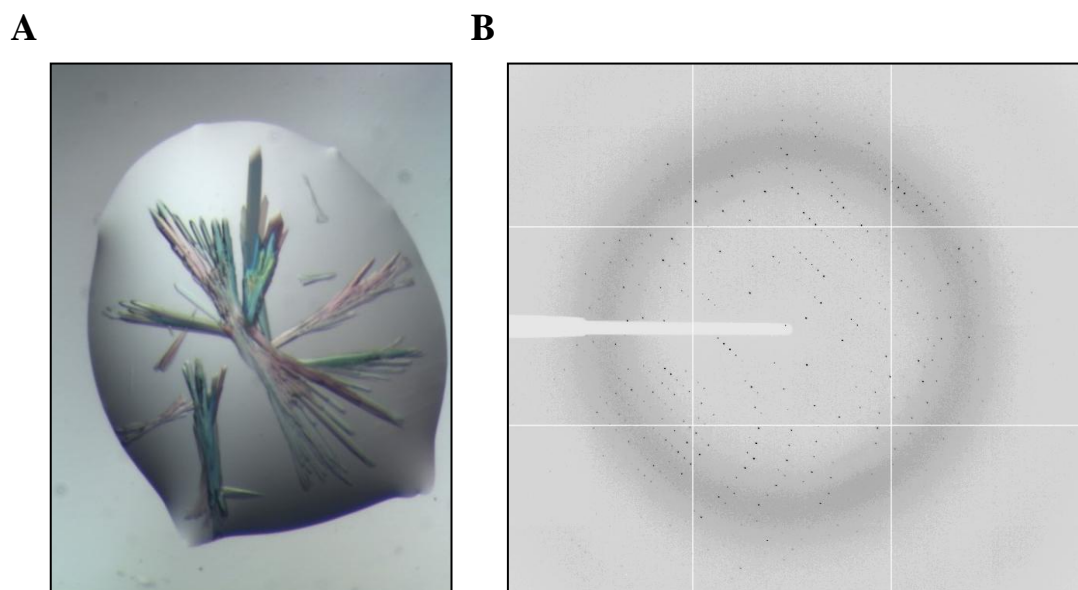


**Figure 4.11 Image of N2N3T crystals and corresponding diffraction pattern. (A)** Clusters of N2N3T crystals in a sitting drop containing polyethylene glycol (PEG) 20000 (8% (w/v)), PEG monomethyl ether (mme) 550 (8% (v/v)), 0.2 M calcium acetate, with added 50 mM Tris-HCl, 50 mM NaCl, pH 7.4. **(B)** The diffraction pattern corresponding to a single crystal originating from the cluster.

Parameter	N2N3T
Beamline	ID29
Space group	P2 <sub>1</sub> 2 <sub>1</sub> 2 <sub>1</sub>
Cell dimensions a, b, c (Å)	62.6, 75.2, 85.5
Cell dimensions $\alpha$ , $\beta$ , $\gamma$ (°)	90.0, 90.0, 90.0
Wavelength (Å)	0.9763
Resolution (Å)	56.5-2.2
R <sub>merge</sub>	0.10 (0.52)
I/ $\sigma$ I	8.6 (6.0)
Completeness	99.2 (87.3)
Redundancy	6.7 (3.6)
No. of unique reflections	21217
R <sub>factor</sub>	0.19
R <sub>free</sub>	0.24
Average B-factor (Å <sup>2</sup> )	18.3
r.m.s.d. bond lengths (Å <sup>2</sup> )	0.02
r.m.s.d. bond angles (°)	1.89

**Table 4.3 Data collection and refinement statistics for N2N3T.** Data for the highest resolution shell are shown in brackets where applicable.

The structure of N2N3T, like SdrG<sub>(273-597)</sub> and ClfA<sub>(229-545)</sub>, is formed by two distinct  $\beta$ -strand dominated domains, N2 and N3, linked by an eight residue linker (Figure 4.12). The N-terminal N2 domain (residues 195-335) consists of nine  $\beta$ -strands arranged in a sandwich of  $\beta$ -sheets. The N3 domain (residues 344-503) has a similar structure comprising two  $\beta$ -sheets formed by five  $\beta$ -strands each (Figure 4.12 and Figure 4.13). Unlike N2, however, the two  $\beta$ -sheets within the N3 domain are linked by a short  $\alpha$ -helical feature. The structures of N2 and N3 superpose with a root mean square deviation (r.m.s.d.) of 3.17 Å. The structures of both domains resemble a distorted  $\beta$ -barrel rather than a typical  $\beta$ -sandwich (Figure 4.12).

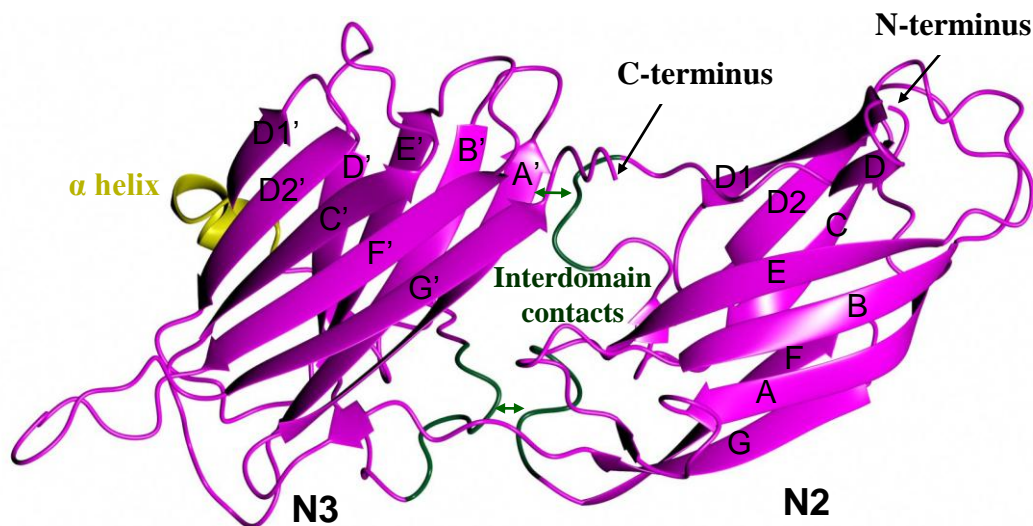


**Figure 4.12 Ribbon representation of the N2N3T structure.** The ribbon diagram depicts the two domains N2 and N3 with the  $\beta$ -strands labelled (N2 A-G and N3 A'-G'); adopted from Deivanayagam and colleagues, 2002). The single  $\alpha$ -helical feature (yellow), loops involved in inter-domain contacts (green) and both termini (arrows) are also shown.

The N2 domain adopts a fold with high resemblance to a constant domain (C-type) of IgG, albeit with two additional anti-parallel strands between the D and E strands. This altered version of a C-type IgG fold is called the DEv-IgG and has been identified in other proteins including ClfA (Deivanayagam et al., 2002). The asymmetric unit comprises a single copy of N2N3T with electron density for residues 189-194 and 504-506 absent, most likely due to the flexible nature of these regions. A surface representation of the N2N3T structure reveals a predominantly hydrophobic cleft formed in the space between the N2 and N3 domains, which is the predicted binding site for the Fg  $\gamma$  chain C-terminus (Figure 4.14). The solvent accessible surface area of N2N3T is 16033 Å<sup>2</sup> with 1024 Å<sup>2</sup> buried in the N2 and N3 interface. The main N2 and N3 inter-domain contacts originate from two regions. First, interactions between two protruding loops that connect strands D' and D1' within the N3 domain with the E and F strands of the N2 domain. Second, interactions of the A' strand of the N3 domain with a loop connecting the C and D strands, in the N2 domain (Figure 4.12).

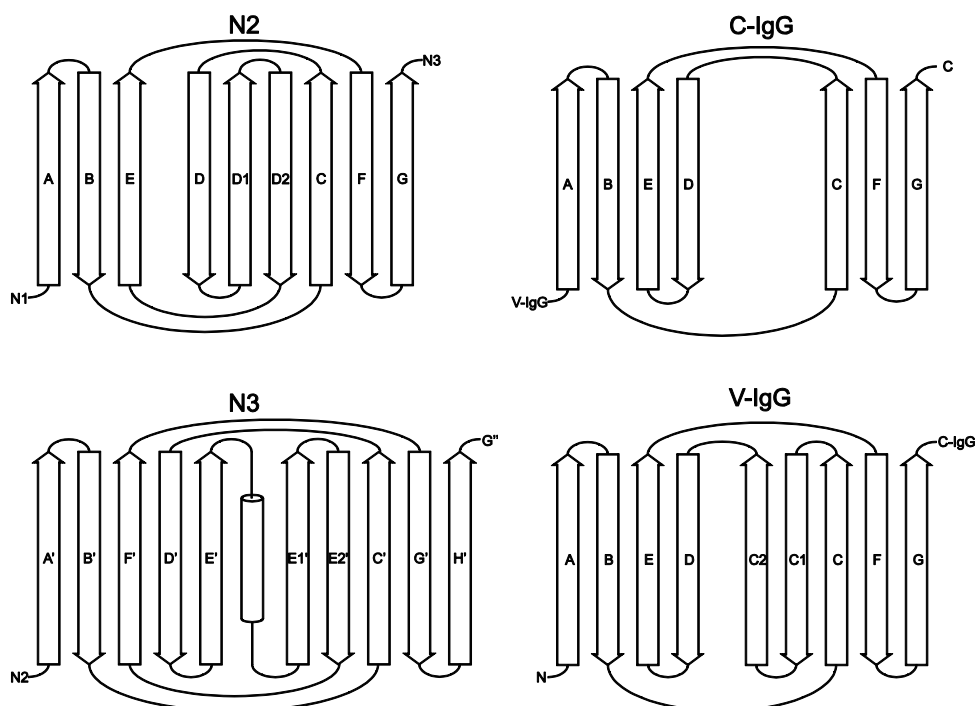


**Figure 4.13 The topology of the domain folds.** Schematic diagrams depict N2 and N3 domains with  $\beta$ -strands labelled A to G and A' to G', respectively. Neighbouring C- and N-terminal features are indicated. Diagrams of constant (C) and variable (V) IgG folds are also shown for comparison. Figure adapted from Deivanayagam and colleagues, 2002.

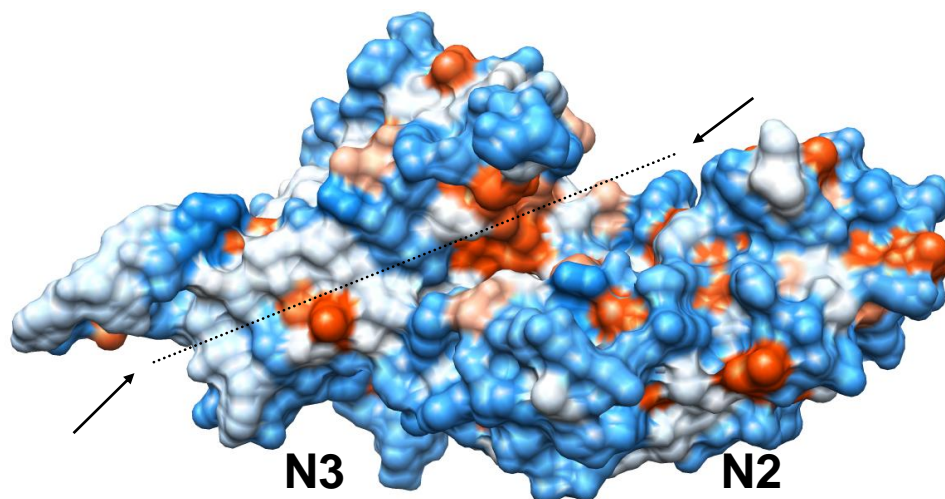


**Figure 4.14 Hydrophobicity surface representation of the N2N3T structure.** The surface model represents hydrophobicity of individual amino acids as determined by the Kyte-Doolittle scale (Kyte and Doolittle, 1982). The colours range from blue for the most hydrophilic residues such as Arg, through white to orange-red for the most hydrophobic residues such as Ile. The predominantly hydrophobic cleft between the N2 and N3 domains is indicated by arrows. The figure was generated using the UCSF Chimera molecular graphics software (Pettersen et al., 2004).

## 4.9 Crystal structure of the N2N3T-Fg1 complex

Crystals of the N2N3T-Fg1 complex did not grow in conditions identical or similar to that for N2N3T, thus trials and optimization procedures were repeated to obtain the optimum conditions (Section 2.8.9). Unlike apoN2N3T, the N2N3T-Fg1 complex crystallization resulted in a multitude of single crystals of various dimensions present within a single sitting drop. Diffraction properties of selected crystals were tested and 1.83Å was identified as the highest resolution (Figure 4.15). Crystallization, data collection and structure refinement were carried out as described in detail in Section 2.8.10. The refinement statistics are shown in Table 4.4.

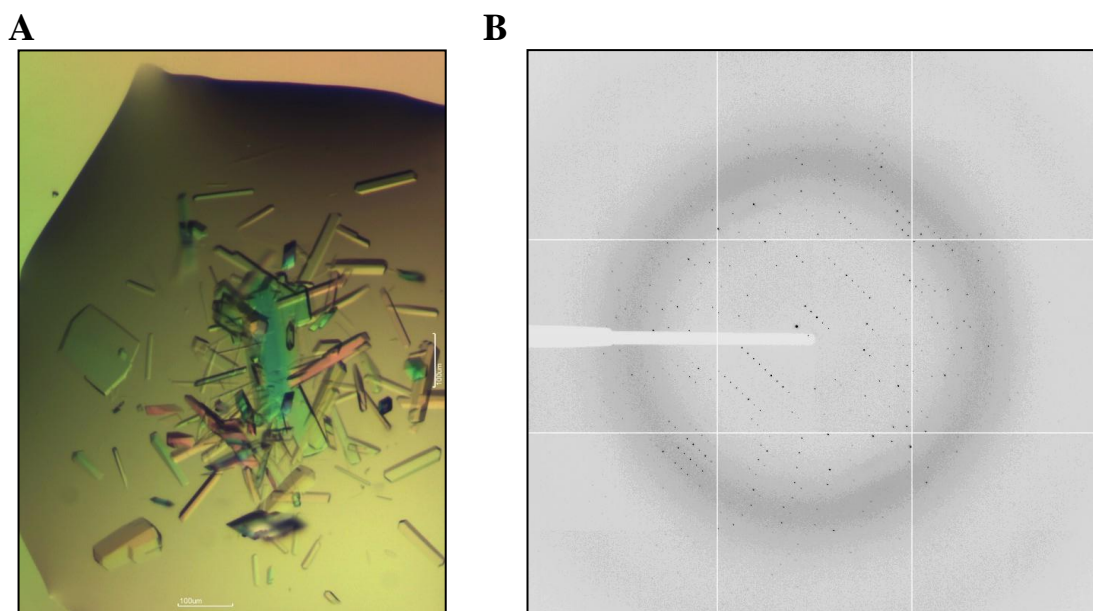


**Figure 4.15 Image of N2N3T-Fg1 crystals and corresponding diffraction pattern. (A)** N2N3T-Fg1 crystals in a sitting drop containing PEG mme 2000 (15% (w/v)), 0.2 M Ca Acetate, 50 mM Tris, 100 mM NaCl, isopropanol 10% (v/v), pH 7.4 **(B)** Diffraction pattern generated by a single crystal extracted from the drop.



Parameters	N2N3T-Fg1
Beamline	I041
Space group	P1
Cell dimensions a, b, c (Å)	37.5, 59.1, 73.5
Cell dimensions $\alpha$ , $\beta$ , $\gamma$ (°)	91.8, 98.1, 97.9
Wavelength (Å)	0.91731
Resolution (Å)	58.4-1.8
$R_{\text{merge}}$	0.07 (0.36)
$I/\sigma I$	9.1 (2.0)
Completeness	93.6 (67.4)
Redundancy	2.2 (2.2)
No. of unique reflections	51268
$R_{\text{factor}}$	0.194
$R_{\text{free}}$	0.247
Mean B-factor (Å <sup>2</sup> )	7.58
r.m.s.d. bond lengths (Å <sup>2</sup> )	0.02
r.m.s.d. bond angles (°)	1.95

**Table 4.4 Data collection and refinement statistics for the N2N3T-Fg1 complex.** Data for the highest resolution shell are shown in brackets where applicable.

The asymmetric unit comprises two copies of the N2N3T-Fg1 complex referred to as A:C and B:D, which are almost identical, as confirmed by the r.m.s.d. value of 0.33 Å between the A and B chains (secondary structure matching (s.s.m.) of 292 residues). Overall, the quality of the electron density map corresponding to the A:C complex was the marginally better of the two. As a result, a larger proportion of the molecule could be modelled into the A:C electron density map producing a more complete model of the protein complex. The calculated electron density maps contained clearly defined regions of electron density corresponding to 14 and 12 amino acid residues of the full length Fg1 chains C and D (17 residues), respectively (Figure 4.16). The electron density corresponding to the N-terminal residues 189-194 and C-terminal residues 504 and 505 of the A:C and B:D complexes was absent. Missing electron density within the N3 loop region that connects the F' and G' strands (residues 479-489), which is clearly visible in the N2N3T structure (Figure 4.17), suggests this region is flexible in solution and stabilised in N2N3T as a result of crystal packing.

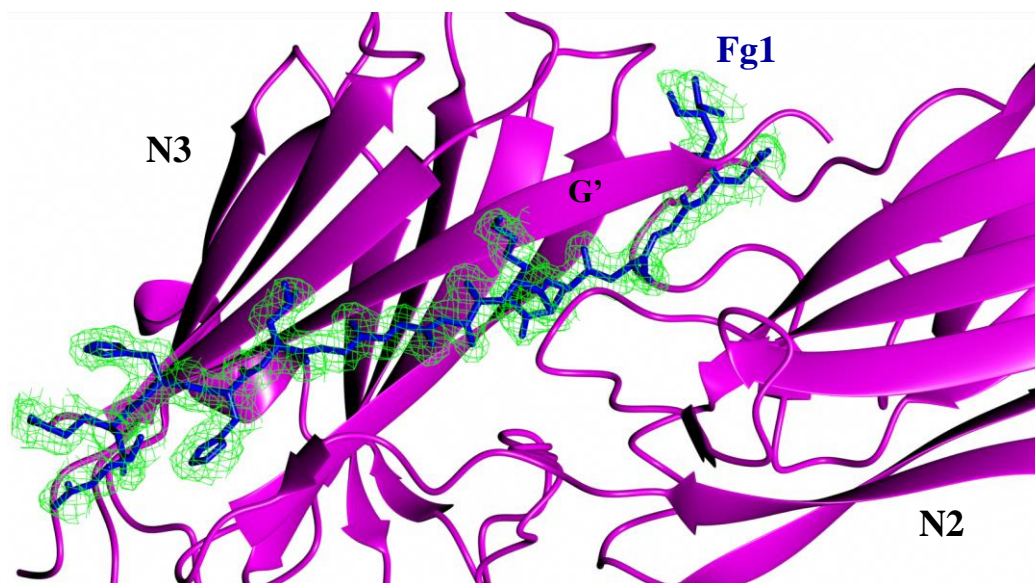


**Figure 4.16** Electron density map for Fg1. Cylindrical representation of Fg1 (blue), modelled into the corresponding electron density map (green) within the N2N3T (magenta)-Fg1 complex (chains A:C) contoured at  $1.5 \sigma$  of the Fg1 residues.

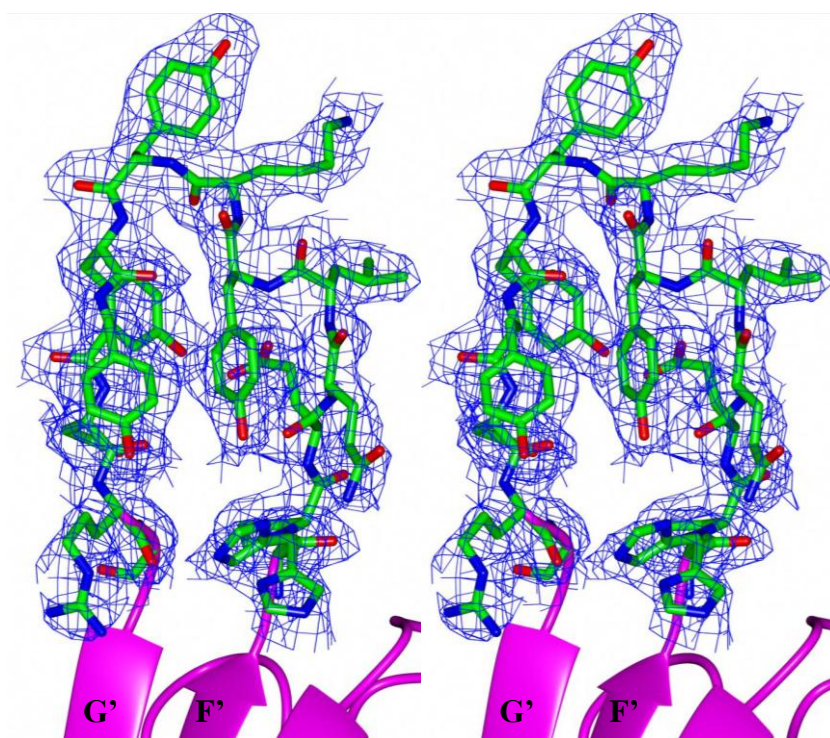


**Figure 4.17** Structure of the F'- G' loop. Stereo view of the N2N3T F'-G' loop region (cylinders; carbon – green, nitrogen – blue and oxygen – red), including electron density map (blue) contoured at  $1.5 \sigma$  of the N2N3T residues.

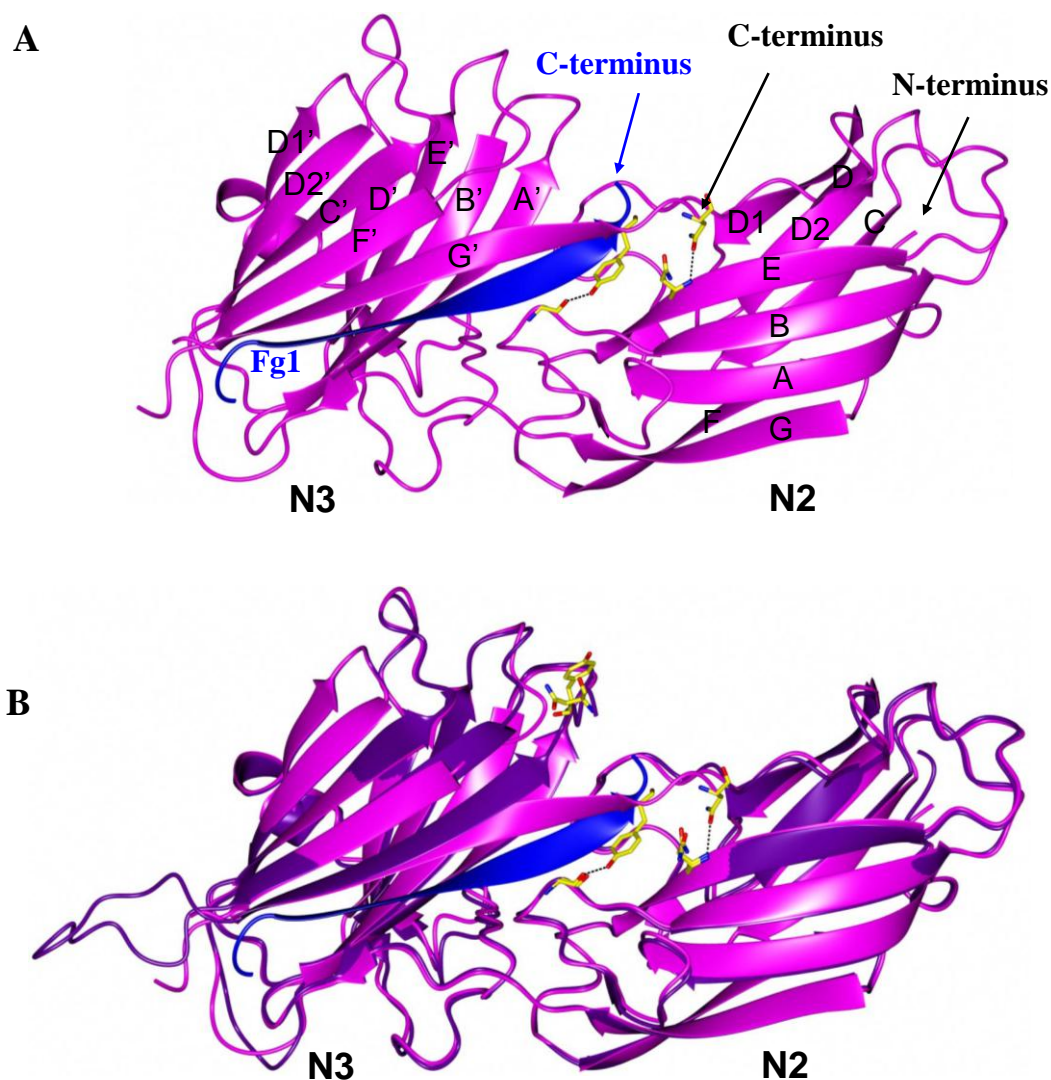


**Figure 4.18** Ribbon representation of the N2N3T-Fg1 complex. (A) The ribbon diagram depicts N2N3T (magenta) in complex with Fg1 (blue). The N- and C-termini are indicated. The G222-Y501 and N304-N503 hydrogen bonds (dotted line) are indicated. Residues G222, Y501, N304 and N503 are shown as yellow cylinders (B) Superposition of N2N3T (purple) and N2N3T-Fg1 (magenta) with the Fg1.

The Fg-binding site is located in the (mostly hydrophobic) cleft between N2 and N3 (Figure 4.19). Bound Fg1 forms an additional  $\beta$ -strand parallel to the G' strand in N3 (Figure 4.18A), presenting a classic example of a  $\beta$ -zipper interaction (Waksman and Hultgren, 2009). The N2N3-Fg1 interaction is dominated by backbone hydrogen bonds (Figure 4.20). Fg1 binding does not induce any large conformational changes in the structure of N2N3T as confirmed by the r.m.s.d. value of 0.81 Å (s.s.m. of 295 residues) between the free and Fg-bound N2N3T structures (Figure 4.18B) (Krissinel and Henrick, 2004). The only significant conformational change between the structures of unbound and Fg-bound N2N3T is the translocation of the N3-G' strand.



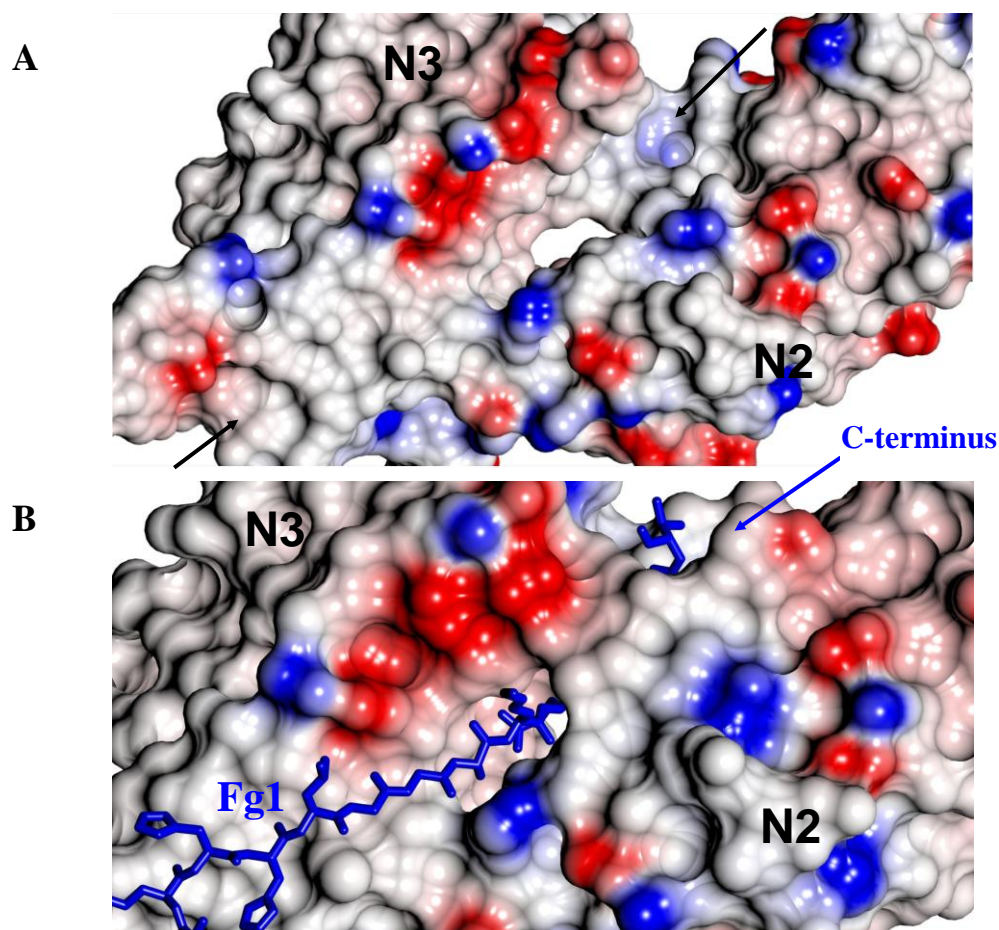


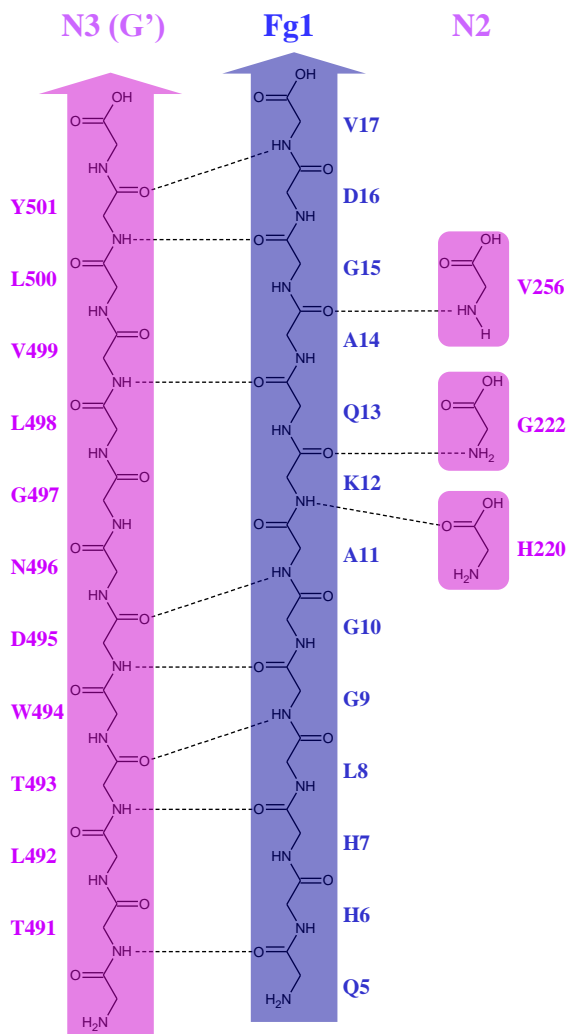
**Figure 4.19 Electrostatic surface representation of the Fg-binding site.** Comparison of the surface representations (blue - positive, red - negative and white - neutral) of (A) free and (B) Fg1-bound N2N3T shows the exposed (predominantly neutral) cleft (arrows) between the N2 and N3 domains and the formation of the tunnel-like feature upon Fg1 (blue cylinders) binding.

In the unbound N2N3T, the N3-G' strand aligns anti-parallel with the neighbouring F' strand. In the Fg-bound form, the strand 'wraps' around the last few C-terminal residues (Q13, A14 and G15) of Fg1 and interacts with the N2 domain forming a tunnel-like feature (Figure 4.18B and Figure 4.19B). Y501 and N503, which protrude away from the rest of the unbound N2N3T structure, are in close proximity to G222 and N304, respectively in bound N2N3T, forming a Y501-G222 and N503-N304 hydrogen bonds (Figure 4.18). The solvent accessible surface area of N2N3T that is buried as a result of Fg1 binding is  $796 \text{ \AA}^2$  and the combined buried surface of N2N3T and Fg1 within the N2N3T-Fg1 interface is  $1880 \text{ \AA}^2$  in the A:C chain interface (Krissinel and Henrick, 2007). Three Fg1 residues (Q13, A14 and G15) are buried within the tunnel-like feature upon binding and the Q13 appears to be the only Fg1 residue whose sidechain could potentially form hydrogen bond with S351 or I352.

A



B



C

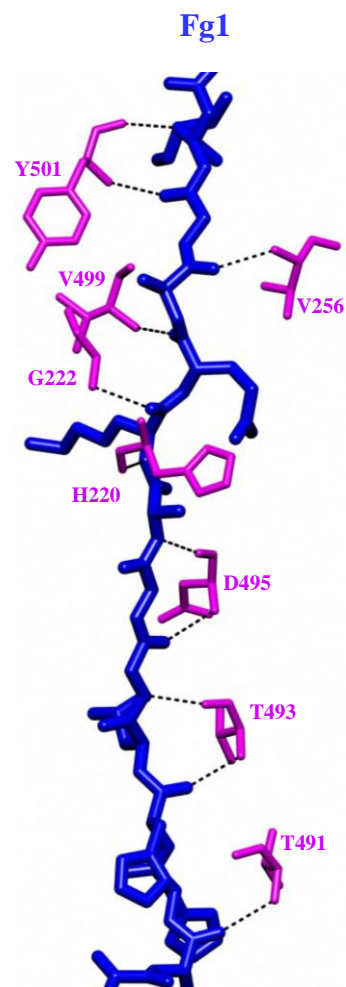


**Figure 4.20 Hydrogen bonds between Fg1 and N2N3T.** (A) Fg1 amino acid sequence including the N- (Ac) and C-terminal (NH<sub>2</sub>) caps. (B) Schematic diagram of the backbone hydrogen bonding interactions (dotted lines; max donor-acceptor distance - 3Å) between N2N3T (magenta) and Fg1 (blue). Figure generated using ChemSketch Freeware (ACD, 2006) (C) Representation of the relative positions of the Fg1 and N2N3T residues involved in the hydrogen binding.

## **4.10 Discussion**

### **4.10.1 N2N3T retains the Fg-binding ability of the full A-domain**

The preliminary SPR experiment indicated that N2N3 is the minimum region of FnBPA containing the full Fg-binding domain (Section 4.3). This was further confirmed when the  $K_d$  for the N2N3-Fg interaction, determined by ITC and SPR experiments (Section 4.4), agreed with published data regarding the Fg interaction with the A-domain (Wann et al., 2000). Other publications have reported affinities three orders of magnitude higher for the N2N3-Fg interaction measured by ELISA (Keane et al., 2007b; Loughman et al., 2008). It is difficult to reconcile such a discrepancy in the results. Nevertheless, given that ITC and SPR are more accurate techniques than ELISA, the values presented here are more likely to represent the actual  $K_d$ .

### **4.10.2 The putative latch strand is not required for Fg binding**

The importance of the putative latch strand (Figure 1.9) for Fg binding was also tested. The dock-lock-latch (SdrG) and latch-dock (ClfA) models (Section 1.6.3) for Fg binding were proposed based on the solved crystal structures of SdrG and ClfA in complex with Fg peptides (Ponnuraj et al., 2003; Bowden et al., 2008; Ganesh et al., 2008). Both models attributed an important stabilizing role to the latch strand in the SdrG/ClfA-Fg interactions. However, the SPR experiments presented here clearly showed that the affinities of N2N3 and N2N3T for FgD were very similar, demonstrating that the putative latch strand is not required for the rFnBPA-Fg interaction (Section 4.5).

### **4.10.3 Fg1 is a good model for the Fg-FnBPA interaction**

The high molecular mass of intact Fg (~ 340 kDa) renders it unsuitable for chemical shift perturbation assays. Fg1 (1730 Da), on the other hand, would be much more suitable for NMR experiments and, providing it retains the FnBPA-binding activity of intact Fg, it could be utilized as a model for the N2N3-Fg interaction. Results from both ITC and SPR experiments demonstrated that Fg1 confers most of the N2N3-binding activity (Section 4.6). However, the  $K_d$  for the N2N3-Fg1 interaction

is slightly higher compared with the  $K_d$  for the N2N3-Fg interaction. Moreover, the SPR data show that a high concentration of Fg1 is required to block the N2N3-Fg interaction (Figure 4.5). These results suggest that Fg1 might not contain the entire binding site of intact Fg. No such effects were reported in the original studies by Strong and colleagues, 1982 and Hawiger and colleagues, 1982, aimed at defining the ClfA binding site on intact Fg. However, this could have been due to the low sensitivity of the agglutination technique used (Strong et al., 1982; Hawiger et al., 1982). A later study by Wann and colleagues, 2000 reported that an excess concentration of Fg1 (100  $\mu$ M) was required for complete inhibition of the interactions between FnBPA or ClfA (1  $\mu$ M) and immobilized Fg using a solid-phase assay.

#### **4.10.4 Structural similarities of N2N3 from FnBPA, SdrG and ClfA**

As expected, the  $\beta$ -strand dominated crystal structure of N2N3T revealed striking similarities with structures of equivalent Fg-binding regions from SdrG and ClfA as confirmed by the r.m.s.d. values of 1.88 Å and 4.07 Å (s.s.m. of 270 SdrG and 261 ClfA residues), respectively (Figure 4.21). Joined by a short linker, both N2 and N3 domains have well defined folds resembling distorted  $\beta$ -barrels rather than a typical  $\beta$ -sandwich (Branden and Tooze, 1991). Similarly to SdrG and ClfA, the topology of N2 is another example of the novel DEv-IgG fold described previously (Section 4.8) (Deivanayagam et al., 2002). A cleft of mostly hydrophobic character forms in the space between the two domains.

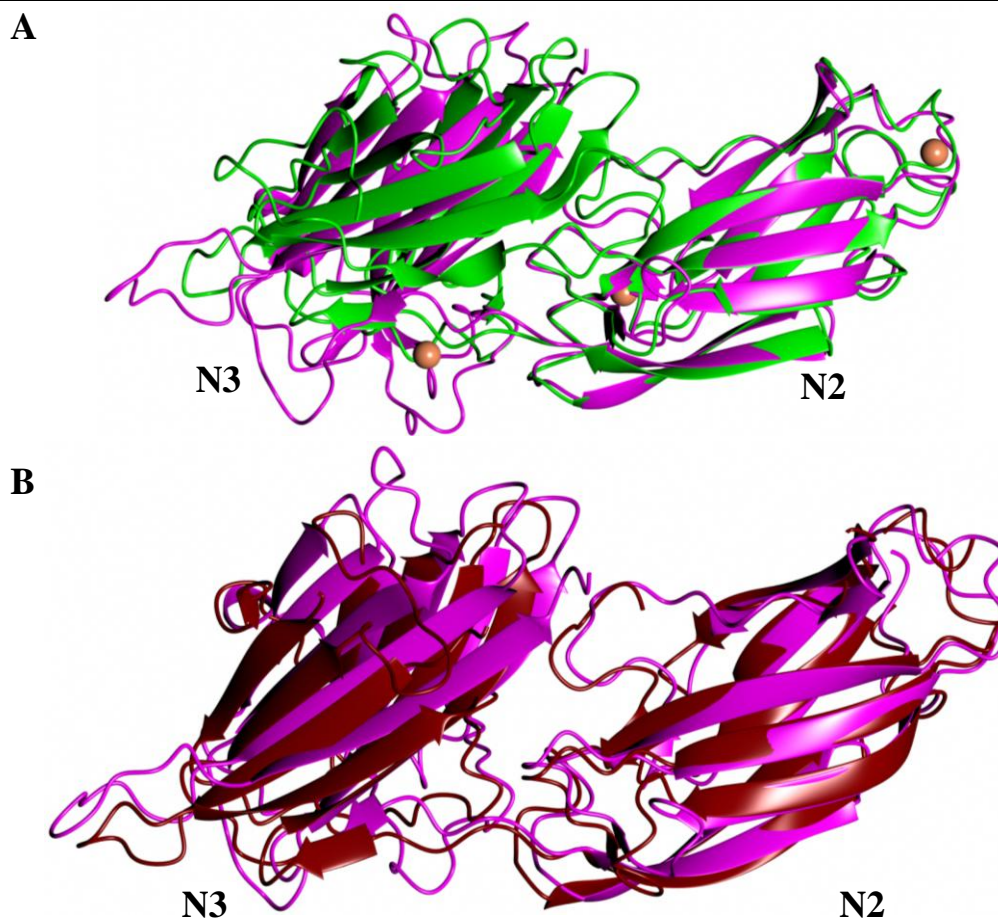


**Figure 4.21 Comparison of N2N3T with ClfA<sub>(229-545)</sub> and SdrG<sub>(273-597)</sub>.** (A) Ribbon representation of the N2N3T structure (magenta) with N2 domain superposed on those of ClfA<sub>(229-545)</sub> (PDB entry – 1N67) (Ganesh et al., 2008) (green; Ca<sup>2+</sup> ions are shown as light brown spheres) and (B) SdrG<sub>(273-597)</sub> (brown) (PDB entry – 1R19) (Ponnuraj et al., 2003).

#### 4.10.5 Fg1 binds N2N3 as a parallel $\beta$ -strand

The overall structure of the N2N3T-Fg1 complex is similar to that of the ClfA<sub>(229-545)</sub>-Fg1<sub>(D16A)</sub> complex, including the orientation of the bound Fg1; i.e. also parallel to the N3-G' strand. This is in contrast with the SdrG<sub>(273-597)</sub>-Fg $\beta$  peptide, where the Fg $\beta$  peptide aligns antiparallel to the N3-G' strand (Figure 4.22). Considering the structure of native Fg, it is plausible the difference in orientation of the bound Fg peptides arises due to steric reasons. Both ClfA and FnBPA bind to the C-terminal end of the Fg  $\gamma$  chain, while SdrG targets the region containing the thrombin cleavage site located near the N-terminus of the  $\beta$  chain (Figure 4.23).



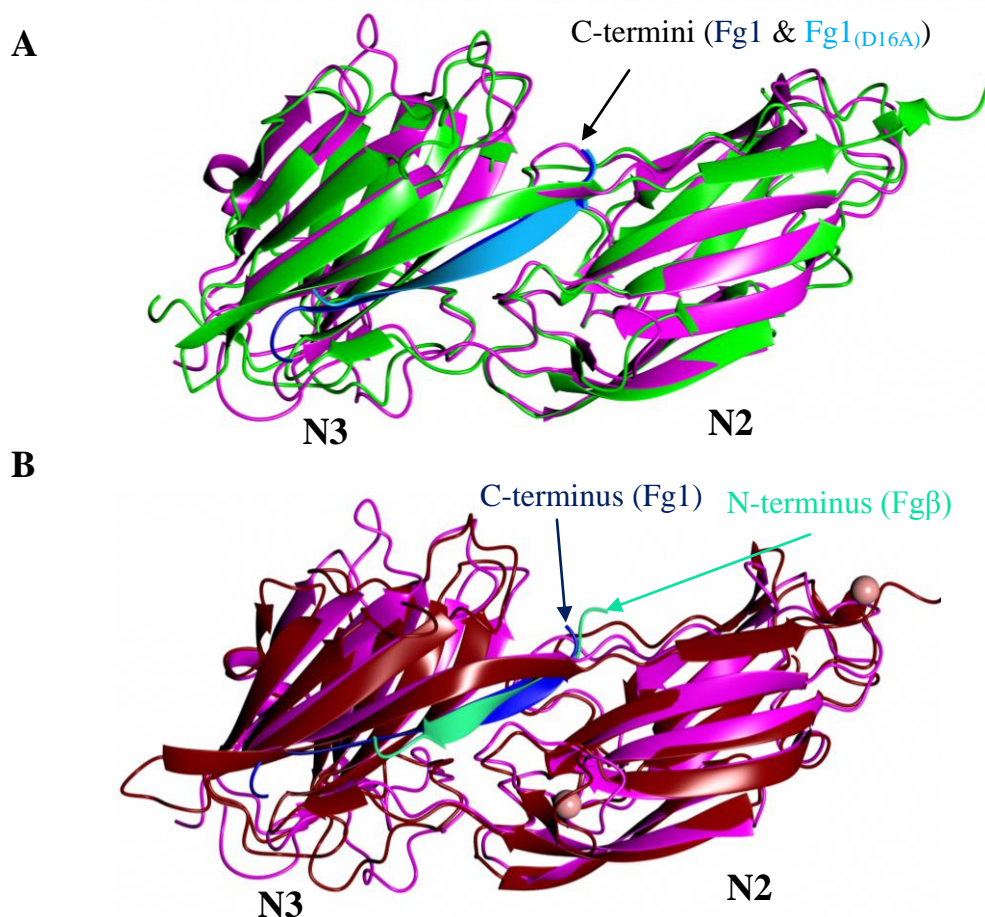


**Figure 4.22 Comparison of N2N3T-Fg1 with ClfA<sub>(229-545)</sub>-Fg1<sub>(D16A)</sub> and SdrG<sub>(273-597)</sub>-Fgβ.** Structural superposition of the N2 domain from the N2N3T (magenta)-Fg1 (blue) complex with (A) ClfA<sub>(229-545)</sub> (green)-Fg1<sub>(D16A)</sub> (cyan) (PDB entry 2VR3) and (B) SdrG<sub>(273-597)</sub> (brown)-Fgβ (light green) (PDB entry 1R17) using s.s.m. Orientations of the Fg peptides are also indicated.

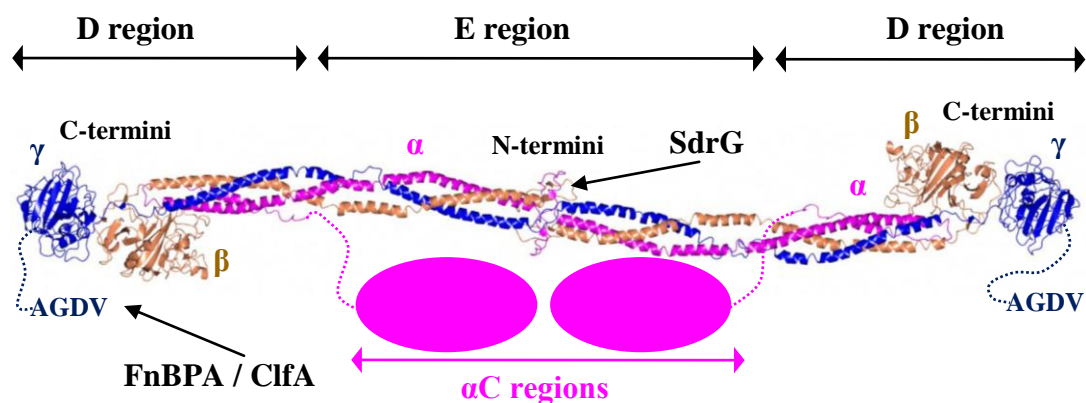


**Figure 4.23 The crystal structure of Fg.** Similar to Figure 1.4 but now showing the FnBPA, ClfA and SdrG binding sites as well (PDB entry - 3GHG) (Kollman et al., 2009).

#### 4.10.6 The N2N3T-Fg1 interface

A TROSY-HSQC experiment was utilized in  $^{15}\text{N}$ -N2N3/N2N3T-Fg1 binding studies, where spectra of  $^{15}\text{N}$ -N2N3/N2N3T were recorded with increasing concentrations of Fg1 and compared (Section 4.7.2). The large proportion of peaks undergoing a change in chemical shift indicates either formation of an extensive interface between N2N3 and Fg1 or significant conformational rearrangement of N2N3 upon Fg1 binding, or a mixture of both. A comparison of the N2N3T and N2N3T-Fg1 crystal structures revealed that the conformation of N2N3T remains almost identical, as confirmed by the r.m.s.d. value (0.81 Å, s.s.m. of 295 N2N3 residues) (Section 4.9; Figure 4.18). This is in contrast with ClfA, where the relative orientations of the N2 and N3 domains undergo a more substantial change upon Fg binding, demonstrated by the r.m.s.d. value (3.13 Å, s.s.m. of 142 N2 residues) (Figure 4.24). Interestingly, the ClfA latch strand in apoClfA folds back, forming an antiparallel  $\beta$ -strand along the N3-G' strand.

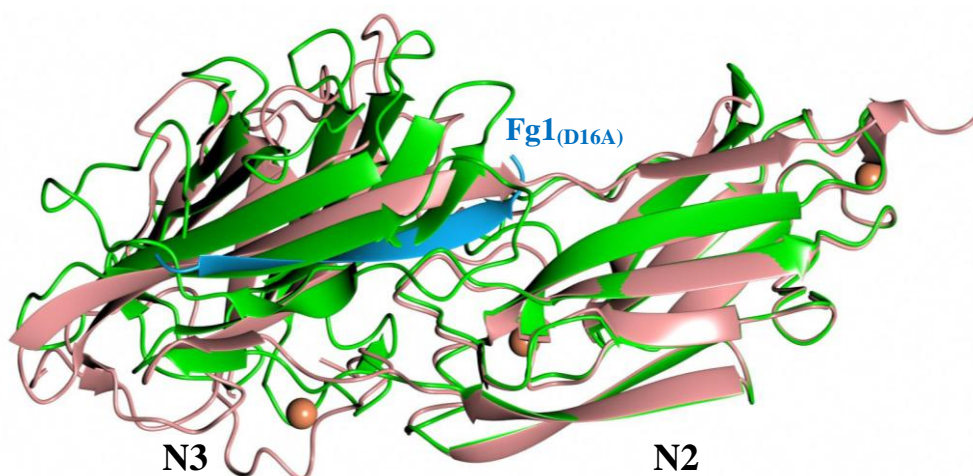


**Figure 4.24 Comparison of the ClfA<sub>(229-545)</sub> and ClfA<sub>(229-545)</sub>-Fg1<sub>(D16A)</sub> structures.** Structural superposition of the N2 domain from the ClfA<sub>(229-545)</sub> (green)-Fg1<sub>(D16A)</sub> (light blue) (PDB entry 2VR3) and ClfA<sub>(229-545)</sub> (light pink; Ca<sup>2+</sup> - brown spheres) (PDB entry 1N67) using s.s.m (Krissinel and Henrick, 2004).

The N2N3T-Fg1 interaction exhibits characteristics typical of a  $\beta$ -zipper, an efficient binding mechanism common in disordered proteins regions and peptides (Derrick and Wigley, 1992; Schwarz-Linek et al., 2003; Waksman and Hultgren, 2009). Here, Fg1 aligns along the N3-G' strand augmenting the  $\beta$ -sheet (Figure 4.18). N2N3T contains a pair of  $\beta$ -sandwich-like folds providing four potential sites for  $\beta$ -zipper binding. However, all but the actual Fg1 binding site, formed by  $\beta$ -strands G' and

A', appear to have some level of edge-strand protection. Exposed  $\beta$ -sheet edges are susceptible to a backbone dominated interaction with another  $\beta$ -strand, often leading to edge-to-edge aggregation (Siepen et al., 2003). Consequently, a variety of edge-strand protection mechanisms are present within protein folds. The main strategy includes an inward-pointing, long and charged sidechain (usually lysine), and a  $\beta$ -bulge or proline present in the edge-strands (Richardson and Richardson, 2002; Richardson et al., 1978). Figure 4.25 shows the edge-strand protection mechanisms adopted by N2N3, leaving only one site suitable for  $\beta$ -zipper binding.

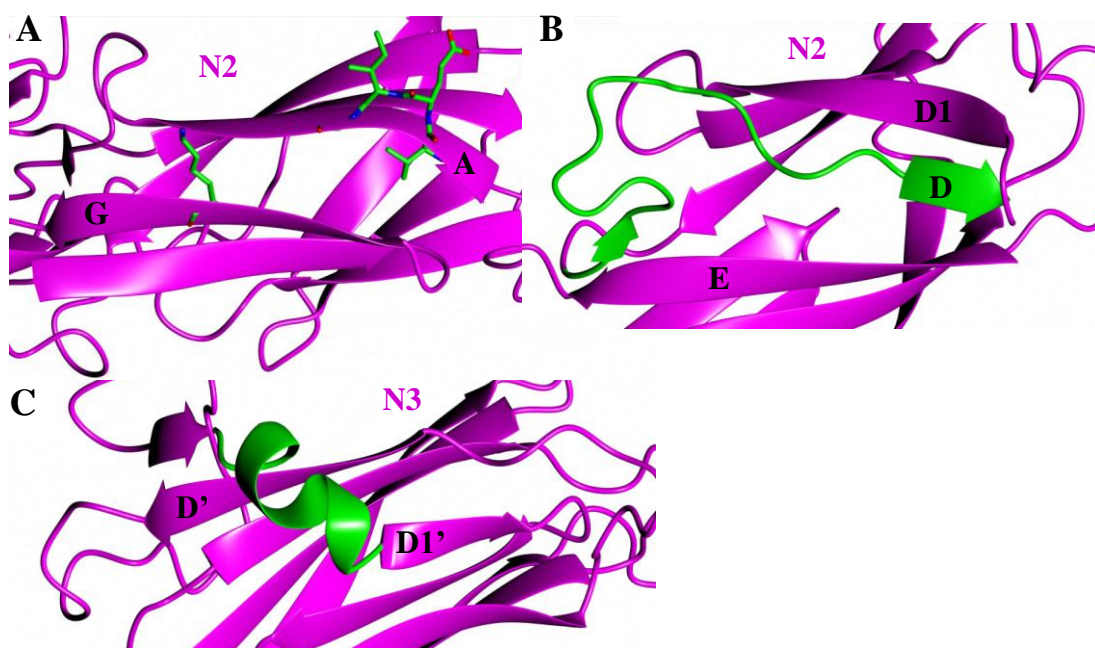


**Figure 4.25 N2N3 edge-strand protection.** Ribbon representation of the three N2N3 regions protected against edge-to-edge interaction. (A) Inward-pointing Lys residue (green sticks) and a  $\beta$ -bulge (green sticks) are indicated (N2). (B) Ribbon representation of the short D strand and a long loop (green) blocking the access to the D1 and E edge-strands (N2). (C) Ribbon representation of the short  $\alpha$ -helical feature (green) blocking the access to the edge strands D' and D1' (N3).

#### 4.10.7 The putative latch strand ‘structural flexibility’ hypothesis

An interesting observation was made upon comparison of the NMR spectra of N2N3 +/- Fg1 and N2N3T +/- Fg1. The spectrum of N2N3T contained several extra peaks compared with N2N3 (Section 4.7.2). Considering the only difference between the two proteins is the six missing residues (N506-N511), which form the majority of the putative latch strand (Figure 1.9), it can be presumed that the putative latch affects the NMR signal of some residues in N2N3. The most likely explanation involves the putative latch strand remaining in exchange between multiple

conformational states, leading to weakened NMR signals from the residues within the putative latch strand and those that interact with the putative latch. The fact that the spectrum of N2N3-Fg1 has more peaks than that of N2N3 indicates that the putative latch strand residues may be somewhat stabilised on Fg1 binding. Also, the spectrum of N2N3-Fg1 has a few additional peaks compared with the N2N3T-Fg1 spectrum. Those additional peaks could correspond to the stabilised N2N3 N506-N511 residues missing in N2N3T. Although some of these NMR data indicate the putative latch strand region might be ordered in Fg-bound N2N3, both the SPR and crystallization/crystallographic data suggest this region is not involved in Fg binding, might not fully augment the N2  $\beta$ -sheet and could remain mostly disordered even in Fg-bound N2N3. The electron density corresponding to the N3 C-terminal residues 504 and 505 was absent from the electron density maps of N2N3T and N2N3T-Fg1, suggesting this region might be disordered. The potential structural flexibility of the putative latch region would also provide an explanation for the inability of N2N3 and N2N3-Fg1 to produce stable and diffracting crystals, unlike N2N3T and N2N3T-Fg1 which crystallized readily in multiple solution conditions.

#### **4.10.8 The minimum Fg-binding region**

The N2N3T and N2N3T-Fg1 structures (Figure 4.12 and Figure 4.18) revealed that the first N-terminal residue contributing to the formation of the N2  $\beta$ -sheet appears to be K200. Electron density corresponding to the residues 189-194 is missing and the region 195-199 is not part of any secondary structure feature. It is probable that the entire region consisting of residues 189-199 is unstructured in solution and could form the C-terminus of the N1 domain. Moreover, the structure of N2N3T-Fg1 reveals the most C-terminal residue involved in Fg binding is probably N503. As a result, the 'latch' strand might not be an appropriate name for the 501-511 region, and it probably should not be regarded as a part of the N3 domain. The residues K200 and G503 could potentially form the N- and C-terminal boundaries of N2N3, respectively, thus rFnBPA<sub>(200-503)</sub> might be the minimum region conferring Fg-binding activity similar to that of intact FnBPA.

## 5 Does AF1 form a ternary complex with Fn and Fg?

### 5.1 Introduction

The bacterial protein FnBPA interacts with multiple Fn molecules (Kuusela, 1978; Froman et al., 1987). The Fn-binding site was defined as a 363 residue region comprising 11 homologous intrinsically disordered repeats (Figure 1.8) (Massey et al., 2001; Bingham et al., 2008; Meenan et al., 2007; Foster and Hook, 1998). Recently, the presence of a single Fg-binding site within the multifunctional FnBPA and its involvement in the aetiology of IE have also been demonstrated (Wann et al., 2000; Piroth et al., 2008; Que et al., 2005). The Fg-binding activity was assigned to the N-terminal A-domain (Wann et al., 2000; Fitzgerald and et al, 2006; Piroth et al., 2008). The results presented in Chapter 4 confirmed N2N3 as the minimal region conferring native-like Fg-binding ability. Consequently, FnBPA has the potential to bind Fg and Fn, however, to date there is no evidence for the existence of such a complex. As both Fg and Fn are dimeric and intact FnBPA contains eleven FnBRs, there is also the potential for the formation of a vast multi-protein complex (Figure 5.1); the physiological relevance of this is unknown. Here the question is asked whether Fg and Fn bind simultaneously to FnBPA, and whether there is cooperativity in FnBPA binding to Fg and Fn (native Fn and Fg do not interact with each other). As the Fg-binding site and the most N-terminal FnBR (FnBPA1) are in close proximity in FnBPA, there is the potential for positive or negative cooperativity, either through conformational changes or steric hindrance.

### 5.2 Aims

The primary aims were to test whether Fg and Fn can bind AF1 simultaneously to form a ternary complex and to investigate the positive/negative putative cooperativity between the Fg- and Fn-binding sites. AF1 (contains N2N3 and FnBPA1) (Table 3.1 and Figure 5.1) was utilized, as a model of FnBPA.

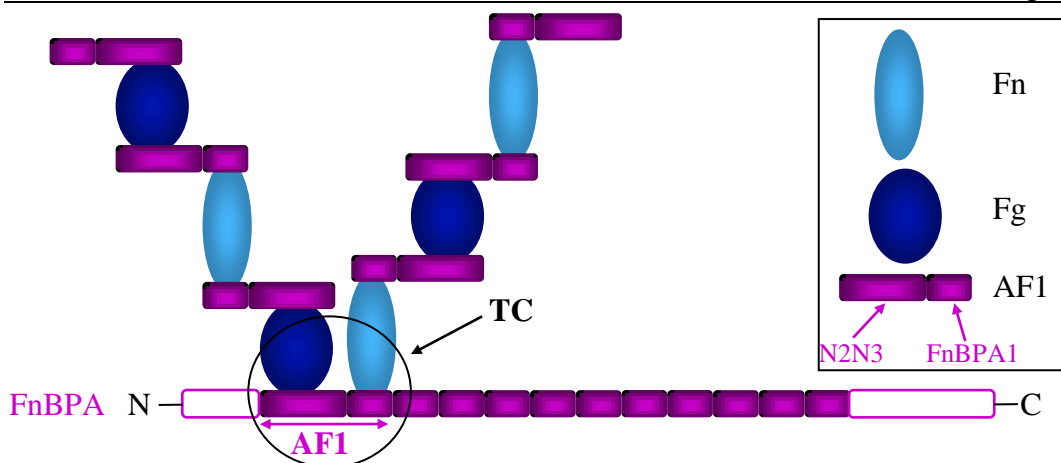


**Figure 5.1 Schematic diagram of the potential Fn-FnBPA-Fg complex.** For simplicity only AF1 and three molecules of Fn and Fg are shown in the multiprotein complex. The Fn-AF1-Fg ternary complex is highlighted (TC). The molecule sizes are not to scale.

### 5.3 AF1 interacts individually with Fn and Fg

#### 5.3.1 Determination of the $K_d$ for the AF1-NTD interaction

Initially, the affinity of the interaction between AF1 and NTD was determined using SPR. NTD was immobilized on the chip, and AF1 was used as the analyte (Figure 5.2). The character of the sensorgrams precluded the determination of a reliable dissociation constant by evaluation of kinetics or equilibrium binding. The main issue stems from the dual character of the association phase which does not reach the steady state, an effect evident primarily at higher analyte concentrations. This is probably a consequence of an additional weaker interaction of AF1 with ligands whose activity was compromised by the immobilization process.

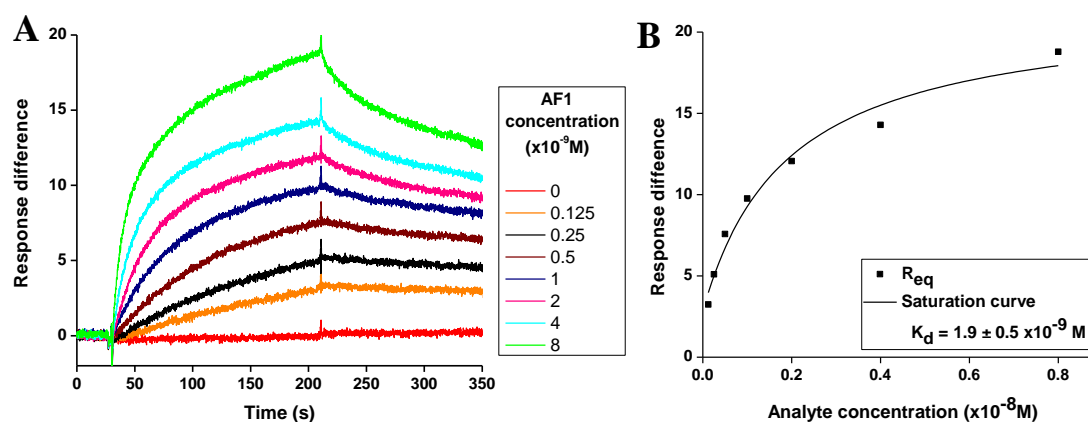


**Figure 5.2 Determination of the  $K_d$  for the NTD-AF1 interaction.** (A) Representative SPR sensorgrams show responses generated upon interaction of immobilized NTD with increasing concentrations of AF1. (B) Affinity evaluation using equilibrium analysis.



While the kinetic evaluation could not be used as the  $k_a$  ( $1.3 \times 10^7 \pm 2.3 \times 10^4 \text{ M}^{-1}\text{s}^{-1}$ ) was outside the measurable limit of the T100 instrument (Section 1.7.2.4), the analysis of equilibrium binding lead to a more reasonable  $K_d$  of  $1.9 \pm 0.5 \text{ nM}$ , albeit with high error (27%). As mentioned above, the most likely source of error relates to the fact that none of the responses reach  $R_{eq}$ . In order to confirm the results of the SPR experiment, and to determine a more reliable  $K_d$  for the AF1-NTD interaction, an ITC experiment was performed.

The ITC experiment involved titration of AF1 (20  $\mu\text{M}$ ) within the syringe into the cell with NTD (2  $\mu\text{M}$ ) at 25°C. Details of the experimental set-up are in Section 1.7.2.2. The ‘single set of sites’ model was utilized to fit the binding isotherm and obtain a  $K_d$  of  $0.7 \pm 0.2 \text{ nM}$  (Figure 5.3). Specific thermodynamic parameters for the interaction are summarised in Table 5.1. The steep transition of the binding curve precludes a reliable fit of the ITC data, resulting in a relatively high error (28%). Nevertheless, the final  $K_d$  value is similar to that obtained by SPR (Figure 5.2) and also to the  $K_d$  value of  $4.8 \pm 0.6 \text{ nM}$  for the FnBPA1-NTD interaction obtained previously (Meenan et al., 2007). As a result it can be concluded that AF1 retains the NTD-binding ability of FnBPA1, and is not affected by the presence of N2N3.

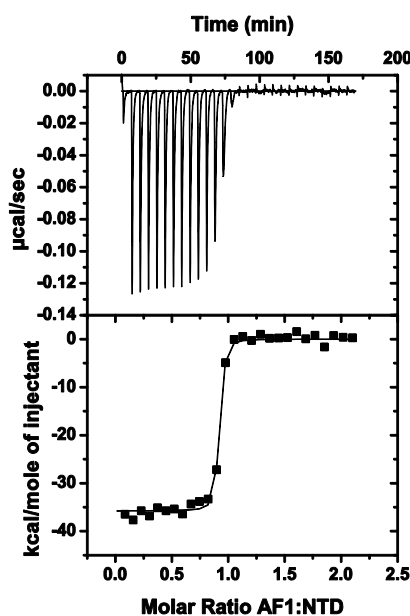


**Figure 5.3 Determination of the  $K_d$  for the AF1-NTD interaction.** Peaks in the upper panel represent heats generated upon ligand injection. Measured heats were integrated and the best fit was calculated based on the ‘single set of sites’ model in Origin 7 (Microcal), resulting in an ITC binding isotherm (lower panel). Thermodynamic parameters are listed in Table 5.1.

### 5.3.2 Determination of the $K_d$ for the AF1-Fn interaction

Following the characterization of the AF1-NTD interaction by ITC, it was essential to show that AF1 can interact with intact Fn. The  $K_d$  for the AF1-Fn interaction was determined by SPR where an AF1-coated sensor chip was exposed to increasing concentrations of Fn, as described in Section 2.8.2.4 (Figure 5.4). The rate constants ( $k_a$   $2.8 \times 10^5 \pm 1.7 \times 10^3 \text{ M}^{-1}\text{s}^{-1}$  and  $k_d$   $2.7 \times 10^{-4} \pm 8.6 \times 10^{-7} \text{ s}^{-1}$ ) for the interaction were determined and utilized to derive a  $K_d$  of  $1.0 \pm 0.1 \text{ nM}$ . Although the  $K_d$  is almost identical to that obtained for NTD binding ( $1.9 \pm 0.5 \text{ nM}$ ), the  $k_a$  is significantly lower than the  $k_a$  for the AF1-NTD interaction ( $1.3 \times 10^7 \pm 2.3 \times 10^4 \text{ M}^{-1}\text{s}^{-1}$ ). This is consistent with the results from previous studies, which revealed that NTD is probably occluded in intact Fn (Erickson and Carrell, 1983; Johnson et al., 1999) (Section 1.5.2).

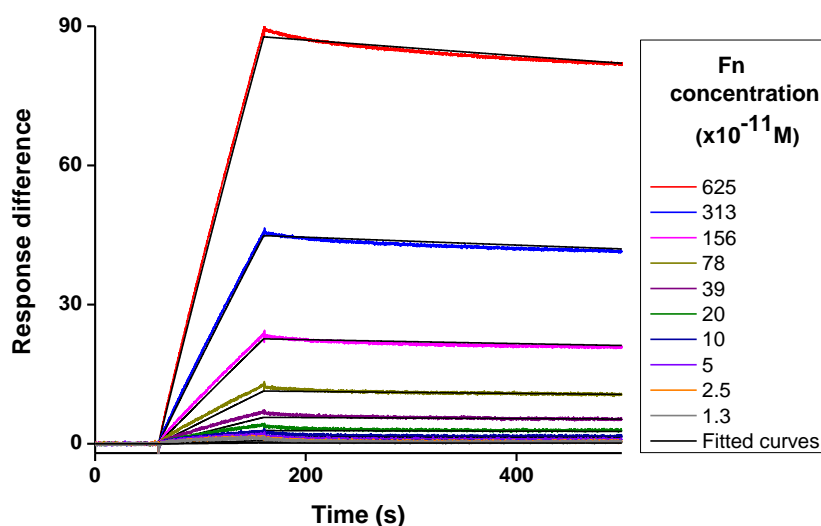


**Figure 5.4 Determination of the  $K_d$  for the AF1-Fn interaction.** Representative sensorgrams generated on exposure of an AF1-coated sensor chip to increasing concentrations of Fn. The curves fitted based on a 1:1 binding model also shown (black).

### 5.3.3 AF1 binding to Fg

The  $K_d$  for the AF1-Fg1 interaction was measured by ITC, where Fg1 (2.68 mM) within the syringe was titrated into AF1 (273  $\mu\text{M}$ ) in the cell (Figure 5.5A). The ‘single set of sites’ model was used to fit the binding isotherm and the  $K_d$  was  $25.0 \pm 1.0 \mu\text{M}$ . In a second experiment, AF1 (50  $\mu\text{M}$ ) in the cell was titrated with intact Fg (250  $\mu\text{M}$ ) in the syringe and the  $K_d$  was  $1.1 \pm 0.0 \mu\text{M}$  (Figure 5.5B). Both  $K_d$ s are



similar to those for the N2N3-Fg1/Fg interactions (Sections 4.4 and 4.6) demonstrating that AF1, like N2N3, retains Fg-binding ability and that adding FnBPA1 to the construct does not interfere with Fg binding. The AF1:Fg binding stoichiometry of 2:1 confirms the dimeric nature of Fg (Table 5.1). The endothermic character and significantly higher heats of dilution for the blank titration of Fg compared with those for the Fg1 titration is most likely a consequence of the high viscosity of the Fg solution (Figure 5.5B).

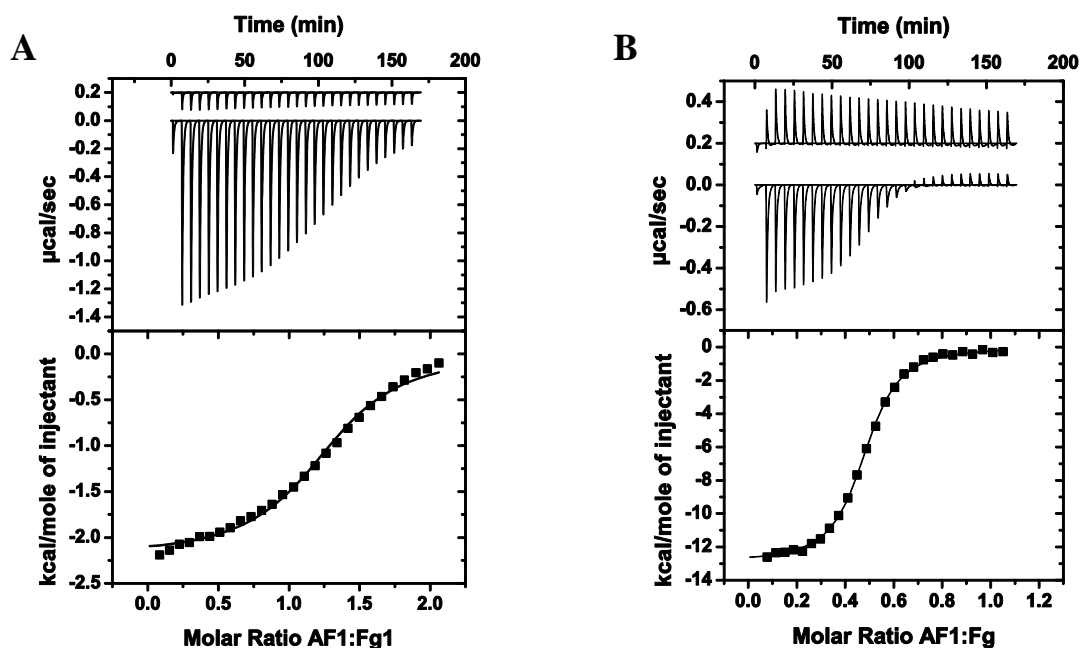


**Figure 5.5 Determination of the  $K_d$  for the AF1-Fg1 and AF1-Fg interactions.** ITC binding isotherms for the titrations of AF1 with (A) Fg1 and (B) native Fg. Peaks in the upper panel represent heats generated on ligand injection. Both experiments contain a blank titration of the ligand into the cell buffer which was used to evaluate the heats of dilution. Measured heats were integrated, heats of dilution subtracted, and the best fit was calculated based on the ‘single set of sites’ model in Microcal Origin 7 software, as shown in the lower panel. Thermodynamic parameters are listed in Table 5.1.

An SPR experiment to determine the  $K_d$  for the AF1-FgD interaction was also performed (Figure 5.6). A  $K_d$  of  $1.5 \pm 0.0 \mu\text{M}$ , determined by equilibrium analysis, is consistent with the  $K_d$  for the N2N3-FgD interaction ( $1.48 \pm 0.1 \mu\text{M}$ ) (Section 4.5). Also, the character of the individual sensorgrams, including the association and dissociation phases, resembled those for the N2N3-FgD interaction.

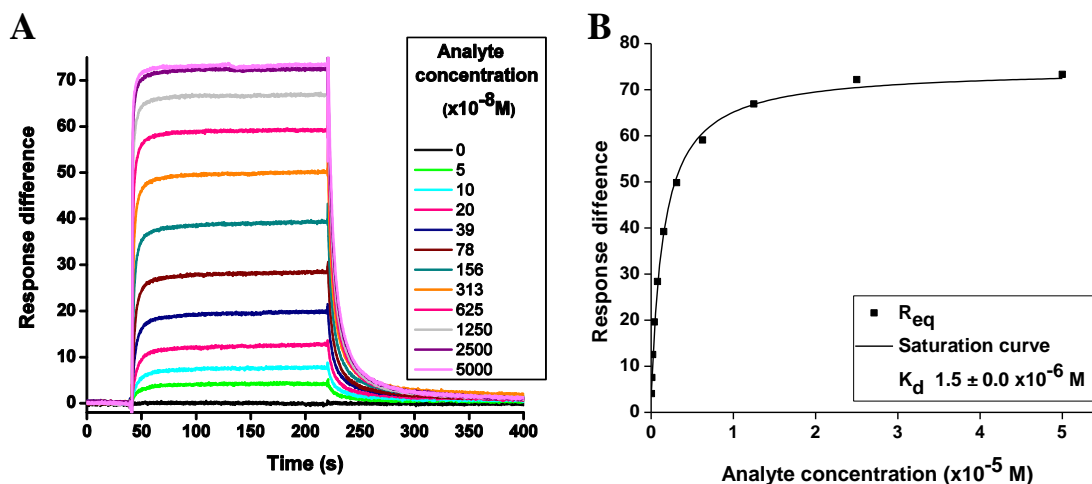


**Figure 5.6** Determination of the  $K_d$  for the AF1-FgD interaction. (A) Representative SPR sensorgrams show responses generated upon interaction of immobilized FgD with increasing concentrations of AF1. (B) Affinity evaluation using equilibrium analysis.

Interaction	$K_d$	$\Delta H /$ kcal mol $^{-1}$	$\Delta S /$ cal mol $^{-1}$ K $^{-1}$	n	Technique
AF1-NTD	$1.9 \pm 0.5$ nM	-	-	-	SPR
AF1-NTD	$0.7 \pm 0.2$ nM	$-35.77 \pm 0.3$	-78.10	0.89	ITC
AF1-Fn	$1.0 \pm 0.1$ nM	-	-	-	SPR
AF1-Fg1	$25.0 \pm 1.0$ $\mu$ M	$-2.7 \pm 0.01$	11.90	1.36	ITC
AF1-FgD	$1.5 \pm 0.0$ $\mu$ M	-	-	-	SPR
AF1-Fg	$1.1 \pm 0.0$ $\mu$ M	$-6.11 \pm 0.02$	6.70	2.11	ITC

**Table 5.1** Summary of kinetic and thermodynamic parameters for the interactions with AF1. The table includes  $K_d$ s determined by either ITC or SPR. Values for enthalpy ( $\Delta H$ ) and entropy change ( $\Delta S$ ) and stoichiometry (n) are listed where applicable.

#### 5.4 Analysis of AF1 by NMR spectroscopy.

The following NMR experiment was performed for preliminary structural characterization of AF1 and to test whether NMR spectroscopy would be a suitable technique for studying the putative cooperativity of Fn and Fg binding. A 2D  $^1\text{H}^{15}\text{N}$  TROSY-HSQC spectrum (Pervushin et al., 1997) of uniformly  $^{15}\text{N}$ -labelled AF1 was acquired (Figure 5.7). The spectrum is dominated by several high intensity peaks within a narrow region of chemical shift in the  $^1\text{H}$  dimension (7.6 – 8.6 ppm); these peaks are absent from the TROSY-HSQC N2N3 spectrum (Figure 5.7A) and are

likely to correspond to the intrinsically disordered FnBPA1 region of AF1. This was subsequently confirmed by comparing the spectrum with a 2D  $^1\text{H}^{15}\text{N}$  TROSY-HSQC spectrum of uniformly  $^{15}\text{N}$ -labelled FnBPA1, acquired under similar conditions and with identical acquisition parameters. A comparison of the two spectra at high contour level (Figure 5.7B) highlights the similarity of chemical shifts between AF1 and FnBPA1. The low intensity of the N2N3 peaks in the spectrum of AF1 (Figure 5.7A) suggest that NMR spectroscopy might not be suitable for studying the putative cooperativity in Fg- and Fn-binding to AF1.

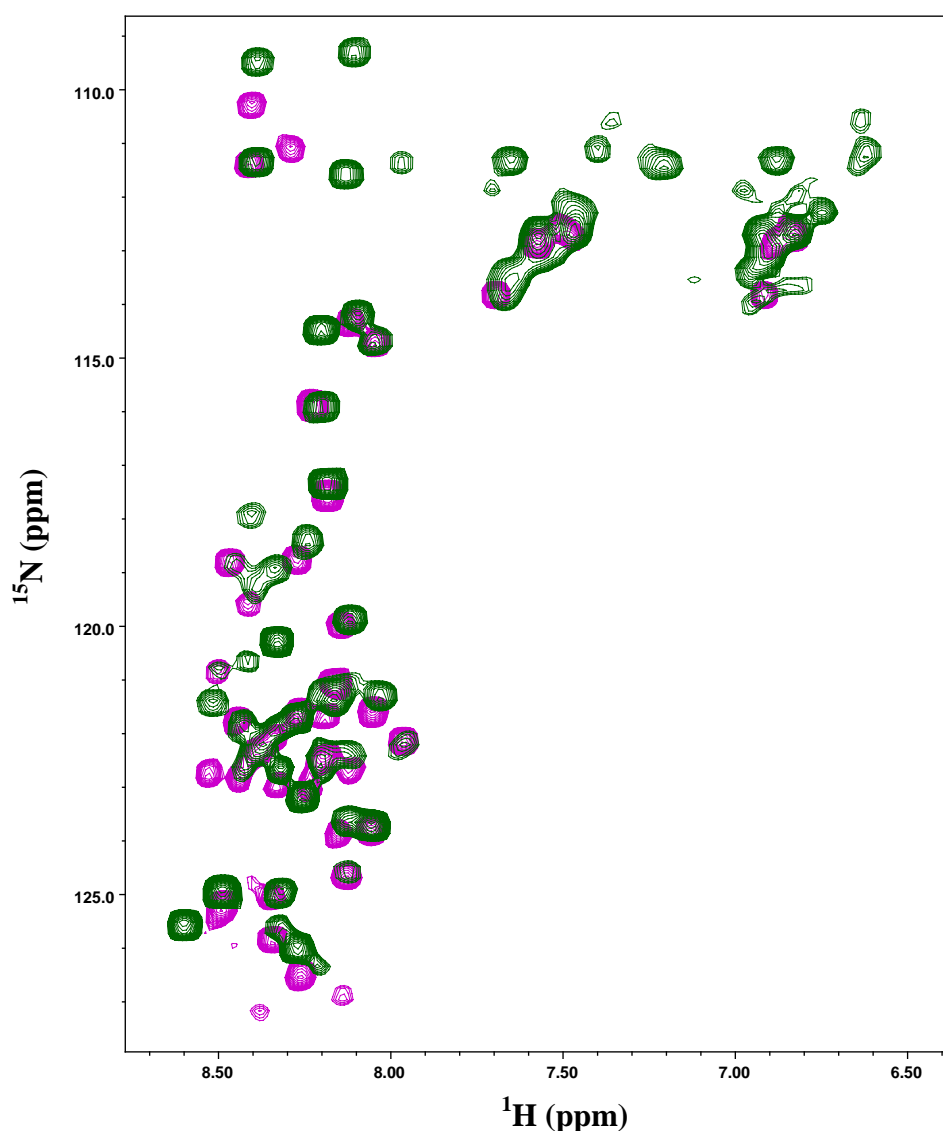


**Figure 5.7** 2D  $^1\text{H}^{15}\text{N}$  TROSY-HSQC spectra of  $^{15}\text{N}$ -AF1 (green) and  $^{15}\text{N}$ -FnBPA1 (magenta). Spectra were acquired on a 700 MHz spectrometer (Section 2.8.1) at 310 K and pH 7.4. Data were processed using NMRPipe (Delaglio et al., 1995) and analysed using NMRView (Johnson and Blevins, 1994). Spectra were overlaid at similar contour levels.

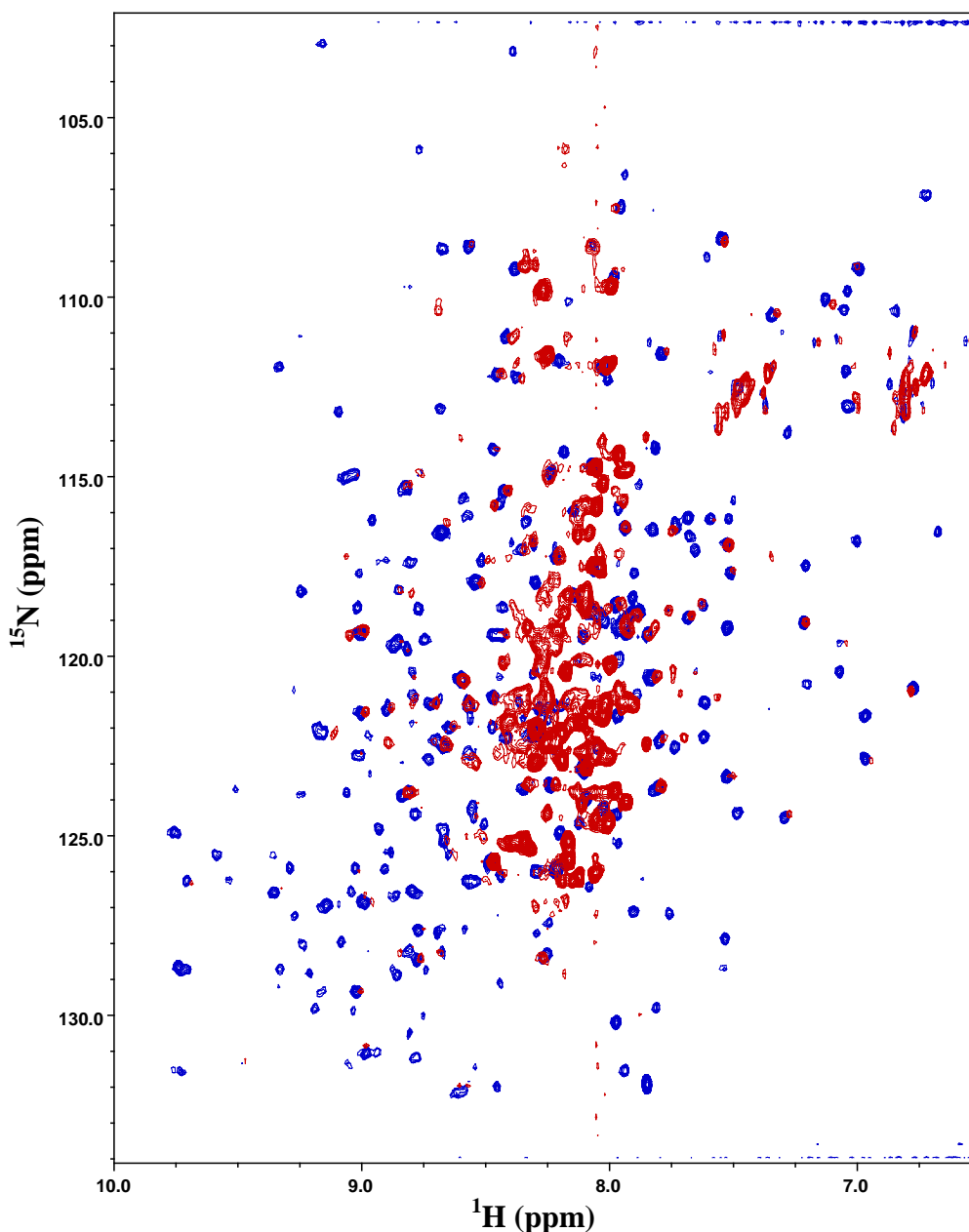


**Figure 5.8** 2D  $^1\text{H}^{15}\text{N}$  TROSY-HSQC spectra of  $^{15}\text{N}$ -AF1 (red) and  $^{15}\text{N}$ -N2N3T (blue). Spectra were acquired on a 700 MHz spectrometer (Section 2.8.1) at 310 K and pH 7.4. Data were processed using NMRPipe (Delaglio et al., 1995) and analysed using NMRView (Johnson and Blevins, 1994). Spectra were overlaid at similar contour levels.

## 5.5 Can NTD and FgD/Fg/Fg1 bind AF1 simultaneously to form ternary complexes?

### 5.5.1 Determination of the $K_d$ s for the FgD-AF1+/-NTD interactions

To test the effects of NTD on the AF1-FgD interaction, increasing concentrations of AF1 or the AF1-NTD complex, were flowed over an FgD-coated sensor chip (Figure 5.9). Due to the very fast character of both the association and dissociation rates,

analysis of the equilibrium binding was used for evaluation. Comparison of the two  $K_d$ s revealed they were very similar;  $1.6 \pm 0.1 \mu\text{M}$  and  $7.2 \pm 0.5 \mu\text{M}$  in the absence and presence of NTD, respectively. The  $K_d$ s are also consistent with the  $K_d$  for the AF1-FgD interaction, determined using ITC ( $1.5 \pm 0.0 \mu\text{M}$ ) (Table 5.1, Section 5.3.1). The AF1+NTD SPR sample contained equimolar concentrations of each protein to ensure the majority of AF1 is bound within the AF1-NTD complex.

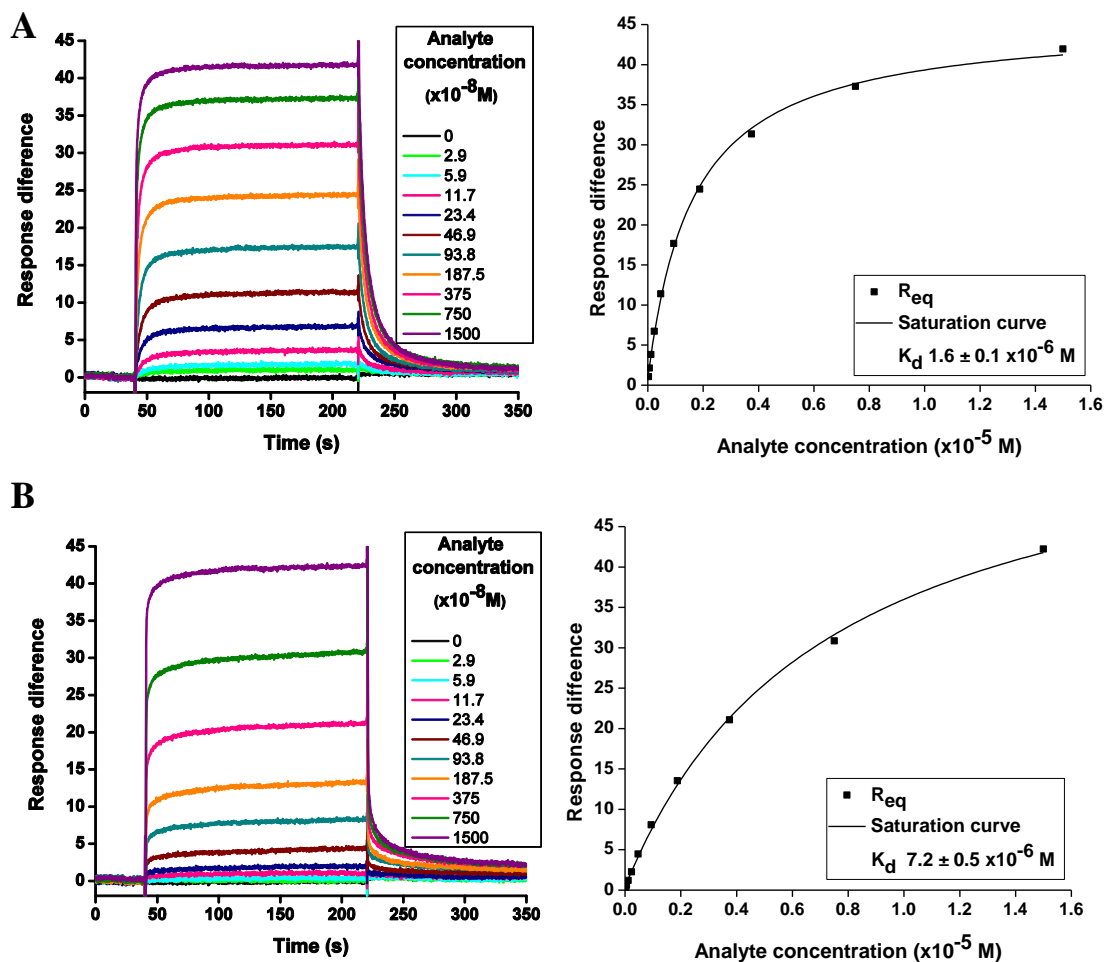


**Figure 5.9** Determination of the  $K_d$ s for the FgD-AF1 and FgD-AF1+NTD interactions. Representative SPR sensorgrams generated upon interactions of immobilized FgD with increasing concentrations of (A) AF1 and (B) the AF1-NTD complex. The  $K_d$ s were determined using equilibrium analysis.

### 5.5.2 Determination of the $K_d$ s for the NTD-AF1+Fg1 interactions

To test the effects of Fg1 on AF1 binding to NTD, the  $K_d$  for the NTD-AF1+Fg1 interaction was determined by SPR (Figure 5.10) and compared with the  $K_d$  for the NTD-AF1 interaction determined in Section 5.3.1 (Figure 5.3). Due to the fast association and dissociation rates, analysis of the equilibrium binding was used for evaluation. Comparison of the  $K_d$  values revealed very little difference; i.e.  $1.8 \pm 0.6$

nM and  $1.9 \pm 0.5$  nM in the absence and presence of Fg1, respectively. The AF1+Fg1 sample contained a six-fold molar excess of Fg1 relative to the concentration of AF1 to ensure that the majority of AF1 was bound to Fg1. The relatively high errors of the fit are most likely caused by the character of the sensorgrams (see Section 5.3.1). Nevertheless, it is clear that the two SPR experiments produced similar results suggesting that the presence of Fg1 has no effect on the NTD-AF1 interaction.

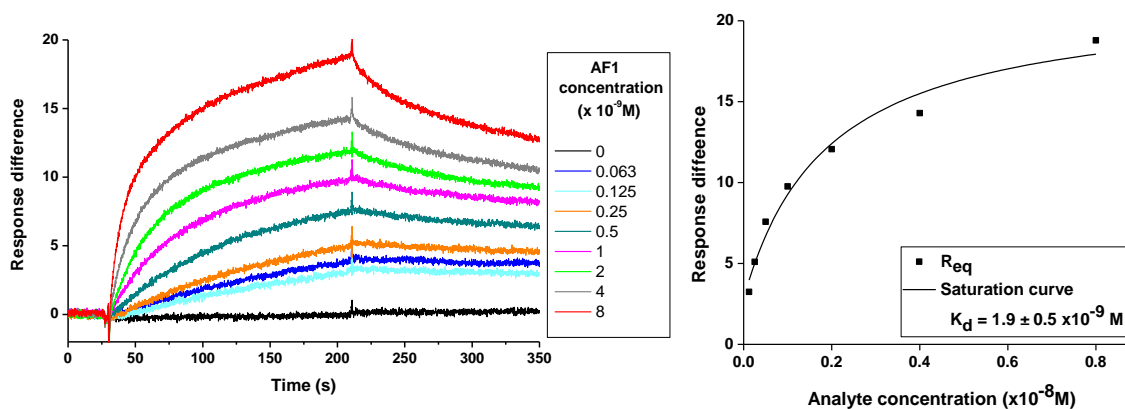


**Figure 5.10 Determination of the  $K_d$  for the NTD-AF1+Fg1 interaction.** (A) Representative SPR sensorgrams generated by interactions of immobilized NTD with increasing concentrations of AF1 + Fg1. (B) Affinity evaluation using equilibrium analysis.

### 5.5.3 Formation of the NTD-AF1-Fg ternary complex

The putative cooperativity in Fg and Fn binding to AF1 was also investigated in the following experiment, which involved exposure of an NTD-coated sensor chip to AF1 and the AF1-Fg complex (Section 2.8.2.5). Given that the intensity of the SPR response is directly proportional to the molecular mass of the analyte, a significant difference in the response generated upon the injection of AF1 and the AF1-Fg complex should be observed providing the ternary complex is formed (Figure 5.11).

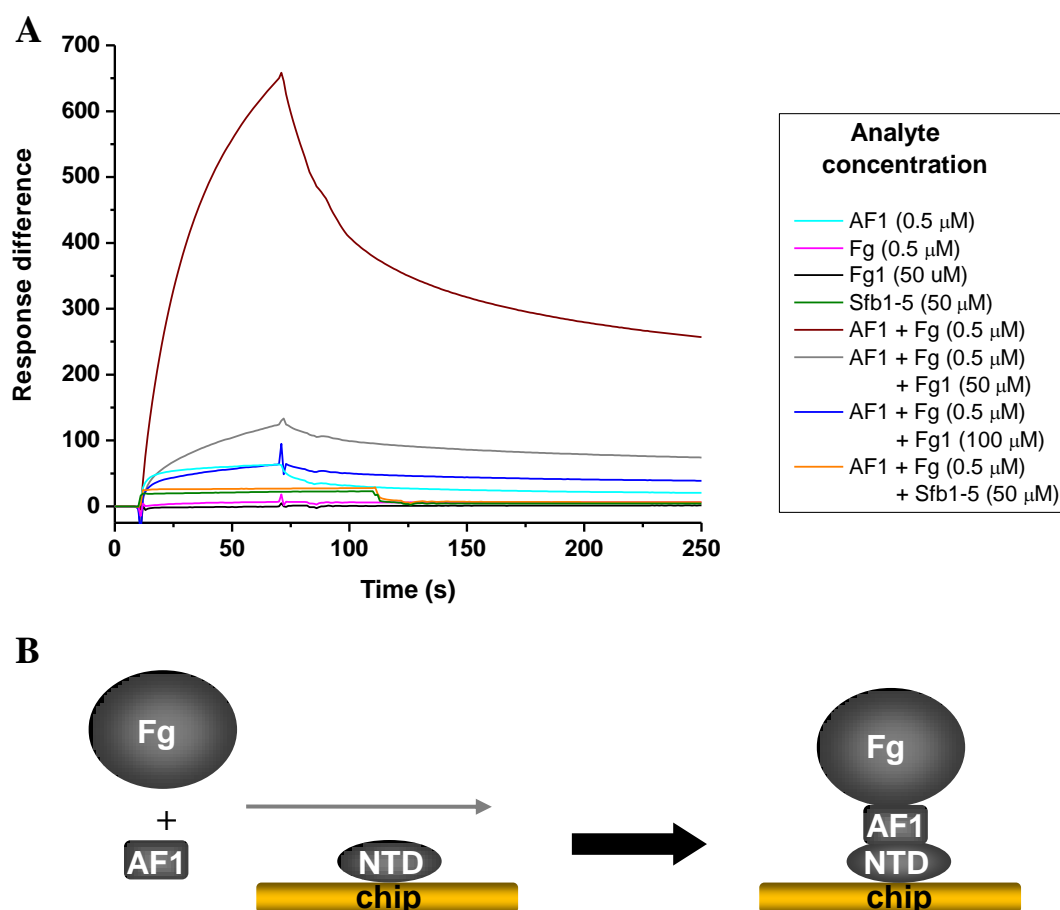


**Figure 5.11 Formation of the NTD-AF1-Fg ternary complex.** (A) Representative SPR sensorgrams show responses from the interactions of immobilized NTD with AF1 (0.5  $\mu$ M) in the presence or absence of equimolar concentration of Fg. The effects of specific inhibitors on the formation of the NTD-AF1-Fg ternary complex are also shown. (B) Overview of the SPR experiment (RIGHT) illustrating the formation of the ternary complex on the surface of the sensor chip.

A strong response, exceeding 650 RU, was generated upon exposure of the NTD-coated chip to the AF1-Fg complex (brown), while separate injections of AF1 (cyan) and Fg (magenta) only produced approximately 50 RU and 0 RU responses, respectively. The result clearly demonstrates that the Fg-AF1 complex interacts with the immobilized NTD, and that the NTD-AF1-Fg ternary complex is formed (Figure 5.11B). To confirm that AF1 binds Fg and NTD simultaneously and that the interactions involved are specific, several control experiments were performed. Initially, a two hundred-fold molar excess of Fg1 was added to the AF1-Fg complex solution prior to sample injection (blue). The result shows that excess Fg1 completely blocks the interaction between AF1 and Fg. In the second control experiment, a hundred-fold molar excess of the NTD-binding Sfb1-5 peptide

(Section 2.3.2) was added to the sample of AF1 prior to injection (orange). Sfb1-5 inhibits the NTD-AF1 interaction, reducing the final response to that of Sfb1-5 only (20 RU). The character of the sensorgram and the complexity of the binding events on the surface of the sensor chip prevented the evaluation of the  $K_d$  for the NTD-AF1+Fg interaction, however, these experiments clearly demonstrate ternary complex formation for the first time.

## 5.6 Steric hindrance prevents formation of an Fn-AF1-Fg ternary complex.

In Section 5.5.3, the formation of an NTD-AF1-Fg ternary complex was demonstrated for the first time. However, the goal was to determine whether intact Fn and Fg can bind AF1 simultaneously or whether the formation of the ternary complex is prevented by steric effects. To test the simultaneous binding of Fn and Fg to AF1, an SPR experiment was performed. This involved exposure of an AF1-coated sensor chip surface to a solution containing Fg and Fn at various concentration ratios (Figure 5.12). Given the significant difference between  $K_d$ s for Fg-AF1 and Fn-AF1 interactions, it was vital that the relative concentrations of Fg and Fn used in the experiment reflect those present in human plasma (Sections 1.4.1 and 1.5.1).

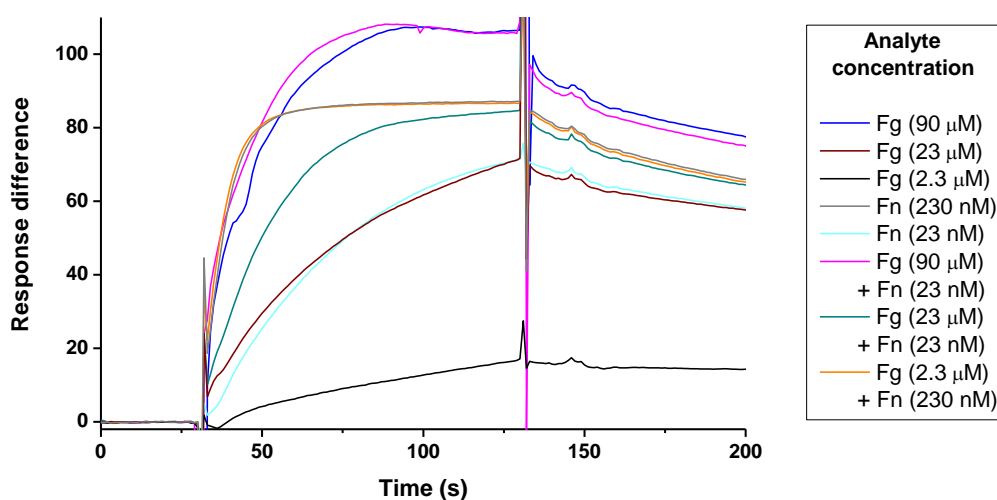


**Figure 5.12 Fg and Fn binding to AF1.** Representative SPR sensorgrams from interactions of immobilized AF1 with Fn and Fg at three different relative concentration ratios, leading to the AF1-coated surface saturation, first by Fn (orange) then Fg (magenta) and also by a combination of both (dark cyan).



Initially, the AF1-coated surface was exposed to a solution containing Fg and Fn at concentrations of 2.3  $\mu\text{M}$  and 230 nM respectively, reflecting the 10:1 Fg:Fn concentration ratio found in human plasma (Hynes and Yamada, 1982; Kamath and Lip, 2003). The generated  $R_{\text{eq}}$  of 87 RU was identical to that given by Fn only, suggesting no Fg was interacting with AF1 in the presence of Fn. When only Fg (at a concentration of 2.3  $\mu\text{M}$ ) was injected over the sensor chip surface, an  $R_{\text{eq}}$  of 17 RU was produced demonstrating Fg binds AF1 in the absence of Fn (Figure 5.12; traces: orange, grey and black).  $R_{\text{eq}}$  of 84 RU was obtained when a solution containing a higher Fg:Fn ratio (Fg 23  $\mu\text{M}$  and Fn 23 nM) was used. Since both glycoproteins generated identical  $R_{\text{eq}}$  of 71 RU when injected over the sensor chip surface individually at this concentration, it can be assumed both Fg and Fn binding contributed to the final  $R_{\text{eq}}$  of 84 RU (Figure 5.12; traces: dark cyan, brown and cyan). However, it was not clear whether either of the two glycoproteins saturated the AF1-coated surface, thus the possibility that Fn and Fg are binding to separate AF1 molecules could not be ruled out. Consequently, a higher molar excess of Fg (90  $\mu\text{M}$ ) was added to the solution of Fn (23 nM) and injected over the AF1-coated sensor surface. The  $R_{\text{eq}}$  of 106 RU was almost identical to that given upon injection of Fg (90  $\mu\text{M}$ ) only (Figure 5.12; traces: magenta, blue and cyan). The result indicates that the molar excess of Fg saturated the AF1-coated surface and blocked the AF1-Fn interaction.

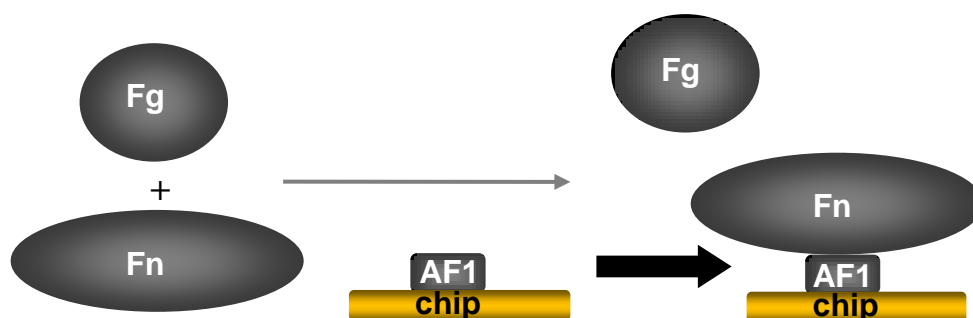


**Figure 5.13 Overview of the SPR experiment.** The right side of the diagram illustrates the steric hindrance effect that prevents Fg from binding to Fn-bound AF1 at physiological concentrations of Fg and Fn.

## 5.7 Fg and Fn binding to AF1 under physiological conditions demonstrated by a plasma pull-down assay

A combination of the previous ITC and SPR experiments showed AF1 retains Fg- and Fn-binding ability and that only Fn binds AF1 when the relative concentrations of Fg and Fn reflect those present in human plasma. The aims of the pull-down assay were to reiterate the results from the two previous SPR experiments and to test the physiological relevance of AF1 by assessing its binding to Fg and Fn within the environment of human plasma. Following expression and purification of AF1 and N2N3, the assay was designed with the help of Andrew Brentnall (Department of Biology, University of York), who also performed the experiment. The assay involved covalent immobilization of AF1 and N2N3 to the column resin, exposure to human plasma and subsequent elution of the AF1 and N2N3 bound proteins by acetate buffer pH 3.0 (Figure 5.14A). A solution containing a mixture of purified Fg and Fn at physiological pH was used as a positive control (Figure 5.14B). A column with uncharged resin was used as a negative control (data not shown). The experimental set-up is described in detail in Section 2.7. Analysis of the eluted samples was performed using SDS-PAGE. A relatively high amount of AF1 and N2N3 had to be immobilized on the column resin to allow for visualization of the eluted proteins by SDS-PAGE. Consequently, the AF1-coated resin was expected to bind both Fg and Fn as the concentrations of the glycoproteins in plasma are not sufficient to saturate the immobilized AF1 (Henderson et al., 2010; Herrick et al., 1999). The results of the experiment show that both N2N3 and AF1 bind purified Fg as well as Fg within the plasma sample. However, AF1 also interacts with both purified and plasma Fn. A significant amount of Fg was present in the wash fractions from both the N2N3 and AF1 columns, while no Fn could be detected in the wash fractions from the AF1 column. This finding correlates with the difference between the individual  $K_d$  values for the AF1-Fg ( $1.1 \pm 0.0 \mu\text{M}$ ) and AF1-Fn ( $1.0 \pm 0.1 \text{ nM}$ ) interactions (Table 5.1), suggesting Fg is slowly dissociating from the N2N3 region even in the absence of elution buffer.

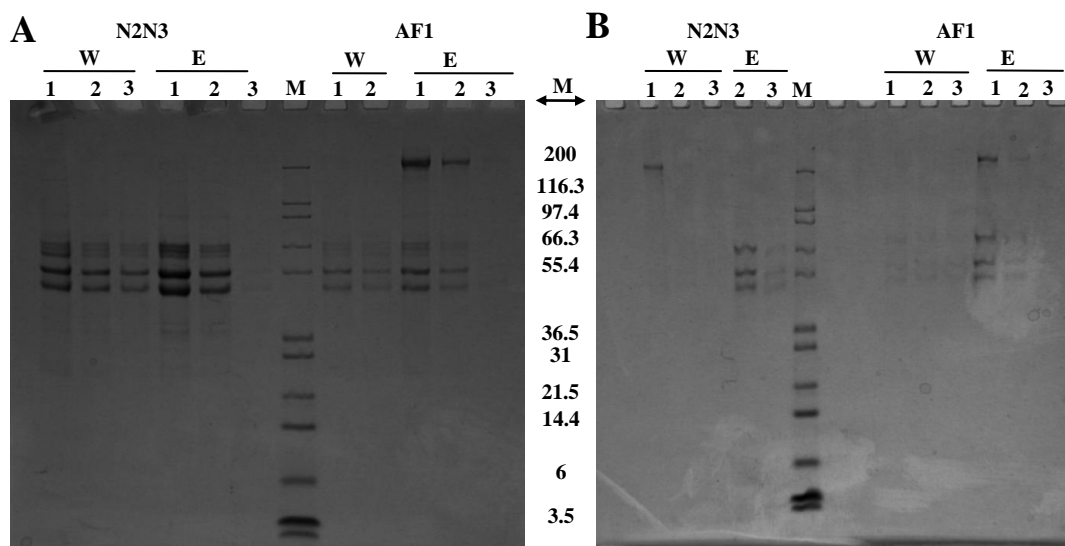


**Figure 5.14** SDS-PAGE analysis of fractions from the plasma pull-down assay with N2N3 and AF1 resin columns. SDS-PAGE analysis of (A) the plasma pull down and (B) the control experiment with the solution of purified Fg and Fn include the protein marker (M / kDa) as well as multiple wash (W) and elution cycles (E). Fg appears as three separate bands (between 36.5 and 66.3 kDa) corresponding to the three individual Fg chains  $\alpha$ ,  $\beta$  and  $\gamma$  (Figure 1.4) due to the reducing conditions of the sample buffer. Monomeric Fn is visible as a single band just above the 200 kDa mark.

## 5.8 Discussion

### 5.8.1 Determination of the $K_d$ for the AF1-NTD interaction

SPR and ITC experiments were used to characterise the interaction between AF1 and NTD (Section 5.3.1). The final  $K_d$ s for the AF1-NTD interaction determined by SPR and ITC were  $1.9 \pm 0.5$  nM (Figure 5.2) and  $0.7 \pm 0.2$  nM (Figure 5.3), respectively. Although, the associated errors of the fit are relatively large, the obtained  $K_d$ s are very similar and also consistent with the  $K_d$  for the interaction of FnBPA1 with NTD determined previously ( $4.8 \pm 0.6$  nM) (Meenan et al., 2007). This clearly demonstrates that FnBPA1 retains the NTD-binding activity within AF1 context. The errors associated with the SPR and ITC results could be reduced through optimization. For example, the SPR data could be improved by altering the level of immobilized NTD or by using a more specific ligand immobilization approach. The issue with the steepness of the isotherm transition in the ITC experiment could not be overcome by adjusting the concentrations of NTD (cell) and/or AF1 (syringe), due to the limited solubility of NTD and the limiting VP-ITC sensitivity ( $0.1 \mu\text{cal}$ ). An improvement could probably be achieved by increasing the reaction temperature

or by altering the solution conditions. However, as the purpose of these preliminary experiments was only to test whether AF1 contains similar NTD-binding ability to FnBPA1, no further optimization was performed.

### 5.8.2 Determination of the $K_d$ for the AF1-Fn interaction

The  $K_d$  for the AF1-Fn interaction ( $1.0 \pm 0.1$  nM) was determined using SPR and a kinetic evaluation (Figure 5.4) (Section 5.3.2). The obtained  $K_d$  was similar to that for the AF1-NTD interaction ( $1.9 \pm 0.5$  nM), but the  $k_a$  ( $2.8 \times 10^5 \pm 1.7 \times 10^3$  M<sup>-1</sup>s<sup>-1</sup>) was significantly lower than that for the AF1-NTD interaction ( $k_a$   $1.3 \times 10^7 \pm 2.3 \times 10^4$  M<sup>-1</sup>s<sup>-1</sup>). Since previous studies have shown that NTD is occluded in intact Fn (Erickson and Carrell, 1983; Johnson et al., 1999), the results presented here indicate that this might affect the kinetics of the AF1-Fn interaction.

The reliability limitations of the equilibrium and rate constants for the AF1-Fn interaction had to be considered, as it was derived using a simple 1:1 binding model, yet native Fn is a dimeric molecule comprising two NTDs. The main issue associated with using a 1:1 binding model stems from avidity. Although, binding of the first Fn site to AF1 gives a response, no response is generated upon binding of the second site while the overall binding is strengthened, shifting the equilibrium constant (Figure 5.15A). Biacore analysis software contains a bivalent analyte evaluation model, thus two sets of association/dissociation rates can be determined. However, use of this model also has its limitations. Firstly, the association rate constant for the second binding site can only be presented in RU<sup>-1</sup>s<sup>-1</sup> (not M<sup>-1</sup>s<sup>-1</sup>), therefore the final equilibrium constant cannot be determined. Secondly, applying the bivalent analyte model will only result in a good fit providing the majority of the analyte molecules bind via both binding sites. When applied to the AF1-Fn data, the bivalent model did not produce an improved fit compared with the 1:1 model. Consequently, it is likely that most of the AF1-bound Fn molecules interact with the immobilized AF1 via a single NTD molecule.

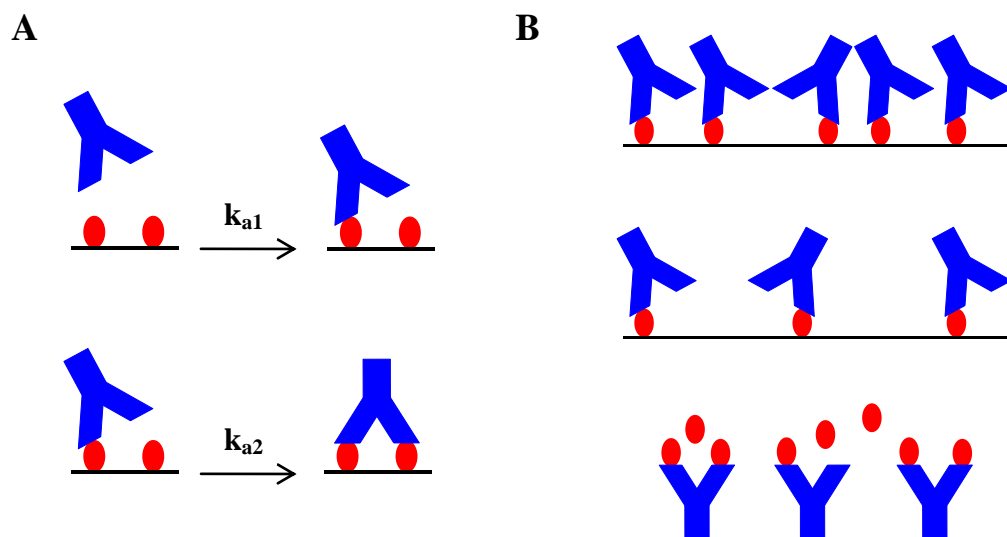


**Figure 5.15** The avidity effect associated with the binding of a bivalent analyte. **(A)** Schematic diagram of the two step process of bivalent analyte (blue) binding to an immobilized ligand (red). Attachment of the first analyte site gives a response. However the engagement of the second binding site does not generate a response as the analyte is already bound. **(B)** Alternative solutions to the problem of bivalent analyte, namely; very high analyte concentration (**top**), low level of ligand immobilization (**middle**) or immobilization of the bivalent analyte instead (**bottom**).

The experimental parameters favouring formation of a binary complex include low levels of ligand immobilization, where the analyte can only reach a single ligand molecule, or high analyte concentrations resulting in elevated competition for the immobilized ligand (Figure 5.15B). Hence the experiment should ideally be repeated with varying levels of immobilized ligand in order to confirm the reliability of the obtained  $K_d$ . Immobilizing Fn on the surface of the sensor chip instead of AF1 would also allow the use of a 1:1 binding model (Figure 5.15B). However the immobilization compromised Fn's ability to interact with AF1. It is likely that Fn was immobilised in the compact conformation (Section 1.5.2) with occluding NTD, thus rendering it inaccessible to AF1. The use of ITC could avoid the issues associated with the dimeric nature of Fn. Unfortunately the occurrence of heavy precipitation during the titration interfered with ITC data acquisition, thus ITC was not used.

### 5.8.3 Determination of the $K_d$ for the AF1-Fg1/FgD/Fg interactions

The interaction between AF1 and Fg was also characterized using Fg1, FgD and Fg and a combination of ITC and SPR (Section 5.3.3). The thermodynamic parameters,

including  $K_d$ s for the interactions of AF1 with Fg1 and Fg determined by ITC (Table 5.1) were very similar to those obtained for N2N3-Fg1 and N2N3-Fg interactions (Table 4.2). Like N2N3, AF1 binding to Fg is marginally stronger compared with the binding to Fg1, which could be indicative of incompleteness of the N2N3 binding site on the Fg1 peptide (Section 4.10.3). The 2:1 stoichiometry (Table 5.1) for the AF1-Fg interaction confirms the dimeric nature of intact Fg (two  $\gamma$  chains) (Section 1.4). Further confirmation of the Fg-binding ability of AF1 was provided by the  $K_d$  for the AF1-FgD interaction obtained by SPR, and the subsequent inhibition of that interaction by an excess of Fg1. All of the above experiments point to the conclusion that AF1 retains the full Fg-binding activity of N2N3, which is not affected by the additional adjacent FnBPA1.

#### **5.8.4 Characterization of AF1 by NMR spectroscopy**

Although the poor quality of the 2D  $^1\text{H}^{15}\text{N}$  TROSY-HSQC spectra of  $^{15}\text{N}$ -AF1 revealed that NMR spectroscopy was not the optimum technique for studying the putative cooperativity of Fg and Fn binding, the spectrum revealed some basic information regarding the structural features of AF1 (Section 5.4). The appearance of intense peaks within a narrow region in the  $^1\text{H}$  dimension as well as weaker peaks dispersed over a much wider range in the  $^1\text{H}$  dimension indicates the presence of both structured and unstructured regions within AF1. Direct comparison of the TROSY-HSQC spectra of  $^{15}\text{N}$ -AF1 with that of  $^{15}\text{N}$ -N2N3 and  $^{15}\text{N}$ -FnBPA1 recorded under similar conditions and with identical acquisition parameters clearly demonstrates that both the structured N2N3 and unstructured FnBPA1 regions are present within AF1.

#### **5.8.5 NTD does not affect the FgD-AF1 interaction significantly**

Potentially, only twelve residues separate the Fg and Fn binding sites on AF1 (Section 4.10.8), which suggests that besides the negative/positive putative cooperativity, the simultaneous binding of Fg and Fn to AF1 could also be influenced by steric effects. The presence of putative cooperativity in binding of Fg and Fn was tested first, using FgD and NTD (Section 5.5.1). The SPR experiment showed only a small decrease in affinity of AF1 for FgD in the presence of NTD (FgD-AF1;  $K_d$   $1.6 \pm 0.1$   $\mu\text{M}$  and FgD-AF1+NTD;  $K_d$   $7.2 \pm 0.5$   $\mu\text{M}$ ). Subtle

differences were also detected in the kinetics, as comparison of the sensorgrams revealed that both the association and dissociation rates are slightly faster for the FgD-AF1+NTD interaction (Figure 5.16). The results suggest that NTD might have an effect on the FgD-AF1 interaction, and although relatively small, it could be indicative of a much more significant effect associated with binding of intact Fn.

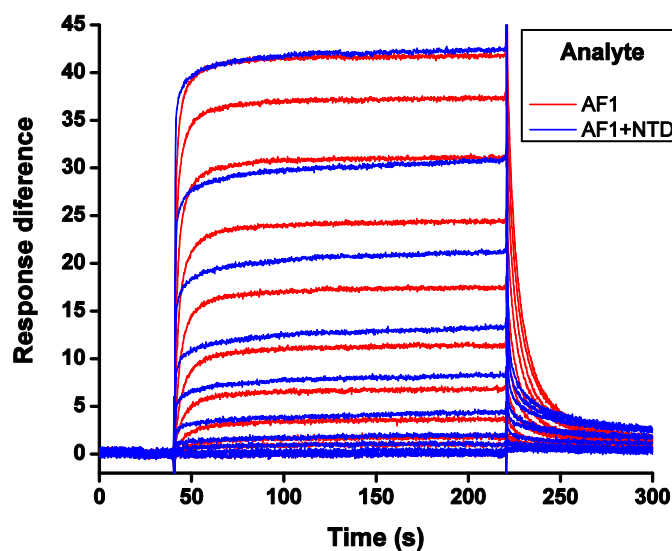


**Figure 5.16 Comparison of the SPR sensorgrams given by the FgD-AF1 and FgD-AF1+NTD interactions.** Overlay of the raw data corresponding to the experiment in Section 5.5.1. Sensorgrams corresponding to the FgD-AF1 and FgD-AF1-NTD interactions shown in red and blue respectively.

Although the experiment showed that AF1 binds FgD in the presence of NTD and that NTD does not significantly affect the FgD-AF1 interaction, the results do not provide direct evidence that NTD is bound to AF1 and that the FgD-AF1-NTD ternary complex is formed on the surface of the chip (Figure 5.16). An indication of the analyte form (i.e. whether AF1 or the AF1-NTD complex binds FgD) can be obtained by comparing estimated binding activities of the immobilized ligand (FgD) between the two experiments (Figure 5.9A, B). The estimate of the FgD activity is determined using the  $tR_{MAX}$  (Equation 1.13, Section 4.3) /  $R_{MAX}$  ratio and the final value should be similar for both experiments. The FgD activity estimates were 43% and 35% for the first and second experiment, respectively (assuming NTD-bound AF1 was the analyte in the second experiment) (Figure 5.17A). The values indicate a slight decrease in FgD activity in the second experiment, probably as a consequence of the repetitive usage of the chip. As the  $tR_{MAX}$  is directly proportional to the analyte molecular mass, using the analyte mass of AF1 (40900 Da) (Figure 5.17B) instead of AF1-NTD (69780 Da) in the FgD activity calculations for the second experiment should result in a less realistic value. The estimated FgD activity was

60%. Since a 17% increase in FgD activity in the second experiment is unlikely, it appears that it is indeed the AF1-NTD complex that interacts with FgD.



**Figure 5.17** Schematic diagram representing the two possible scenarios in the SPR measurements of the  $K_d$  for the FgD-AF1+NTD interaction. (A) FgD-bound AF1 can interact with NTD thereby forming a ternary complex on the chip surface. (B) Binding of FgD to AF1 inhibits the AF1-NTD interactions thus only the FgD-AF1 complex is formed and detected.

### 5.8.6 Fg1 does not affect the NTD-AF1 interaction

To test whether Fg1 affects the NTD-AF1 interaction, an SPR experiment was performed where AF1 was flowed over an NTD-coated chip surface in the presence of a six-fold molar excess of Fg1 (Figure 5.10) (Section 5.5.2). The  $K_d$  was determined using analysis of the equilibrium binding as  $1.9 \pm 0.5$  nM and compared with the  $K_d$  for the NTD-AF1 interaction ( $1.8 \pm 0.6$  nM) (Figure 5.3). While the results of the previous experiment revealed a small decrease in FgD-AF1 affinity in the presence of NTD (Section 5.8.5), the results of this experiment showed no detectable effect of Fg1 on the AF1-NTD interaction. Both the  $K_d$  and the character of the sensorgrams are virtually identical. The combined results from this and the previous SPR experiments suggest there is a lack of either positive or negative cooperativity between the Fg and Fn binding sites on AF1.

### 5.8.7 Formation of the NTD-AF1-Fg ternary complex

Figure 5.11 provides the first biophysical evidence that NTD and Fg can bind simultaneously to AF1 forming a ternary complex. The significantly higher intensity of the response given by the NTD-AF1+Fg interaction compared with that given by the NTD-AF1 interaction is a clear indication that Fg-bound AF1 interacts with the NTD-coated sensor chip surface (Section 5.5.3). The set of control experiments demonstrated that both interactions (NTD-AF1 and AF1-Fg) are specific as they can be inhibited by the known N2N3 and NTD-binding peptides Fg1 and Sfb1-5,





### 5.8.8 Steric effects prevent simultaneous binding of Fg and Fn to AF1.

Although the above SPR experiments (using FgD and NTD) demonstrated the independence of the two binding sites, the potential influence of steric effects on the simultaneous binding of Fg and Fn was not addressed. Several factors were likely to influence the formation of the ternary complex and therefore had to be considered in the experimental design and the subsequent analysis of the results. These included the relative concentrations of Fg and Fn present in human plasma and the individual  $K_d$ s for the AF1-Fg and AF1-Fn interactions. While Fg is present in ten-fold molar excess in plasma compared with Fn (Hynes and Yamada, 1982; Kamath and Lip, 2003), it is the latter glycoprotein that has higher affinity for AF1, with the  $K_d$  lower by three orders of magnitude (Table 5.1). The other important element was the amount of immobilized AF1 in relation to the Fg and Fn concentrations used. Achieving AF1 saturation by Fg and Fn was a key step in the experiment as it was the only means of ensuring the differences in response correspond to a simultaneous binding of Fg and Fn to the same molecule of AF1. It is possible to estimate the amount of the immobilized ligand using the relationship between response units and the mass of protein within the dextran layer ( $1 \text{ RU} \sim \text{pg/mm}^2$ ) (Stenberg et al., 1991). The correlation can be combined with the approximate thickness of the dextran layer (100 nm) and converted to a molar concentration according to Equation 5.1 (Muller et al., 1998); where  $R_L$  represents the level of ligand immobilization and  $M_L$  the molecular mass of the ligand.

$$[\text{Ligand}](\text{mol/litre}) = \frac{R_L}{100 \times M_L} \quad (5.1)$$

The concentration of the immobilized AF1 was estimated at  $35 \mu\text{M}$  ( $R_L$  143 RU,  $M_L$  40900 Da), based on Equation 5.1. However, this value represents concentrations of both the active and inactive immobilized ligand, thus is often used only as guidance prior to the initial testing of the analyte binding activity of the ligand-coated surface.

The SPR experiment revealed that saturation of the AF1-coated surface with Fn prevented Fg from binding to immobilized AF1 and *vice versa* (Figure 5.12). Exposure of the AF1-coated surface to the Fg:Fn concentration ratio that is found in human plasma, produced an identical response to that obtained with Fn alone; suggesting that Fg doesn't bind AF1 under these conditions. These results provide the first biophysical evidence that steric effects could prevent the formation of the

Fg-AF1-Fn ternary complex, and raises a question regarding the physiological role of the Fg-binding site and a potential functional redundancy.

### 5.8.9 AF1 binds Fg and Fn when exposed to human plasma

An array of results from previous SPR and ITC experiments have shown AF1 confers the ability to bind Fg and Fn, and thus serves as a suitable representation of FnBPA for the purpose of studying the cooperativity between Fg and Fn binding to N2N3 and FnBPA1. However, only purified Fg and Fn, or their corresponding proteolytic fragments have been used in all previous experiments. Outcomes of the final experiment, which involved exposure of AF1 to human plasma, confirmed the Fg and Fn-binding ability of AF1 (Section 5.7).

Despite the pull-down assay being a relatively crude technique, the results provided evidence that AF1 retains capacity to bind Fg and Fn individually within the environment of human plasma (Figure 5.14). Although this *in vitro* approach does not allow for a detailed qualitative evaluation of the AF1 interaction with Fg or Fn, the previously established difference in the  $K_{ds}$  (AF1-Fg  $1.1 \pm 0.0 \mu\text{M}$  and AF1-Fn  $1.0 \pm 0.1 \text{ nM}$ ) for the two interactions was detected. While the dissociation of Fn from the AF1-coated resin surface could only be achieved using elution buffer, Fg appeared to dissociate gradually even in the absence of the elution buffer, which is consistent with its lower affinity towards AF1 (Figure 5.14).

The presence of both Fg and Fn in the elution fractions from AF1 column indicates that the AF1-coated resin surface was not saturated by either of the two proteins. As mentioned before, a high level of AF1 immobilization was necessary for the visualization by SDS-PAGE and therefore approximately 20 mg of AF1 was covalently linked to the resin surface. Considering the approximate concentration of Fg and Fn found in human plasma are 3 and 0.3 mg/ml, respectively, a significantly larger volume of plasma would be required to reach saturation. In fact, over 700 ml of plasma would be required to reach a molar equilibrium between AF1 and Fn, assuming 100% of the immobilized AF1 retained binding activity. This clearly demonstrates the AF1-coated resin surface is not saturated, thus able to interact with both Fg and Fn by forming AF1-Fg and AF1-Fn binary rather than Fn-AF1-Fg ternary complexes. Ideally, subsequent experiments would be performed, which

would involve lower level of AF1 immobilization in combination with a more sensitive detection approach, such as a Western blot, to ensure AF1 saturation with Fn.

## 6 General discussion

This work set out to characterise the FnBPA Fg-binding domain, its interaction with Fg and to test whether simultaneous binding of Fg and Fn is affected/prevented by cooperativity or potential steric effects. FnBPA was previously identified as a major virulence factor in *S. aureus* IE, utilizing both the Fg- and Fn-binding sites (Wann et al., 2000) to synergistically promote the infection (Piroth et al., 2008; Que et al., 2005). While the FnBPA-Fn interaction has been the subject of an extensive research (Bingham et al., 2008; Meenan et al., 2007; Edwards and Massey, 2011), little attention has been paid to Fg-binding. The knowledge of the structural aspects of the FnBPA-Fg interaction and the putative cooperativity between the two adjacent binding sites on FnBPA would contribute significantly to our understanding of the complex network of processes leading to the full development of IE and potentially other *S. aureus* infections.

### 6.1 The FnBPA-Fg interaction

Sequence similarity indicated that the minimal Fg-binding region of FnBPA might have structural features in common with other Fg-binding MSCRAMMs. The structure of N2N3T was solved using X-ray crystallography and revealed that the conformation does indeed share many structural features with ClfA<sub>(229-545)</sub> (*S. aureus*) and SdrG<sub>(273-597)</sub> (*S. epidermidis*). This includes the topology of N2, described previously as DEV-IgG fold identified in numerous other proteins including ClfA, SdrG, CNA or integrin  $\alpha_V\beta_3$  (Deivanayagam et al., 2002). The structural similarity suggested that the interaction with Fg might also resemble that discovered in SdrG and ClfA, which was later confirmed when a structure of the N2N3T-Fg1 complex was solved, also by X-ray crystallography.

The structure revealed a typical  $\beta$ -zipper binding within a cleft formed predominantly by residues with hydrophobic sidechains, stretching between the N2 and N3 domains. Studies by Blumentstein and colleagues (1992) and Mayo and colleagues (1990) suggested the C-terminus of the Fg  $\gamma$  chain is intrinsically disordered. Thus it is likely to undergo a disorder-to-order transition upon binding to FnBPA. It fits snugly into the cleft, causing the N3-G' strand to translocate and 'wrap' around the Fg C-terminus forming a tunnel-like feature, establishing a

relatively large interface. Thus the solvent exposed hydrophobic cleft is buried in the N2N3T-Fg1 complex in an interaction driven mainly by the hydrophobic effect. Given that only thirteen Fg residues are involved in the binding, this interaction appears rather efficient. Surprisingly the interaction is dominated by backbone-hydrogen bonds with Gln13 the only residue whose sidechain may form hydrogen bonds with N2N3. This type of interaction is not unique to FnBPA and has been identified previously in other Fg-binding MSCRAMMs including FnBPB, ClfA/B or SdrG. Moreover, the Fg-binding sites on FnBPA and ClfB exhibit promiscuity as they can interact with elastin and cytokeratin 10 (K10), respectively, as well as Fg. Crystal structures of ClfB<sub>(199-542)</sub>-Fg $\alpha$ /K10 solved recently by Ganesh and colleagues (2011) are almost identical (including overlapping binding sites) and both resemble the structures of N2N3T-Fg1 and ClfA<sub>(229-545)</sub>-Fg1<sub>(D16A)</sub>. Furthermore, a study by Ganesh and colleagues (2008) revealed that mutations in Fg1 can lead to either increase or decrease in affinity of ClfA for Fg1, suggesting Fg1 might not be the optimum ligand. A comparison of the crystal structures of homologous N2N3 regions from five Fg-binding proteins FnBPA, ClfA, ClfB (*S. aureus*) and SdrG (*S. epidermidis*) in complex with Fg1, Fg1<sub>(D16A)</sub>, Fg $\alpha$ /K10 and Fg $\beta$  peptides, respectively, reveals that the peptides do not always bind in the same orientation (Ganesh et al., 2011; Ganesh et al., 2008; Ponnuraj et al., 2003). Whilst in FnBPA, ClfA and ClfB the peptide aligns parallel to the N3-G' strand, the Fg $\beta$  peptide binds antiparallel to SdrG (Figure 6.1). Interestingly, the  $K_{ds}$  for all the above interactions are very similar (i.e. micromolar) (Ganesh et al., 2008; Ponnuraj et al., 2003; Burke et al., 2010; Walsh et al., 2004).

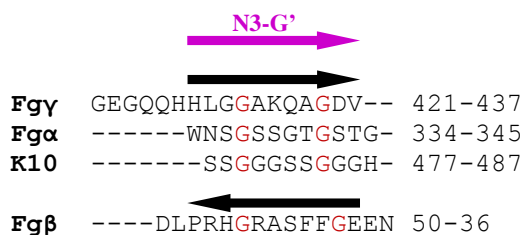


**Figure 6.1** Sequence alignment of ligands for the Fg-binding MSCRAMMs. Sequence of the Fg  $\gamma$  chain C-terminus (Fgy) (UniProt entry P02679) was aligned with that of the ClfB binding site on Fg  $\alpha$  chain (Fg $\alpha$ ) (UniProt entry P02671), on K10 (UniProt entry P13645) and the SdrG binding site on Fg  $\beta$  chain (Fg $\beta$ ) (UniProt entry P02675) followed by some manual editing. The residue numbering corresponds to that in the UniProt database. The N3-G'  $\beta$ -strand (magenta) and the relative orientation of the bound ligands (black) are indicated. The conserved Gly residues are highlighted in red. The multiple sequence alignment was performed using ClustalW2 (Larkin et al., 2007)

Sequence alignment of FnBPA, ClfA/B and SdrG ligands reveals relatively high content of Gly residues (Figure 6.1). The FnBPA-binding site on elastin has not yet been identified, however, a high proportion of Gly residues (29%) throughout the entire elastin sequence is also clear. It appears that although promiscuous, the Fg-binding MSCRAMMs interact preferably with regions rich in Gly residues. Moreover, Gly is conserved at two positions, which are within a close proximity to W494 and F/Y306 conserved in FnBPA/B, ClfA/B and SdrG. Studies by Keane and colleagues (2007) and Ganesh and colleagues (2011) showed substitution at these two positions leads to inhibition of the binding, though the mutated recombinant proteins were not structurally characterised. A systematic alanine scanning of the FnBPA hydrophobic cleft would lead to identification of the key interactions within the intermolecular interface, thus provide new data with regard to specificity of the FnBPA-Fg interaction. Also, obtaining the structure of the N2N3T-elastin complex would reveal whether FnBPA does indeed bind two different ligands through the same mechanism. The results published previously and those presented here point to a conclusion that the N2N3-Fg interaction identified in this work might be an example of a versatile binding mechanism adopted by multiple proteins across different species in binding Fg as well as other ligands.

Although the above evidence points to high similarity between the Fg-SdrG/ClfA/FnBPA interactions, a more detailed analysis of the N2N3T and N2N3T-Fg1 structures revealed differences in the binding mechanism which were supported by a body of results from an array of biophysical experiments. The Fg-SdrG interaction has been described as a three-step process commonly referred to as the dock-lock-latch model (Ponnuraj et al., 2003). Initial 'docking' of the Fg  $\gamma$  chain C-terminus into the hydrophobic cleft is followed by 'locking' of the Fg C-terminus in the cleft by N2 and N3 domains relocating closer to each other, and subsequent 'latching' of the N3 extension (latch strand) to the N2 domain, which has a stabilizing effect on the overall structure (Section 1.6.3). While the open conformation is necessary for Fg binding to SdrG, Ganesh and colleagues (2008) showed the Fg-ClfA interaction is enhanced in a closed conformation (with the latch strand 'latched' to the N2 domain) and is described by the latch-dock model. On the other hand, the results presented here show FnBPA to be the first Fg-binding MSCRAMM that might not adopt the dock-lock-latch or latch-dock Fg-binding

models. The relative orientations of the N2 and N3 domains in N2N3T do not change upon Fg1 binding, unlike in the latch-dock binding of ClfA to Fg1<sub>(A16D)</sub>. Moreover, the  $K_d$  values determined by SPR demonstrated that Fg binding is not affected by the presence or absence of the putative latch strand in FnBPA. The crystallographic and NMR data obtained here suggest that only the first residues of the putative latch region (Y501 and N503) might be required for Fg-binding, while the rest of the latch could remain disordered even in the Fg-bound FnBPA. As such, FnBPA would emerge as the first known member of the family of the Fg-binding MSCRAMMs that does not contain the latch strand yet retains comparable affinity for Fg. This finding could potentially be even more significant within the context of the FnBPA's Fg- and Fn-binding bifunctionality. The original hypothesis predicted that the putative latch strand interacts with the N2 domain, thus forming an N-terminal  $\beta$ -zipper extension to the tandem  $\beta$ -zippers of FnBRs. Such an arrangement would also be likely to favour the putative cooperativity between N2N3 and FnBPA1. However, these assumptions had to be reconsidered in light of the new data regarding the N2N3-Fg1 interaction and the role of the putative latch region in particular.

The structures of N2N3T and the N2N3T-Fg1 complex allowed, for the first time, the assessment of the boundaries of the N2N3 region of FnBPA. Discrepancies can be found in previous studies regarding the layout of FnBPA and the boundary between the N-terminal A-domain and the Fn-binding region in particular (Wann et al., 2000; Fitzgerald et al., 2006b; Heilmann et al., 2004). In the revised layout of FnBPA (Schwarz-Linek et al., 2003), G512 was identified as the N-terminal end of the FnBR region. Analysis of a crystal structure of the <sup>4</sup>F1<sup>5</sup>F1-STAFF1 complex published later (Bingham et al., 2008) suggests I514 is the most N-terminal FnBPA1 residue involved in the <sup>4</sup>F1<sup>5</sup>F1-STAFF1 interaction. The N2N3 region comprising residues 194-511 was previously identified as the minimal region retaining most of the Fg-binding activity of FnBPA (Loughman et al., 2008; Keane et al., 2007b). However, the X-ray crystallography of N2N3T and the N2N3T-Fg1 complex indicate the 189-199 region might be unstructured in solution thus the K200 residue might be the most N-terminal residue of the N2 domain. The C-terminal end of the N3 domain also appears shorter than predicted, with the residue N503 being probably the most C-terminal residue of N3 involved in Fg binding. It can therefore



be assumed that rFnBPA<sub>(200-503)</sub> is the minimum Fg-binding region and that K504 and the subsequent residues are not part of the N3 fold or indeed a latch strand. To confirm the identity of the minimum Fg-binding region and the importance of Y501 and N503 for the N2N3-Fg interaction, truncated derivatives of the N2N3T construct would have to be expressed and submitted to identical experiments as N2N3T/N2N3. Based on the above evidence, the two binding sites (N2N3 and FnBPA1) appear to be separated by more residues than originally thought, in the form of a ten-residue (K504-P513) flexible linker. This conclusion provided the first indication that the two binding sites might act independently, as the intrinsically disordered linker would allow free adjustment in the relative orientations and/or conformational changes of the two binding sites (Figure 6.2). An assigned NMR spectrum of N2N3E (residues 189 to 515) +/- Fg1 would provide the ultimate confirmation of the intrinsically disordered nature of the N3-FnBPA1 linker region. Although the NMR spectra of N2N3 presented here were of insufficient quality (Section 4.7.2), preliminary NMR experiments utilizing triple-labelled <sup>2</sup>D<sup>15</sup>N<sup>13</sup>C N2N3T lead to a significant improvement in resolution of the acquired spectra.

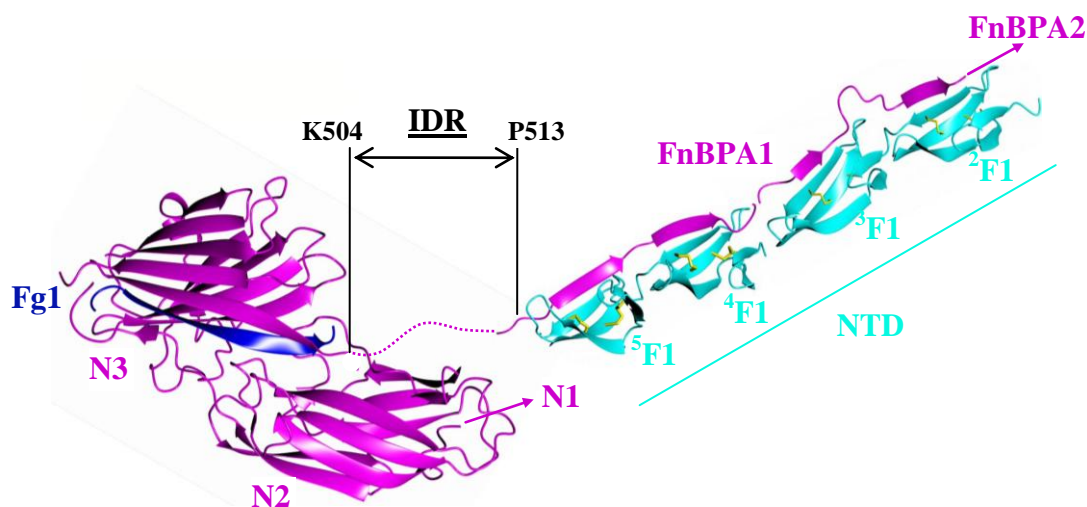


**Figure 6.2** Predicted conformation of the Fg1-AF1-NTD ternary complex. The intrinsically disordered region (IDR) separating N2N3 and FnBPA1 is highlighted, including the residues forming the boundaries.

## 6.2 The putative cooperativity of Fg- and Fn-binding to FnBPA

Negative/positive putative cooperativity and potential steric effects in Fg and Fn binding to FnBPA were investigated in Chapter 5. Although it has been shown previously that FnBPA can bind Fg and Fn individually, and that both interactions

are key to FnBPA's virulence, to date there are no data available regarding simultaneous binding of Fg and Fn. Here, AF1, a construct which contains both N2N3 and FnBPA1 (Section 3.3.6), was used as model for the cooperativity studies. Results of numerous SPR and ITC experiments showed that N2N3 and FnBPA1 retain the Fg- and Fn-binding abilities, respectively, within the context of AF1 (Section 5.3). The  $K_{dS}$  for the N2N3-Fg and FnBPA1-Fn interactions were consistent with the  $K_{dS}$  determined previously (Wann et al., 2000; Meenan et al., 2007). The physiological relevance of AF1 was demonstrated by a plasma pull-down assay, proving AF1 interacts with Fg and Fn individually within the environment of human plasma (Chapter 5). The first indication that Fg- and Fn-binding sites on AF1 act independently was provided by a set of SPR experiments, which showed that the presence of NTD or Fg1 had no effect (positive/negative) on the interactions of AF1 with Fg or NTD, respectively. This was eventually confirmed, when the formation of the NTD-AF1-Fg ternary complex was shown for the first time, using SPR (Section 5.5.3). The result provided the first biophysical evidence for the simultaneous binding of Fg and NTD to the adjacent N2N3 and FnBPA1 sites, respectively.

Despite the above evidence demonstrating that both NTD and Fg bind AF1 simultaneously forming a ternary complex, it was not clear whether AF1 can form a ternary complex with intact Fn and Fg. Given the sizes of the intact glycoproteins and the close proximity of their binding sites on AF1, it was possible that the steric effects would prevent simultaneous binding. This was determined by SPR, results of which suggest that only one of the two glycoproteins can be bound to a single AF1 molecule at anyone time. Outcomes of the SPR experiments revealed, for the first time, that both N2N3 and FnBPA1 cannot be occupied at the same time by intact Fg and Fn, respectively. In order to determine which of the two glycoproteins is likely to bind AF1 *in vivo*, the Fg:Fn concentration ratio was adjusted according to that found in plasma under normal circumstances (~10:1) (Kamath and Lip, 2003; Hynes and Yamada, 1982). The results implied that despite Fg being the more abundant plasma protein, it is the Fn-FnBPA1 interaction that prevails. This is likely to be the consequence of the thousand-fold higher affinity of FnBPA for Fn than for Fg. Such evidence gives rise to the question of the potential functional redundancy of the Fg-binding site. Studies *in vivo* by Piroth and colleagues (2008) and Que and

colleagues (2005) revealed that both Fg and Fn are essential for the full development of IE, with Fg linked predominantly to the disease induction while Fn is associated with severity of the infection. Taking this into account, FnBPA, which contains both Fg- and Fn-binding sites, should clearly emerge as a key virulence factor in IE. This was demonstrated in a study by Moreillon and colleagues (2001), which showed that FnBPA confers the ability to promote experimental endocarditis when expressed heterologously in non-pathogenic *L. lactis*. Surprisingly, the results presented here appear to contradict these findings by suggesting the Fg-binding site on FnBPA might be redundant. The key element in the discussion regarding the role of the Fg-binding site is the complexity of the IE aetiology. Although Fn alone is predicted to bind FnBPA under normal circumstances, dramatic changes in host local environments in response to vascular injury and/or the onset of infection, could potentially favour the Fg-FnBPA interaction. As discussed in the introduction, exposure of the sub-endothelial matrix due to vessel wall damage triggers a haemostatic response (including release of Fg by platelet  $\alpha$ -granules) leading to the formation of a blood clot, the integrity of which is maintained by fibrin network (Sections 1.4.2 and 1.4.3). Given the increase in local Fg concentration and that fibrin is a polymerised form of Fg containing multiple targets for FnBPA, it is possible the Fg-binding site is engaged and utilized during infection. A study by Niemann and colleagues (2004) suggested that soluble fibrin, rather than Fg, might be the primary mediator for MSCRAMM-mediated *S. aureus* adhesion to platelets. Adding to the complexity of the FnBPA mediated *S. aureus*-host interaction, intact Fg was shown to contain a cryptic Fn-binding site within the  $\alpha$ C region, which is exposed on Fg polymerisation into fibrin (Makogonenko et al., 2002). This implies that apart from binding to cell surface integrins, intact Fn also mediates FnBPA attachment to the ECM. The potential implications of this interaction on the Fg and Fn binding to FnBPA and its physiological relevance within the aetiology of *S. aureus* IE remains to be identified.

One of the drawbacks associated with using AF1 as a model in the cooperativity studies is that only the activities of the neighbouring N2N3 and FnBPA1 regions are assessed. Thus the extent of the steric effects within the context of the intact FnBPA (e.g. how many FnBRs would be occluded by FnBPA-bound Fg) is not considered in the experiments. This could be consolidated by a solid-phase assay and rFnBPA

truncated derivatives expressed heterologously on *L. lactis*. The other aspect of the cooperativity between Fg and Fn binding to FnBPA that was not addressed is the potential effect of the intrinsically disordered N1 domain. N1 is not directly linked to FnBPA1 or the Fg binding site, however the N2N3T structure indicates that N1 might be oriented within a close proximity of the N3-FnBPA1 flexible linker. Although N1 does not bind N2N3, FnBPA1, Fg or Fn and no other role has yet been assigned to N1, it might influence Fg-/Fn-binding to FnBPA due to its disordered nature and position within the FnBPA conformation. This could be tested by utilizing a new rFnBPA construct fAF1 (consisting of N1, N2, N3 and FnBPA1) as a model in the cooperativity studies, instead of AF1.

FnBPA-mediated binding to Fg and Fn is fundamental to platelet aggregation and endothelial cell colonization, events closely associated with development of *S. aureus* IE. It has been shown that the activities of Fg and Fn are intertwined within the context of IE aetiology, however the complex mechanism of *S. aureus* action and the individual roles of FnBPA, Fg and Fn within the overall process remain unknown. The outcomes of this work will contribute to the general understanding of the process by providing new information regarding the structural aspects of the Fg-FnBPA interaction and its potential effects on Fn binding to FnBR.

## 7 Appendices

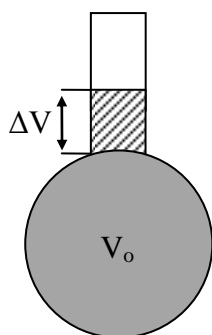
### Appendix I: Composition of growth media

SOLUTION/MEDIUM	COMPOSITION
LB – Kan broth	10 g Tryptone 10 g NaCl 5 g Yeast Extract 50 mg Kanamycin Dissolve in 1 L of H <sub>2</sub> O, pH 7.5
LB Agar	15 g agar 1 L LB pH 7.4
M9 - stock solution (x 10)	60 g Na <sub>2</sub> PO <sub>4</sub> 30 g KH <sub>2</sub> PO <sub>4</sub> 5 g NaCl, Dissolve in 1 L of H <sub>2</sub> O
Trace metals - stock solution (x1000)	1.62 g FeCl <sub>3</sub> 0.30 g CaCl <sub>2</sub> .2H <sub>2</sub> O 0.20 g MnCl <sub>2</sub> .4H <sub>2</sub> O 0.29 g ZnSO <sub>4</sub> .7H <sub>2</sub> O 0.05 g CoCl <sub>2</sub> .6H <sub>2</sub> O 0.03 g CuCl <sub>2</sub> 0.10 g NiCl <sub>2</sub> .6H <sub>2</sub> O 0.05 g Na <sub>2</sub> MoO <sub>4</sub> .2H <sub>2</sub> O 0.05 g NaSeO <sub>3</sub> .5H <sub>2</sub> O 0.01 g H <sub>3</sub> BO <sub>3</sub> Dissolve in 100 ml of H <sub>2</sub> O
Vitamins - stock solution (x1000)	0.1 g Riboflavin 0.1 g Nicotinamide 0.1 g Pyridoxine 0.1 g Thiamine Dissolve in 100 ml of H <sub>2</sub> O
Minimal M9 growth media	100 ml M9 (x 10) 0.5 g <sup>15</sup> N NH <sub>4</sub> Cl 1 ml trace elements (x1000) 1 ml vitamins (x1000) 20 ml glucose (20% (w/v)) 0.50 g MgSO <sub>4</sub> 0.22 g CaCl <sub>2</sub> 50 mg Kanamycin Dissolve in 1 L of H <sub>2</sub> O, pH 7.4

## Appendix II: Equations used for fitting ITC binding data

### Volume displacement effect

Each ligand injection is associated with displaced volume effects which are corrected for by the Origin software using equations 1 and 2.



$$M_t = M_t^o \left( \frac{1 - \frac{\Delta V}{2V_o}}{1 + \frac{\Delta V}{2V_o}} \right) \quad (1)$$

$$X_t = X_t^o \left( 1 - \frac{\Delta V}{2V_o} \right) \quad (2)$$

$M_t$  – Concentration of the macromolecule in the cell corrected for the displaced volume effects (M)

$X_t$  – Concentration of the ligand in the cell corrected for the displaced volume effects (M)

$M_t^o$  – Initial concentration of the macromolecule in the cell (before the ligand first injection) (M)

$X_t^o$  – Hypothetical ligand concentration in the cell ( $V_o$ ) after injection (M)

$V_o$  – Working (calorimetrically sensed) cell volume (L)

$\Delta V$  – Injected (displaced) volume (L)

### Single set of identical sites model

The binding isotherm is fitted using non-linear least square regression to a binding model represented by Equations 3 and 4.

$$Q = \frac{nM_t \Delta H V_o}{2} \left[ 1 + \frac{X_t}{nM_t} + \frac{1}{nKM_t} - \sqrt{1 + \left( \frac{X_t}{nM_t} + \frac{1}{nKM_t} \right)^2} - \frac{4X_t}{nM_t} \right] \quad (3)$$

$Q$  – Total heat content of the solution within  $V_o$  (cal)

$\Delta H$  – Molar heat of ligand binding (cal)

$K$  – Binding constant ( $M^{-1}$ )

$$\Delta Q(i) = Q(i) + \frac{dV_i}{V_o} \left[ \frac{Q(i) - Q(i-1)}{2} \right] - Q(i-1) \quad (4)$$

$\Delta Q(i)$  – Change of the heat content upon completion of  $i^{\text{th}}$  injection (cal)

$V_i$  – Injection volume (L)

## Appendix III: Sequences of the domains comprising the truncated rFnBPA derivatives

### His<sub>6</sub>-tag

atgggcagcagccatcatcatcatcatcacagcagcggcctggaagttctgttccagggga  
 M G S S H H H H H H S S G L E V L F Q G  
 ccagcaatg  
 P A M

### N1

gcgagcgaacagaaaaccaccaccgtggaagaaaacggcaacagcgcgaccgataacaaa  
 A S E Q K T T T V E E N G N S A T D N K  
 accagcgaaccagaccaccgacccaacgtgaaccatattgaagaaaccagagctat  
 T S E T Q T T A T N V N H I E E T Q S Y  
 aacgcgaccgtgaccgaacagccgagcaacgcgaccaggtgaccaccgaagaagcgcgg  
 N A T V T E Q P S N A T Q V T T E E A P  
 aaagcgggtgcagggcggcagaccgcgagccggcgaacattgaaaccgtgaaagaagaa  
 K A V Q A P Q T A Q P A N I E T V K E E  
 gtggtgaaagaagaagcgaaaccgcaggtgaaagaaccaccagagccaggataacagc  
 V V K E E A K P Q V K E T T Q S Q D N S  
 ggcgatcagcggcaggtgatctgaccccgaaaaagcgaccagaaccaggtggcgga  
 G D Q R Q V D L T P K K A T Q N Q V A E  
 acccaggtggaagtggcgcagccgcgaccgagcgaaagcaaaccgcgctgacccgc  
 T Q V E V A Q P R T A S E S K P R V T R  
 agcgcggatgtggcggaagcgaaagaagcgagcaacgcgaaagtggaaaccggc  
 S A D V A E A K E A S N A K V E T G

### N2

acagatgtaacaagtaaagttacagtagaaaattggttctattgaggggcataacaataca  
 T D V T S K V T V E I G S I E G H N N T  
 aataaagtagaacctcatgcaggacaacgagcgggtactaaaatataagttgaaatttgag  
 N K V E P H A G Q R A V L K Y K L K F E  
 aatggtttacatcaaggtgactactttgactttactttatcaaataatgtaaatacgc  
 N G L H Q G D Y F D F T L S N N V N T H  
 ggcgatcaactgctagaaaagtaccagaaattaaatggttcagtcgtaatggcgaca  
 G V S T A R K V P E I K N G S V V M A T  
 ggtgaagttttagaaggtggaaagattagatatacattttacaaatgatattgaagataag  
 G E V L E G G K I R Y T F T N D I E D K  
 gttgatgtaacggctgaactagaaattaattttattttattgatcctaaaactgtacaaact  
 V D V T A E L E I N L F I D P K T V Q T  
 aatggaaatcaaactataaacttcaactaaatgaagaacaaacttcaaaggaattagat  
 N G N Q T I T S T L N E E Q T S K E L D  
 gttaaatat  
 V K Y

**N3**

aaagatgggtattgggaattattatgccaatTTAAATGGATCGATTGAGACATTTAATAAA  
K D G I G N Y Y A N L N G S I E T F N K  
gcgaataatagatTTTCGCATGTTGCATTTATTAACCTAATAATGGTAAAACGACAAGT  
A N N R F S H V A F I K P N N G K T T S  
gtgactgttactggaactTTAATGAAAGGTAGTAATCAGAATGGAAATCAACAAAAGTT  
V T V T G T L M K G S N Q N G N Q P K V  
aggatatttgaataacttgggtaataatgaagacatagcgaagagtgtatatgcaaatacg  
R I F E Y L G N N E D I A K S V Y A N T  
acagatacttctaaatTTAAAGAAGTCACAAGTAATATGAGTGGGAATTTGAATTTACAA  
T D T S K F K E V T S N M S G N L N L Q  
aataatggaagctattcattgaatatagaaaatctagataaaaacttatgttgttcactat  
N N G S Y S L N I E N L D K T Y V V H Y  
gatggagagtattTAAATGGTACTGATGAAGTTGATTTTAGAACACAAATGGTAGGACAT  
D G E Y L N G T D E V D F R T Q M V G H  
ccagagcaactTTATAAGTATTATTATGATAGAGGATATACCTTAACTTGGGATAATGGT  
P E Q L Y K Y Y Y D R G Y T L T W D N G  
ttagttttatacagtaataaagcgaacggaaatgagaaaaat  
L V L Y S N K A N G N E K N

**FnBPA1**

ggtccgattattcaaaataataaatttgaatataaagaagataacaattaagaaactctt  
G P I I Q N N K F E Y K E D T I K E T L  
acaggTCAATATGATAAGAATTTAGTAACTACTGTTGAAGAGGAATATGATTCATCA  
T G Q Y D K N L V T T V E E E Y D S S



## 8 Abbreviations

ADMIDAS	Adjacent to metal ion-dependent adhesion site
ADP	Adenosine diphosphate
AF1	rFnBPA construct (N2N3-FnBPA1; residues 189-550)
AUC	Analytical ultracentrifugation
bp	base pair
CCP4	Collaborative computational project No. 4
CifA	Clumping factor A ( <i>S. aureus</i> )
CifB	Clumping factor B ( <i>S. aureus</i> )
CNA	Collagen binding protein ( <i>S. aureus</i> )
CSI	Chemical shift anisotropy
CSS	Clear Strategy Screen
CV	Column volume
DD	Dipole-dipole
DNA	Deoxyribonucleic acid
dNTPs	Deoxyribonucleotide triphosphates
DSC	Differential scanning calorimetry
DSS	2,2-Dimethyl-2-silapentane-5-sulfonate
DTT	Dithiothreitol ((2S,3S)-1,4-Bis-sulfanylbutane-2,3-diol)
dTTP	Deoxythymidine triphosphate
ECM	Extracellular matrix
EDC	N-hydroxysuccinimide
EDTA	Ethylenediaminetetraacetic acid (2,2',2'',2'''-(Ethane-1,2-diyl)dinitrilo)tetraacetic acid)
EE	Experimental endocarditis
EGF	Epidermal growth factor
ELISA	Enzyme-linked immunosorbent assay
ESI/MS	Electrospray ionisation mass spectrometry
ESRF	European synchrotron radiation facility
F1	Fibronectin type one module
F2	Fibronectin type two module

F3	Fibronectin type three module
fA	rFnBPA construct (A-domain; residues 37-511)
FcγRIIa	Immunoglobulin G receptor on platelets
Fg	Fibrinogen
Fg1	Synthetic peptide representing the last 17 C-terminal residues of Fg $\gamma$ chain
Fg $\alpha$	Synthetic peptide representing ClfB binding site on Fg $\alpha$ chain
Fg $\beta$	Synthetic peptide representing SdrG binding site on Fg $\beta$ chain
FgD	Fibrinogen proteolytic fragment (D-region)
Fn	Fibronectin
FnBPA	Fibronectin-binding protein A
FnBPA1	First fibronectin-binding repeat
FnBPB	Fibronectin-binding protein B
FnBR	Fibronectin-binding region
FnBRs	Fibronectin-binding repeats
FP	Fluorescent polarisation
G'' (latch)	C-terminal extension of the N3 domain (latch strand)
GPIIaIIIb ( $\alpha_{IIb}\beta_{III}$ )	Glycoprotein IIaIIIb (Platelet integrin; binds fibrinogen and fibronectin)
GPIb/GPVI	Glycoproteins Ib and VI, platelets receptors for collagen and von Willebrand factor
His <sub>6</sub> -	Affinity tag composed of six histidine residues
HPLC	High performance liquid chromatography
HRV 3C	Human rhinovirus 3C protease
HSQC	Heteronuclear single quantum coherence
IDR	Intrinsically disordered region
IE	Infective endocarditis
IEX	Ion-exchange chromatography
IgG	Immunoglobulin G
eR <sub>MAX</sub>	Estimated maximum SPR response
IPTG	Isopropyl $\beta$ -D-1-thiogalactopyranoside
ITC	Isothermal titration calorimetry
K <sub>a</sub>	Association constant

---

$k_a$	Association rate constant
$K_d$	Dissociation constant
$k_d$	Dissociation rate constant
Kan	Kanamycin
LIC	Ligation independent cloning
LB	Luria-Bertani media
MES	2-(N-morpholino)ethanesulfonic acid
MIDAS	Metal ion-dependent adhesion site
mme	Monomethyl ether
MRSA	Methicillin-resistant <i>Staphylococcus aureus</i>
MSCRAMM	Microbial Surface Components Recognising Adhesive Matrix Molecules
MOPS	3-(N-morpholino)propanesulfonic acid
N1	Residues 37-189 of FnBPA
N1N2	Recombinant FnBPA protein (residues 37-335)
N2	Residues 189-335 of FnBPA
N2-E	N2 domain edge strand
N2N3	Recombinant FnBPA protein (residues 189-511)
N2N3T	Recombinant FnBPA protein (residues 189-515)
N2N3E	Recombinant FnBPA protein (residues 189-505)
N3	Residues 335-511 of FnBPA
N3-G'	N3 domain edge strand
NHS	1-ethyl-3-(3-dimethylaminopropyl) carbodiimide
NMR	Nuclear magnetic resonance
NTD	N-terminal domain
OD <sub>600</sub>	Optical density at 600 nm
PBS	Phosphate buffered saline
PCR	Polymerase chain reaction
PDB	Protein data bank
PEG	Polyethylene glycol
pI	Isoelectric point
R <sub>eq</sub>	SPR response generated on steady state binding

---

$R_L$	SPR response generated on ligand immobilization
$R_{MAX}$	Maximum SPR response generated on ligand saturation
r.m.s.d	Root mean square deviation
RNA	Ribonucleic acid
rpm	Rotation per minutes
RU	Response units (response difference)
SDL	Specificity determining loop
SdrG	Serine-aspartate repeat-containing protein G
SDS-PAGE	Sodium dodecyl sulphate polyacrylamide gel electrophoresis
Sfb1-5	Fifth FnBR of Fibronectin-binding protein I of <i>Streptococcus pyogenes</i>
SPR	Surface plasmon resonance
s.s.m.	Secondary structure matching
STAFF1	Synthetic peptide representing residues 508-530 of FnBPA
STATT1	Synthetic peptide representing residues 529-549 of FnBPA
TBE	Tris-Borate-EDTA buffer
TBS	Tris buffered saline
$tR_{MAX}$	Theoretical maximum SPR response generated on ligand saturation
Tris	2-Amino-2-hydroxymethyl-propane-1,3-diol
TROSY	Transverse relaxation optimized spectroscopy
UV	Ultra violet
VRSA	Vancomycin-resistant <i>Staphylococcus aureus</i>
vWF	von Willebrand factor

## 9 References

- ACD, I. (2006) ACD/ChemSketch Freeware. 10.00 ed. Toronto, ON, Canada.
- ADAMS, R. L. & BIRD, R. J. (2009) Review article: Coagulation cascade and therapeutics update: relevance to nephrology. Part 1: Overview of coagulation, thrombophilias and history of anticoagulants. *Nephrology (Carlton)*, 14, 462-70.
- ADHIKARI, R. P., COOK, G. M., LAMONT, I., LANG, S., HEFFERNAN, H. & SMITH, J. M. (2002) Phenotypic and molecular characterization of community occurring, Western Samoan phage pattern methicillin-resistant *Staphylococcus aureus*. *J Antimicrob Chemother*, 50, 825-31.
- AGERER, F., LUX, S., MICHEL, A., ROHDE, M., OHLSEN, K. & HAUCK, C. R. (2005) Cellular invasion by *Staphylococcus aureus* reveals a functional link between focal adhesion kinase and cortactin in integrin-mediated internalisation. *J Cell Sci*, 118, 2189-200.
- ALTSCHUL, S. F., MADDEN, T. L., SCHAFFER, A. A., ZHANG, J., ZHANG, Z., MILLER, W. & LIPMAN, D. J. (1997) Gapped BLAST and PSI-BLAST: a new generation of protein database search programs. *Nucleic Acids Res*, 25, 3389-402.
- ANDREWS, R. K. & BERNDT, M. C. (2004) Platelet physiology and thrombosis. *Thromb Res*, 114, 447-53.
- ANDREWS, R. K., GARDINER, E. E., SHEN, Y. & BERNDT, M. C. (2004) Platelet interactions in thrombosis. *IUBMB Life*, 56, 13-8.
- ARRECUBIETA, C., ASAI, T., BAYERN, M., LOUGHMAN, A., FITZGERALD, J. R., SHELTON, C. E., BARON, H. M., DANG, N. C., DENG, M. C., NAKA, Y., FOSTER, T. J. & LOWY, F. D. (2006) The role of *Staphylococcus aureus* adhesins in the pathogenesis of ventricular assist device-related infections. *Journal of Infectious Diseases*, 193, 1109-1119.
- ASHERIE, N. (2004) Protein crystallization and phase diagrams. *Methods*, 34, 266-72.
- BABA, T., TAKEUCHI, F., KURODA, M., YUZAWA, H., AOKI, K., OGUCHI, A., NAGAI, Y., IWAMA, N., ASANO, K., NAIMI, T., KURODA, H., CUI, L., YAMAMOTO, K. & HIRAMATSU, K. (2002) Genome and virulence determinants of high virulence community-acquired MRSA. *Lancet*, 359, 1819-27.

- BADDOUR, L. M., WILSON, W. R., BAYER, A. S., FOWLER, V. G., JR., BOLGER, A. F., LEVISON, M. E., FERRIERI, P., GERBER, M. A., TANI, L. Y., GEWITZ, M. H., TONG, D. C., STECKELBERG, J. M., BALTIMORE, R. S., SHULMAN, S. T., BURNS, J. C., FALACE, D. A., NEWBURGER, J. W., PALLASCH, T. J., TAKAHASHI, M. & TAUBERT, K. A. (2005) Infective endocarditis: diagnosis, antimicrobial therapy, and management of complications: a statement for healthcare professionals from the Committee on Rheumatic Fever, Endocarditis, and Kawasaki Disease, Council on Cardiovascular Disease in the Young, and the Councils on Clinical Cardiology, Stroke, and Cardiovascular Surgery and Anesthesia, American Heart Association: endorsed by the Infectious Diseases Society of America. *Circulation*, 111, e394-434.
- BARBU, E. M., GANESH, V. K., GURUSIDDAPPA, S., MACKENZIE, R. C., FOSTER, T. J., SUDHOF, T. C. & HOOK, M. (2010) beta-Neurexin Is a Ligand for the Staphylococcus aureus MSCRAMM SdrC. *Plos Pathogens*, 6, 11.
- BENITO, N., MIRO, J. M., DE LAZZARI, E., CABELL, C. H., DEL RIO, A., ALTCLAS, J., COMMERFORD, P., DELAHAYE, F., DRAGULESCU, S., GIAMARELLOU, H., HABIB, G., KAMARULZAMAN, A., KUMAR, A. S., NACINOVICH, F. M., SUTER, F., TRIBOUILLOY, C., VENUGOPAL, K., MORENO, A. & FOWLER, V. G., JR. (2009) Health care-associated native valve endocarditis: importance of non-nosocomial acquisition. *Ann Intern Med*, 150, 586-94.
- BENNETT, J. S. (2005) Structure and function of the platelet integrin alpha(IIb)beta(3). *Journal of Clinical Investigation*, 115, 3363-3369.
- BERA, A., HERBERT, S., JAKOB, A., VOLLMER, W. & GOTZ, F. (2005) Why are pathogenic staphylococci so lysozyme resistant? The peptidoglycan O-acetyltransferase OatA is the major determinant for lysozyme resistance of Staphylococcus aureus. *Mol Microbiol*, 55, 778-87.
- BERGFORS, T. (2003) Seeds to crystals. *J Struct Biol*, 142, 66-76.
- BERGQVIST, S. (1950) Observations concerning the presence of pyrogenic staphylococci in the nose and their relationship to the antistaphylolysin titre. *Acta Med Scand*, 136, 343-50.

- BINGHAM, R. J., RUDINO-PINERA, E., MEENAN, N. A. G., SCHWARZ-LINEK, U., TURKENBURG, J. P., HOOK, M., GARMAN, E. F. & POTTS, J. R. (2008) Crystal structures of fibronectin-binding sites from *Staphylococcus aureus* FnBPA in complex with fibronectin domains. *Proceedings of the National Academy of Sciences of the United States of America*, 105, 12254-12258.
- BLAIR, P. & FLAUMENHAFT, R. (2009) Platelet alpha-granules: basic biology and clinical correlates. *Blood Rev*, 23, 177-89.
- BLOMBACK, B., HESSEL, B., HOGG, D. & THERKILDSEN, L. (1978) A two-step fibrinogen--fibrin transition in blood coagulation. *Nature*, 275, 501-5.
- BLOW, D. (2002) *Outline of Crystallography for Biologists*, Oxford, Oxford University Press.
- BLUMENSTEIN, M., MATSUEDA, G. R., TIMMONS, S. & HAWIGER, J. (1992) A BETA-TURN IS PRESENT IN THE 392-411 SEGMENT OF THE HUMAN FIBRINOGEN GAMMA-CHAIN - EFFECTS OF STRUCTURAL-CHANGES IN THIS SEGMENT ON AFFINITY TO ANTIBODY 4A5. *Biochemistry*, 31, 10692-10698.
- BONSOR, D., BUTZ, S. F., SOLOMONS, J., GRANT, S., FAIRLAMB, I. J. S., FOGG, M. J. & GROGAN, G. (2006) Ligation independent cloning (LIC) as a rapid route to families of recombinant biocatalysts from sequenced prokaryotic genomes. *Organic & Biomolecular Chemistry*, 4, 1252-1260.
- BOWDEN, M. G., DAVIS, S. L., GURUSIDDAPPA, S., LIANG, X., KARTHE, P., NARAYANA, S. V. L. & HOOK, M. (2003) A "dock, lock and latch" structural model for staphylococcal fibrinogen-binding adhesins. *Abstracts of the General Meeting of the American Society for Microbiology*, 103, B-095.
- BOWDEN, M. G., HEUCK, A. P., PONNURAJ, K., KOLOSOVA, E., CHOE, D., GURUSIDDAPPA, S., NARAYANA, S. V. L., JOHNSON, A. E. & HOOK, M. (2008) Evidence for the "Dock, Lock, and Latch" ligand binding mechanism of the staphylococcal microbial surface component recognizing adhesive matrix molecules (MSCRAMM) SdrG. *Journal of Biological Chemistry*, 283, 638-647.
- BRANDEN, C. & TOOZE, J. (1991) *Introduction to Protein Structure*, New York, Garland Publishing.

- BUNDI, A. & WUTHRICH, K. (1977)  $^1\text{H}$  NMR titration shifts of amide proton resonances in polypeptide chains. *FEBS Lett*, 77, 11-4.
- BUNDI, A. & WUTHRICH, K. (1979a) H-1-Nmr Parameters of the Common Amino-Acid Residues Measured in Aqueous-Solutions of the Linear Tetrapeptides H-Gly-Gly-X-L-Ala-Oh. *Biopolymers*, 18, 285-297.
- BUNDI, A. & WUTHRICH, K. (1979b) Use of Amide H-1-Nmr Titration Shifts for Studies of Polypeptide Conformation. *Biopolymers*, 18, 299-311.
- BURKE, F. M., MCCORMACK, N., RINDI, S., SPEZIALE, P. & FOSTER, T. J. (2010) Fibronectin-binding protein B variation in *Staphylococcus aureus*. *BMC Microbiology*, 10, 15.
- CDC (2008) Public Health Image Library.
- CHEN, V. B., ARENDALL, W. B., 3RD, HEADD, J. J., KEEDY, D. A., IMMORMINO, R. M., KAPRAL, G. J., MURRAY, L. W., RICHARDSON, J. S. & RICHARDSON, D. C. (2010) MolProbity: all-atom structure validation for macromolecular crystallography. *Acta Crystallogr D Biol Crystallogr*, 66, 12-21.
- CHESNEY, P. J., BERGDOLL, M. S., DAVIS, J. P. & VERGERONT, J. M. (1984) The disease spectrum, epidemiology, and etiology of toxic-shock syndrome. *Annu Rev Microbiol*, 38, 315-38.
- CHIROUZE, C., CABELL, C. H., FOWLER, V. G., JR., KHAYAT, N., OLAISON, L., MIRO, J. M., HABIB, G., ABRUTYN, E., EYKYN, S., COREY, G. R., SELTON-SUTY, C. & HOEN, B. (2004) Prognostic factors in 61 cases of *Staphylococcus aureus* prosthetic valve infective endocarditis from the International Collaboration on Endocarditis merged database. *Clin Infect Dis*, 38, 1323-7.
- CLARO, T., WIDAA, A., O'SEAGHDHA, M., MIAJLOVIC, H., FOSTER, T. J., O'BRIEN, F. J. & KERRIGAN, S. W. (2011) *Staphylococcus aureus* protein A binds to osteoblasts and triggers signals that weaken bone in osteomyelitis. *PLoS One*, 6, e18748.
- CLEGG, W. (1998) *Crystal Structure Determination*, Oxford, Oxford University Press.
- COOPER, A., JOHNSON, C. M., LAKEY, J. H. & NOLLMANN, M. (2001) Heat does not come in different colours: entropy-enthalpy compensation, free energy windows, quantum confinement, pressure perturbation calorimetry,



- solvation and the multiple causes of heat capacity effects in biomolecular interactions. *Biophysical Chemistry*, 93, 215-230.
- COOPER, M. A. (2002) Optical biosensors in drug discovery. *Nat Rev Drug Discov*, 1, 515-28.
- CROFT, L. B., DONNINO, R., SHAPIRO, R., INDES, J., FAYNGERSH, A., SQUIRE, A. & GOLDMAN, M. E. (2004) Age-related prevalence of cardiac valvular abnormalities warranting infectious endocarditis prophylaxis. *Am J Cardiol*, 94, 386-9.
- DAVEY, R. & GARSIDE, J. (2000) *From Molecules to Crystallizers: An Introduction to Crystallization*, NY, Oxford University Press.
- DAVIS, S. L., GURUSIDDAPPA, S., MCCREA, K. W., PERKINS, S. & HOOK, M. (2001) SdrG, a fibrinogen-binding bacterial adhesin of the microbial surface components recognizing adhesive matrix molecules subfamily from *Staphylococcus epidermidis*, targets the thrombin cleavage site in the Bbeta chain. *J Biol Chem*, 276, 27799-805.
- DE SA, D. D., TLEYJEH, I. M., ANAVEKAR, N. S., SCHULTZ, J. C., THOMAS, J. M., LAHR, B. D., BACHUWAR, A., PAZDERNIK, M., STECKELBERG, J. M., WILSON, W. R. & BADDOUR, L. M. (2010) Epidemiological trends of infective endocarditis: a population-based study in Olmsted County, Minnesota. *Mayo Clin Proc*, 85, 422-6.
- DEIVANAYAGAM, C. C. S., WANN, E. R., CHEN, W., CARSON, M., RAJASHANKAR, K. R., HOOK, M. & NARAYANA, S. V. L. (2002) A novel variant of the immunoglobulin fold in surface adhesins of *Staphylococcus aureus*: crystal structure of the fibrinogen-binding MSCRAMM, clumping factor A. *Embo Journal*, 21, 6660-6672.
- DELAGLIO, F., GRZESIEK, S., VUISTER, G. W., ZHU, G., PFEIFER, J. & BAX, A. (1995) Nmrpipe - a Multidimensional Spectral Processing System Based on Unix Pipes. *Journal of Biomolecular Nmr*, 6, 277-293.
- DELAHAYE, F., GOULET, V., LACASSIN, F., ECOCHARD, R., SELTON-SUTY, C., HOEN, B., ETIENNE, J., BRIANCON, S. & LEPORT, C. (1995) Characteristics of infective endocarditis in France in 1991. A 1-year survey. *Eur Heart J*, 16, 394-401.
- DERRICK, J. P. & WIGLEY, D. B. (1992) Crystal structure of a streptococcal protein G domain bound to an Fab fragment. *Nature*, 359, 752-4.

- DIEKEMA, D. J., PFALLER, M. A., SCHMITZ, F. J., SMAYEVSKY, J., BELL, J., JONES, R. N. & BEACH, M. (2001) Survey of infections due to Staphylococcus species: frequency of occurrence and antimicrobial susceptibility of isolates collected in the United States, Canada, Latin America, Europe, and the Western Pacific region for the SENTRY Antimicrobial Surveillance Program, 1997-1999. *Clin Infect Dis*, 32 Suppl 2, S114-32.
- DODSON, E. (2008) The before and afters of molecular replacement. *Acta Crystallogr D Biol Crystallogr*, 64, 17-24.
- DOOLITTLE, R. F., CHEN, R. & LAU, F. (1971) Hybrid fibrin: proof of the intermolecular nature of - crosslinking units. *Biochem Biophys Res Commun*, 44, 94-100.
- DRENTH, J. (2007) *Principles of Protein X-Ray Crystallography*, NY, Springer.
- DU, X. P., PLOW, E. F., FRELINGER, A. L., OTOOLE, T. E., LOFTUS, J. C. & GINSBERG, M. H. (1991) LIGANDS ACTIVATE INTEGRIN ALPHA-IIIB-BETA-3 (PLATELET GPIIB-IIIA). *Cell*, 65, 409-416.
- DUFOUR, P., GILLET, Y., BES, M., LINA, G., VANDENESCH, F., FLORET, D., ETIENNE, J. & RICHEL, H. (2002) Community-acquired methicillin-resistant Staphylococcus aureus infections in France: emergence of a single clone that produces Panton-Valentine leukocidin. *Clin Infect Dis*, 35, 819-24.
- DUNCAN, I. B., COLLINS, A. M., NEELIN, E. M. & ROY, T. E. (1957) Nasal carriage of staphylococcus pyogenes by student nurses. *Can Med Assoc J*, 77, 1001-9.
- EDGCOMB, S. P. & MURPHY, K. P. (2000) Structural energetics of protein folding and binding. *Current Opinion in Biotechnology*, 11, 62-66.
- EDWARDS, A. M. & MASSEY, R. C. (2011) How does Staphylococcus aureus escape the bloodstream? *Trends Microbiol*, 19, 184-90.
- EDWARDS, A. M., POTTS, J. R., JOSEFSSON, E. & MASSEY, R. C. (2010) Staphylococcus aureus Host Cell Invasion and Virulence in Sepsis Is Facilitated by the Multiple Repeats within FnBPA. *Plos Pathogens*, 6, 16.
- EMSLEY, P. & COWTAN, K. (2004) Coot: model-building tools for molecular graphics. *Acta Crystallographica Section D-Biological Crystallography*, 60, 2126-2132.

- ERICKSON, H. P. & CARRELL, N. A. (1983) Fibronectin in extended and compact conformations. Electron microscopy and sedimentation analysis. *J Biol Chem*, 258, 14539-44.
- EVANS, P. (2006) Scaling and assessment of data quality. *Acta Crystallogr D Biol Crystallogr*, 62, 72-82.
- FERRY, J. D. (1952) The Mechanism of Polymerization of Fibrinogen. *Proc Natl Acad Sci U S A*, 38, 566-9.
- FITZGERALD, J. R. & ET AL (2006) Fibronectin-binding proteins of *Staphylococcus aureus* mediate activation of human platelets via fibrinogen and fibronectin bridges to integrin GPIIb/IIIa and IgG binding to the FcγRIIa receptor. *Molecular Microbiology*, 59, 212-230.
- FITZGERALD, J. R., FOSTER, T. J. & COX, D. (2006a) The interaction of bacterial pathogens with platelets. *Nature Reviews Microbiology*, 4, 445-457.
- FITZGERALD, J. R., LOUGHMAN, A., KEANE, F., BRENNAN, M., KNOBEL, M., HIGGINS, J., VISAI, L., SPEZIALE, P., COX, D. & FOSTER, T. J. (2006b) Fibronectin-binding proteins of *Staphylococcus aureus* mediate activation of human platelets via fibrinogen and fibronectin bridges to integrin GPIIb/IIIa and IgG binding to the FcγRIIa receptor. *Mol Microbiol*, 59, 212-30.
- FLUIT, A. C., VERHOEF, J. & SCHMITZ, F. J. (2001) Frequency of isolation and antimicrobial resistance of gram-negative and gram-positive bacteria from patients in intensive care units of 25 European university hospitals participating in the European arm of the SENTRY Antimicrobial Surveillance Program 1997-1998. *Eur J Clin Microbiol Infect Dis*, 20, 617-25.
- FOSTER, T. J. (2004) The *Staphylococcus aureus* "superbug". *Journal of Clinical Investigation*, 114, 1693-1696.
- FOSTER, T. J. (2005) Immune evasion by *Staphylococci*. *Nature Reviews Microbiology*, 3, 948-958.
- FOSTER, T. J. & HOOK, M. (1998) Surface protein adhesins of *Staphylococcus aureus*. *Trends in Microbiology*, 6, 484-488.
- FOWLER, W. E., HANTGAN, R. R., HERMANS, J. & ERICKSON, H. P. (1981) Structure of the fibrin protofibril. *Proc Natl Acad Sci U S A*, 78, 4872-6.

- FRIEDLAND, J. C., LEE, M. H. & BOETTIGER, D. (2009) Mechanically activated integrin switch controls alpha5beta1 function. *Science*, 323, 642-4.
- FROMAN, G., SWITALSKI, L. M., SPEZIALE, P. & HOOK, M. (1987) Isolation and characterization of a fibronectin receptor from *Staphylococcus aureus*. *J Biol Chem*, 262, 6564-71.
- FURIE, B. & FURIE, B. C. (2005) Thrombus formation in vivo. *J Clin Invest*, 115, 3355-62.
- GANESH, V. K., BARBU, E. M., DEIVANAYAGAM, C. C., LE, B., ANDERSON, A. S., MATSUKA, Y. V., LIN, S. L., FOSTER, T. J., NARAYANA, S. V. & HOOK, M. (2011) Structural and biochemical characterization of *Staphylococcus aureus* Clumping Factor B:ligand interactions. *J Biol Chem*.
- GANESH, V. K., RIVERA, J. J., SMEDS, E., KO, Y. P., BOWDEN, M. G., WANN, E. R., GURUSIDDAPPA, S., FITZGERALD, J. R. & HOOK, M. (2008) A Structural Model of the *Staphylococcus aureus* ClfA-Fibrinogen Interaction Opens New Avenues for the Design of Anti-Staphylococcal Therapeutics. *Plos Pathogens*, 4, 10.
- GASTEIGER, E., GATTIKER, A., HOOGLAND, C., IVANYI, I., APPEL, R. D. & BAIROCH, A. (2003) ExPASy: The proteomics server for in-depth protein knowledge and analysis. *Nucleic Acids Res*, 31, 3784-8.
- GEDIG, E. T. (2008) Surface Chemistry in SPR Technology. IN SCHASFOORT, R. B. M. & TUDOS, A. J. (Eds.) *Handbook of Surface Plasmon Resonance*. Cambridge, RSC Publishing.
- GEORGE, J. N. (2000) Platelets. *Lancet*, 355, 1531-9.
- GEORGE, J. N., CAEN, J. P. & NURDEN, A. T. (1990) Glanzmann's thrombasthenia: the spectrum of clinical disease. *Blood*, 75, 1383-95.
- GEORGE, J. N. & SHATTIL, S. J. (1991) The clinical importance of acquired abnormalities of platelet function. *N Engl J Med*, 324, 27-39.
- GOLOVANOV, A. P., HAUTBERGUE, G. M., WILSON, S. A. & LIAN, L. Y. (2004) A simple method for improving protein solubility and long-term stability. *Journal of the American Chemical Society*, 126, 8933-8939.
- GOULD, J. C. & MC, K. E. (1954) The carriage of *Staphylococcus pyogenes* var. *aureus* in the human nose. *J Hyg (Lond)*, 52, 304-10.

- GUNASEKARAN, K., TSAI, C. J., KUMAR, S., ZANUY, D. & NUSSINOV, R. (2003) Extended disordered proteins: targeting function with less scaffold. *Trends Biochem Sci*, 28, 81-5.
- HABIB, G., HOEN, B., TORNOS, P., THUNY, F., PRENDERGAST, B., VILACOSTA, I., MOREILLON, P., DE JESUS ANTUNES, M., THILEN, U., LEKAKIS, J., LENGYEL, M., MULLER, L., NABER, C. K., NIHOYANNOPOULOS, P., MORITZ, A. & ZAMORANO, J. L. (2009) Guidelines on the prevention, diagnosis, and treatment of infective endocarditis (new version 2009): the Task Force on the Prevention, Diagnosis, and Treatment of Infective Endocarditis of the European Society of Cardiology (ESC). Endorsed by the European Society of Clinical Microbiology and Infectious Diseases (ESCMID) and the International Society of Chemotherapy (ISC) for Infection and Cancer. *Eur Heart J*, 30, 2369-413.
- HALL, D. A., KOOI, C. W. V., STASIK, C. N., STEVENS, S. Y., ZUIDERWEG, E. R. P. & MATTHEWS, R. G. (2001) Mapping the interactions between flavodoxin and its physiological partners flavodoxin reductase and cobalamin-dependent methionine synthase. *Proceedings of the National Academy of Sciences of the United States of America*, 98, 9521-9526.
- HASBUN, R., VIKRAM, H. R., BARAKAT, L. A., BUENCONSEJO, J. & QUAGLIARELLO, V. J. (2003) Complicated left-sided native valve endocarditis in adults: risk classification for mortality. *JAMA*, 289, 1933-40.
- HAWIGER, J., TIMMONS, S., STRONG, D. D., COTTRELL, B. A., RILEY, M. & DOOLITTLE, R. F. (1982) IDENTIFICATION OF A REGION OF HUMAN-FIBRINOGEN INTERACTING WITH STAPHYLOCOCCAL CLUMPING FACTOR. *Biochemistry*, 21, 1407-1413.
- HEILMANN, C., NIEMANN, S., SINHA, B., HERRMANN, M., KEHREL, B. E. & PETERS, G. (2004) Staphylococcus aureus fibronectin-binding protein (FnBP)-mediated adherence to platelets, and aggregation of platelets induced by FnBPA but not by FnBPB. *Journal of Infectious Diseases*, 190, 321-329.
- HENDERSON, B., NAIR, S., PALLAS, J. & WILLIAMS, M. A. (2010) Fibronectin: a multidomain host adhesin targeted by bacterial fibronectin-binding proteins. *Fems Microbiology Reviews*, 35, 147-200.

- HERRICK, S., BLANC-BRUDE, O., GRAY, A. & LAURENT, G. (1999) Fibrinogen. *International Journal of Biochemistry & Cell Biology*, 31, 741-746.
- HEYING, R., VAN DE GEVEL, J., QUE, Y. A., MOREILLON, P. & BEEKHUIZEN, H. (2007) Fibronectin-binding proteins and clumping factor A in *Staphylococcus aureus* experimental endocarditis: FnBPA is sufficient to activate human endothelial cells. *Thrombosis and Haemostasis*, 97, 617-626.
- HEYING, R., VAN DE GEVEL, J., QUE, Y. A., PIROTH, L., MOREILLON, P. & BEEKHUIZEN, H. (2009) Contribution of (sub)domains of *Staphylococcus aureus* fibronectin-binding protein to the proinflammatory and procoagulant response of human vascular endothelial cells. *Thromb Haemost*, 101, 495-504.
- HIRAMATSU, K., ARITAKA, N., HANAKI, H., KAWASAKI, S., HOSODA, Y., HORI, S., FUKUCHI, Y. & KOBAYASHI, I. (1997) Dissemination in Japanese hospitals of strains of *Staphylococcus aureus* heterogeneously resistant to vancomycin. *Lancet*, 350, 1670-3.
- HOEKSTRA, W. J., BEAVERS, M. P., ANDRADEGORDON, P., EVANGELISTO, M. F., KEANE, P. M., PRESS, J. B., TOMKO, K. A., FAN, F., KLOCZEWIAK, M., MAYO, K. H., DURKIN, K. A. & LIOTTA, D. C. (1995) DESIGN AND EVALUATION OF NONPEPTIDE FIBRINOGEN GAMMA-CHAIN BASED GPIIB/IIIa ANTAGONISTS. *Journal of Medicinal Chemistry*, 38, 1582-1592.
- HOWE, P. W. (2004) A straight-forward method of optimising protein solubility for NMR. *J Biomol NMR*, 30, 283-6.
- HUMPHRIES, M. J. (2000) Integrin structure. *Biochemical Society Transactions*, 28, 311-340.
- HUTSELL, S. Q., KIMPLE, R. J., SIDEROVSKI, D. P., WILLARD, F. S. & KIMPLE, A. J. (2011) High-affinity immobilization of proteins using biotin- and GST-based coupling strategies. *Methods Mol Biol*, 627, 75-90.
- HYNES, R. O. (1985) FIBRONECTINS - MULTIFUNCTIONAL MODULAR GLYCOPROTEINS. *Federation Proceedings*, 44, R7-R7.
- HYNES, R. O. (1992) Integrins - Versatility, Modulation, and Signaling in Cell-Adhesion. *Cell*, 69, 11-25.

- HYNES, R. O. & YAMADA, K. M. (1982) Fibronectins: multifunctional modular glycoproteins. *J Cell Biol*, 95, 369-77.
- INDYK, L. & FISHER, H. F. (1998) Theoretical aspects of isothermal titration calorimetry. *Methods Enzymol*, 295, 350-64.
- JACKSON, S. P. (2007) The growing complexity of platelet aggregation. *Blood*, 109, 5087-5095.
- JELESAROV, I. & BOSSHARD, H. R. (1999) Isothermal titration calorimetry and differential scanning calorimetry as complementary tools to investigate the energetics of biomolecular recognition. *J Mol Recognit*, 12, 3-18.
- JOHNSON, B. A. & BLEVINS, R. A. (1994) Nmr View - a Computer-Program for the Visualization and Analysis of Nmr Data. *Journal of Biomolecular Nmr*, 4, 603-614.
- JOHNSON, K. J., SAGE, H., BRISCOE, G. & ERICKSON, H. P. (1999) The compact conformation of fibronectin is determined by intramolecular ionic interactions. *J Biol Chem*, 274, 15473-9.
- JOHNSON, B., LOFAS, S. & LINDQUIST, G. (1991) IMMOBILIZATION OF PROTEINS TO A CARBOXYMETHYLDEXTRAN-MODIFIED GOLD SURFACE FOR BIOSPECIFIC INTERACTION ANALYSIS IN SURFACE-PLASMON RESONANCE SENSORS. *Analytical Biochemistry*, 198, 268-277.
- JOSEFSSON, E., HIGGINS, J., FOSTER, T. J. & TARKOWSKI, A. (2008) Fibrinogen Binding Sites P-336 and Y-338 of Clumping Factor A Are Crucial for Staphylococcus aureus Virulence. *Plos One*, 3, 7.
- KAMATH, S. & LIP, G. Y. (2003) Fibrinogen: biochemistry, epidemiology and determinants. *QJM*, 96, 711-29.
- KARLSSON, R., MICHAELSSON, A. & MATTSSON, L. (1991) Kinetic-Analysis of Monoclonal Antibody-Antigen Interactions with a New Biosensor Based Analytical System. *Journal of Immunological Methods*, 145, 229-240.
- KEANE, F. M., CLARKE, A. W., FOSTER, T. J. & WEISS, A. S. (2007a) The N-terminal a domain of Staphylococcus aureus fibronectin-binding protein a binds to tropoelastin. *Biochemistry*, 46, 7226-7232.
- KEANE, F. M., LOUGHMAN, A., VALTULINA, V., BRENNAN, M., SPEZIALE, P. & FOSTER, T. J. (2007b) Fibrinogen and elastin bind to the same region

- within the A domain of fibronectin binding protein A, an MSCRAMM of *Staphylococcus aureus*. *Molecular Microbiology*, 63, 711-723.
- KELLY, A. E., OU, H. D., WITHERS, R. & DOTSCHE, V. (2002) Low-conductivity buffers for high-sensitivity NMR measurements. *J Am Chem Soc*, 124, 12013-9.
- KERRIGAN, S. W. & COX, D. (2009) Platelet-bacterial interactions. *Cellular and Molecular Life Sciences*, 67, 513-523.
- KOLLMAN, J. M., PANDI, L., SAWAYA, M. R., RILEY, M. & DOOLITTLE, R. F. (2009) Crystal Structure of Human Fibrinogen. *Biochemistry*, 48, 3877-3886.
- KRISSINEL, E. & HENRICK, K. (2004) Secondary-structure matching (SSM), a new tool for fast protein structure alignment in three dimensions. *Acta Crystallographica Section D-Biological Crystallography*, 60, 2256-2268.
- KRISSINEL, E. & HENRICK, K. (2007) Inference of macromolecular assemblies from crystalline state. *J Mol Biol*, 372, 774-97.
- KUUSELA, P. (1978) Fibronectin Binds to *Staphylococcus-Aureus*. *Nature*, 276, 718-720.
- KYTE, J. & DOOLITTLE, R. F. (1982) A simple method for displaying the hydrophobic character of a protein. *J Mol Biol*, 157, 105-32.
- LAMZIN, V. S. & WILSON, K. S. (1993) AUTOMATED REFINEMENT OF PROTEIN MODELS. *Acta Crystallographica Section D-Biological Crystallography*, 49, 129-147.
- LARKIN, M. A., BLACKSHIELDS, G., BROWN, N. P., CHENNA, R., MCGETTIGAN, P. A., MCWILLIAM, H., VALENTIN, F., WALLACE, I. M., WILM, A., LOPEZ, R., THOMPSON, J. D., GIBSON, T. J. & HIGGINS, D. G. (2007) Clustal W and Clustal X version 2.0. *Bioinformatics*, 23, 2947-8.
- LAUE, T. M., SHAH, B. D., RIDGEWAY, T. M. & PELLETIER, S. L. (1992) Computer-aided interpretation of analytical sedimentation data for proteins. IN HARDING, S. E., ROWE, A. J. & HORTON, J. C. (Eds.) *Analytical Ultracentrifugation in Biochemistry and Polymer Science*. Cambridge, The Royal Society of Chemistry.
- LOFAS, S., JOHANSSON, B., EDSTROM, A., HANSSON, A., LINDQUIST, G., HILLGREN, R. M. M. & STIGH, L. (1995) Methods for Site Controlled



- Coupling to Carboxymethyl-dextran Surfaces in Surface-Plasmon Resonance Sensors. *Biosensors & Bioelectronics*, 10, 813-822.
- LONG, F., VAGIN, A. A., YOUNG, P. & MURSHUDOV, G. N. (2008) BALBES: a molecular-replacement pipeline. *Acta Crystallographica Section D-Biological Crystallography*, 64, 125-132.
- LOUGHMAN, A., FITZGERALD, J. R., BRENNAN, M. P., HIGGINS, J., DOWNER, R., COX, D. & FOSTER, T. J. (2005) Roles for fibrinogen, immunoglobulin and complement in platelet activation promoted by *Staphylococcus aureus* clumping factor A. *Molecular Microbiology*, 57, 804-818.
- LOUGHMAN, A., SWEENEY, T., KEANE, F. M., PIETROCOLA, G., SPEZIALE, P. & FOSTER, T. J. (2008) Sequence diversity in the A domain of *Staphylococcus aureus* fibronectin-binding protein A. *BMC Microbiology*, 8, Article No.: 74.
- LUFT, J. R. & DETITTA, G. T. (1999) A method to produce microseed stock for use in the crystallization of biological macromolecules. *Acta Crystallogr D Biol Crystallogr*, 55, 988-93.
- MAIN, A. L., HARVEY, T. S., BARON, M., BOYD, J. & CAMPBELL, I. D. (1992) The three-dimensional structure of the tenth type III module of fibronectin: an insight into RGD-mediated interactions. *Cell*, 71, 671-8.
- MAKOGONENKO, E., TSURUPA, G., INGHAM, K. & MEDVED, L. (2002) Interaction of fibrin(ogen) with fibronectin: Further characterization and localization of the fibronectin-binding site. *Biochemistry*, 41, 7907-7913.
- MANN, K. G., BRUMMEL-ZIEDINS, K., ORFEO, T. & BUTENAS, S. (2006) Models of blood coagulation. *Blood Cells Mol Dis*, 36, 108-17.
- MAO, Y. & SCHWARZBAUER, J. E. (2005) Fibronectin fibrillogenesis, a cell-mediated matrix assembly process. *Matrix Biol*, 24, 389-99.
- MARLEY, J., LU, M. & BRACKEN, C. (2001) A method for efficient isotopic labeling of recombinant proteins. *J Biomol NMR*, 20, 71-5.
- MASSEY, R. C., KANTZANOU, M. N., FOWLER, T., DAY, N. P. J., SCHOFIELD, K., WANN, E. R., BERENDT, A. R., HOOK, M. & PEACOCK, S. J. (2001) Fibronectin-binding protein A of *Staphylococcus aureus* has multiple, substituting, binding regions that mediate adherence to

- fibronectin and invasion of endothelial cells. *Cellular Microbiology*, 3, 839-851.
- MATSUDA, M., YOSHIDA, N., AOKI, N. & WAKABAYASHI, K. (1978) Distribution of cold-insoluble globulin in plasma and tissues. *Ann N Y Acad Sci*, 312, 74-92.
- MCALISTER, M. S., MOTT, H. R., VAN DER MERWE, P. A., CAMPBELL, I. D., DAVIS, S. J. & DRISCOLL, P. C. (1996) NMR analysis of interacting soluble forms of the cell-cell recognition molecules CD2 and CD48. *Biochemistry*, 35, 5982-91.
- MCCOY, A. J. (2004) Liking likelihood. *Acta Crystallogr D Biol Crystallogr*, 60, 2169-83.
- MCDEVITT, D., FRANCOIS, P., VAUDAUX, P. & FOSTER, T. J. (1995) IDENTIFICATION OF THE LIGAND-BINDING DOMAIN OF THE SURFACE-LOCATED FIBRINOGEN RECEPTOR (CLUMPING FACTOR) OF STAPHYLOCOCCUS-AUREUS. *Molecular Microbiology*, 16, 895-907.
- MCDEVITT, D., NANAVATY, T., HOUSEPOMPEO, K., BELL, E., TURNER, N., MCINTIRE, L., FOSTER, T. & HOOK, M. (1997) Characterization of the interaction between the Staphylococcus aureus clumping factor (ClfA) and fibrinogen. *European Journal of Biochemistry*, 247, 416-424.
- MCNICHOLAS, S., POTTERTON, E., WILSON, K. S. & NOBLE, M. E. (2011) Presenting your structures: the CCP4mg molecular-graphics software. *Acta Crystallogr D Biol Crystallogr*, 67, 386-94.
- MCPHERSON, A. (1999) *Crystallization of Biological Macromolecules*, Cold Spring Harbor, NY, Cold Spring Harbor Laboratory Press.
- MCPHERSON, A. (2004) Introduction to protein crystallization. *Methods*, 34, 254-65.
- MEDVED, L. & WEISEL, J. W. (2009) Recommendations for nomenclature on fibrinogen and fibrin. *Journal of Thrombosis and Haemostasis*, 7, 355-359.
- MEENAN, N. A. G., VISAI, L., VALTULINA, V., SCHWARZ-LINEK, U., NORRIS, N. C., GURUSIDDAPPA, S., HOOK, M., SPEZIALE, P. & POTTS, J. R. (2007) The tandem beta-zipper model defines high affinity fibronectin-binding repeats within staphylococcus aureus FnBPA. *Journal of Biological Chemistry*, 282, 25893-25902.

- MENESTRINA, G., DALLA SERRA, M., COMAI, M., CORAIOLA, M., VIERO, G., WERNER, S., COLIN, D. A., MONTEIL, H. & PREVOST, G. (2003) Ion channels and bacterial infection: the case of beta-barrel pore-forming protein toxins of *Staphylococcus aureus*. *FEBS Lett*, 552, 54-60.
- MICHELSON, A. D. (2003) How platelets work: Platelet function and dysfunction. *Journal of Thrombosis and Thrombolysis*, 16, 7-12.
- MICROCAL, I. (2008) Ultrasensitive Calorimetry for the Life Sciences.
- MOREILLON, P. & QUE, Y. A. (2004) Infective endocarditis. *Lancet*, 363, 139-149.
- MOREILLON, P., QUE, Y. A. & BAYER, A. S. (2002) Pathogenesis of streptococcal and staphylococcal endocarditis. *Infect Dis Clin North Am*, 16, 297-318.
- MOREILLON, P., QUE, Y. A., FRANCOIS, P., HAEFLIGER, J. A., ENTENZA, J. M. & VAUDAUX, P. (2001) Reassessing the role of *Staphylococcus aureus* clumping factor and fibronectin-binding protein by expression in *Lactococcus lactis*. *Infection and Immunity*, 69, 6296-6302.
- MOSESSON, M. W. (2005) Fibrinogen and fibrin structure and functions. *Journal of Thrombosis and Haemostasis*, 3, 1894-1904.
- MULLER, K. M., ARNDT, K. M. & PLUCKTHUN, A. (1998) Model and simulation of multivalent binding to fixed ligands. *Analytical Biochemistry*, 261, 149-158.
- MURDOCH, D. R., COREY, G. R., HOEN, B., MIRO, J. M., FOWLER, V. G., JR., BAYER, A. S., KARCHMER, A. W., OLAISON, L., PAPPAS, P. A., MOREILLON, P., CHAMBERS, S. T., CHU, V. H., FALCO, V., HOLLAND, D. J., JONES, P., KLEIN, J. L., RAYMOND, N. J., READ, K. M., TRIPODI, M. F., UTILI, R., WANG, A., WOODS, C. W. & CABELL, C. H. (2009) Clinical presentation, etiology, and outcome of infective endocarditis in the 21st century: the International Collaboration on Endocarditis-Pro prospective Cohort Study. *Arch Intern Med*, 169, 463-73.
- MURSHUDOV, G. N., VAGIN, A. A. & DODSON, E. J. (1997) Refinement of macromolecular structures by the maximum-likelihood method. *Acta Crystallographica Section D-Biological Crystallography*, 53, 240-255.

- MUSHER, D. M., LAMM, N., DAROUICHE, R. O., YOUNG, E. J., HAMILL, R. J. & LANDON, G. C. (1994) The current spectrum of *Staphylococcus aureus* infection in a tertiary care hospital. *Medicine (Baltimore)*, *73*, 186-208.
- NAIMI, T. S., LEDELL, K. H., BOXRUD, D. J., GROOM, A. V., STEWARD, C. D., JOHNSON, S. K., BESSER, J. M., O'BOYLE, C., DANILA, R. N., CHEEK, J. E., OSTERHOLM, M. T., MOORE, K. A. & SMITH, K. E. (2001) Epidemiology and clonality of community-acquired methicillin-resistant *Staphylococcus aureus* in Minnesota, 1996-1998. *Clin Infect Dis*, *33*, 990-6.
- NESHEIM, M. E., TASWELL, J. B. & MANN, K. G. (1979) The contribution of bovine Factor V and Factor Va to the activity of prothrombinase. *J Biol Chem*, *254*, 10952-62.
- NI, H., DENIS, C. V., SUBBARAO, S., DEGEN, J. L., SATO, T. N., HYNES, R. O. & WAGNER, D. D. (2000) Persistence of platelet thrombus formation in arterioles of mice lacking both von Willebrand factor and fibrinogen. *J Clin Invest*, *106*, 385-92.
- NORMAND, J., BOZIO, A., ETIENNE, J., SASSOLAS, F. & LE BRIS, H. (1995) Changing patterns and prognosis of infective endocarditis in childhood. *Eur Heart J*, *16 Suppl B*, 28-31.
- O'BRIEN, L., KERRIGAN, S. W., KAW, G., HOGAN, M., PENADES, J., LITT, D., FITZGERALD, D. J., FOSTER, T. J. & COX, D. (2002a) Multiple mechanisms for the activation of human platelet aggregation by *Staphylococcus aureus*: roles for the clumping factors ClfA and ClfB, the serine-aspartate repeat protein SdrE and protein A. *Molecular Microbiology*, *44*, 1033-1044.
- O'BRIEN, L. M., WALSH, E. J., MASSEY, R. C., PEACOCK, S. J. & FOSTER, T. J. (2002b) *Staphylococcus aureus* clumping factor B (ClfB) promotes adherence to human type I cytokeratin 10: implications for nasal colonization. *Cell Microbiol*, *4*, 759-70.
- O'SHANNESY, D. J., BRIGHAM-BURKE, M. & PECK, K. (1992) Immobilization chemistries suitable for use in the BIAcore surface plasmon resonance detector. *Anal Biochem*, *205*, 132-6.
- O'SHANNESY, D. J., BRIGHAM-BURKE, M., SONESON, K. K., HENSLEY, P. & BROOKS, I. (1993) Determination of rate and equilibrium binding

- constants for macromolecular interactions using surface plasmon resonance: use of nonlinear least squares analysis methods. *Anal Biochem*, 212, 457-68.
- OTWINOWSKI, Z. & MINOR, W. (1997) Processing of X-ray diffraction data collected in oscillation mode. *Macromolecular Crystallography, Pt A*. San Diego, Academic Press Inc.
- PANKOV, R. & YAMADA, K. M. (2002) Fibronectin at a glance. *J Cell Sci*, 115, 3861-3.
- PATTI, J. M. & HOOK, M. (1994) Microbial Adhesins Recognizing Extracellular-Matrix Macromolecules. *Current Opinion in Cell Biology*, 6, 752-758.
- PATTNAIK, P. (2005) Surface plasmon resonance: applications in understanding receptor-ligand interaction. *Appl Biochem Biotechnol*, 126, 79-92.
- PEACOCK, S. J., DAY, N. P. J., THOMAS, M. G., BERENDT, A. R. & FOSTER, T. J. (2000) Clinical isolates of *Staphylococcus aureus* exhibit diversity in *fnb* genes and adhesion to human fibronectin. *Journal of Infection*, 41, 23-31.
- PELLECCHIA, M., MONTGOMERY, D. L., STEVENS, S. Y., VANDER KOOI, C. W., FENG, H. P., GIERASCH, L. M. & ZUIDERWEG, E. R. (2000) Structural insights into substrate binding by the molecular chaperone DnaK. *Nat Struct Biol*, 7, 298-303.
- PEREIRA, M., RYBARCZYK, B. J., ODRLJIN, T. M., HOCKING, D. C., SOTTILE, J. & SIMPSON-HAIDARIS, P. J. (2002) The incorporation of fibrinogen into extracellular matrix is dependent on active assembly of a fibronectin matrix. *J Cell Sci*, 115, 609-17.
- PERRAKIS, A., SIXMA, T. K., WILSON, K. S. & LAMZIN, V. S. (1997) wARP: Improvement and extension of crystallographic phases by weighted averaging of multiple-refined dummy atomic models. *Acta Crystallographica Section D-Biological Crystallography*, 53, 448-455.
- PERVUSHIN, K., RIEK, R., WIDER, G. & WUTHRICH, K. (1997) Attenuated T2 relaxation by mutual cancellation of dipole-dipole coupling and chemical shift anisotropy indicates an avenue to NMR structures of very large biological macromolecules in solution. *Proc Natl Acad Sci U S A*, 94, 12366-71.
- PETTERSEN, E. F., GODDARD, T. D., HUANG, C. C., COUCH, G. S., GREENBLATT, D. M., MENG, E. C. & FERRIN, T. E. (2004) UCSF

- Chimera--a visualization system for exploratory research and analysis. *J Comput Chem*, 25, 1605-12.
- PIERCE, M. M., RAMAN, C. S. & NALL, B. T. (1999) Isothermal titration calorimetry of protein-protein interactions. *Methods*, 19, 213-21.
- PIROTH, L., QUE, Y. A., WIDMER, E., PANCHAUD, A., PIU, S., ENTENZA, J. M. & MOREILLON, P. (2008) The fibrinogen- and fibronectin-binding domains of *Staphylococcus aureus* fibronectin-binding protein synergistically promote endothelial invasion and experimental endocarditis. *Infection and Immunity*, 76, 3824-3831.
- PONNURAJ, K., BOWDEN, M. G., DAVIS, S., GURUSIDDAPPA, S., MOORE, D., CHOE, D., XU, Y., HOOK, M. & NARAYANA, S. V. L. (2003) A "dock, lock, and latch" structural model for a staphylococcal adhesin binding to fibrinogen. *Cell*, 115, 217-228.
- POTTS, J. R., BRIGHT, J. R., BOLTON, D., PICKFORD, A. R. & CAMPBELL, I. D. (1999) Solution structure of the N-terminal F1 module pair from human fibronectin. *Biochemistry*, 38, 8304-12.
- POTTS, J. R. & CAMPBELL, I. D. (1996) Structure and function of fibronectin modules. *Matrix Biol*, 15, 313-20; discussion 321.
- QUE, Y., HAEFLIGER, J., FRANCOIS, P., PIU, S., SINHA, B., ENTENZA, J., VOUILLAMOZ, J., HERRMANN, M., VAUDAUX, P. & MOREILLON, P. (2001a) Expression of *Staphylococcus aureus* fibronectin-binding protein A (FnBPA) mediates bacterial internalization by endothelial cells in vitro and in rats with experimental endocarditis (EE). *Abstracts of the Interscience Conference on Antimicrobial Agents and Chemotherapy*, 41, 43.
- QUE, Y. A., FRANCOIS, P., HAEFLIGER, J. A., ENTENZA, J. M., VAUDAUX, P. & MOREILLON, P. (2001b) Reassessing the role of *Staphylococcus aureus* clumping factor and fibronectin-binding protein by expression in *Lactococcus lactis*. *Infection and Immunity*, 69, 6296-6302.
- QUE, Y. A., HAEFLIGER, J. A., PIROTH, L., FRANCOIS, P., WIDMER, E., ENTENZA, J. M., SINHA, B., HERRMANN, M., FRANCIOLI, P., VAUDAUX, P. & MOREILLON, P. (2005) Fibrinogen and fibronectin binding cooperate for valve infection and invasion in *Staphylococcus aureus* experimental endocarditis. *Journal of Experimental Medicine*, 201, 1627-1635.

- QUE, Y. A. & MOREILLON, P. (2011) Infective endocarditis. *Nat Rev Cardiol*, 8, 322-36.
- RHODES, G. (2000) *Crystallography Made Crystal Clear*, San Diego, Academic Press.
- RICHARDSON, J. S., GETZOFF, E. D. & RICHARDSON, D. C. (1978) The beta bulge: a common small unit of nonrepetitive protein structure. *Proc Natl Acad Sci U S A*, 75, 2574-8.
- RICHARDSON, J. S. & RICHARDSON, D. C. (2002) Natural beta-sheet proteins use negative design to avoid edge-to-edge aggregation. *Proceedings of the National Academy of Sciences of the United States of America*, 99, 2754-2759.
- RICHARZ, R., SEHR, P., WAGNER, G. & WUTHRICH, K. (1979) Kinetics of the exchange of individual amide protons in the basic pancreatic trypsin inhibitor. *J Mol Biol*, 130, 19-30.
- RIEK, R., WIDER, G., PERVUSHIN, K. & WUTHRICH, K. (1999) Polarization transfer by cross-correlated relaxation in solution NMR with very large molecules. *Proc Natl Acad Sci U S A*, 96, 4918-23.
- RIPPON, J. E. & VOGELSANG, T. M. (1956) Carriage of pathogenic staphylococci in the upper respiratory tract of children. *Acta Pathol Microbiol Scand*, 39, 284-96.
- RIVERA, J., LOZANO, M. L., NAVARRO-NUNEZ, L. & VICENTE, V. (2009) Platelet receptors and signaling in the dynamics of thrombus formation. *Haematologica-the Hematology Journal*, 94, 700-711.
- ROCCO, M., ROSANO, C., WEISEL, J. W., HORITA, D. A. & HANTGAN, R. R. (2008) Integrin conformational regulation: Uncoupling extension/tail separation from changes in the head region by a multiresolution approach. *Structure*, 16, 954-964.
- ROCHE, F. M., DOWNER, R., KEANE, F., SPEZIALE, P., PARK, P. W. & FOSTER, T. J. (2004) The N-terminal A domain of fibronectin-binding proteins A and B promotes adhesion of *Staphylococcus aureus* to elastin. *Journal of Biological Chemistry*, 279, 38433-38440.
- RUGGERI, Z. M., DENT, J. A. & SALDIVAR, E. (1999) Contribution of distinct adhesive interactions to platelet aggregation in flowing blood. *Blood*, 94, 172-178.

- RUGGERI, Z. M. & MENDOLICCHIO, G. L. (2007) Adhesion mechanisms in platelet function. *Circ Res*, 100, 1673-85.
- RUOSLAHTI, E., ENGVALL, E., HAYMAN, E. G. & SPIRO, R. G. (1981) Comparative studies on amniotic fluid and plasma fibronectins. *Biochem J*, 193, 295-9.
- SARAVIA-OTTEN, P., MULLER, H. P. & ARVIDSON, S. (1997) Transcription of *Staphylococcus aureus* fibronectin binding protein genes is negatively regulated by *agr* and an *agr*-independent mechanism. *Journal of Bacteriology*, 179, 5259-5263.
- SCHAFFER, A. C., SOLINGA, R. M., COCCHIARO, J., PORTOLES, M., KISER, K. B., RISLEY, A., RANDALL, S. M., VALTULINA, V., SPEZIALE, P., WALSH, E., FOSTER, T. & LEE, J. C. (2006) Immunization with *Staphylococcus aureus* clumping factor B, a major determinant in nasal carriage, reduces nasal colonization in a murine model. *Infect Immun*, 74, 2145-53.
- SCHASFOORT, R. B. M. & TUDOS, A. J. (Eds.) (2008) *Handbook of Surface Plasmon Resonance*, RSC Publishing.
- SCHRODER, A., SCHRODER, B., ROPPENSER, B., LINDER, S., SINHA, B., FASSLER, R. & AEPFELBACHER, M. (2006) *Staphylococcus aureus* fibronectin binding protein-A induces motile attachment sites and complex actin remodeling in living endothelial cells. *Molecular Biology of the Cell*, 17, 5198-5210.
- SCHUCK, P. (1997) Use of surface plasmon resonance to probe the equilibrium and dynamic aspects of interactions between biological macromolecules. *Annu Rev Biophys Biomol Struct*, 26, 541-66.
- SCHUCK, P. (2000) Size-distribution analysis of macromolecules by sedimentation velocity ultracentrifugation and lamm equation modeling. *Biophys J*, 78, 1606-19.
- SCHWARZ-LINEK, U., HOOK, M. & POTTS, J. R. (2004) The molecular basis of fibronectin-mediated bacterial adherence to host cells. *Molecular Microbiology*, 52, 631-641.
- SCHWARZ-LINEK, U., WERNER, J. M., PICKFORD, A. R., GURUSIDDAPPA, S., KIM, J. H., PILKA, E. S., BRIGGS, J. A. G., GOUGH, T. S., HOOK, M.,



- CAMPBELL, I. D. & POTTS, J. R. (2003) Pathogenic bacteria attach to human fibronectin through a tandem beta-zipper. *Nature*, 423, 177-181.
- SCHWARZBAUER, J. E. (1991) Identification of the fibronectin sequences required for assembly of a fibrillar matrix. *J Cell Biol*, 113, 1463-73.
- SCHWARZBAUER, J. E. & SECHLER, J. L. (1999) Fibronectin fibrillogenesis: a paradigm for extracellular matrix assembly. *Curr Opin Cell Biol*, 11, 622-7.
- SCHWARZINGER, S., KROON, G. J., FOSS, T. R., WRIGHT, P. E. & DYSON, H. J. (2000) Random coil chemical shifts in acidic 8 M urea: implementation of random coil shift data in NMRView. *J Biomol NMR*, 18, 43-8.
- SHEEHAN, D. (2000) *Physical Biochemistry: Principles and Applications*, John Wiley & Sons Ltd.
- SHINJI, H., YOSIZAWA, Y., TAJIMA, A., IWASE, T., SUGIMOTO, S., SEKI, K. & MIZUNOE, Y. (2011) Role of Fibronectin-Binding Proteins A and B in In Vitro Cellular Infections and In Vivo Septic Infections by *Staphylococcus aureus*. *Infect Immun*, 79, 2215-23.
- SIEPEN, J. A., RADFORD, S. E. & WESTHEAD, D. R. (2003) beta Edge strands in protein structure prediction and aggregation. *Protein Science*, 12, 2348-2359.
- SINHA, B., FRANCOIS, P. P., NUSSE, O., FOTI, M., HARTFORD, O. M., VAUDAUX, P., FOSTER, T. J., LEW, D. P., HERRMANN, M. & KRAUSE, K. H. (1999) Fibronectin-binding protein acts as *Staphylococcus aureus* invasin via fibronectin bridging to integrin alpha5beta1. *Cell Microbiol*, 1, 101-17.
- SOTTILE, J. & CHANDLER, J. (2005) Fibronectin matrix turnover occurs through a caveolin-1-dependent process. *Mol Biol Cell*, 16, 757-68.
- SOTTILE, J. & HOCKING, D. C. (2002) Fibronectin polymerization regulates the composition and stability of extracellular matrix fibrils and cell-matrix adhesions. *Mol Biol Cell*, 13, 3546-59.
- SOTTILE, J. & WILEY, S. (1994) Assembly of amino-terminal fibronectin dimers into the extracellular matrix. *J Biol Chem*, 269, 17192-8.
- SPRINGER, T. A., ZHU, J. H. & XIAO, T. (2008) Structural basis for distinctive recognition of fibrinogen gamma C peptide by the platelet integrin alpha(IIB)beta(3). *Journal of Cell Biology*, 182, 791-800.
- STANDEVEN, K. F., ARIENS, R. A. & GRANT, P. J. (2005) The molecular physiology and pathology of fibrin structure/function. *Blood Rev*, 19, 275-88.

- STEBBENS, W. E., DELAHUNT, B. & ZUCCOLLO, J. M. (2000) The histopathology of endocardial sclerosis. *Cardiovasc Pathol*, 9, 161-73.
- STENBERG, E., PERSSON, B., ROOS, H. & URBANICZKY, C. (1991) Quantitative-Determination of Surface Concentration of Protein with Surface-Plasmon Resonance Using Radiolabeled Proteins. *Journal of Colloid and Interface Science*, 143, 513-526.
- STEVENS, S. Y., SANKER, S., KENT, C. & ZUIDERWEG, E. R. (2001) Delineation of the allosteric mechanism of a cytidyltransferase exhibiting negative cooperativity. *Nat Struct Biol*, 8, 947-52.
- STICHT, H., PICKFORD, A. R., POTTS, J. R. & CAMPBELL, I. D. (1998) Solution structure of the glycosylated second type 2 module of fibronectin. *J Mol Biol*, 276, 177-87.
- STRONG, D. D., LAUDANO, A. P., HAWIGER, J. & DOOLITTLE, R. F. (1982) ISOLATION, CHARACTERIZATION, AND SYNTHESIS OF PEPTIDES FROM HUMAN-FIBRINOGEN THAT BLOCK THE STAPHYLOCOCCAL CLUMPING REACTION AND CONSTRUCTION OF A SYNTHETIC CLUMPING PARTICLE. *Biochemistry*, 21, 1414-1420.
- STURA, E. A. & WILSON, A. (1990) Analytical and production seeding techniques. *Methods* 1, 38-49.
- TIEMERSMA, E. W., BRONZWAER, S. L., LYYTIKAINEN, O., DEGENER, J. E., SCHRIJNEMAKERS, P., BRUINSMA, N., MONEN, J., WITTE, W. & GRUNDMAN, H. (2004) Methicillin-resistant *Staphylococcus aureus* in Europe, 1999-2002. *Emerg Infect Dis*, 10, 1627-34.
- TRACY, P. B., NESHEIM, M. E. & MANN, K. G. (1992) Platelet factor Xa receptor. *Methods Enzymol*, 215, 329-60.
- UHLEN, M., GUSS, B., NILSSON, B., GATENBECK, S., PHILIPSON, L. & LINDBERG, M. (1984) Complete sequence of the staphylococcal gene encoding protein A. A gene evolved through multiple duplications. *J Biol Chem*, 259, 1695-702.
- VANDERMERWE, P. A., BROWN, M. H., DAVIS, S. J. & BARCLAY, A. N. (1993) AFFINITY AND KINETIC-ANALYSIS OF THE INTERACTION OF THE CELL-ADHESION MOLECULES RAT CD2 AND CD48. *Embo Journal*, 12, 4945-4954.

- VELAZQUEZ-CAMPOY, A., LEAVITT, S. A. & FREIRE, E. (2004a) Characterization of protein-protein interactions by isothermal titration calorimetry. *Methods Mol Biol*, 261, 35-54.
- VELAZQUEZ-CAMPOY, A., OHTAKA, H., NEZAMI, A., MUZAMMIL, S. & FREIRE, E. (2004b) Isothermal titration calorimetry. *Curr Protoc Cell Biol*, Chapter 17, Unit 17 8.
- VENTERS, R. A., THOMPSON, R. & CAVANAGH, J. (2002) Current approaches for the study of large proteins by NMR. *Journal of Molecular Structure*, 602, 275-292.
- VRANKEN, W. F., BOUCHER, W., STEVENS, T. J., FOGH, R. H., PAJON, A., LLINAS, P., ULRICH, E. L., MARKLEY, J. L., IONIDES, J. & LAUE, E. D. (2005) The CCPN data model for NMR spectroscopy: Development of a software pipeline. *Proteins-Structure Function and Bioinformatics*, 59, 687-696.
- WAKSMAN, G. & HULTGREN, S. J. (2009) Structural biology of the chaperone-usher pathway of pilus biogenesis. *Nat Rev Microbiol*, 7, 765-74.
- WALSH, E. J., O'BRIEN, L. M., LIANG, X. W., HOOK, M. & FOSTER, T. J. (2004) Clumping factor B, a fibrinogen-binding MSCRAMM (microbial surface components recognizing adhesive matrix molecules) adhesin of *Staphylococcus aureus*, also binds to the tail region of type I cytokeratin 10. *Journal of Biological Chemistry*, 279, 50691-50699.
- WANG, A., ATHAN, E., PAPPAS, P. A., FOWLER, V. G., JR., OLAISON, L., PARE, C., ALMIRANTE, B., MUNOZ, P., RIZZI, M., NABER, C., LOGAR, M., TATTEVIN, P., IARUSSI, D. L., SELTON-SUTY, C., JONES, S. B., CASABE, J., MORRIS, A., COREY, G. R. & CABELL, C. H. (2007) Contemporary clinical profile and outcome of prosthetic valve endocarditis. *JAMA*, 297, 1354-61.
- WANN, E. R., GURUSIDDAPPA, S. & HOOK, M. (2000) The fibronectin-binding MSCRAMM FnbpA of *Staphylococcus aureus* is a bifunctional protein that also binds to fibrinogen. *Journal of Biological Chemistry*, 275, 13863-13871.
- WATANABE, I., ICHIKI, M., SHIRATSUCHI, A. & NAKANISHI, Y. (2007) TLR2-mediated survival of *Staphylococcus aureus* in macrophages: a novel bacterial strategy against host innate immunity. *J Immunol*, 178, 4917-25.

- WIDER, G. & WUTHRICH, K. (1999) NMR spectroscopy of large molecules and multimolecular assemblies in solution. *Current Opinion in Structural Biology*, 9, 594-601.
- WILLIAMSON, R. A., CARR, M. D., FRENKIEL, T. A., FEENEY, J. & FREEDMAN, R. B. (1997) Mapping the binding site for matrix metalloproteinase on the N-terminal domain of the tissue inhibitor of metalloproteinases-2 by NMR chemical shift perturbation. *Biochemistry*, 36, 13882-13889.
- WILSON, L. E., THOMAS, D. L., ASTEMBORSKI, J., FREEDMAN, T. L. & VLAHOV, D. (2002) Prospective study of infective endocarditis among injection drug users. *J Infect Dis*, 185, 1761-6.
- WINES, B. D., WILLOUGHBY, N., FRASER, J. D. & HOGARTH, P. M. (2006) A competitive mechanism for staphylococcal toxin SSL7 inhibiting the leukocyte IgA receptor, Fc alphaRI, is revealed by SSL7 binding at the C alpha2/C alpha3 interface of IgA. *J Biol Chem*, 281, 1389-93.
- WINN, M. D., BALLARD, C. C., COWTAN, K. D., DODSON, E. J., EMSLEY, P., EVANS, P. R., KEEGAN, R. M., KRISINEL, E. B., LESLIE, A. G., MCCOY, A., MCNICHOLAS, S. J., MURSHUDOV, G. N., PANNU, N. S., POTTERTON, E. A., POWELL, H. R., READ, R. J., VAGIN, A. & WILSON, K. S. (2011) Overview of the CCP4 suite and current developments. *Acta Crystallogr D Biol Crystallogr*, 67, 235-42.
- WINTER, G. (2009) xia2: an expert system for macromolecular crystallography data reduction. *Journal of Applied Crystallography*, 43, 186-190.
- WISHART, D. S., SYKES, B. D. & RICHARDS, F. M. (1991) Relationship between nuclear magnetic resonance chemical shift and protein secondary structure. *J Mol Biol*, 222, 311-33.
- WOLBERG, A. S. (2007) Thrombin generation and fibrin clot structure. *Blood Reviews*, 21, 131-142.
- WOODWARD, C. K. & HILTON, B. D. (1979) Hydrogen exchange kinetics and internal motions in proteins and nucleic acids. *Annu Rev Biophys Bioeng*, 8, 99-127.
- WUTHRICH, K. (1986) *NMR of Proteins and Nucleic Acids*, New York, Wiley-Interscience

- 
- WUTHRICH, K. (1998) The second decade--into the third millenium. *Nat Struct Biol*, 5 Suppl, 492-5.
- XIAO, T., TAKAGI, J., COLLER, B. S., WANG, J. H. & SPRINGER, T. A. (2004) Structural basis for allostery in integrins and binding to fibrinogen-mimetic therapeutics. *Nature*, 432, 59-67.
- YEE, V. C., PRATT, K. P., COTE, H. C. F., LETRONG, I., CHUNG, D. W., DAVIE, E. W., STENKAMP, R. E. & TELLER, D. C. (1997) Crystal structure of a 30 kDa C-terminal fragment from the gamma chain of human fibrinogen. *Structure*, 5, 125-138.
- ZONG, Y., XU, Y., LIANG, X., KEENE, D. R., HOOK, A., GURUSIDDAPPA, S., HOOK, M. & NARAYANA, S. V. (2005) A 'Collagen Hug' model for *Staphylococcus aureus* CNA binding to collagen. *EMBO J*, 24, 4224-36.
- ZUIDERWEG, E. R., HAMERS, L. F., ROLLEMA, H. S., DE BRUIN, S. H. & HILBERS, C. W. (1981) <sup>31</sup>P NMR study of the kinetics of binding of myo-inositol hexakisphosphate to human hemoglobin. Observation of fast-exchange kinetics in high-affinity systems. *Eur J Biochem*, 118, 95-104.